

Washington University in St. Louis
Washington University Open Scholarship

Engineering and Applied Science Theses &
Dissertations


McKelvey School of Engineering

Spring 5-15-2016

Modeling, Simulation, and Analysis of Lithium-Ion Batteries for Grid-Scale Applications

Matthew Thomas Lawder
Washington University in St. Louis

Follow this and additional works at: https://openscholarship.wustl.edu/eng_etds

 Part of the [Chemical Engineering Commons](#), [Environmental Engineering Commons](#), and the [Oil, Gas, and Energy Commons](#)

Recommended Citation

Lawder, Matthew Thomas, "Modeling, Simulation, and Analysis of Lithium-Ion Batteries for Grid-Scale Applications" (2016).
Engineering and Applied Science Theses & Dissertations. 164.
https://openscholarship.wustl.edu/eng_etds/164

This Dissertation is brought to you for free and open access by the McKelvey School of Engineering at Washington University Open Scholarship. It has been accepted for inclusion in Engineering and Applied Science Theses & Dissertations by an authorized administrator of Washington University Open Scholarship. For more information, please contact digital@wumail.wustl.edu.

WASHINGTON UNIVERSITY IN ST. LOUIS

School of Engineering & Applied Science
Department of Energy, Environmental, and Chemical Engineering

Dissertation Examination Committee:

Venkat R. Subramanian, Chair

Pratim Biswas, Co-Chair

Parag Banerjee

Babu Chalamala

Palghat Ramachandran

Yinjie Tang

Jay Turner

Li Yang

Modeling, Simulation, and Analysis of Lithium-Ion Batteries for Grid-Scale Applications

by

Matthew T. Lawder

A dissertation presented to the
Graduate School of Arts & Sciences
of Washington University in
partial fulfillment of the
requirements for the degree
of Doctor of Philosophy

May 2016

St. Louis, Missouri

© 2016, Matthew T. Lawder

Table of Contents

List of Figures	vi
List of Tables	xiii
Acknowledgements	xv
Abstract of the Dissertation	xx
Chapter 1 Introduction to Batteries and Battery Models	1
1.1 Motivation.....	1
1.2 Secondary Batteries	1
1.3 Advantages of Lithium-ion Batteries.....	2
1.4 Lithium-ion Battery Operation	3
1.5 Modeling the Battery Process	7
1.5.1 Single Particle Model	8
1.5.2 Porous Electrode Pseudo Two Dimensional Model.....	10
1.5.3 Other Battery Models	12
1.6 Battery Degradation.....	13
1.6.1 The Solid-Electrolyte Interface Layer	15
1.7 Scope of Dissertation and Research Objectives	17
Chapter 2 Computational Methods for Efficient Simulation of Battery Models	20
2.1 Reducing the Model.....	20
2.2 Model Reformulation.....	21
2.3 Perturbation and Switch DAE solving method.....	22
2.3.1 Initialization and Simulation Method.....	24
2.3.2 Example 1: Index-1 DAE (1 Algebraic and 1 Differential Variable).....	30
2.3.3 Example 2: Finite Difference Single Particle Lithium-ion Battery Model	35
Chapter 3 Analysis of Solar-Battery Hybrid Systems from Systems Level Modeling ...	39
3.1 The Need for Energy Storage with Solar Power	39
3.2 Systems Level Solar-Battery Model	43
3.2.1 Solar Component.....	44
3.2.2 Local Demand Load	46

3.2.3 Battery Component with Solid-Electrolyte Interface Layer.....	49
3.2.4 Technologic Metrics.....	51
3.2.5 Techno-Economic Analysis	53
3.3 Comparison of SPM and ECM.....	55
3.4 Single Day Case Study	57
3.5 The Standard Case (for autonomy and battery utilization studies).....	60
3.6 Simulation of the Battery-Solar Hybrid System.....	61
3.7 Results from Study A.....	61
3.7.1 Influence of Solar Intermittency.....	61
3.7.2 Autonomy and Utilization Results	62
3.7.3 Discussion from Study A	69
3.7.4 Conclusions from Study A	71
3.8 Results from Study B.....	72
3.8.1 Solar Irradiance Data.....	72
3.8.2 Irradiance Resolution Comparison.....	79
3.8.3 Technical Benefit of Energy Storage	81
3.8.4 Economic Value of Energy Storage	89
3.8.5 SEI Effects of Cycling on Battery Life	93
3.8.6 Demand Size and Type Effects	96
3.8.7 Discussion of Study B with Lifetime Economic Value	100
3.8.8 Conclusions from Study B	102
3.9 Conclusions to Solar-Battery Hybrid Modeling	104
Chapter 4 Optimization of Storage in Solar-Battery Hybrid System	105
4.1 Battery Management Systems	105
4.2 Optimal Model-based Protocols	109
Chapter 5 Analysis of Batteries under Electric Vehicle Constraints	115
5.1 Electric Vehicle Battery Modeling	115
5.1.1 P2D Model with SEI Layer Growth.....	116
5.2 Comparison of SEI Growth Expressions	118
5.3 EV Driving Cycles.....	121
5.4 EV Charging Characteristics	124
5.5 Results and Discussion	125
5.5.1 SEI Growth Results	129

5.6 Conclusions.....	137
Chapter 6 Experimental Analysis of Capacity Fade.....	139
6.1 Value of LiFePO ₄ cells	139
6.2 Methods	141
6.2.1 Equipment	141
6.2.2 Procedure.....	142
6.3 Experimental Cycling Results	143
6.3.1 Initial Fade Rate as a Function of Cycling Rate.....	146
6.3.2 Analyzing Fade Characteristics.....	149
6.3.3 Extending Battery Life through Secondary Applications	151
6.3.4 Effect of Charge and Discharge on Capacity Fade	156
6.4 Discussion.....	157
6.4.1 Energy Capacity Increases through Application Switching.....	159
6.4.2 Added Lifetime Value	160
6.5 Conclusions.....	163
Chapter 7 Conclusions and Future Directions	165
7.1 Efficient Simulation of Battery Models.....	165
7.2 Advances to the Solar-Battery Hybrid Model	166
7.3 Advances to the EV Battery Model	169
7.4 Advances to Model-based Optimization	170
7.5 Experimental Cycling	172
References	174
Appendix A: Additional Examples of the Perturbation and Switch Method.....	187
A.1: Wu and White Problem	187
A.2: Implicit ODE converted to DAE solved with Explicit Solver.....	189
A.3: Partial Differential Equation Discretized to DAEs.....	191
Appendix B: Methods for Optimization	194
B.1 Optimization Simulation: Objectives and Constraints.....	194
B.2 Graphical User Interface for Battery Optimization.....	196
Appendix C: Drive Cycles	200
Appendix D: List of Abbreviations & Variables.....	204

Curriculum Vitae 207

List of Figures

Figure 1-1: Schematic of Li-ion battery.....	4
Figure 1-2: Single CC-CV charge and CC discharge cycle from the SPM at a 1C rate.....	5
Figure 1-3: Discretization of the battery for modeling and a schematic showing the physical processes occurring during battery operation. For explanation of the processes labeled by number please read the text.....	10
Figure 1-4: Possible mechanisms leading to capacity loss within the battery.....	14
Figure 1-5: A schematic of the SEI layer growth process.	16
Figure 2-1: Diagram of the proposed single-step approach.....	29
Figure 2-2: Comparison of different q values for the switch function.	31
Figure 2-3: Comparison of Example 1 solution for two-step perturbation approach and proposed single-step approach.....	33
Figure 2-4: Initialization portion of the single-step simulation showing different initial guesses for the algebraic variable (z) from Example 1.....	34
Figure 2-5: Initialization portion of the single-step simulation showing different perturbation values for the algebraic variable (z) from Example 1.	34
Figure 2-6: SPM concentration solutions for $N=5$	37
Figure 3-1: Concept showing the use of energy storage with renewables.....	40
Figure 3-2: Control hierarchy for power flow through solar-battery hybrid system.	44
Figure 3-3: Comparison of ECM to SPM over 10 cycles.....	57
Figure 3-4: Solar array plus battery storage with trapezoidal demand. A) Power from solar array is shown in conjunction with the demand of grid and the output of the system. B) Shows distribution of power that is supplied directly from solar array and power supplied from battery.....	58
Figure 3-5: Solar array plus battery storage with trapezoidal demand. In this case the system cannot meet demand at all times. A) Power from solar array is shown in conjunction with the demand of grid and the output of the system. B) Shows distribution of power that is supplied directly from solar array and power supplied from battery.	59
Figure 3-6: SOC for cases in Figures 3-4 and 3-5.	59
Figure 3-7: Sinusoidal approximation versus real data from Phoenix site July 18th, 2012. ¹³²	62

Figure 3-8: Autonomy and uncaptured solar energy for solar array with no storage and constant demand.....	63
Figure 3-9: Autonomy and battery utilization of constant demand for different battery sizes.....	64
Figure 3-10: Autonomy and battery utilization of each of the four demand types under the same sized system (BCSC 0.5).....	65
Figure 3-11: Autonomy and battery utilization based on timing of trapezoidal demand. The time represents the trapezoid's variation from maximum solar insolation.....	66
Figure 3-12: Autonomy for TOU demand shape with different amounts of daily demanded energy and length of TOU demand. Solar array of 30.5kW and battery of 116.5kWh.	67
Figure 3-13: Battery Utilization for TOU demand shape with different amounts of daily demanded energy and length of TOU demand. Solar array of 30.5kW and battery of 116.5kWh. Note the reversed x-axis (demand) for highlighting the plot's contours.....	68
Figure 3-14: Autonomy for parabolic demand shape with different amounts of daily demanded energy and length of parabolic demand. Solar array of 30.5kW and battery of 116.5kWh.....	68
Figure 3-15: Battery Utilization for parabolic demand shape with different amounts of daily demanded energy and length of parabolic demand. Solar array of 30.5kW and battery of 116.5kWh. Note the reversed x-axis (demand) for highlighting the plot's contours.	69
Figure 3-16: Normalized battery lifetime cost as a function of average DOD and increase in nominal life due to shallower DOD (shown as nominal cycle life slope). All costs are normalized to the cost of a 100% DOD system. The black line represents no change in nominal cycle life due to shallower DOD (Nominal Cycle Life Slope=1). Assumes a linear approximation of nominal cycle life as a function of DOD.	71
Figure 3-17: Map of sites from Study B.....	73
Figure 3-18: Variation in irradiance patterns for Phoenix in July 2012.	74
Figure 3-19: Difference between satellite and ground-based insolation yearly average by site as a function of ground based yearly insolation average, showing a mild but statistically significant (p-value=0.006) correlation.....	76
Figure 3-20: Strong inverse correlation between average daily insolation and average daily variation of irradiance.....	76

Figure 3-21: Los Angeles (A) and Swink (B) Irradiance patterns for 2012.	78
Figure 3-22: Irradiance data from LA on July 7th, 2011 for minute, hour, and daily resolution.....	80
Figure 3-23: Strong correlation between average daily insolation and site autonomy without storage.....	82
Figure 3-24: Autonomy and battery utilization as a function of battery energy storage capacity for Milford in 2012 with a 30.5kW solar array and a sinusoidal demand of 100kWh of daily energy.....	83
Figure 3-25: Solar power generated, solar power unused by system, and battery SOC during March 14-21, 2012 at the Milford site under the standard case.	84
Figure 3-26: Monthly autonomy and battery utilization for Milford 2012 under the standard case.	86
Figure 3-27: Strong correlation between average daily insolation and added autonomy from 50kWh of battery storage.	87
Figure 3-28: Autonomy and battery utilization values for all sites under the standard case.	88
Figure 3-29: Yearly site autonomy, battery utilization, and percentage of energy supplied from battery as a function of ground-based average daily insolation for all sites.	89
Figure 3-30: Diagram of time-of-use pricing setup.	90
Figure 3-31: Economic value under TOU pricing in 2012 for all sites.	91
Figure 3-32: Strong correlation between average daily insolation and the economic value under TOU pricing without storage and no statistically significant correlation between average daily insolation and economic value from 50kWh of added storage.	91
Figure 3-33: Strong correlation between the amount of solar power generated coincident with on-peak demand and relative value added from storage.....	92
Figure 3-34: Mild correlation between absolute value added from storage and the amount of SEI layer growth.....	95
Figure 3-35: SEI layer growth for three sites in 2012 under TOU pricing scenario. SEI layer growth is normalized to the amount of growth experience by LA.	95
Figure 3-36: Autonomy and battery utilization demand as a function of total daily demanded energy for a system of 30.5kW solar array and 116.5kWh battery at Lowry Range in 2011 with Sinusoidal demand.....	96

Figure 3-37: Autonomy and battery utilization demand as a function of total daily demanded energy for a system of 30.5kW solar array and 116.5kWh battery at Lowry Range in 2011 with TOU demand.....	98
Figure 3-38: SOC values for TOU and sine demand from April 1-10, 2011 at Lowry Range with battery energy capacity was 116.5kWh and solar array was 30.5kW and 100kWh of energy demanded.....	99
Figure 3-39: SOC values for TOU and sine demand from April 1-10, 2011 at Lowry Range with battery energy capacity was 116.5kWh and solar array was 30.5kW and 200kWh of energy demanded.....	99
Figure 3-40: Break even battery installation prices for Lowry Range (using 2011 data) as a function of two-tiered TOU price difference and nominal battery cycle life.	102
Figure 4-1: Schematic for the implementation of a battery pack and BMS into a BESS.....	107
Figure 4-2: Different charging patterns for a battery powered from a solar array with different optimization objectives and constraints. The solid line (red) shows standard charging with no optimization constraints; the dashed line (green) attempts to maximize the charge stored while not increasing fade from the standard case; and the dashed-dotted line (blue) reduces capacity fade to 90% of the standard charging case while maximizing the amount of charge stored. The solar irradiance curve and demand curve are shown as well.	111
Figure 4-3: Normalized SEI layer growth as a function of SOC during the charging cycle for the three cases.	112
Figure 4-4: Comparison of energy benefit per cycle and over the complete life of the battery.	113
Figure 5-1: SEI growth shown for charging at 1C, C/4, and C/8 rates for three SEI growth mechanisms. SEI growth is scaled and normalized for the total growth over one charging cycle to be equal across cases.	118
Figure 5-2: SEI layer growth during the DST driving cycle for each SEI growth mechanism over a complete discharge. Time has been scaled over the entire discharging cycle (Note: Regenerative charging will occur during the driving cycle). SEI growth is scaled and normalized for the total growth over one discharge cycle to be equal across cases.....	119
Figure 5-3: The power and velocity seen under vehicle conditions shown in Table 5-2 for the ECE-15 drive cycle.	122
Figure 5-4: The power and velocity seen under vehicle conditions shown in Table 5-2 for the UDDS drive cycle.	123

Figure 5-5: SEI growth over a single charge-discharge cycle, for six different rates of CC-CV charging. The discharge cycle in all cases was the standard DST driving cycle. “Total Charge Energy” is scaled based on the total amount of energy used to charge the battery (including regenerative charging during the discharge cycle). SEI growth is scaled and normalized for the total growth over one charge-discharge cycle to be equal across cases.124

Figure 5-6: Percentage of total VMT driven using the all-electric mode for different PHEV (assuming charge depletion).....128

Figure 5-7: Amount of daily VMT for American vehicles. Blue represents all vehicles drive less than 15 miles per day. Blue and Red represent all vehicles driven less than 30 miles per day, etc.128

Figure 5-8: SEI growth for all 8 driving cycles for two hours of driving. The SEI growth was scaled to the amount of growth from the NEDC case over two hours in order to show a relative comparison among the driving cycles.....129

Figure 5-9: SEI growth for all 8 driving cycles for 30km of driving. The SEI growth was scaled to the amount of growth from the NEDC case over 30 km in order to show a relative comparison among the driving cycles.130

Figure 5-10: SEI growth over multiple driving cycles using the HWFET driving cycle for differing DOD. Only SEI growth during discharging is shown (no charging growth). The SEI growth is measured in comparison to the amount of discharged energy since more energy will be discharged during a deeper DOD (and we would expect more SEI layer growth). This method allows for comparison between cases even though they stored different amounts of energy during a single cycle. The discharge energy and SEI growth is scaled to the amount seen during two cycles of 100% DOD. For all cases discharge will begin at 100% SOC.133

Figure 5-11: SEI growth over multiple driving cycles using the UDDS driving cycle for differing DOD. Only SEI growth during discharging is shown (no charging growth). The SEI growth is measured in comparison to the amount of discharged energy since more energy will be discharged during a deeper DOD (and we would expect more SEI layer growth). This method allows for comparison between cases even though they stored different amounts of energy during a single cycle. The discharge energy and SEI growth is scaled to the amount seen during two cycles of 100% DOD. For all cases discharge will begin at 100% SOC.134

Figure 5-12: SEI growth over multiple driving cycles using the UDDS driving cycle for differing DOD. Only SEI growth during discharging is shown (no charging growth). The SEI growth is measured in comparison to the amount of discharged energy since more energy will be discharged during a deeper DOD (and we would expect more SEI layer growth). This method allows for comparison between cases even though they stored

different amounts of energy during a single cycle. The discharge energy and SEI growth is scaled to the amount seen during two cycles of 100% DOD. For all cases discharge will end at 0% SOC.....	135
Figure 5-13: SEI growth over 500 charge-discharge cycles (100% DOD) for the HWFET, NEDC, and UDDS driving cycles. The SEI growth was scaled to the amount of growth from the NEDC case over 500 cycles in order to show a relative comparison among the driving cycles.....	136
Figure 6-1: Variability of Capacity for cells cycled at 3C (Tests 5, 14-16, and 19-21).	144
Figure 6-2: Correlation between the capacity fade and initial capacity or first 100 cycle slope.	145
Figure 6-3: Capacity loss per cycle for Test 6.	147
Figure 6-4: The average capacity fade per cycle for the first 1,000 cycles of operation for all tests as a function of cycling rate.	148
Figure 6-5: The capacity fade per cycle for the first 1,000 cycles for different rates (Test 2, 3, 5, and 6).	148
Figure 6-6: The Capacity fade for all control cycles. (Tests 1-7).	151
Figure 6-7: Simulated and Experimental capacity fade rates for tests 12 and 13.	155
Figure 6-8: Simulated and Experimental Capacity for tests 12 and 13.	155
Figure 6-9: Capacity for Tests 1, 2, and 6-11.	157
Figure 6-10: Voltage discharge curves for first 500 cycles of test 9.	158
Figure 6-11: Voltage discharge curves for first 500 cycles of test 11.	159
Figure 6-12: Voltage curve before and after switch.	160
Figure 6-13: Value Ratio for Test 6.	161
Figure 6-14: Value Ratio for Test 12 (Primary storage value of \$0.40/kWh and Battery cost of \$800/kWh) with three different secondary storage values (\$0.25/kWh, \$0.15/kWh, and \$0.05/kWh) as well as the value ratio for the cell simulated remaining in primary storage (\$0.40/kWh).	163
Figure A-1: Solution to Example 1.	189
Figure A-2: Solution to Example 2.	190
Figure A-3: Solution to Example 3 for $N=2$ and $N=11$ at four different x -values.	193
Figure B-1: GUI for battery optimization.	197

Figure B-2: Results from the GUI.198

Figure B-3 Two comparisons of different cases.199

List of Tables

Table 1-1: Secondary battery characteristics. ^{5,6}	3
Table 1-2: Summary of several battery models. EC stands for electrochemical.	8
Table 2-1: Parameters for SPM.....	36
Table 2-2: Computational time for solving concentration profiles in Example 5 using Maple's dsolve. Standard finite difference fails to solve SPM beyond N=50.	38
Table 3-1: Demand curves studied.	48
Table 3-2: SPM model equations including SEI reaction. ^{13, 15, 41, 115, 116}	50
Table 3-3: Parameters for SPM model.....	51
Table 3-4: Battery Utilization for the maximum power output demanded that still yields 100% autonomy for each of the four types of demand under three different battery sizes.....	63
Table 3-5: Site information for each site studied. Autonomy values are averaged over all years of data for each site and the w/ Storage values include 116.5kWh of battery storage capacity.....	75
Table 3-6: Results of standard case simulations for Los Angeles and Oak Ridge in 2011 using 1-minute and 1-hour resolution irradiance patterns.	80
Table 3-7: Comparison of monthly SEI growth for 1-minute and 1-hour resolution for Oak Ridge in 2011.	81
Table 5-1: When completing a full charge-discharge cycle, the SEI growth contributed will be less than the amount contributed through CC-CV charging. This table shows the percentage of total SEI growth that the DST driving cycle contributes one a single charge-discharge cycle when charging rates are 1C, C/4, and C/8.....	119
Table 5-2: Parameters used for converting velocity profiles into power profiles for use in electric batteries. ^{168, 169}	123
Table 5-3: Characteristics of 2013 production EV batteries. ^{158, 179-187} *The Prius-Plug-in energy capacity is an estimated amount. *The Honda Fit EV is only available to lease.	127
Table 5-4: Characteristics for the eight drive cycles studied. Average velocity, duration, distance, and R-P Ratio are the characteristic for one driving cycle (not repeated unless end of discharge) while the remaining categories show values for drive cycles repeated unless battery has reach 100% DOD.	

Regen Energy Added is the percentage of energy gained during the driving cycle, compared to the amount from a full charge. Regen SEI Added is the percentage of SEI layer thickness gained during the driving cycle, compare to the amount from a full charge cycle. R-P Ratio is the ratio of regenerative energy during a driving cycle to the amount of energy used for vehicle propulsion during a driving cycle. SEI growth/ min and SEI growth/ km are scaled to the amount of SEI growth/min and SEI growth/ km of the NEDC cycle. These value represent a relative comparison of how much growth each driving cycle will accumulate per min or km. *DST characteristic were back calculated from Power curve.....131

Table 5-5: Summary of the ratio of SEI layer growth for different DOD in comparison to 100% DOD for all eight driving cycles beginning at 100% SOC for all cases.	133
Table 6-1: Summary of Tests.....	143
Table 6-2: Characteristics of capacity fade before (pre-) and in accelerated fade regime. Test 1-4 currently under continued cycling to verify the result.....	151
Table 6-3: Lifetime Energy added by switching application.....	156
Table 6-4: Summary of increase in discharged energy after switching applications.	160
Table A-1: Parameters for Nickel Hydroxide Electrode.....	188
Table A-2: Comparison of working ranges of initial algebraic guess for Example 2 using different solvers. The Maple dsolve approach uses Maple’s rkf45 method. 49, 50, 212, 213	189

Acknowledgements

Over the four and half year I have studied at Washington University in St. Louis, I have received advisement, help, and support from numerous people and organizations for which I am very grateful. I hope to recognize as many of you as possible here. First and foremost, Professor Subramanian, you have always provided a great balance between involved advisor, enthusiastic supporter, and empathetic mentor. I can remember joining the M.A.P.L.E. lab during my first year and you saying that, “I think we should do something with solar modeling” and then giving me the leeway to figure out how to connect solar to our battery models. It took a few false starts to figure out how that would work and I thank you for your patience during that first year, but it ultimately led to the work that follows in this dissertation. You’ve always been very supportive of testing out new ideas and I think that has greatly benefited the lab and led to some of the best work we have been able to produce. I know that it was difficult over this final year after most of the group moved to Seattle, but I think we have done a good job of staying on top of our projects and expanding into new areas.

I would also like to thank Professor Biswas, especially since the move, you have been immensely helpful in staying involved and on track this past year. You have always been very supportive of the solar and storage initiatives and have given me many opportunities outside of the lab to continue to grow my knowledge. I would also like to acknowledge the rest of my committee for their advisement during my time at Washington University in St. Louis. Professor Turner, I enjoyed my rotation in your lab and getting my first taste of graduate student research. You were always very personable and easy to work with. Professor Banerjee, it has been great to work together on the SEES initiative and I hope that we will be able to celebrate having a global test facility soon. Dr. Chalamala, your industry expertise has been of great help and always

inspired me to remember that the systems we are modeling need to work in the real world. Professor Ramachandran, you taught my first ever graduate level course and it was a pleasure to learn transport phenomena from you. Professor Yang and Professor Tang, while I have only had limited interaction with both of you, I thank you for your support and feedback.

I would like to acknowledge funding sources that made this work possible including the US Department of Energy-Advanced Research Projects Agency-Energy award #DE-AR0000275 and the Solar Energy Research Institute for India and the U.S. (SERIUS) funded jointly by the U.S. Department of Energy subcontract DE AC36-08G028308 (Office of Science, Office of Basic Energy Sciences, and Energy Efficiency and Renewable Energy, Solar Energy Technology Program, with support from the Office of International Affairs) and the Government of India subcontract IUSSTF/JCERDC-SERIIUS/2012 dated 22nd Nov. 2012.

To the members of the M.A.P.L.E lab past and present you have truly inspired me over the years to become a better engineer. The lab was much smaller when I first joined. Venkat R. and Paul were instrumental in learning the ropes of the lab. Sitting next Paul was the best resource I could of asked for when I was first learning the modeling process. Thank you for answering all of those questions both simple and complicated. Also, it was great to have another sports fan in the lab and I really enjoyed starting up all the intramural sports for the department with you. Venkat, I really don't know how we continued to run the lab after you left, you did so many thing in addition to the research to make the lab run smoothly. Also, thank you to you (and the rest of the lab) for introducing me to so much great Indian food. Sumitava, I appreciated your help on projects and going to the Scottish Arms hasn't been the same since you left. Bharat, you are the only person who has been in the lab during my entire time here. You have been

invaluable as a colleague and as a friend. I will miss working with you and our conversations beyond just batteries.

Nathan, anytime you want to race again, I'll be ready. Seongbeom, I'm glad you'll be taking over some of the MapleSim models. It's been great teaching you the models. Derek, it was great having you in the lab and I hope your transition into the Biswas lab continues to go smoothly. Manan, while we didn't get to work together too long, I enjoyed my time with you and catching up at ECS conferences since the move. Thaigu, it was nice to finally have someone working in the wet lab with me. I'd also like to thank the members of AARQL, they have been very gracious in welcoming me into the lab over the past year. It's been great to get to work with all of you.

I would also like to mention Phil Valko and everyone involved with the Office of Sustainability. Phil, you offered me a wonderful opportunity to get outside of the lab and work across a wide range of interesting areas. I have learned so much from working with you and your endless energy to tackle sustainability issues is inspiring.

My work inside the lab has only been made possible by the support of my family and friends. Thank you to all my friends in the department (too many to name) and outside the department. To my friends at the Big River Racing team, running with you guys has been the best stress relief out there and kept my mind from exploding at times from the work load at the university. Mom and Dad, there is nothing I could say here to adequately thank you for everything you have done for me. You started me down this academic path from a young age and have been supportive of my endeavors for so many years. Linda you gave me the drive needed to complete a PhD. I wouldn't have been able to finish without you instilling your competitive spirit in me. Kevin you have always been available to talk and hang out. You have been a great

outlet to take my mind off of work. John, it's great to have another scientist in the family. Your quiet work ethic and laid back style is something that I have tried to incorporate more in my life.

Finally, Allie (and Abigail), two years ago I could not have imagined how amazing my life is today and so much of it is because of you. You keep me intellectually challenged and have broadened my horizons. So many of my wonderful experiences over the last two years have been because of you. Thank you so much for your support.

Dedicated to My Family

ABSTRACT OF THE DISSERTATION

Modeling, Simulation, and Analysis of Lithium-Ion Batteries for Grid-Scale Applications

by

Matthew T. Lawder

Doctor of Philosophy in Energy, Environmental, and Chemical Engineering

Washington University in St. Louis, 2016

Professor Venkat R. Subramanian, Chair

Professor Pratim Biswas, Co-Chair

Lithium-ion batteries have become universally present in daily life, being used across a wide range of portable consumer electronics. These batteries are advantageous compared to other forms of energy storage due to their high energy density and long cycle life. These characteristics make lithium-ion batteries advantageous for many new and developing applications that require large scale energy storage such as electric vehicles and the utility grid. Typical uses for lithium-ion batteries require consistent cycling patterns that are predictable and easy to approximate across all uses, but new large scale applications will have much more dynamic demands. The cycling patterns for electric vehicles will vary based on each individual's driving patterns and batteries used for energy storage in the grid must be flexible enough to account for continuous fluctuations in demand and generation with little advanced notice. Along with these requirements, large scale applications do not want to sacrifice on cycle life and need to know that adding batteries will make operational and economic sense in specific cases.

It is not possible to experimentally validate every possible driving pattern or grid storage need because of the great expense of these large systems and the long timescale required for testing. Therefore modeling of these systems is advantageous to help study specific application

constraints and understand how lithium-ion batteries operate under those constraints. A systems level model is developed to study lithium-ion battery systems for use with solar energy (in a solar-battery hybrid system) and electric vehicles. Electrochemical based battery models are used as a component within larger systems. To facilitate fast simulation a single step perturbation and switch method is outlined for increasing the speed and robustness of solving the systems of DAEs that result from the systems level model.

Operational characteristics are studied for lithium-ion batteries used to store solar energy within the electric grid. Different grid demands are tested against the system model to better understand the best uses for the solar-battery hybrid system. Both generic site studies and site specific studies were conducted. Solar irradiance data from 2010-2014 was obtained from 10 US based sites and used as an input to the system model to understand how the same system will operate differently at various locations. Technological benefits such as system autonomy were simulated for each site as well as economic benefits based on a time-of-use pricing scenario. These models included the growth of the solid-electrolyte interface layer on the battery electrodes to measure capacity fade during operation. This capacity fade mechanism allowed tracking of the site specific effects on battery life.

A systems level model for an electric vehicle was also developed to simulate the growth of the SEI layer caused from different types of driving cycles and charging patterns. Results from both system models are presented along with an optimization method for the solar-battery hybrid model. In addition to modeling, experimental tests of LiFePO_4 lithium-ion battery cells were conducted to measure capacity fade associated with different types of cycling throughout a battery's life. Cycling protocols were tested to study traditional capacity fade and also to focus on increasing a cell's lifetime benefit through application switching.

Chapter 1

Introduction to Batteries and Battery Models

1.1 Motivation

The need for battery storage has grown rapidly in the past decade as the need for more portable and flexible power has expanded. Many of these new needs have been met with Lithium-ion (Li-ion) batteries. The market for Li-ion batteries has grown at 25% per year from 2000-2012 going from only 2GWh of global storage capacity in 2000 to 34GWh of storage capacity in 2012.¹ Over the same time the price for Li-ion cells has dropped by over an order of magnitude, helping to increase their usage.

While the first types of applications that used Li-ion batteries were small portable electronic devices with low energy and power needs, the need for large scale battery storage continues to grow. Electric vehicles (EV) require large amounts of portable energy capacity and the electric grid requires energy storage to smooth renewable energy and make generation more flexible. These types of applications require efficient and long lasting batteries that are useful across a wide range of cycling patterns. Understanding how batteries are operating in these new scenarios and how their life is being affected by different applications is of utmost importance if batteries are to continue to grow and meet the needs and desires of society.

1.2 Secondary Batteries

There are two main types of batteries, primary cells, which can only be discharged a single time, and secondary cells, which can go through many cycles of charge and discharge. Secondary cells have become more prominent over the last two decades because of their use in portable electronic devices, electric and plug-in vehicles, and large scale energy storage. Many

different chemistries have been studied for secondary batteries with the Li-ion being one of the most prominently used systems today.

1.3 Advantages of Lithium-ion Batteries

Li-ion batteries have become popular in many applications due to their high energy density which allows them to be used in portable devices. Earlier versions of electrochemical energy storage could not hold enough charge to power the devices in use today while allowing them to remain portable. The first galvanostatic cell was created by Alessandro Volta in 1800 when he stacked zinc and silver disks between a sodium chloride soaked cloth. Advancing from this primary cell, the lead-acid battery became the first rechargeable system when it was created in 1859 by Gaston Plante.² While lead-acid batteries were novel at the time, they suffered from low energy density and would fail at meeting the demands of many power and energy hungry electronic devices in today's world. Nickel-Cadmium (Ni-Cd) was proposed as an alternative chemistry in the early 1900's and Nickel Metal Hydride (NiMH) became prominent in the latter half of the century. Both batteries improved upon the lead-acid battery's energy density and were used in many first generation consumer electronics and hybrid vehicles. But Ni-Cd and NiMH suffered from several deficiencies. Both nickel and cadmium are toxic materials and the cell voltage for both types of batteries is only 1.2V which limits the energy and power density for these chemistries.

Searching for a material that could store more energy, lithium metal was investigated because it is a lightweight metal with a high electropositive potential (which leads to high storage densities).³ When early lithium batteries were introduced, their weight and volume energy densities were about double that of Ni-Cd.⁴

1.4 Lithium-ion Battery Operation

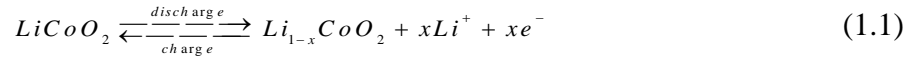
The term Li-ion battery actually encompasses many different chemistries that all have a lithium based electrode as part of their system and transfer charge between electrode using lithium ions. Table 1-1 shows a list of different possible battery chemistries (including non-lithium chemistries) and some of their characteristics. All Li-ion systems will be made up of a cathode (positive electrode), separator, and anode (negative electrode), with an electrolyte in all three regions (shown in Figure 1-1). The cathode is typically made of a lithium metal oxide, while the anode is usually a graphite compound. The electrolyte contains a lithium salt (LiPF₆, LiBF₄, etc.) in an organic solvent (commonly ethylene carbonate) allowing for the transport of lithium ions between the electrodes. The separator allows for the electrolyte to flow between the electrodes, but keeps the two electrodes apart to prevent short circuits.

Table 1-1: Secondary battery characteristics.^{5,6}

Chemistry	Nominal Voltage (V)	Specific Energy (Wh/kg)	Charging Efficiency	Comments
NiCd	1.2	45-80	60%	High self-discharge; Maintenance required; Toxic material
NiMH	1.2	60-120	60%	High self-discharge; Low nom. voltage; Toxic material
Lead-Acid	2.0	30-50	75%	Low energy density; Short cycle life
Li-ion			95%+	
<i>LiCoO₂</i>	3.8	150-200		Safety risk
<i>LiMn₂O₄</i>	3.8	100-150		Safe and cheap; Short cycle life
<i>LiNiMnCoO₂</i>	3.6	150-220		High energy density; Safety risk
<i>LiFePO₄</i>	3.2	90-120		Long cycle life; Low energy density
<i>Li₄Ti₅O₁₂</i>	2.2	60-75		High power rating; Low nom. voltage

Energy is stored in the battery based on the electrochemical potential of the electrode materials. Lithium cobalt oxide (LiCoO₂) was one of the first feasible cathode materials for reversible reactions using lithium ions. John Goodenough and Koichi Mizushima discovered the potential for this material in 1980⁷, but the first commercially available Li-ion batteries, using a

LiCoO₂ cathode and a graphite anode, were not produced until 1991. Lithium metal was first tested as an anode complement to LiCoO₂, but these anodes formed dendrites and often failed after a small amount of cycles. The LiCoO₂ cathode chemistry remains the most common chemistry for consumer electronics batteries.⁸ In this type of Li-ion battery the following reaction takes place at the cathode:



with an electrochemical potential of 3.9V (compared to the base Lithium Reaction). At the graphite based anode the reaction is:

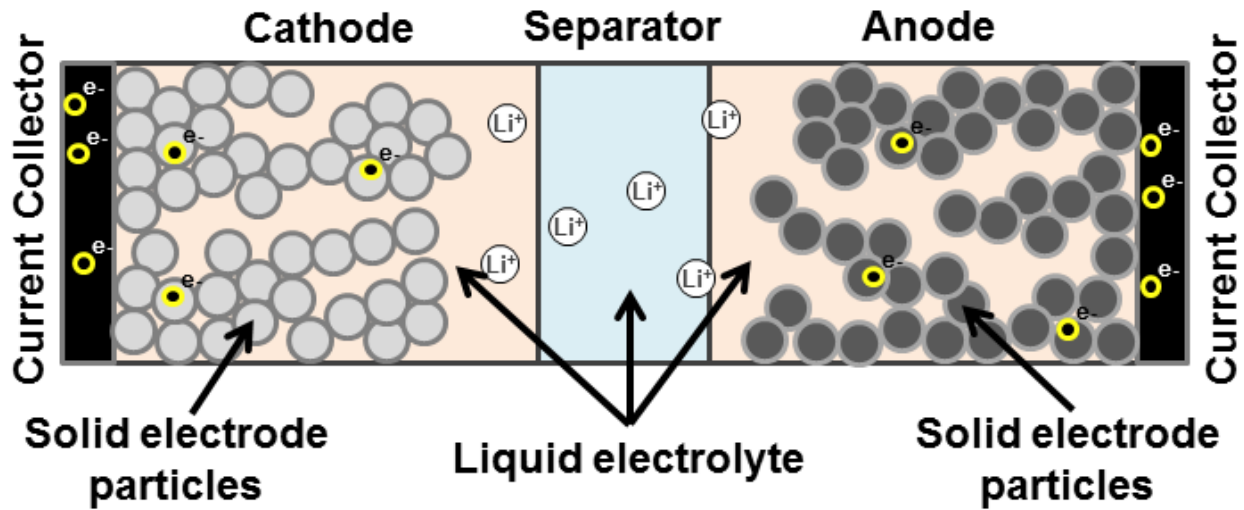
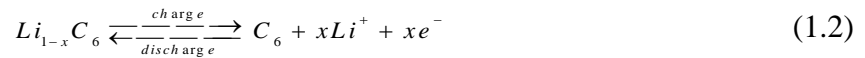


Figure 1-1: Schematic of Li-ion battery.

with an electrochemical potential of 0.1V (compared to the base Lithium Reaction).⁹ Combining these electrodes create a cell potential of 3.8V. This value is the nominal cell voltage. During normal operation of the battery the voltage will fluctuate between 4.2 and 2.5V based on the State-of-Charge (SOC) of the battery and the charge rate (See Figure 1-2).

At both electrodes the reaction occurring is an intercalation/deintercalation reaction where the lithium is inserted/removed between layers of the host material. The lithium attaches in between layers of the graphite for the anode and the metal oxide for the cathode allowing for an easily reversible reaction because the basic structure is not greatly altered.¹⁰ Rather than rearranging the atoms during the reaction, the lithium inserts within the existing structure. This process will cause the material to expand (although a perfect intercalation material would exhibit no expansion) and adds stress to the material which can lead to fracturing, delamination, or exfoliation. Many commonly used electrodes have been chosen because, in addition to their chemical stability, they have limited expansion caused by intercalation. Reducing expansion remains a challenge for researchers working with new electrode materials. Silicon has shown promise as a replacement for a graphite anode because it can hold much more energy, but expansion during insertion of the lithium into silicon causes rapid degradation of electrodes reducing their viability.¹¹

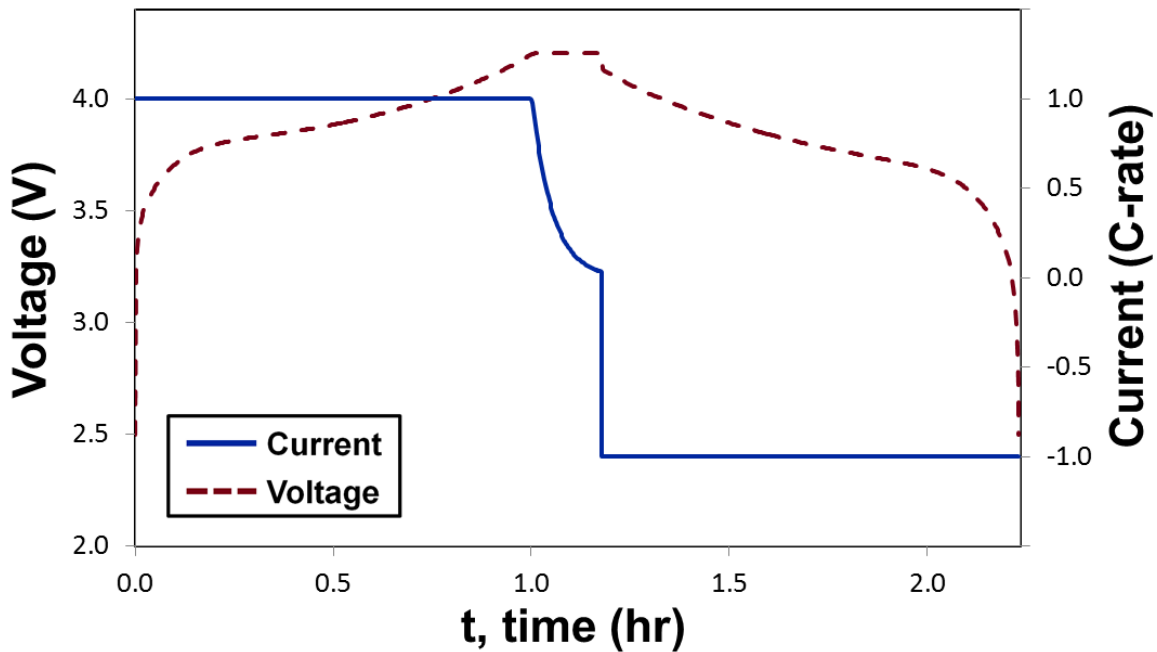


Figure 1-2: Single CC-CV charge and CC discharge cycle from the SPM at a 1C rate.

Originally, lithium metal was tested as an anode material coupled with a lithium metal oxide cathode. However, using a graphite anode which allows for lithium to be hosted in between its layers with minimal expansion is favorable to using metal lithium because the pure lithium will form dendrites during cycling which can reach into and across the separator leading to short circuiting, thermal runaway, and degradation.¹²

During cycling, charge is carried between the two electrodes by lithium ions within the electrolyte. During deintercalation, lithium undergoes a topochemical reaction with a lithium ion being formed in the electrolyte and the resulting free electron migrating to the current collector where it will pass through the external circuit. In order to facilitate better cycling, the electrodes are a porous material, so that there will be a large surface area between the electrolyte and electrode for intercalation/deintercalation reactions to occur. While total energy capacity will be primarily dependent on the mass and chemistry of the electrode materials, the surface area of the electrodes (along with the transport properties of the electrolyte and cell geometry) will play a greater part in determining the power density of the battery. Larger surface area is required to allow more electrode reactions to occur simultaneously.

During the discharging process, lithium deintercalates from the cathode, and is transported across the separator in the form of an ion while the resulting electron performs work in the external circuit, eventually reaching the anode. The lithium ion will again react with the electron, this time intercalating into the anode. A schematic of this process is shown in Figure 1-3 (see Section 1.5.2). During intercalation, the reverse of this process occurs with external energy facilitating the reactions.

Figure 1-3 shows 1) lithium diffusing through the solid electrode particles; 2) free electrons from the deintercalation reaction moving through the electrode; 3) the deintercalation

reaction occurring at the surface between the electrode and electrolyte; 4) the resulting lithium ion being transported across the separator to the opposing electrode in the electrolyte; and 5) conservation of charge accounting for the various charge carriers. Each of these steps must be accounted for when modeling the battery system.

1.5 Modeling the Battery Process

Experimental study of batteries can be difficult and time consuming. The battery is a closed system and the only state which are measurable *in situ* are applied current and voltage (and sometimes skin temperature). These measurements offer a limited view of the operation of the battery. In order to obtain more information, labor intensive off-line studies must be done. In addition to the limited measurements obtained through experimental cycling, studies looking across multiple cycles can be very time intensive. To study capacity fade in a cell experimentally, cycling may be required for many months or years depending on the cycling protocol. Model-based studies that can accurately represent the battery system offer a way to gather more information about the internal workings of the battery while reducing the time required for analysis.

Different types of battery models have been developed to study the operation and design of Li-ion batteries. The goal of any model is to emulate the system that it is representing as closely as possible. However, with most modeling, higher fidelity comes with the cost of higher complexity. More complex models may be more difficult to solve and require longer computation time. Therefore the type of model chosen for a study should reflect the desired accuracy in simulation. Table 1-2 summarizes several types of models available to study a Li-ion battery. The two models that used for the majority of work in later chapters are the single particle model and porous electrode pseudo two dimensional model.

Table 1-2: Summary of several battery models. EC stands for electrochemical.

Model	EC based	Uses	Comments
Empirical	No	Basic Control App.	Limited range of operation; Non-predictive; Poor SOC/SOH estimation
Equivalent Circuit	No	Control App. and Simple Modeling	Non-predictive; Limited variable tracking; Poor SOH estimator
Single Particle	Yes	Low Rate Cycling Modeling and Control	Increased number of internal states monitored; Restriction on cycling
Porous Electrode P2D	Yes	Wide Range of Cycle Modeling	Tracks wide range of internal variables; Can include degradation mechanisms
Kinetic Monte Carlo	Yes	Surface Reaction Modeling	Computationally Heavy; Only models small portions of surface

1.5.1 Single Particle Model

The single particle battery model (SPM) simplifies the battery system by treating the each electrode of the battery as a single individual particle.¹³ This model will track the concentration of lithium throughout the electrode as well as the individual electrode potentials (in addition to current and voltage). One advantage of electrochemical based battery models is they allow for the tracking of internal states which cannot be measured through normal experimental battery cycling. When cycling batteries in normal operation, only the current and voltage of the system can be easily measured.

Inside the electrode particles the process of lithium diffusion (Item 1 in Figure 1-3) is represented through Fick's 2nd Law of diffusion:¹⁴

$$\frac{\partial c_i^s}{\partial t} = \frac{1}{r^2} \frac{\partial}{\partial r} \left(r^2 D_{s,i} \frac{\partial c_i^s}{\partial r} \right) \quad i = n, p \quad (1.3)$$

where c_s is the solid phase lithium concentration, D_s is the diffusion coefficient, r is the radius of the particle and i represents either the positive (cathode) or negative (anode) electrode. All variables used in this dissertation will be shown in a table in Appendix D. At the center of the

particles, there will be a zero flux boundary condition and at the external surface of the particles the flux of lithium into the electrolyte will be a function of pore wall flux, j_i :¹⁵

$$\left. \frac{\partial c_i^s}{\partial r} \right|_{r=0} = 0 \quad \left. \frac{\partial c_i^s}{\partial r} \right|_{r=R_p} = \frac{j_i}{FD_i} \quad (1.4)$$

where the pore wall flux is a function of the current density. The pore wall flux is a measure of the intercalation/deintercalation occurring at the particle surface and is governed by Butler-Volmer kinetics shown as:¹⁶

$$j_i = 2k_i \left(c_{max,i}^s - c_{surf,i}^s \right)^{0.5} c_{surf,i}^s{}^{0.5} c_e^{0.5} \sinh \left[\frac{0.5F}{RT} (\Phi_1 - \Phi_2 - U_i) \right] \quad i = n, p \quad (1.5)$$

where j is the flux into the electrode particle, k is the reaction rate constant for intercalation/deintercalation, c_{max}^s is the maximum solid-phase concentration of the electrode, c is the electrolyte concentration, F is Faraday's constant, R is the gas constant, T is the temperature, Φ_1 is the solid phase potential, Φ_2 is the liquid phase potential, and U is the open circuit potential.

When charging and discharging under high rates, a gradient for lithium ion concentration will form as a result of the intercalation/deintercalation reaction and the transport of lithium ions across the separator. But for low to medium charging rates the lithium ion concentration in the electrolyte can be approximated to steady-state.¹⁷ The SPM assumes that the gradient in lithium ion concentration is negligible and therefore no equations are necessary for transport of lithium through the electrolyte and there is no liquid phase potential in the Butler-Volmer equation for the SPM.

The SPM is a good model for studying systems operating under long charge and discharge time when fast computation time is required. When monitoring more intricate internal battery states and studying faster charging times, more detailed model may be useful.

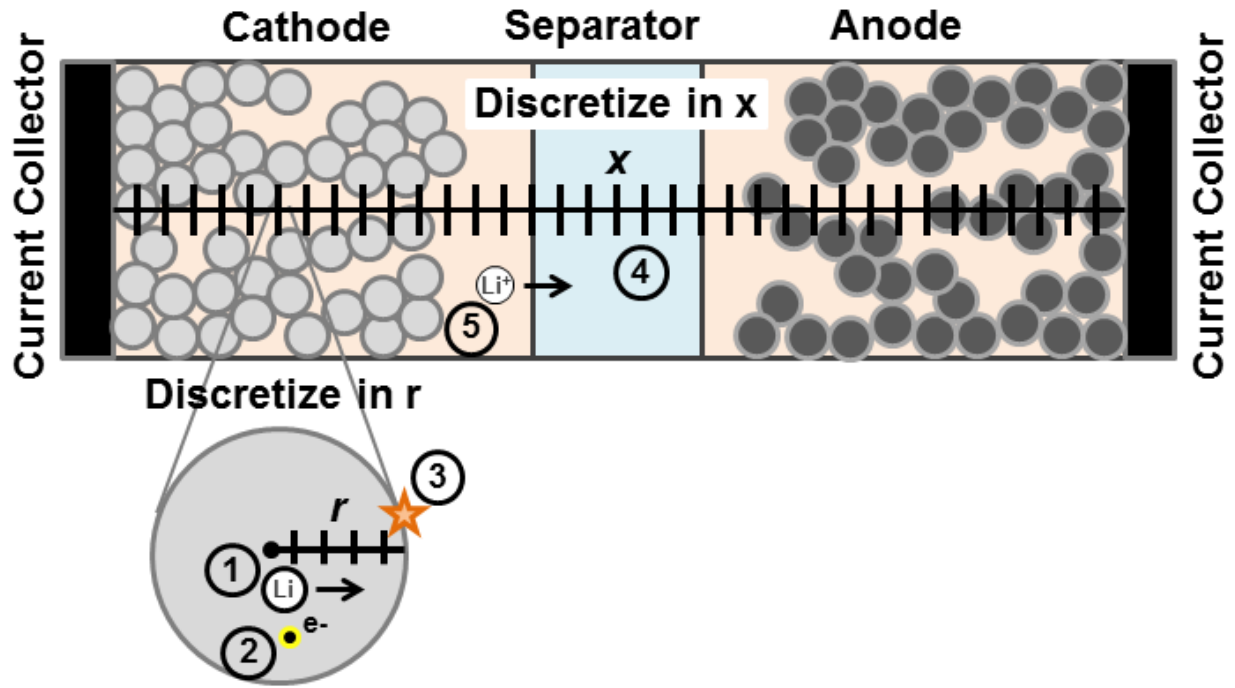


Figure 1-3: Discretization of the battery for modeling and a schematic showing the physical processes occurring during battery operation. For explanation of the processes labeled by number please read the text.

1.5.2 Porous Electrode Pseudo Two Dimensional Model

The porous electrode pseudo two dimensional (P2D) model allows for more accurate tracking of internal states throughout the electrodes and separator of the battery. The governing equations track the state variables in two spatial directions x and r and one temporal direction t . In the electrodes, instead of representing the active material through a single particle, the electrodes are discretized in the x -direction (across the electrode) and each node point represents an individual particle. This particle, which is assumed to be spherical, is then discretized in the r -direction, thus creating the second pseudo dimension of the model. In the separator, since there are no solid phase particles, only the x -direction is discretized. Figure 1-3 shows the discretization of the three regions of the battery for the P2D model.

The governing equations in the P2D model are based on porous electrode and concentrated solution theory.¹⁸ Again in the solid-phase the diffusion of lithium through the electrode particles is governed by Fick's 2nd law (Item 1 in Figure 1-3):

$$\frac{\partial c_i^s}{\partial t} = \frac{1}{r^2} \frac{\partial}{\partial r} \left(r^2 D_{s,i} \frac{\partial c_i^s}{\partial r} \right) \quad i = n, p \quad (1.6)$$

The electronic conduction of the solid-phase (Item 2 in Figure 1-3) is governed with a solid-phase charge balance:

$$\frac{\partial^2}{\partial x^2} (\sigma_{eff,i} \Phi_1) = a_i F j_i \quad i = n, p \quad (1.7)$$

where σ_{eff} is the effective conductivity of the electrode, a is the specific surface area of the electrode, and j is the flux at the electrode-electrolyte interface. The flux term, j , remains governed by Butler-Volmer kinetics (Item 3 in Figure 1-3) described as:

$$j_i = 2k_i (c_{max,i}^s - c_{surf,i}^s)^{0.5} c_{surf,i}^s c_e^{0.5} \sinh \left[\frac{0.5F}{RT} (\Phi_1 - \Phi_2 - U_i) \right] \quad (1.8)$$

Balancing the flow of ions through the electrolyte is a material balance (Item 4 in Figure 1-3):

$$\frac{\partial}{\partial t} (\varepsilon_i c) = \frac{\partial^2}{\partial x^2} (D_{eff,i} c) + a_i (1 - t_+) j_i \quad i = n, p \quad (1.9)$$

where ε is the porosity, D_{eff} is the effective diffusion coefficient of the electrolyte, and t_+ is the transfer number. And a charge balance accounts for the contributions to the total current throughout the cell (Item 5 in Figure 1-4):¹⁶

$$\frac{2RT}{F} (1 - t_+) \frac{\partial}{\partial x} (\kappa_{eff,i} c) - \frac{\partial}{\partial x} (\sigma_{eff,i} \Phi_1) - \frac{\partial}{\partial x} (\kappa_{eff,i} \Phi_2) = i_{app} \quad i = n, p \quad (1.10)$$

where i_{app} is the applied current. Figure 1-3 pictorially shows the phenomena that each equation governs.

The P2D model allows for the tracking of solid and liquid-phase potentials as well as lithium concentration in the solid and liquid-phase through the battery. Note that since there is no solid-phase in the separator only equations (1.9) & (1.10) will be used in the separator region. The P2D and SPM models provide a good balance between model accuracy and computational complexity for simulation.

1.5.3 Other Battery Models

There are many other types of battery models that can be used in simulation. The simplest models are empirical in nature. Some empirical models employ look-up tables or mathematical fits to existing data to create a model that equates voltage to SOC. Some empirical models will represent the battery system as an equivalent circuit.¹⁹ Empirical models are often very robust and fast because they involve few, if any, equations that require solving. However, these empirical models do not represent the underlying physics of the system. Rather they try to approximate past data with the best fit possible. Because they are fit to a specific set of data, these models are only accurate inside a limited set of conditions. If a study wants to analyze the model outside of the area in which the system was calibrated, large amounts of uncertainty will be introduced. These models are not predictive in nature.

On the other side of the spectrum, full 3D battery models can be built. Also individual reactions occurring at the electrode surface can be modeled through kinetic Monte Carlo (KMC) simulations with those reaction results being coupled to continuum level modeling. KMC modeling considers discrete events occurring at the electrode surface that each have a statistical probability of happening. Simulations step through each event one at a time to simulate how the reactions will be occurring in reality. The time steps between events are often very small and therefore many events are required to simulate battery system for a complete cycle. KMC

modeling is extremely computationally intensive, but can be useful for studying the nature of reactions at the electrode surface.²⁰

While neither of these types of models are extensively used in the following work, they offer a flavor of the other types of models (both computational lean and intensive) available to study battery systems.

1.6 Battery Degradation

When attempting to predict the useful life of a battery within an application, the mechanisms that cause a battery to degrade must be understood. Natural degradation of the battery will occur over time regardless of the charge/discharge cycle of the battery. The lifetime associated with natural degradation is referred to as “calendar life”. Degradation will also occur due to the cyclic charging and discharging of the battery. The lifetime associated with the charge/discharge cycle is called “cycle life”. Calendar life is an important consideration for applications that have very few cycles spread out over a long duration of time, such as standby power sources, while cycle life is more important for applications going through repeated charge and discharge cycles, such as a cell phone battery.²¹ Both types of degradation will occur in batteries, but the battery use will determine the relative strengths of each type of degradation. The following chapters that study capacity fade focus mainly on cycle life.

Capacity loss within a Li-ion battery can be caused by many different mechanisms and the importance of these various mechanisms is not well understood. Certain factors are known to increase capacity fade such as extreme temperatures, and high charging rates.^{22, 23} Many different internal mechanisms contribute to capacity fade, including mechanical stress effects which can lead to volume changes, as well as side reactions, which can increase cell resistance and remove active material from the cycling process.²⁴⁻²⁷ Side reactions can include many different types of

reactions leading to effects such as electrode pore clogging, lithium metal plating or passive layer growth at the electrode-electrolyte interface.²⁸ Figure 1-4 shows some of the possible fade mechanisms occurring within a Li-ion battery.

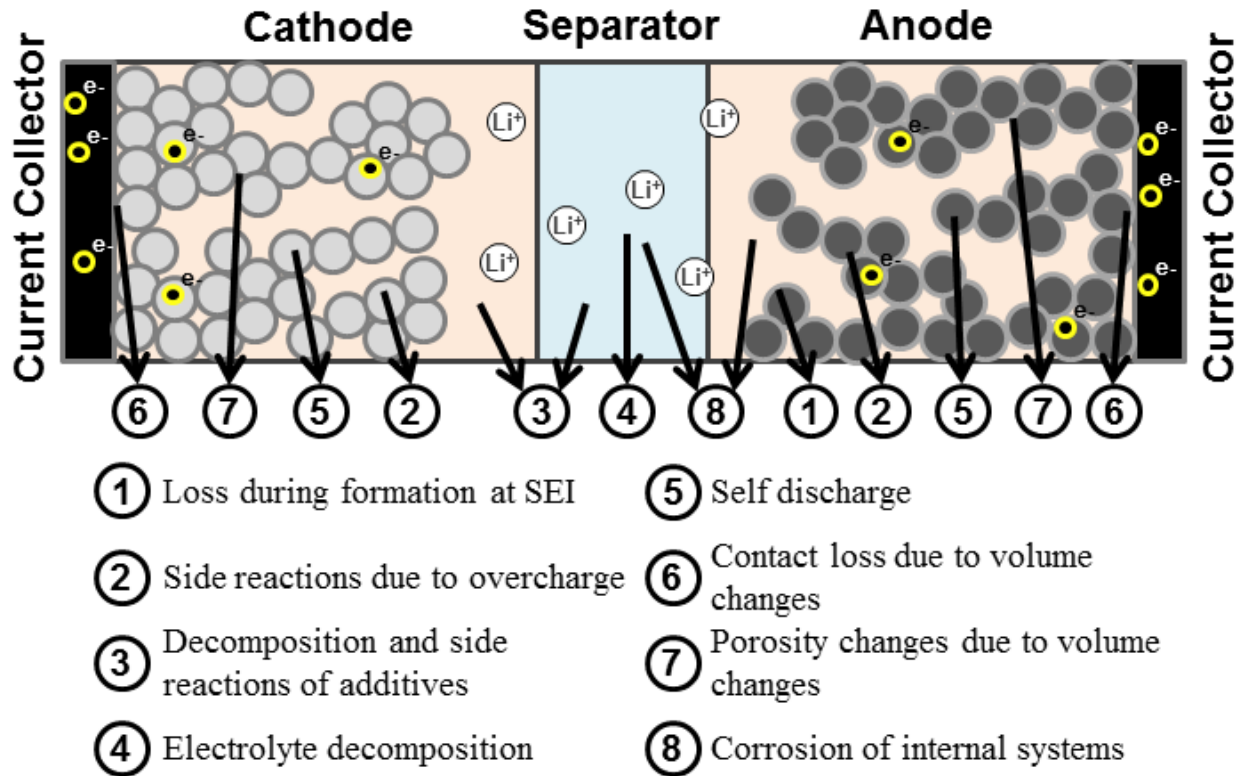


Figure 1-4: Possible mechanisms leading to capacity loss within the battery.

Empirical approaches for modeling capacity fade have used experimental data and correlated parameter degradation estimation to allow for certain physical parameters that change with each cycle to account for reduced capacity.²⁷ Other studies use mathematical fits such as power laws with existing data to predict future levels of capacity.²⁹ Semi-empirical approaches have represented fade mechanisms such as rate capability loss with equations that are specific to a single battery chemistry and type of cell and use an equation to account for the mechanism causing fade.³⁰ These approaches work well for a limited number of cases, but lack the robustness to be applied generally.

Theoretical approaches study the physics behind the side reactions within the battery, which are the drivers behind capacity fade. The side reactions occurring at the electrodes have been shown to increase the resistance of the cell, which has been measured experimentally through electrochemical impedance spectroscopy and cyclic voltammetry of highly cycled cells.^{31, 32} The effects of the increased cell resistance and loss of active lithium can be partly explained by studying the solid-electrolyte interface (SEI) growth.

1.6.1 The Solid-Electrolyte Interface Layer

During cycling, a layer of growth forms between the anode and electrolyte. Initially, this layer, known as the SEI layer, acts as a protective barrier between the anode and electrolyte, allowing the lithium ions to transfer through it to the graphitic anode and intercalate while keeping the electrolyte separated physically from the anode which reduces side reactions along the anode surface, maintaining stability between the anode and electrolyte.³³⁻³⁵ The SEI layer grows due to irreversible side reactions (non-intercalation) of lithium at the anode surface with the electrolyte (plus an electron) and has been shown to contain many different chemical compounds.^{36, 37} The SEI layer is not electronically conductive and the pores of the layer are generally too small for electrolyte molecules to reach the electrode surface. But these pores remain large enough to allow for ions to reach the electrode and intercalate. While the initial protective layer will slow the SEI reaction, some reactants will still reach the surface and continued growth of the SEI layer will occur with further cycling, increasing the resistive layer and removing active lithium from the system. This process lowers the energy and power capacity of the battery. The reaction occurs at the electrode surface so the SEI layer grows from the inside out.³⁸ Figure 1-5 shows the process of normal intercalation and the SEI side reaction occurring at the electrode.

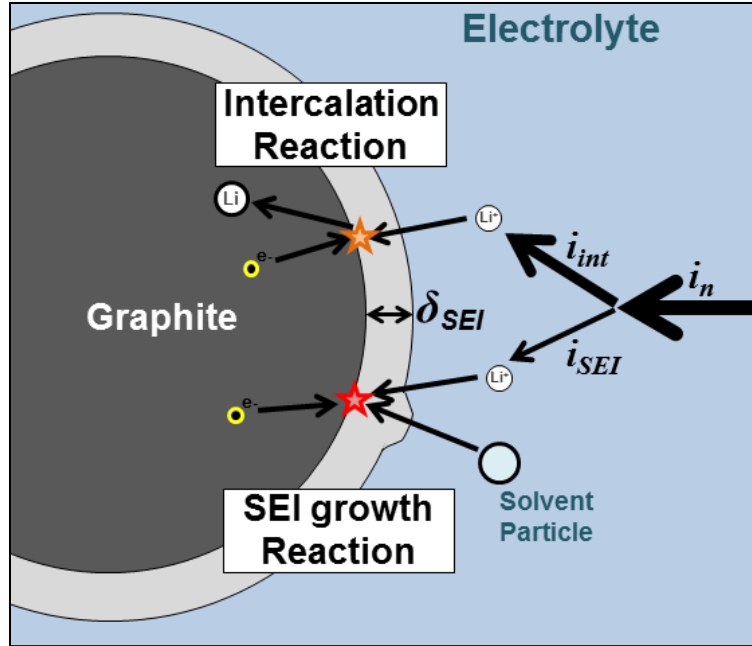


Figure 1-5: A schematic of the SEI layer growth process.

Representations of the reactions causing SEI layer growth have been used to model effects on State-of-Health (SOH) and remaining capacity.³⁹ Although many mechanisms contribute to capacity fade, SEI layer growth has been able to accurately account for overall capacity fade for some chemistries using graphite anodes.^{34, 35} While this growth can be directly modeled (by using a KMC simulation), such models have high computational cost requiring large amounts of time to model only small portion of electrode surface.²⁰

Depending on the model being used in a simulation, the equations used for SEI layer growth will vary slightly, but the following outline of the process will be the basis for all of the SEI layer modeling performed in subsequent chapters. SEI layer growth is affected by voltage, charge time, charge rate, Depth-of Discharge (DOD), and SOC window. The SEI layer side reaction is accounted for by splitting the applied current term at the negative electrode into an intercalation current and a side reaction current that is attributed to the irreversible SEI layer

growth. SEI layer thickness, δ_{SEI} , is included based on the formulation outlined in Safari, et al.⁴⁰

The current at the anode is shown as:

$$i_{app} = i_{int} + i_{SEI} \quad (1.11)$$

where i_{int} is the current associated with intercalation. The current associated with the SEI side reaction, i_{SEI} , is governed by the following rate equation:⁴⁰

$$i_{SEI} = -F k_{SEI} c \exp\left(\frac{-F}{RT} \left(\Phi_1 - \frac{\delta_{SEI} i_{app}}{\kappa_{SEI}} \right)\right) \quad (1.12)$$

The governing equation for the growth of the SEI layer is:

$$\frac{d\delta_{SEI}}{dt} = \frac{k_{SEI} c M_{SEI}}{2\rho_{SEI}} \exp\left(\frac{-F}{RT} \left(\Phi_{1,n} - \frac{\delta_{SEI} i_{app}}{\kappa_{SEI}} \right)\right) \quad (1.13)$$

Additionally, the Butler-Volmer equation at the anode will now include a resistance term from the SEI layer based on the increase in layer thickness:⁴¹

$$j_n = 2k_n (c_{max,n}^s - c_n^s)^{0.5} c_n^{s0.5} c_e^{0.5} \sinh\left[\frac{0.5F}{RT} \left(\Phi_1 - \Phi_2 - U_n - \frac{\delta_{SEI} i_{int}}{\kappa_{SEI}} \right)\right] \quad (1.14)$$

Note that in the Butler-Volmer equation at the anode the anode current, i_n , has been replaced by only the portion of the current that is used for intercalation, i_{int} .

Including the SEI layer growth allows for tracking of the relative capacity fade of the battery based on the different charging patterns. The mechanisms outlined above will be used in later chapters to model capacity fade.

1.7 Scope of Dissertation and Research Objectives

The work in this dissertation primarily focuses on analyzing the use of Li-ion batteries in various applications through modeling (Chapter 6 focuses on experimental study). While the models utilized for the following studies have been shown in the introduction, Chapter 2 shows

methods for efficiently solving the models and outlines some of the mathematical processes used to ensure fast and accurate simulations.

The majority of the remaining work focuses on studying the battery models under different application constraints that vary from traditional galvanostatic cycling patterns. Most previous model-based studies have focused on simple and predictable cycling patterns. However, many new applications utilizing large capacity batteries experience cycling patterns that are continuously changing based on the needs of the application. Two examples of applications that are implementing large scale energy storage with variable cycling patterns are batteries coupled to renewable energy and batteries in EVs. Chapter 3 analyzes battery models coupled in a systems level model with a solar array and local demand loads. This coupled system is referred to as the solar-battery hybrid system. Studies of the system include analyzing the effects of component sizing, demand shape and individual site irradiance patterns. Both technological and economic studies of the systems are included.

Chapter 5 conducts simulations of Li-ion batteries under different driving cycles experienced by EVs. Chapters 3-5 include a degradation mechanism in the models, specifically the SEI layer growth mechanism. Studying this mechanism and how the SEI layer will grow under different circumstances helps to analyze the lifetime of the batteries within these applications.

While Chapters 3-5 focus on how the batteries will operate within these systems, Chapter 4 outlines a method for optimization based charging of the solar-battery hybrid system. This chapter begins to move beyond analyzing sites that would benefit from energy storage to more intricately studying how best to use predictive modeling to increase the systems value.

Chapter 6 is a deviation from modeling work. This chapter summarizes the experimental studies that were conducted for Li-ion cells. While individual capacity fade mechanisms were analyzed with the models, the experimental studies helped to better understand how all of the degradation mechanisms can affect the battery simultaneously. Long term cycling studies evaluated the available energy capacity of batteries over their entire useful life.

The simulation and experimental studies conducted for this dissertation give a thorough picture of how batteries operate when coupled with solar power or EVs and helps to understand some of the causes of capacity fade within these applications. Chapter 7 summarizes the work for each chapter and expands on possible future directions of study.

Chapter 2

Computational Methods for Efficient Simulation of Battery Models

This chapter contains excerpts from the following journal article, reproduced here with permission from Elsevier:

Lawder, Matthew T., Ramadesigan, Venkat, Suthar, Bharat K., Subramanian, Venkat R. “Extending explicit and linearly implicit ODE solvers for index-1 DAEs” *Computers and Chemical Engineering*, 82(2015) 283-292.

2.1 Reducing the Model

As stated in the introduction, when determining the best model for a specific simulation, a balance must be made between accuracy and computational speed. Other than building a faster computer, there are two main ways to increase the computational speed of a model simulation. You can reduce the model or reformulate the model. Reducing the model will remove or simplify equations based on certain assumptions or conditions of operation. Model reduction sacrifices on the accuracy of the model and too much reduction can lead to a model that is no longer relevant for a problem.

For many simulations, including the majority of simulations performed in the following chapters, exact knowledge of the variation of lithium concentration in the radial direction is not required within electrode particles. Rather the important values required for tracking pore wall flux and system SOC are surface concentration and average solid-phase concentration. Therefore, a model reduction can be performed to reduce the computational load of radially discretizing the electrode particles. Fick’s law for solid phase diffusion can be replaced by simpler equations that tracks average and surface concentrations in the solid particle through a parabolic profile approximation.⁴² This approximation assumes that the concentration of lithium in the solid-phase follows a parabolic shape and is valid for low to medium rates over long

cycling times. Fick's law (in either the SPM or P2D model) can be replaced by the following two equations:¹⁵

$$\frac{dc^{avg}}{dt} = \frac{3j_i}{R_i^p} \quad (2.1)$$

$$c^{avg} - c^{surf} = \frac{j_i R_i^p}{5D_i} \quad (2.2)$$

which introduces c^{avg} and c^{surf} in place of c^s . Although two equations now replace one governing equation, there is no radial dependence in either of these equations and therefore they will not be discretized in the r -direction and the system only has to be discretized in the x -direction before being simulated. Using this approximation can reduce the computational cost of simulation without greatly increasing error as long as the model is not required for high rates and short times. This approximation is used for the SPM and P2D in Chapters 3-5.

Other common battery model reductions include linearization of equations for more robust optimization and control schemes.⁴³ Optimization of battery models without linearization can be performed and is shown in Chapter 4 for a battery system tied to solar arrays.

2.2 Model Reformulation

A second method for increasing computational speed is model reformulation, which involves keeping the original equations intact, but altering the mathematical way the variables are managed and the system is solved. For the P2D model (with the parabolic profile approximation), when a large number node points are desired for high accuracy, the discretization creates a very large system of stiff differential algebraic equations (DAE). For example, if 50 node points (in the x -direction) were desired in each region (cathode, anode, and separator), the resulting system of equations would contain 600 DAEs (250 in each of the

electrodes and 100 in the separator). Large systems like this can be inefficient to solve. In order to lower the computational load, the P2D model used in the subsequent chapters uses the following reformulation.

A full explanation for the reformulation is shown in Northrop et al. 2011.⁴⁴ First, a coordinate transformation is performed in order to convert the three regions of the model (cathode, separator, and anode) to each range between $X=0$ and $X=1$ where X is a shared dimensionless dummy variable. Then the state variables of the system are approximated with a series of trial functions within each region. These trial functions are collocated to points in the region where they match the finite difference (FD) solution exactly. The number of terms in each trial function (representing a variable) will depend on the desired number of collocation points. The more collocation points, the more terms in each trial function, and the higher level of accuracy for the approximation. The system can be accurately represented with a small number of collocation points while allowing for a large reduction in the number of equations in the system of DAEs being simulated. In our reformulation, the trial functions are approximated using Chebyshev polynomials. While these trial functions will be more complex functions than the original variables, in terms of solver efficiency, the reduction in the number of equations outweighs the increased complexity of the function.

2.3 Perturbation and Switch DAE solving method

Many different solvers are available for computing systems of DAEs.⁴⁵⁻⁵³ More information on the method and solution procedure of several ordinary differential equation (ODE) and DAE solvers, are provided elsewhere.⁵⁴⁻⁶⁴

For a system of DAEs, a set of consistent ICs must be given in order to solve the system with standard solvers. Some solvers contain initialization routines that help to calculate

consistent ICs from starting guesses. These routines add computational time and often require the additional use of solvers to obtain the ICs used by the primary DAE solver. By having a system that includes both ODEs and algebraic equations (AE), not all ICs offer a possible solution and inconsistent ICs will cause solvers to fail in many instances. Knowledge of the governing equations and the underlying physics of the system can help in choosing consistent ICs.

In many cases though, consistent ICs for all of the variables are not known *a priori* and the effects of operating conditions and system parameters like rate constants or diffusion coefficients may also be unknown. Even small deviations from consistent ICs will cause the solver to fail (using standard solvers).⁵⁶ Many different methods for solving this initialization problem have been proposed. More information about individual methods is provided elsewhere.⁶⁵⁻⁷⁰ Initialization using a perturbation applied to algebraic equations prior to simulation of the complete system was shown by Methekar et al.⁵⁶ This perturbation approach was used to find the ICs for algebraic variables allowing for faster initialization and simulation of index-1 DAEs.

In this dissertation, an approach that combines initialization and simulation proposed in Lawder et al.⁷¹ is used for solving most DAE systems. The approach builds upon the two-step process of 1) Perturbation initialization as outlined in Methekar et al.⁵⁶ and 2) DAE simulation based on the consistent ICs obtained from step 1 using explicit (or linearly implicit) ODE solvers. The proposed approach combines the two steps of initialization and by using a switch function (hyperbolic tangent function) to constrain the differential variables during the time when the perturbation approach finds consistent ICs for the algebraic variables. This approach allows the initialization and simulation to be done continuously with a single solver. The proposed single-step approach increases the robustness of the solution method by allowing for

larger perturbation values to be applied and increases the computational speed of the solvers while enabling explicit ODE solvers to solve nonlinear DAEs.

2.3.1 Initialization and Simulation Method

A general DAE system (shown in semi-explicit form) is considered:

$$\frac{dy}{dt} = f(t, y, z) \quad (2.3)$$

$$0 = g(t, y, z) \quad (2.4)$$

where y are the differential variables and z are the algebraic variables. Function g is differentiable and dg/dt is non-singular as the model considered is an index-1 DAE. The system of DAEs shown above often arises from combining equations governing physical phenomena with constraints or discretizing a PDE's spatial variables (while keeping time continuous as shown in the example from Section 2.2.3). In order to solve the system of DAEs, ICs for all the variables must be given as:

$$t = 0; \quad y(0) = y_0; \quad z(0) = z_0 \quad (2.5)$$

However, exact values for consistent z_0 are not always readily available. Under normal DAE solvers (without initialization routines), ICs must be consistent with the system of DAEs or a solution cannot be obtained. Variables present in the AEs are limited to sets that directly satisfy the algebraic limits. A system of only ODEs will often offer a wider range of consistent ICs because the equations govern the derivatives (change) of the system rather than the variable values. Combining AEs to an ODE system increases the stiffness of the system and necessitates *a priori* knowledge of the exact ICs of the system. In order to loosen the restriction of consistency on the algebraic variables, a perturbation approach is used as outlined in Methekar et al.⁵⁶ A perturbation parameter, ϵ , is introduced such that:

$$\mathbf{g}(t) = \lim_{\varepsilon \rightarrow 0} \mathbf{g}(t + \varepsilon) = 0 \quad (2.6)$$

and when $t=t+\varepsilon$, the AEs represented in \mathbf{g} can be shown as:

$$\mathbf{g}(t + \varepsilon) = 0 \quad (2.7)$$

Using a Taylor series expansion, we rearrange the AEs to the form:

$$-\varepsilon \frac{d\mathbf{g}(t)}{dt} = \mathbf{g}(t) + O(\varepsilon^2) \quad (2.8)$$

More details on the perturbation approach can be found in Methekar et al.⁵⁶ Once in perturbed form, the AEs can be solved first (without any ODEs, but using the given ICs for the differential variables) to find consistent initial values for all algebraic variables. The algebraic variable values found from the perturbation approach will be consistent with the given differential variable ICs and the values can be used with the initial system of DAEs as ICs. When solving the system of DAEs, the set is solved in its initial form (in the example above, semi-explicit form), and the consistent ICs from initialization are provided. Using this approach provides an initialization routine that produces consistent ICs to be fed into the solver along with the original system. The initialization routine allows for a wider range of initial guesses to be used for the algebraic variables of the system. The perturbation value applied to the system must be small enough so that the converged value of the algebraic variables will be consistent. Larger perturbation values may not converge to consistent ICs. In addition, Maple as of today cannot solve systems of DAEs without first converting the system to ODEs, so even having consistent ICs for algebraic variables will not help in solving nonlinear DAEs.

The above procedure involves two steps: 1) initialization using a solver for obtaining the consistent ICs of the algebraic variables, and 2) the solution of the DAE system calling an additional solver and using the consistent ICs obtained from step 1. Instead of taking a two-step

approach to initialization of algebraic variables and solving the complete system, in the proposed approach, a switch function is proposed and used to hold the differential variables static (constant) while the algebraic variables find consistent values using a perturbation approach and then the differential variables are unmasked and the system simulation begins in a continuous manner using the same solver. This single-step approach combines the initialization of the algebraic variables into the solution of the system, offering more robust solutions while reducing system stiffness by relaxing the requirement of the perturbation value. Note that in the proposed approach, the AEs are converted to a perturbed ODE system and therefore many explicit solvers can be directly used (for example, MapleTM,⁶³ a symbolic programming language, can handle the perturbed system as an ODE much better than the original DAE). In addition, Maple provides an option to call the ODE solver in compiled form which can be done in a single step minimizing the RAM requirement and the avoiding second calls to dsolve (Maple's inbuilt ODE solver). When running optimal control based on control vector parameterization or estimating parameters from experimental data, it is convenient and efficient to call a single dsolve procedure as opposed to two separate functional calls. The same behavior is observed in MATLAB as well.

The hyperbolic tangent (switch) function applied to the ODEs is formulated as:

$$T_H = \frac{1}{2} \left(1 + \tanh \left(q(t - t_j) \right) \right) \quad (2.9)$$

where q is a weighting factor determining the discreteness of the function, and t_j is the time allowed for the perturbation approach to find consistent algebraic ICs. The value of t_j will need to be scaled depending on the value of ε used for the perturbation. Subtracting t_j from the total solution time provides the original (simulation) time variable. The switch function is applied to the ODEs as:

$$\frac{dy}{dt} = fT_H \quad (2.10)$$

The switch function allows for the derivative of the differential variables to be set to zero for the duration of the initialization of the algebraic variables and be set to the function f for the simulation after the initialization period. The adaptive solvers used on the system will find time steps as needed from time $t = 0$ to time $= t_j$ and will find the consistent ICs for z . The ability of the switch function to approximate a discrete jump with a continuous function makes this approach useful for standard solvers. The representation of discrete events as continuous functions has been shown to be effective in simulation and the switch function approach has even been used to approximate discontinuities as continuous functions.⁷² The continuous nature of the switch function also allows for minor corrections of the converged ICs at the end of the initialization time (beginning of the actual simulation time). This correction of the converged ICs allows for less restrictive perturbation values to be used in this approach when compared to the two-step approach. In our experience, the proposed approach also saves a considerable amount of time taken in stopping the solver after initialization, substituting the consistent initial values, and starting the ODE solver again for simulating the entire system of DAEs. Additionally, this method can reduce the time required to properly format the set of equations for solving. With this method, the system of DAEs (Eqs. (2.3) & (2.4)) can be restructured as a single-step ODE system shown by:

$$\frac{dy}{dt} = fT_H \quad (2.11)$$

$$\varepsilon \frac{dg}{dt} = -g \quad (2.12)$$

A schematic qualitatively describing the stages of the single-step approach is shown in Figure 2-1. Often the perturbed form of the AE (Eq. (2.12)) remains in implicit form because the left hand side will contain differential variables, y , or their derivatives, $\frac{dy}{dt}$. This form is acceptable for small systems, but may cause solvers to fail for large sets. In order to make the system explicit or linearly implicit, first the derivatives of the differential variable must be removed by substituting the original ODE equations (Eq. (2.3)). Then ICs are substituted for the differential variables that remain. By converting to this form, the single-step process will allow for explicit solvers to be used for both the initialization and solution of the system of DAEs.

One can write an equation for the explicit form as

$$\varepsilon \frac{dg}{dt} \Big|_{y=y_0, z=z_0, \frac{dy}{dt}=f_0} = -g \quad (2.13)$$

where Eq. (2.13) can replace Eq. (2.12) for the single-step solution.

Note that Eqs. (2.11), (2.12), & (2.13) are purely ODEs and can be solved using explicit solvers in time or linearly implicit solvers in time. For example, in Maple, the linearly implicit Rosenbrock stiff ODE solver is very good at handling these systems. One simple example showing how to apply the method and its benefits is included followed by the application of the method to a FD solution of the SPM. Additional examples of the method can be seen in Appendix A.

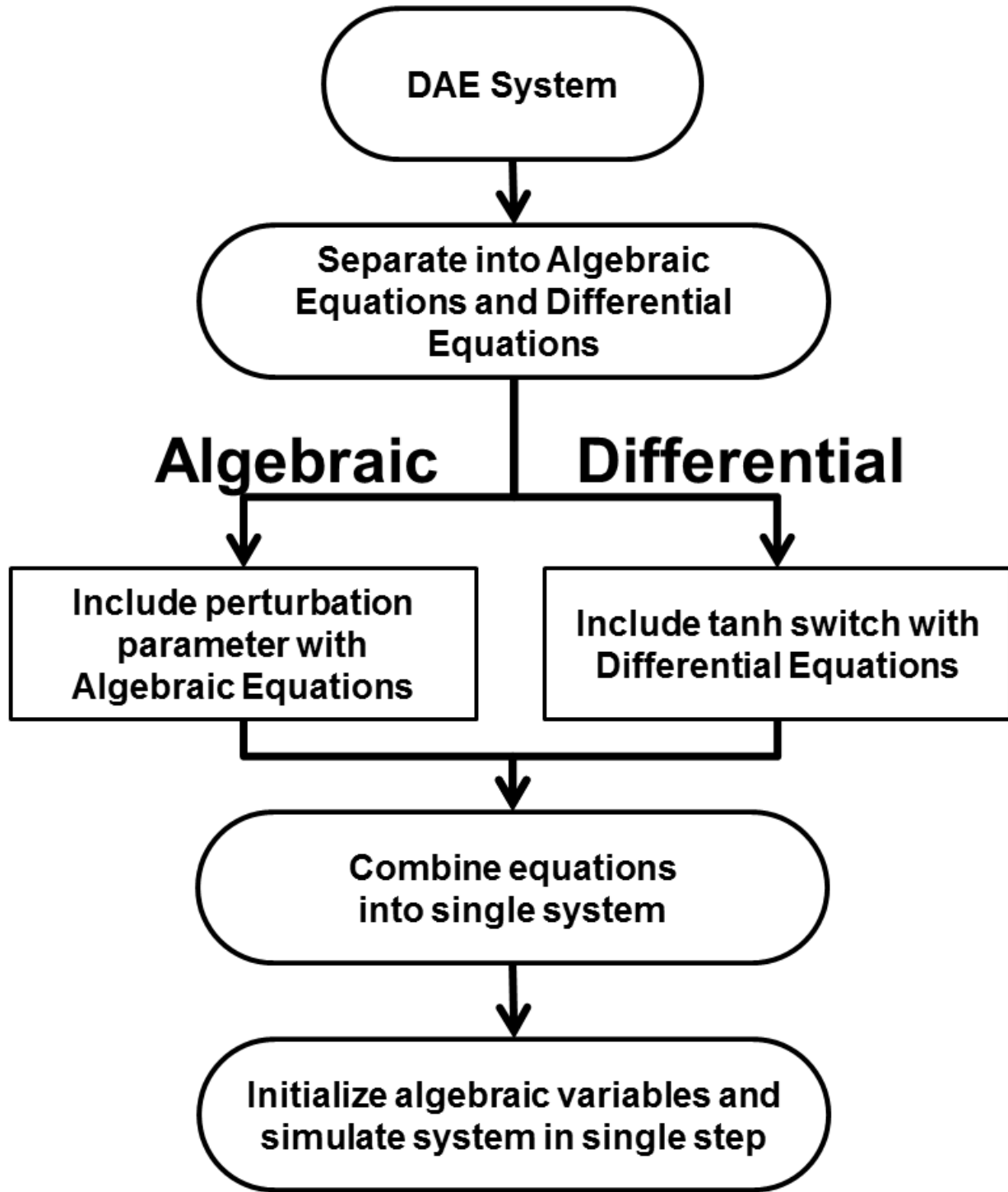


Figure 2-1: Diagram of the proposed single-step approach.

2.3.2 Example 1: Index-1 DAE (1 Algebraic and 1 Differential Variable)

Consider the system below where y is the differential variable and z is the algebraic variable:

$$\frac{dy(t)}{dt} = -y(t)^2 + z(t) \quad (2.14)$$

$$\cos(y(t)) - \sqrt{z(t)} = 0 \quad (2.15)$$

For the example here, we will set the differential variable IC at:

$$y(0) = 0.25 \quad (2.16)$$

Standard DAE solvers would need the consistent IC for z :

$$z(0) = \cos(0.25)^2 \approx 0.938791 \quad (2.17)$$

Standard solver packages might fail when the exact algebraic IC is not given (if the solver did not include initialization routines). Application of the single-step approach is illustrated below.

A switch function is created shown as:

$$T_H = \frac{1}{2}(1 + \tanh(1000(t-1))) \quad (2.18)$$

This function is applied to the right hand side of the differential equation so that:

$$\frac{dy(t)}{dt} = (-y(t)^2 + z(t)) \left(\frac{1}{2} + \frac{1}{2} \tanh(1000(t-1)) \right) \quad (2.19)$$

And a perturbation will be applied to the algebraic equation such that:

$$\varepsilon \left(\sin(y(t)) \left(\frac{dy(t)}{dt} \right) + \frac{1\sqrt{z(t)}}{2z(t)} \frac{dz(t)}{dt} \right) = \cos(y(t)) - \sqrt{z(t)} \quad (2.20)$$

The system of Eqs. (2.19) & (2.20) can now be solved with an explicit (or linearly implicit) ODE solver. The IC of the algebraic variable does not have to be known *a priori*, but rather the combination of the switch function and perturbation will allow the IC for the algebraic variable to reach its consistent value during the first second of the solution because T_H will be 0, holding the differential variable constant during this initialization. After one second, T_H will switch to the value 1 (see Figure 2-2), and the solution of the complete system will begin based on the initialized conditions. A reasonable initial guess must still be provided for the starting value of z . The time of initialization must be removed from the solution time in order to achieve the real simulation time of the system. In the example cases, the initialization time is shown as negative time in the figures and the real simulation time of the problem is shown as positive.

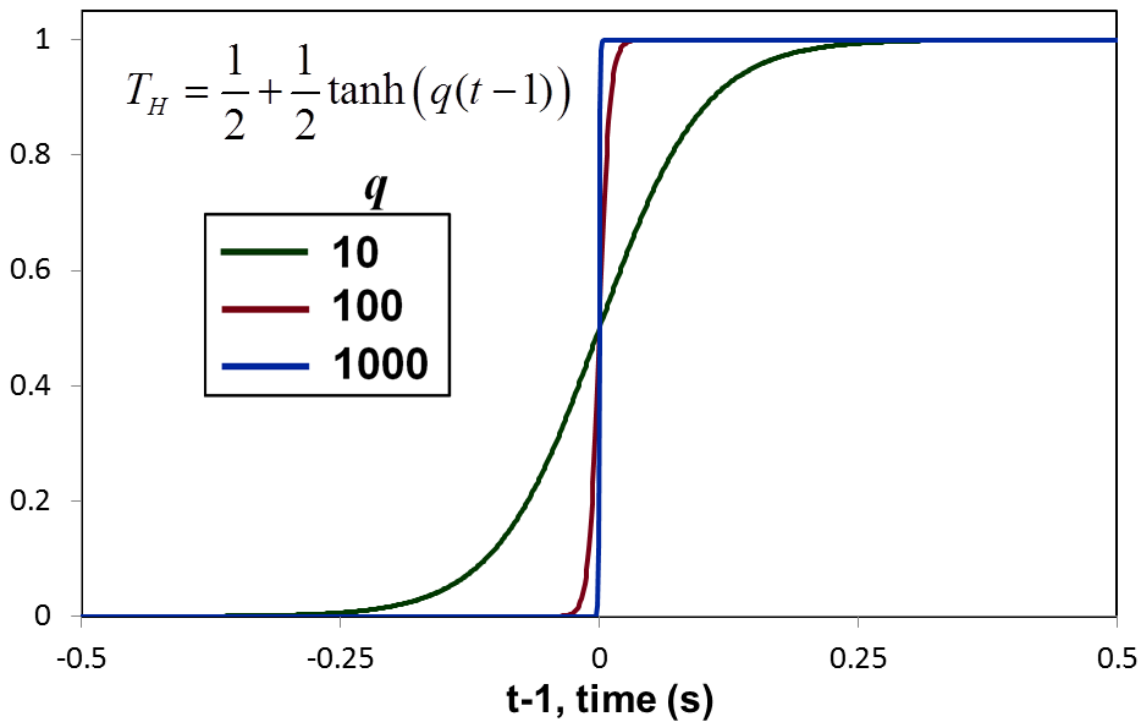


Figure 2-2: Comparison of different q values for the switch function.

Smaller values of ε will increase the accuracy of the converged value ensuring that the converged value can be used as a consistent IC, but a smaller ε will also increase the stiffness of

the system. Applying larger ε will reduce the stiffness, but will also decrease the accuracy of the converged value. When ε becomes large enough, the converged value will no longer work as a consistent IC for the system of DAEs. The single step approach allows for a correction to the converged value at the end of initialization because of the continuous nature of the switch function. As the ODE variables begin to be solved, the converged value of the algebraic variables (as well as the IC for the differential variables) can correct to consistent values. This correction will introduce a small amount of error, but allows for a much more robust approach to solving by increasing the allowable converged value for the algebraic variables which will still solve the system.

For Example 1, the proposed approach with the switch function will solve the system with less than 0.001 error for all points after 0.1s of simulation time for converged values between $0.9377018 < z(0) < 0.9398806$. Even though the range of allowable converged values is small it greatly increases the robustness of the solver and allows for a much wider range of ε . These ranges are dependent on the discreteness of the switch function used ($q=1000$ for the range above). Also, these ranges are only the allowable range of converged solutions and the allowable range of initial guesses will be much larger (see Figure 2-4).

For Example 1 using Maple, if a starting guess of $z(0)=0.8$ was applied, the normal perturbation solution would require no larger than $\varepsilon = 1.1 \times 10^{-6}$ in order to obtain a solution for initialization that is consistent for the system of DAEs. However, the single-step approach can solve the same system with $\varepsilon = 0.1$ (or larger). Figure 2-3 shows a plot for the original two-step perturbation and simulation approach and the single-step solution. In the example discussed here, q is taken as 1000. The value of q will affect the discreteness of the switch function and can have an effect on the increased robustness. The proposed approach can be solved for many different

initial guesses of the algebraic variables. Figure 2-4 shows the initialization period for 8 different initial algebraic guesses where $\varepsilon = 0.1$ and $t_j = 1$ for all cases. All of the guesses converge to the consistent IC of $z(0)=0.938$ and accurately solve the system of DAEs.

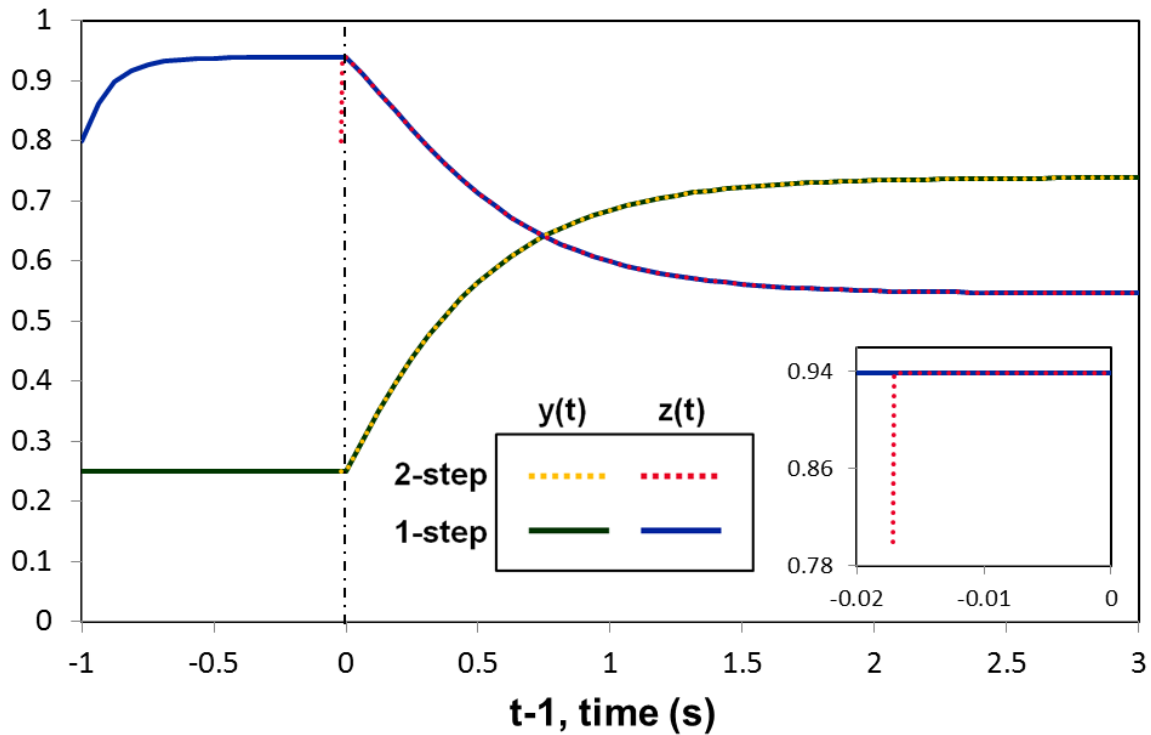


Figure 2-3: Comparison of Example 1 solution for two-step perturbation approach and proposed single-step approach.

The perturbation value does affect the accuracy and convergence of the initialization. Smaller values of ε will allow the initialization to converge over shorter simulation time and when holding t_j constant, larger values of ε may obtain an initialization that is not accurate enough to satisfy the consistency condition. Figure 2-5 shows the initialization of Example 1 for several different perturbation values ($\varepsilon=0.1, 0.05, 0.01, 0.001$).

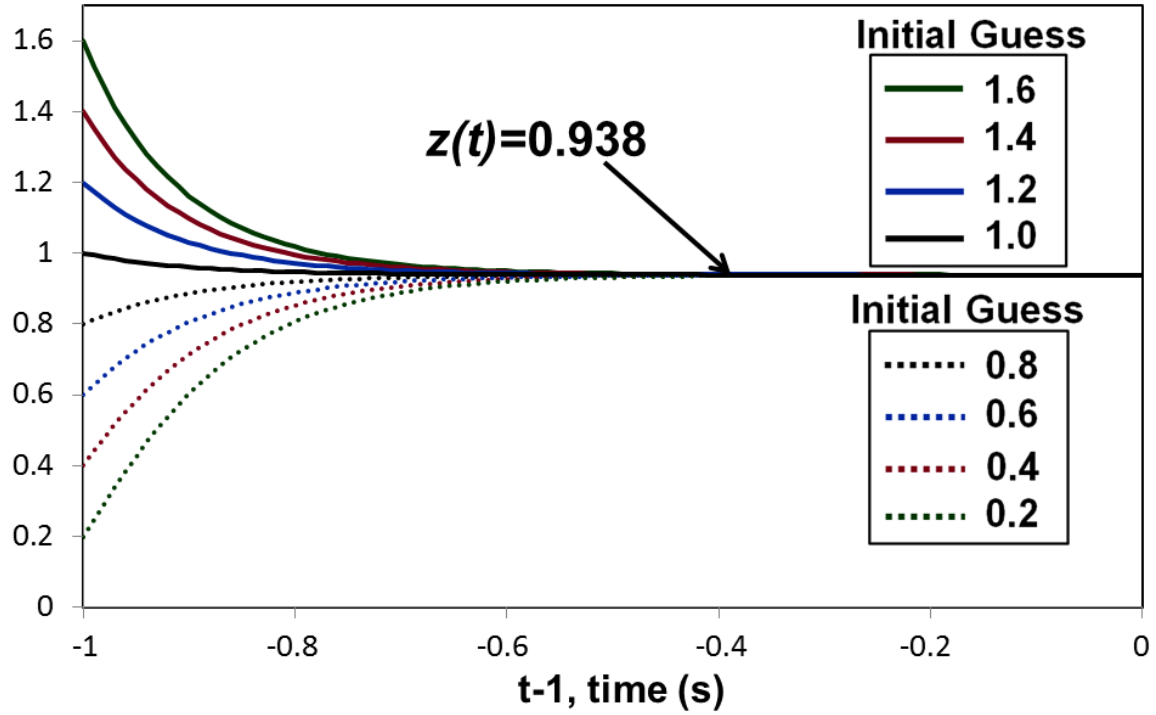


Figure 2-4: Initialization portion of the single-step simulation showing different initial guesses for the algebraic variable (z) from Example 1.

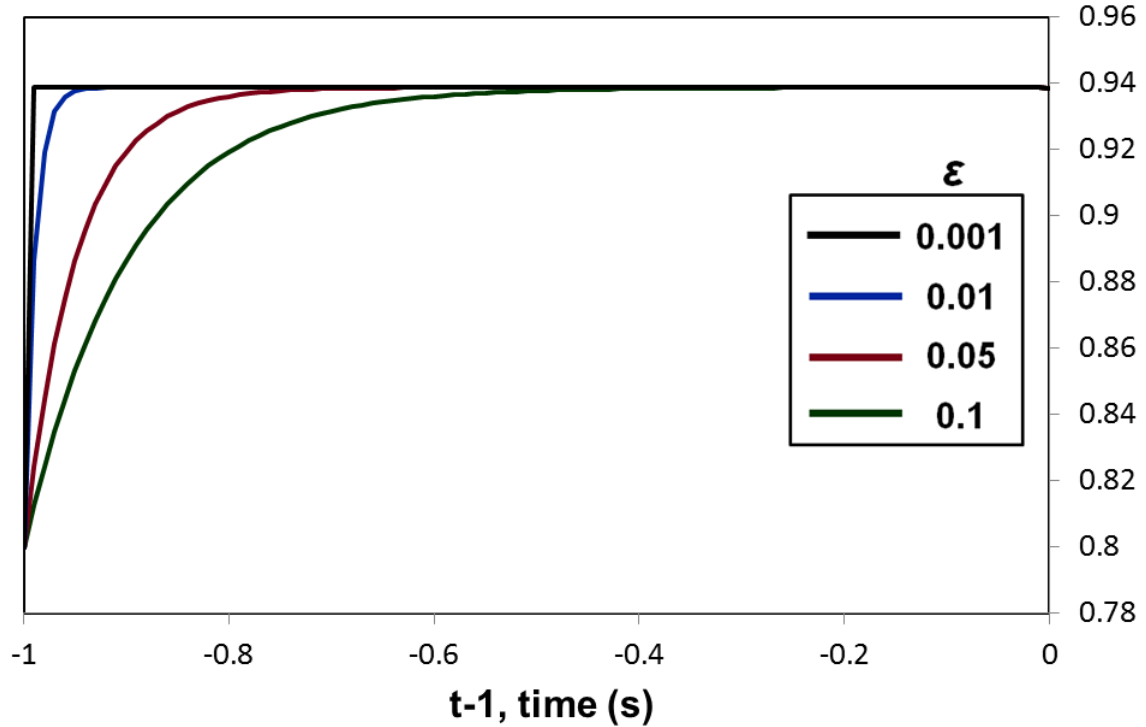


Figure 2-5: Initialization portion of the single-step simulation showing different perturbation values for the algebraic variable (z) from Example 1.

2.3.3 Example 2: Finite Difference Single Particle Lithium-ion Battery Model

This example shows the method applied to the SPM with no parabolic approximation.

Recall the equations (1.3), (1.4), and (1.5) from Section 1.5.1 for the SPM:

$$\frac{\partial c_i}{\partial t} = \frac{1}{r^2} \frac{\partial}{\partial r} \left(r^2 D_i \frac{\partial c_i}{\partial r} \right) \quad i = p, n \quad (2.21)$$

$$\left. \frac{\partial c}{\partial r} \right|_{r=0} = 0 \quad \left. \frac{\partial c_i}{\partial r} \right|_{r=R_i} = - \frac{j_i}{D_i} \quad (2.22)$$

$$j_i = \frac{\pm i_{app}}{a_i l_i F} = \pm 2 k_i c_e^{0.5} (c_{i,max} - c_{i,surf})^{0.5} c_{i,surf}^{0.5} \sinh \left(\frac{F (\Phi_i - U_i)}{2 R T} \right) \quad (2.23)$$

The parameters used for simulation of this example are given in Table 2-1.

The model can be solved using the numerical method of lines which will discretize the spatial derivatives over a series of node points, N , within the particle, while the time derivative will remain. This discretization will create a DAE system with $2N$ differential equations and 4 algebraic equations (the boundary conditions). The system can be solved for the concentration of lithium at every node point in the electrodes and then the electrode potentials, Φ , can be determined from the electrode surface concentrations. In a discharged state, the initial concentration for lithium throughout the electrodes will be:

$$c_p(0) = 305.55, \quad c_n(0) = 49503.11 \quad (2.24)$$

with units of mol/m³.

This model system written in FD form (using second order central difference approach) and applying the single-step approach becomes:

$$\frac{dc_{i,j}}{dt} = \frac{D_i}{j^2 h^2 R_i^2} \left[c_{i,j+1} (j^2 + j) + c_{i,j-1} (j^2 - j) - 2 j^2 c_{i,j} \right] \left(\frac{1}{2} + \frac{1}{2} \tanh(1000(t-1)) \right) \quad (2.25)$$

Table 2-1: Parameters for SPM.

Symbol	Parameter	Values	Units	
F	Faraday's Constant	96,487	C/mol	
R	Gas Constant	8.3143	J/(mol K)	
T	Temperature	303.15	K	
c_e	Electrolyte Concentration	1,000	mol/m ³	
i_{app}	Applied Current	1	C	
		Cathode (p)	Anode (n)	
D	Solid phase Diffusion Coefficient	1.0×10^{-14}	3.9×10^{-14}	m ² /s
a	Particle Surface Area to Volume	8.85×10^5	7.24×10^5	m ² /s
c^{max}	Maximum Lithium Concentration	51,555	30,055	m ² /s
l	Cell Thickness	80×10^{-6}	88×10^{-6}	m ² /s
R	Electrode Particle Radius	2×10^{-6}	2×10^{-6}	m ² /s
k_o	Reaction Rate	2.33×10^{-11}	5.03×10^{-11}	m ² /s
U	Overpotential	is a function of SOC ⁹		

with boundary conditions converted using second order 3-point forward and backward differences as:

$$\frac{-\varepsilon}{2h} \left(4 \frac{dc_{i,1}}{dt} - \frac{dc_{i,2}}{dt} - 3 \frac{dc_{i,0}}{dt} \right) = 4c_{i,1} - c_{i,2} - 3c_{i,0} \quad (2.26)$$

$$\frac{-\varepsilon}{2h} \left(4 \frac{dc_{i,N}}{dt} - \frac{dc_{i,N-1}}{dt} - 3 \frac{dc_{i,N+1}}{dt} \right) = 4c_{i,N} - c_{i,N-1} - 3c_{i,N+1} - \frac{j_i}{D_i} \quad (2.27)$$

Results for the concentration values (five internal node points) are shown in Figure 2-6. Using the Rosenbrock stiff solver in Maple, the system can be solved for a complete 1C rate charge with up to 58 internal node points when not applying the proposed approach after which the solver fails due to memory constraints. Note that Rosenbrock methods for DAEs require additional constraints to satisfy the order requirement.^{45, 73} By using the proposed single-step approach, the same system under the same memory constraints can be solved for over 2,500 internal node points. The proposed approach reduces the computational burden on the solver and allows for larger systems to be solved thereby facilitating more accurate results. Table 2-2 shows

the solving speed for simulating the lithium concentration throughout the electrode particles for a range of node points. The ICs for both cases were given as shown in Eq. (2.24). The switch function was applied with $t_j=1$ and $q=1000$ (same as previous examples) and the perturbation value was $\varepsilon = 1 \times 10^{-5}$. The system was solved with a Rosenbrock solver under both the standard FD scheme and the proposed approach. The computational savings from the proposed approach allow larger systems to be solved. For a SPM with 50 internal node points (resulting in a system of 4 AEs and 100 ODEs) the proposed approach reduced computational time by two orders of magnitude. For more examples of the perturbation and switch method see Appendix A.

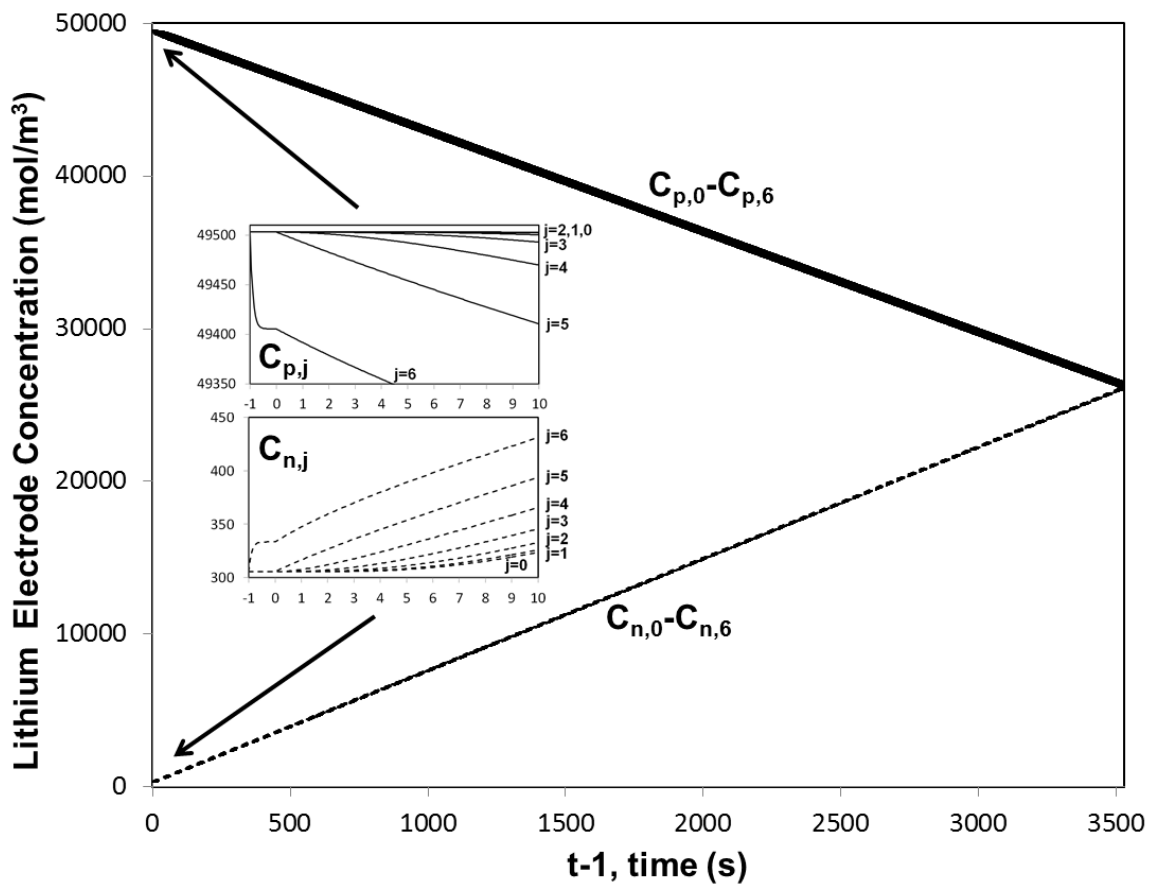


Figure 2-6: SPM concentration solutions for N=5.

Table 2-2: Computational time for solving concentration profiles in Example 5 using Maple's dsolve. Standard finite difference fails to solve SPM beyond N=50.

Internal Node Points	Standard FD Time (ms)	Proposed Single-Step Time (ms)
5	111	55
25	3,340	94
50	23,715	200
100	N/A	404
500	N/A	4,377

Chapter 3

Analysis of Solar-Battery Hybrid Systems from Systems Level Modeling

This chapter contains excerpts from the following journal articles, reproduced here with permissions from Elsevier:

Lawder, M.T., Viswanathan, V., Subramanian V. R. “Balancing autonomy and utilization of solar power and battery storage for demand based microgrids” *Journal of Power Sources* 279(2015) p. 645-655.

And

Lawder, M. T., Viswanathan, V., Subramanian, V. R. “Model-Based Study of Site-Based Irradiance Pattern Effects on Battery Storage for Solar Energy.” *In review with Journal of the Electrochemical Society.*

3.1 The Need for Energy Storage with Solar Power

Distributed generation, specifically solar power, continues to penetrate the electricity generation market.⁷⁴ The intermittent nature of solar power can create difficulties when attempting to dispatch power to match demand. Unbalanced generation and demand can lead to loss of power for customers and cause grid instability. Because of these issues the capacity value of solar panels is often 30% or less of nameplate capacity.⁷⁵ While techniques like demand-side management can help alleviate some of the problems associated with this imbalance, energy storage is one of the few options that can allow intermittent renewable energy to be controlled in a manner similar to conventional generation. Figure 3-1 shows the basic concept behind using energy storage to create constant generation.

Within the electric grid, power generation must match consumer demand in real-time. Since electricity is perishable (it must be used immediately upon creation) and consumer demand can fluctuate on a short (second and minutes) timescale, power generation is often run in excess of actual demand requirements in order to maintain the minimum level of electricity required by the grid.^{76,77} Energy storage can help to remove the perishable nature of electricity.⁷⁸

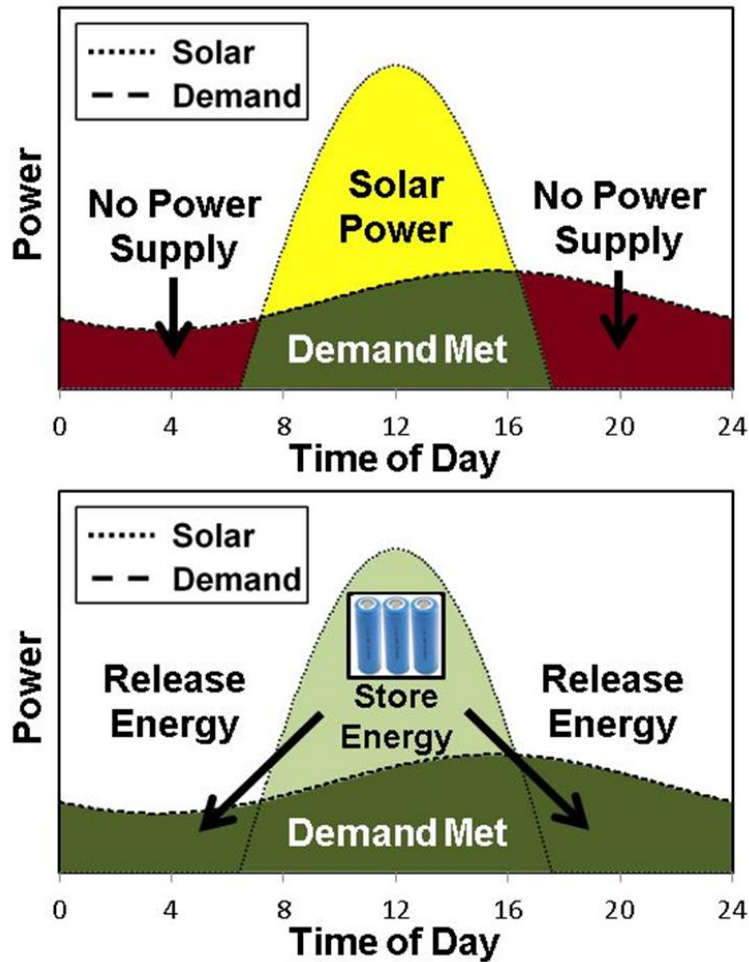


Figure 3-1: Concept showing the use of energy storage with renewables.

Currently, the electric grid employs energy storage to help maintain a stable network by using storage in applications such as: system regulation (frequency and voltage), spinning reserve, peak shaving, peak shifting, load leveling, and transmission support.^{79, 80} For solar power within the grid, energy storage can help shift solar generated energy to be used during peak demand periods when energy is most valuable, increasing a solar array's capacity value. At the utility scale, shifting solar energy can alleviate the need to use expensive peaking plants. At the residential or commercial scale, shifting solar energy can be economically beneficial if the consumer is enrolled in a time-of-use (TOU) electric rate pricing, where electric rates will vary based on the time of day.⁸¹

Adding energy storage to solar panels can help to reduce the need for transmission infrastructure by allowing more of the power that is generated by solar panels to be used locally. In some cases, especially in isolated areas, solar-battery systems will not have any connection to a regional grid, only using distribution level infrastructure. These types of systems are called *islanded* systems and must generate all the power needed to meet local demand.⁸² Any system with a connection to a larger network is known as a *grid tied* system. Grid tied systems can operate in islanded modes (sometimes referred to as emergency modes), however, they maintain a connection to the grid and will typically draw power from the grid during times of high local demand and low internal generation. They will send power to the grid during times of high internal generation and low local demand.⁸³ A grid-tied system will only go into islanded mode when the external grid has a failure and cannot supply power to the local loads.⁸⁴ Grid tied systems are less strict in their requirements for generation and storage sources because they can use the grid to supplement any power shortfalls and will take energy directly from the grid when economically favorable.

This chapter will focus on analyzing solar-battery hybrid systems and their ability to meet power requirements from the local grid. System characteristics such as the effects of battery capacity and demand size are simulated under controlled conditions. Sizing and system performance analyses of battery systems have been performed for grid applications in connection with conventional generation sources⁸⁵, single intermittent renewable sources⁸⁶⁻⁸⁸, and combined hybrid renewable source systems.⁸⁹⁻⁹³ Inclusion of system demand within these studies has increased the fidelity of simulations.⁹⁴ However, when accounting for battery systems, these simulations utilize simple empirical-based or equivalent-circuit based models (ECM). While these model work well for predicting simple metrics such as sizing, analyzing battery

degradation, measuring economic potential, and understanding operation over short time periods requires the use of a higher order model that more accurately represents the system.

Previous work that has used empirical models has restricted the operational SOC range and limited DOD during operation.⁹⁵ Additionally, empirically based models struggle to account for capacity fade and changes to operating conditions, which can cause inaccuracies even when measuring simpler metrics such as system-wide autonomy. Using the SPM, autonomy and battery utilization are tracked accurately over the course of an entire year, avoiding the problem of refitting an ECM for changing seasonal insolation.

Determining the true operational characteristics of a solar-battery hybrid system will require accounting for irradiance patterns at an individual site as well. Using minute-resolution data from individual sites in the United States, this chapter determines both technologic and economic benefits for adding battery storage to a solar array at a given site. Technologic benefits include increasing the level of system autonomy and optimizing the battery utilization as well as the system's capacity value. Adding energy storage to solar arrays cannot increase the total amount of energy produced by the system. Therefore the capacity *factor* or energy value (the amount of energy produced divided by the amount of energy produced if the system operated at 100% of peak output at all times) will not be affected by adding energy storage. However a system's capacity *value* (the power rating of a constant generation source required to replace the solar array and meet the same amount of grid reliability divided by the system's peak power rating) will increase with energy storage because the system will have much greater flexibility in meeting reliability issues.⁹⁶ Capacity value will account for the temporal demand of energy from a system. Note that irradiance is the power delivered by the sun at any given time and insolation is the energy provided from the sun, calculated over a set time interval (in this chapter, one day

was typically used for the time interval). To calculate insolation values, a site's irradiance curve must be integrated over the desired time interval. Sites with similar daily insolation values can have very different daily and seasonal irradiance patterns.

Energy storage becomes even more important to achieving high capacity values for solar arrays as the penetration of solar power increases. Capacity values are not measured in this chapter, rather system autonomy and battery utilization are used as indicators for technologic benefit. The economic benefits for this chapter are measured by determining the dollars gained under a TOU pricing scenario. In addition to measuring system metrics, results for all the sites will be compared to determine which results require high-resolution irradiance models and which results can be more simple determined.

3.2 Systems Level Solar-Battery Model

The systems level model couples Li-ion battery storage with a solar array in order to better supply power to match demand. While many previous models for solar generation plus battery energy storage have studied how total demand met is affected by incorporation of battery storage, they struggle to intricately study battery storage's operation and lifetime, instead simplifying the battery component in order to focus on the combined system. While Li-ion batteries are credited with a long cycle life that would be useful in grid-scale storage, most lifetime estimates are based on simple galvanostatic cycling, as opposed to varying power conditions present in solar-battery hybrid systems. This chapter will look at how the battery's life will be affected under different irradiance patterns or demand shapes and sizes. Included are analyses based on energy throughput life estimates as well as simulation that include a side reaction for SEI layer growth that will help to better estimate the degradation occurring within the battery caused by the different cycling patterns.

In order to simulate the dynamic conditions seen in the solar-battery network, the system-level model also includes components for demand, the grid, and solar generation. For the local grid (system can be considered a self-contained microgrid tied to a larger network), a dispatch protocol will control how power flows between the solar array, battery, demand loads, and external grid. A schematic of system protocol is shown in Figure 3-2. The solar and battery model components as well as demand are outlined below.

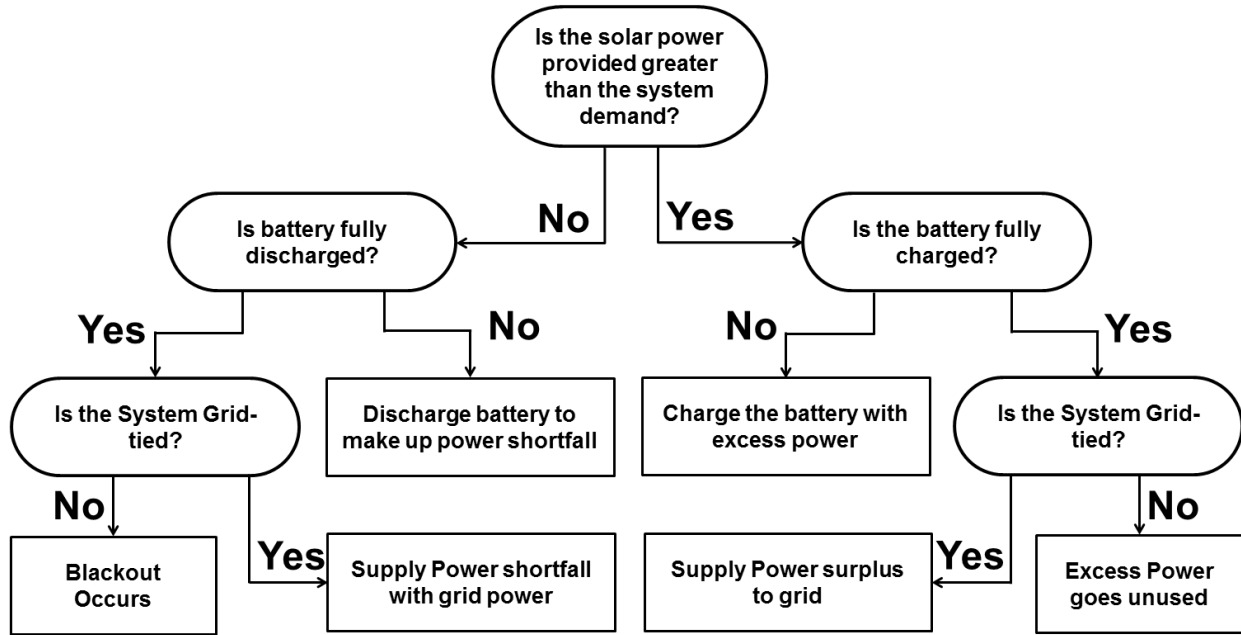


Figure 3-2: Control hierarchy for power flow through solar-battery hybrid system.

3.2.1 Solar Component

For the solar component to convert the irradiance data into a usable power output from a standard photovoltaic cell, an equivalent-circuit based solar array model is used.⁹⁷ The solar array here is represented through an ideal diode in a circuit with one parallel resistance and one series resistance. The equivalent circuit model determines power output for the solar array based on the array's output current (I) and voltage (V) determined by the equation:⁹⁸

$$I = I_{pv} - I_0 \left[\exp \left(\frac{V + R_s I}{V_t b} \right) - 1 \right] - \frac{V + R_s I}{R_p} \quad (3.1)$$

where the I_{PV} is the photovoltaic current from individual cells (a function of irradiance) , I_0 is the saturation current, V_t is the thermal voltage, R_s is the series resistance, R_p is the parallel resistance, and b is the diode ideality constant. At any irradiance value, a set of I and V values can be determined from the equivalent circuit model (they make up what is known as the I-V curve for a solar cell). The maximum power producing point is determined for each irradiance value and these pairs are used to create a look-up table that determines solar array power output based on incident irradiance.

For a set irradiance, the solar array operates in a steady-state unlike the battery which has continuously changing internal states. Therefore the simplified equivalent circuit model can be used for the solar array with a higher accuracy than is possible for an ECM for the battery.

The amount of solar energy produced will be dependent on the size of the solar array and the daily insolation characteristic to the system's site. For complete utilization, the total amount of energy demanded from the system should equal the total amount of energy generated by the system:

$$\int_{t_{s,demand}}^{t_{f,demand}} P_D(t) dt = \int_{sunrise}^{sunset} P_G(t) dt \quad (3.2)$$

where P_D is the instantaneous power demanded and P_G is the instantaneous power generated. Unfortunately, sizing the system is not as simple as equating the demand to the generation because the amount of demand as well as the amount of insolation available for power generation changes daily and seasonally. Therefore yearlong simulations, such as the simulations shown in this chapter, are vital to maximizing the potential of a solar–battery hybrid system.

3.2.2 Local Demand Load

The solar-battery system must determine what portions of demand will be covered by local generation instead of being supplied from the external grid. In practice, some battery systems may be used for arbitrage purposes, meaning charge is stored using the external electric grid when electric prices are cheap and released on the local grid when electric prices are high. This practice focuses on using storage based on the economic variations in the electric market rather than utilizing the available generation most effectively and can cause a system to locally demand more energy than required by its immediate loads. In our study, we exclude the application of arbitrage and assume that the local system demand will never exceed its load.

Different demand structures (driven by different application's needs) will create varying needs among energy generation and storage components. Four different types of demands were studied (shown in Table 3-1): Constant; Parabolic, Sinusoidal, and Trapezoidal (or Time-of-Use [TOU]). These types of demand are representative of different needs for both islanded and grid-tied systems.

The *constant* demand approximates a steady continuous load. The demand remains at the same power requirement for 24 hours without changing.

The *parabolic* demand approximates a peak load increase in the late afternoon. The demand is six hours in duration following a parabolic shape equation:

$$Demand = 4 \left(\frac{t}{T} - \left(\frac{t}{T} \right)^2 \right) \quad (3.3)$$

where t is the time from the beginning of the demand period and T is the period of demand. Eq. (3.3) is normalized to one so that it can be multiplied to be properly sized in the model.




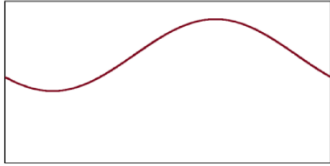
For the *sinusoidal demand*, a sine curve offset from the x -axis by two times the amplitude (maximum demand is double minimum demand) was used to approximate the demand required to meet all of a region's loads throughout the day. The sine curve reaches its maximum at 3:30PM and reaches its lowest point at 3:30AM to coincide with the typical temporal variation in demand. This curve was used to produce the power demanded by a region's loads over the course of an entire day. The size of the demand could be varied (by making the amplitude larger) to show how the addition of more loads would affect autonomy and battery utilization if the solar-battery hybrid components remained the same size. This demand structure is representative of typical load curves for large microgrids and regional or national grids, which can see demand shift by over 100% during the course of a single day.⁹⁹ In general, the times of greatest solar insolation are weakly coincident with times of peak power demand. The lowest levels of power demand are during the nighttime and increase in early morning, reaching their peak in mid-afternoon, slightly after peak solar insolation (Often the peak demand will be ambient-temperature driven with high associated heating or cooling loads).^{85, 100, 101} Additionally, for small systems such as an individual house, demand will often be driven by occupancy. For the example of a single family home, demand will peak in morning before occupants leave for work and will again peak in the evening when they return home. However, more complex demand structures such as this two peak system were beyond the scope of this dissertation.

The *TOU demand* follows a trapezoidal shape, represented by one hour of linear rising demand going from zero power to the maximum power demand, followed by constant maximum power demand and finishing with one hour linearly falling demand. This trapezoid shaped demand is centered around 3:30PM to coincide with peak demand hours (the total length of demand varies for Study A and is 6 hours for Study B). When demand rises in the afternoon,

additional power plants must be turned on or ramped up to match the load. These peaking plants are often expensive to run and the TOU demand curve seeks to offset these plants by demanding energy only during peak hours. TOU demand is used for TOU economic studies in Study B.

The total size and amount of individual loads that are being powered through a solar-battery system affects the discreteness of the demand. For a small number of defined loads the demand can change swiftly depending on when the loads are turned on or off. Individual case studies have looked at discrete loads but have been limited in their scope for being applied generally.^{102, 103} For systems supporting many loads, the demand curve will show smoother characteristics because the relative change caused by any individual load will become much smaller. For our simulations, we used demand curves that were approximate for systems of large enough size to reduce discrete demand fluctuations.

Table 3-1: Demand curves studied.

Demand Type	Duration	Description	Image
TOU (Peak)	4-10 hours	One hour of linear rising demand to max power, constant max power, one hour of linear falling demand	
Parabola	4-10 hours	A parabolic shape curve that reaches max power at its midpoint	
Constant	24 hours	A steady demand curve that remains the same the entire day	
Sinusoid	24 hours	A sine curve with a 24 period (all day) with a minimum of 1/2 max power occurring at 3:30AM and maximum of max power (amplitude 1/4 max power power) occurring at 3:30PM	

3.2.3 Battery Component with Solid-Electrolyte Interface Layer

A Li-ion battery is used for energy storage in these simulations. Most models that study battery storage with renewable energy account for the battery through simplified empirical relations.^{91, 104-111} These types of models are used for their simplicity in allowing optimization algorithms and control strategies to be utilized, but struggle to account for changing operational conditions and their effects on degradation. Most empirical models are calibrated under a single set of cycling conditions, but during operation in solar-battery hybrid systems, the batteries will experience varying cycling conditions. Electrochemical Li-ion battery models have proven to be more accurate and predictive of battery states and degradation when compared to empirical models because they remain valid outside of the calibration range.^{36, 42, 112, 113} These electrochemical models allow for the tracking of additional battery states that are not included in empirical models (potential at electrodes, electrode lithium concentration, etc.), which can allow for physics-based capacity fade equations to be added to the model. A major downfall of empirical models is that they do not track capacity fade well without continual re-calibration of the model.¹¹⁴

An electrochemical based SPM is used to represent the Li-ion battery in the system. The equations for the SPM model are explained in Section 1.5.1 and shown as used for these studies in Table 3-2. The parameter values for the model are shown in Table 3-3. Low rates (less than 1C) will be used during operation because the time scale for the applications studied is multiple hours to days (Short-term energy storage applications such as frequency control were not included in this study). We also assume that the electrodes are not thick enough to create electrolyte gradients. A comparison between the SPM used in this model and a sample ECM is shown in Section 3.3

Table 3-2: SPM model equations including SEI reaction. ^{13, 15, 41, 115, 116}

Governing Equations	
Positive Electrode	Negative Electrode
$\frac{dc_p^{avg}}{dt} = -\frac{3j_p}{r_p}$	$\frac{dc_n^{avg}}{dt} = -\frac{3j_n}{r_n}$
$\frac{D_p}{r_p} (c_p^{surf} - c_p^{avg}) = -\frac{j_p}{5}$	$\frac{D_n}{r_n} (c_n^{surf} - c_n^{avg}) = -\frac{j_n}{5}$
$j_p = \frac{i_{app}}{F a_p l_p}$	$j_n = -\frac{i_{int}}{F a_n l_n}$
Solid-Electrolyte-Interface Equations	
$i_{int} = i_{app} - i_{SEI}$	
$i_{SEI} = -F k_{SEI} c_e \exp\left(\frac{-F}{RT} \left(\Phi_n - \frac{\delta_{SEI} i_{app}}{\kappa_{SEI}}\right)\right)$	
$\frac{d\delta_{SEI}}{dt} = \frac{-i_{SEI} M_{SEI}}{2F \rho_{SEI}}$	
Additional Equations	
$j_p = \frac{1}{2} k_p c_e^{0.5} c_p^{surf 0.5} (c_p^{max} - c_p^{surf})^{0.5} \sinh\left(\frac{F(\Phi_p - U_p)}{2RT}\right)$	$\theta_p = \frac{c_p^{surf}}{c_p^{max}}$
$j_n = \frac{1}{2} k_n c_e^{0.5} c_n^{surf 0.5} (c_n^{max} - c_n^{surf})^{0.5} \sinh\left(\frac{F(\Phi_n - U_n)}{2RT}\right)$	$\theta_n = \frac{c_n^{surf}}{c_n^{max}}$
$U_n = 0.7222 + 0.1387\theta_n + 0.029\theta_n^{0.5} - 0.0172\theta_n^{-1} + 0.019\theta_n^{-1.5} + 0.2808 \exp(0.9 - 15\theta_n) - 0.7984 \exp(0.4465\theta_n - 0.4108)$	
$U_p = \frac{-4.656 + 88.669\theta_p^2 - 401.119\theta_p^4 + 342.909\theta_p^6 - 462.471\theta_p^8 + 3.434\theta_p^{10}}{-1 + 18.933\theta_p^2 - 79.532\theta_p^4 + 37.311\theta_p^6 - 73.083\theta_p^8 + 95.96\theta_p^{10}}$	

Included in the model is a side reaction accounting for SEI layer growth. The SEI layer is explained in more detail in Section 1.6.1 and the equations for the SEI layer have been included in Table 3-2 with the SEI layer parameter in Table 3-3. While energy storage creates flexibility for power delivery, it remains expensive, and therefore only the amount of storage capacity that is required to meet demand should be added. To determine how much storage capacity is needed within a system, the difference between the power generation curve and power demand curve must be ascertained. When generation occurs at the same time as demand, power generated can be sent directly to the local demand without energy storage. The remaining difference will have to be stored for later use as shown below:

Table 3-3: Parameters for SPM model.

Symbol	Parameter	Values	Units	Source	
F	Faraday's Constant	96,487	C/mol		
R	Gas Constant	8.3143	J/(mol K)		
T	Temperature	303.15	K		
c_e	Electrolyte Concentration	1,000	mol/m ³	7	
k_{SEI}	SEI Reaction Rate Constant	1.36×10^{-12}	m/s	8	
M_{SEI}	SEI Molecular Weight	0.162	kg/mol	8	
ρ_{SEI}	SEI Density	1,690	kg/m ³	8	
κ_{SEI}	SEI ionic conductivity	5.0×10^{-6}	S/m	8	
		Cathode (p)	Anode (n)		
a	Particle Surface Area to Volume	8.85×10^5	7.24×10^5	m ² /s	9
c_{max}^s	Maximum Lithium Concentration	51,555	30,055	m ² /s	7
D	Solid phase Diffusion Coefficient	1.0×10^{-14}	3.9×10^{-14}	m ² /s	7
r	Electrode Particle Radius	2×10^{-6}	2×10^{-6}	m ² /s	7
k	Reaction Rate	2.33×10^{-11}	5.03×10^{-11}	m ² /s	9

$$\text{When } P_G > P_D \quad \int (P_G(t) - P_D(t)) dt = \text{Capacity}_{Storage} \quad (3.4)$$

Similar to sizing the solar panels, sizing the battery for a single day would not be a difficult task, but since the demand and generation vary daily, the capacity required to meet demand will vary each day. Full yearly simulations are required to determine the optimal battery size for a site. Additionally, degradation of the battery is affected by the DOD that the battery experiences. Therefore it may be beneficial for the life of battery to operate at lower DOD when possible.

3.2.4 Technologic Metrics

For the solar-battery hybrid system two technologic metrics were measured for each case studied: *system autonomy* and *battery utilization*. *System autonomy* is a measure of the percentage of energy supplied by the solar-battery hybrid system compared to the energy demanded:

$$\text{System Autonomy}_{\text{Annual}} = \frac{\sum_{\text{year}} \text{Energy delivered to microgrid}}{\sum_{\text{year}} \text{Energy demanded by microgrid}} \quad (3.5)$$

If the system operates correctly and meets all of the demand for the duration of a simulation, it will have an autonomy measure of 100%. While autonomy is an energy measure, it is similar to the inverse of the metric Loss of Power Supply Probability (LPSP).⁹² However, LPSP is often used to describe the statistical likelihood that a system will be able to meet power demand at any given time (based on an averaging of historical trends), while the autonomy measure used in this study is based on historical solar data and actual system operation based on that data taken over the duration of a year. The system model can pinpoint which events lead to power loss during the year rather than supplying only a probability of failure. The desire for 100% autonomy can lead systems to be overbuilt (only using their theoretical capacity a few days per year).¹¹⁷ This chapter studies how to maximize capacity usage based on a combination of demand and generation requirements.

Battery utilization is a measure of how much battery energy capacity is used on a daily basis. Because of the variable nature of solar power, the battery may go through many shallow cycles, a few medium length cycles, one deep cycle, or a combination of these over the course of a single day. Therefore, we use battery utilization as a measure of the average energy discharged per day normalized to the energy discharged during a single 100% DOD discharge:

$$\text{Battery Utilization}_{\text{Annual}} = \frac{\sum \text{Energy discharged}}{365(\text{Energy}_{100\% \text{ DOD}})} \quad (3.6)$$

The energy discharged is calculated from the current and voltage outputs of the system integrated in time. Note that by definition battery utilization could reach over 100% if multiple

cycles are experienced over a single day. Battery utilization accounts for all of the energy throughput of a battery during the year.

The percentage of energy supplied by the system that came from the battery (after being generated by solar), known as percentage battery supplied (PBS), over the course of the year will also be measured. The remaining percentage of energy is supplied directly from the solar array without the need to be stored in the battery.

SOC will be tracked based on lithium concentration, C_n^s , at the anode:

$$SOC = \frac{C_n^s}{C_{\max,n}^s} \quad (3.7)$$

When the battery is in a discharged state the anode will contain (almost) no lithium, because it will be stored in the cathode.

DOD, the percentage of capacity used during a discharge cycle, will be track based on SOC shown as:

$$DOD = SOC_{\text{initial}} - SOC_{\text{final}} \quad (3.8)$$

3.2.5 Techno-Economic Analysis

While system autonomy and battery utilization will be used to measure the technologic benefit of adding batteries to the solar array, the economic value of the system will be measured by coupling those metrics (when using TOU type demand) to utility rates based on TOU pricing. TOU has been implemented (mostly on a volunteer basis) in several states throughout the US. The rate structure charges difference prices for electricity depending on if the electricity is used during peak or off-peak times (some utilities offer three-tier or more complicated real-time TOU schedules, but we will only consider the two-tiered fixed structure in this analysis). Electricity prices will be higher during peak demand hours.

We assume a two tiered TOU structure with peak pricing occurring between 12:30 PM and 6:30 PM (the rest of the day is off-peak price). When determining the value of the battery in this scenario there are two cases of the system studied. A *Base Case* (with no battery) assumes that only a solar array is installed and reduces electrical load by the amount of power it produces instantaneously. Any energy produced during peak times will yield an economic savings at the peak rate and the rest of the energy produced will be valued at off-peak rates. In a second case, the *Battery Case*, solar energy generated during off-peak hours will be stored in the battery for use during peak pricing hours. We use the TOU (peak) demand explained in Section 3.2.2 (starting at 12:30 PM and ending at 6:30 PM) to try to maximize energy use during peak pricing periods. When the battery is fully charged during off-peak times, any additional solar power will be valued at off-peak prices. For these cases, we assume that energy can be used internally and does not need to be sold to the external grid. The Base Case Value can be subtracted from the Battery Case Value to determine the savings per year added by the battery.

$$BaseCaseValue = \int \left\{ \begin{array}{ll} V_{Off} (P_{Solar} - P_{Demand}) + V_{On} P_{Demand} & P_{Demand} < P_{Solar} \\ V_{On} P_{Solar} & P_{Demand} > P_{Solar} \end{array} \right\} dt \quad (3.9)$$

$$BatteryCaseValue = \int \left\{ \begin{array}{ll} V_{Off} (P_{Solar} - P_{Demand}) + V_{On} P_{Demand} & P_{Demand} < P_{Solar} \text{ \& Battery at full charge} \\ V_{On} (P_{Solar} + P_{Battery}) & P_{Demand} > P_{Solar} \end{array} \right\} dt \quad (3.10)$$

where V_{off} is the electricity price during off-peak hours, V_{on} is the electricity price during peak hours, P_{solar} is the power of the solar array, P_{demand} is the power demanded, and $P_{battery}$ is the power being supplied from the battery.

The value determined is based on utility bill savings, so the system is only beneficial as long as the real-load continues to demand energy during peak-times. The system sizes studied in the economic analysis section will be smaller systems of residential and commercial size.

Therefore calculations assume that savings at on-peak rates can only incorporate the total amount of energy demanded by the system during peak hours (100kWh in most studies). All other energy produced is valued at off-peak rates.

3.3 Comparison of SPM and ECM

The SPM has proven to be a more accurate model when compared to the ECM because its governing equations reflect the actual electrochemical processes occurring in the battery.¹¹⁸ Electrochemically based models have been shown to achieve higher accuracy than their ECM counterparts, but ECMs continue to be used for real-time battery management systems (BMS) due to their simplicity and robustness within microcontroller environments.¹¹⁹⁻¹²³ For non-BMS studies, electrochemical models such as the SPM are favored.^{13, 17, 112} In some cases, enhanced ECM models have been applied by using the SPM theory to increase model accuracy.^{124, 125} A major challenge for ECMs is accurately measuring the SOC of the battery when charging rates are not constant. For solar charging, the current is constantly changing throughout the day and the rates of charging vary seasonally. ECMs are not well calibrated to accurately predict the SOC, voltage, or energy output during the entire simulation period because they are not valid outside of the operating conditions for which they are developed.¹²⁶ For a battery being charged through solar power and discharged based on grid demand, the operating conditions are constantly changing creating the need for an accurate model that can better account for changing conditions. The SPM particle model has shown to be more adaptive to changing operating conditions. While an accurate ECM using complex circuits can be used for a single case study, the model will not retain its accuracy as well as the SPM over the entire lifetime of the study because of the changing operating conditions.

We compared the SPM to a common ECM that uses a voltage proxy for SOC estimation. The ECM was based on a circuit containing an open circuit voltage source, a series resistance and an element with a parallel resistance and capacitor.¹²⁷⁻¹³⁰ The circuit can be represented by the equations:¹³¹

$$\frac{dV_c}{dt} = \frac{-1}{R_c C_c} V_c + \frac{1}{C_c} i_{app} \quad (3.11)$$

$$V_b = V_{oc} - V_c - R_0 i_{app} \quad (3.12)$$

where V_b is the battery voltage, V_{oc} is the open circuit voltage, V_c is the capacitance voltage, R_0 is the ohmic resistance, C_c is the capacitance, R_c is the capacitor parallel resistance, and i_{app} is the applied current. The ECM was calibrated based on a 1C charge rate and set to match the capacity of the SPM model. For a single charge the percent difference between the ECM and SPM was 1.2% for the voltage and 1.3% for the SOC throughout charging, underestimating values early in the cycle and overestimating values later. While the difference is acceptable of a single cycle, the error will accumulate when the models are used to track multiple cycles. Figure 3-3 shows the variation in measured SOC between the SPM and ECM over ten cycles.

Additionally, changing the applied current from the original current creates error in the ECM. When studying a test case of the solar-battery hybrid system (12 hour day with 1 BCSC (see Section 3.5) and 4 hour demand starting at 6PM) the ECM found the system running at 87.5% Autonomy and 100% battery utilization. The SPM found autonomy of 89.0% and battery utilization of only 94%. A major discrepancy with the ECM is the inaccuracy of the calculated voltage-SOC relationship when the operating conditions are changed. Under the test case the ECM shows 100% SOC being reached before the normal voltage cut-off, which is a response from the empirical nature of the SOC estimation method.

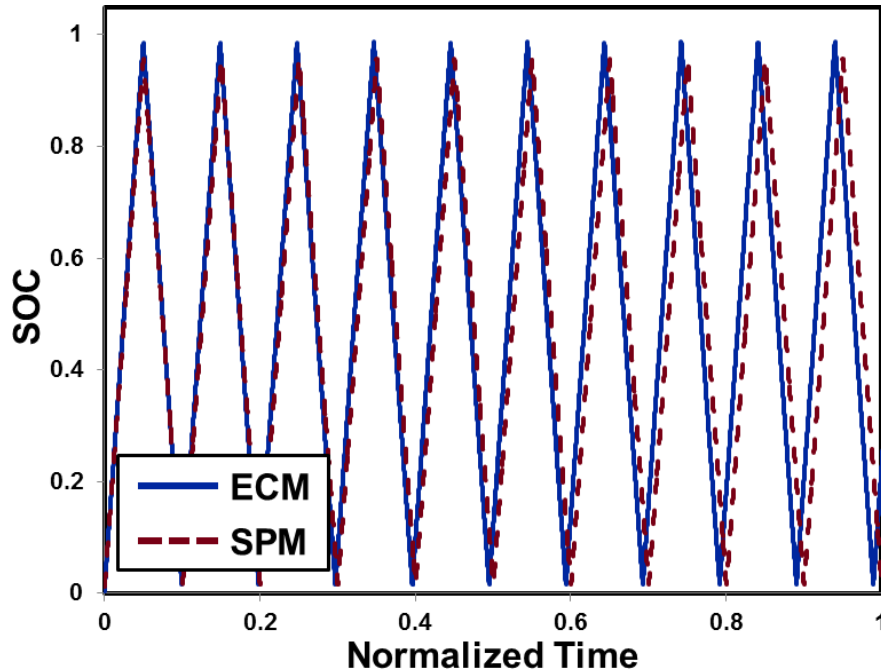


Figure 3-3: Comparison of ECM to SPM over 10 cycles.

While including more rigorous physics-based battery models (beyond the SPM) may be useful for simulating single cycles, the use of the SPM allows for simulation of a year’s worth of system data on the order of minutes which cannot be matched by higher-order models.¹¹⁸ The balance of efficiency with accurate SOC, voltage, and energy output estimation that the SPM offers allows for better analysis without heavily increasing computational time.

3.4 Single Day Case Study

Two examples of the solar-battery system are shown in Figures 3-4 and 3-5 to help explain the dynamic relationship between demand, generation, and storage. For the first case, a 12 hour half sinusoidal solar insolation curve with peak solar insolation of 1000Wm^{-2} is used. The demand for the system is an 8-hour TOU demand with a maximum power demand equal to the maximum power output from the connected solar array with the demand centered at 3:30PM (the TOU demand contains one hour of rising power demand, beginning at 11:30AM, and one hour of falling power demand ending at 7:30PM with a 6 hour period of maximum demand in

between). Figure 3-4 shows the power used directly from the solar array and from the battery storage.

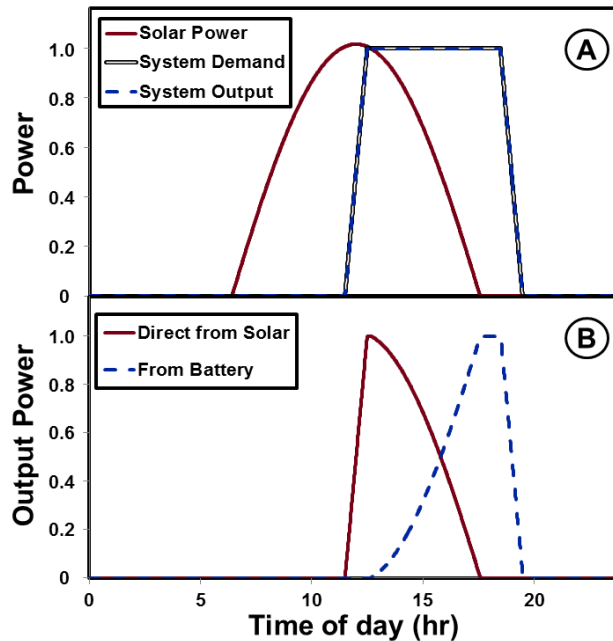


Figure 3-4: Solar array plus battery storage with trapezoidal demand. A) Power from solar array is shown in conjunction with the demand of grid and the output of the system. B) Shows distribution of power that is supplied directly from solar array and power supplied from battery.

Figure 3-5 shows a case where the energy demand is too great for the system under its current size and insolation. For a 12 hour TOU demand with a maximum power demand equal to 83% of maximum power output from the connected solar array with the demand centered at 3:30PM, the solar array (same characteristics as previous case) does not produce enough energy and therefore supplies power only part of the time. In this case, the system does not meet the required demand for 11.5% of the time, and the system can only provide 79.4% of the demanded energy (Autonomy of 79.4%). Also important to note in the second case is that the capacity of the battery is underutilized, never being close to fully charged. Under the second case's conditions, the battery is only utilizing 57.2% of its total capacity during a single cycle (compared to 82.3% in case 1). The SOC is shown in Figure 3-6 for both cases showing how a fully charged battery state was never achieved. In order to satisfy the external demand, the solar

array's output must be increased (increasing the array size 26% while keeping the rest of system constant) or the power demand decreased (decreasing the power demand by 21% while keeping the rest of the system constant).

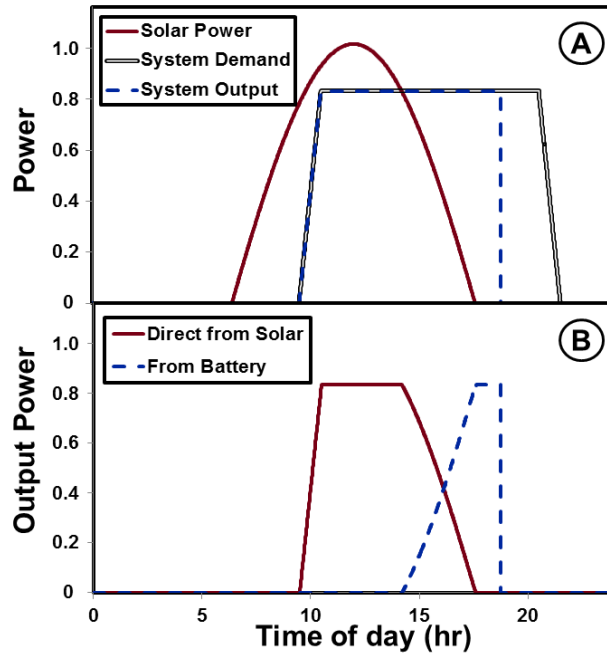


Figure 3-5: Solar array plus battery storage with trapezoidal demand. In this case the system cannot meet demand at all times. A) Power from solar array is shown in conjunction with the demand of grid and the output of the system. B) Shows distribution of power that is supplied directly from solar array and power supplied from battery.

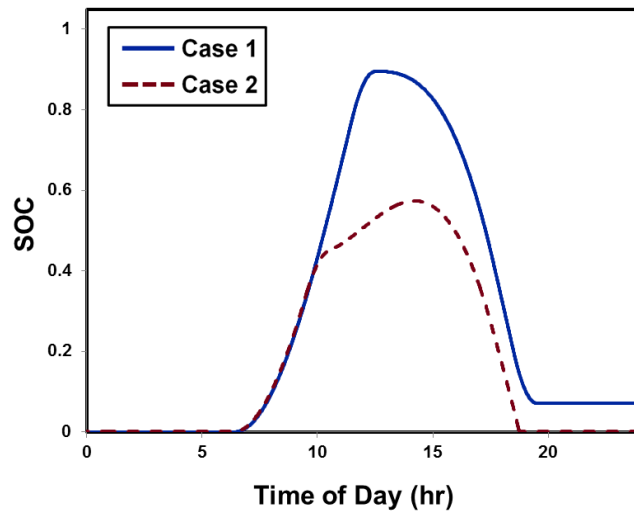


Figure 3-6: SOC for cases in Figures 3-4 and 3-5.

3.5 The Standard Case (for autonomy and battery utilization studies)

For most of the results in the following two studies, the sizes of the system components were set to a standard value unless otherwise stated. This allowed for easier comparison between cases. When all components (solar panel size, battery capacity, and demand load size and shape) are simulated under these standardized parameters, we will refer to those simulation as being run under *the standard case*. In many tests, a simulation will be run with only some of the components under their standard parameters. For example, in Study A, some simulations vary the capacity of the battery and plot the resulting autonomy and battery utilization as a function of demand size. For cases that deviate from the standard case, the details of the simulation will be explained.

For the standard case, the maximum power of the solar array was set to 30.5kW. The energy capacity of the battery was 116.5 kWh. The battery capacity was determined based on the daily amount of solar energy provided from the 30.5kW solar array on average. An irradiance curve approximated by a 12-hour half-sine curve peaking at 1kW/m² applied to the solar array would provide 233kWh of energy.

$$\int_0^{12h} 30.5kW \sin\left(\frac{t\pi}{12}\right) dt = 233kWh \quad (3.13)$$

A half-sine curve is a good approximation of the irradiance pattern of a sunny day for a site without a large angle of irradiance (see Section 3.7.1). The battery capacity was chosen to provide storage for 50% of the solar insolation (116.5kWh). This level of storage will be referred to as 0.5 Battery Capacity to Solar daily Capacity (BCSC). If a battery has 233kWh of capacity, it would have a BCSC of 1 or if it had 58.25kWh of capacity it would have a BCSC of 0.25. In Study B, the value of battery capacity for the standard case is kept constant across all sites, even

though the average insolation will change, so that sites can be compared based only on their differences in irradiance. The energy demanded during a 24 hour period for the standard case was set at 100kWh coming from sinusoidal demand (maximum power of 5.56kW and minimum power of 2.78kW). Any variation to the standard case parameters are noted with each study.

3.6 Simulation of the Battery-Solar Hybrid System

Two different studies were undertaken with the solar-battery hybrid model. The first study focused on the effect that sizing (both for the battery and demand) had on the battery utilization and system autonomy using approximated solar data that only varied seasonally. The second study used real minute resolution data from the National Renewable Energy Lab's (NREL) Measurement and Instrumentation Data Center (MIDC) database to analyze how individual irradiance patterns at various sites would affect both the technologic and economic operation of the solar-battery hybrid system. The results are presented as separate sections below.

3.7 Results from Study A

3.7.1 Influence of Solar Intermittency

For Study A, half sine curves were used to approximate daily solar insolation curves. For completely sunny days, the half sinusoidal approximation compares well with actual solar insolation data. Figure 3-7 shows our approximation compared to actual data for a day from Phoenix, AZ. However, our results will show an overestimate of available solar energy because we assume no daily deviations from the approximated curve. More on the daily variability of solar energy is discussed in Section 3.8.1.

To study the effect of annual averages to autonomy and utilization, we tested each case with insolation curves that ranged from 8 hours of sunlight to 16 hours of sunlight and weighted

the values for how often that type of day length occurs during the year. An eight hour yearly variation in sunlight similar to the one in our study would be experienced near the 49th parallel (around the western US and Canadian border in the northern hemisphere).

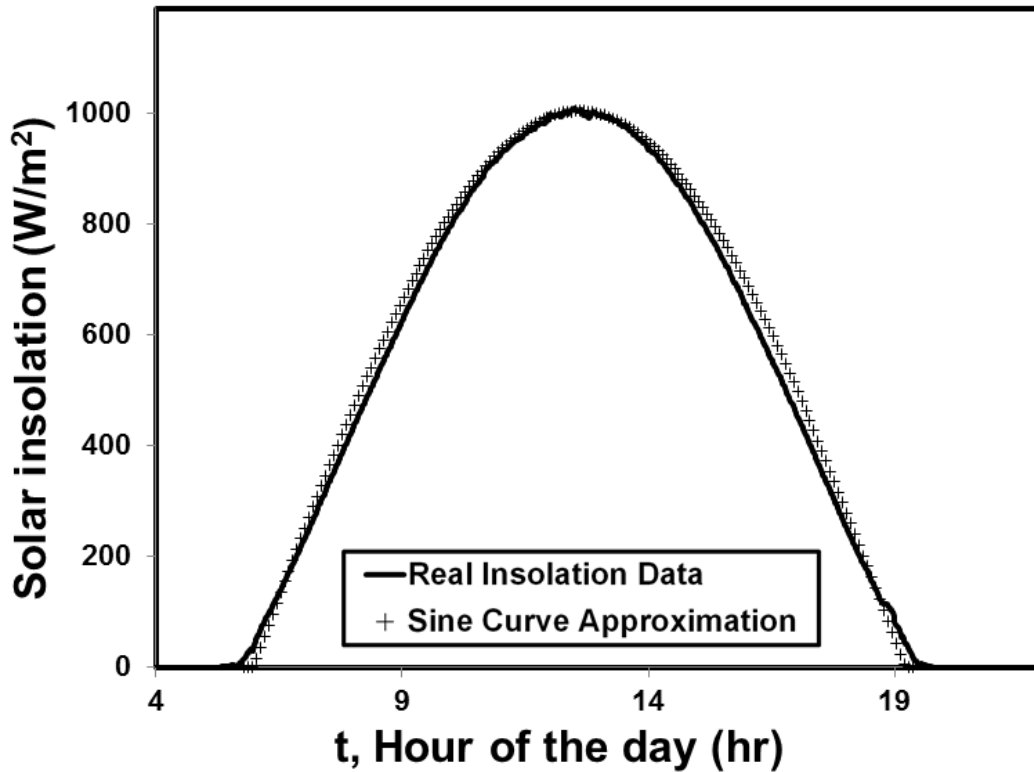


Figure 3-7: Sinusoidal approximation versus real data from Phoenix site July 18th, 2012.¹³²

3.7.2 Autonomy and Utilization Results

A system with no energy storage component can only meet demand when the solar insolation is greater than the required demand. The yearly autonomy for a system with no storage and a constant demand is shown in Figure 3-8 as a function of daily energy demand. As more energy is demanded the autonomy slowly decreases for a system. Adding storage to the system will increase the autonomy, but the energy capacity of the battery will determine how much the autonomy changes. Figure 3-9 shows autonomy and battery utilization as a function of daily energy demanded for three different battery sizes (BCSC 0.25, 0.5, and 1) under constant

demand. As battery capacity increases, autonomy will increase, but only to the point where the power demanded exceeds the combined capacity of the solar array and battery. At this point, autonomy will remain the same (as in the BCSC 0.5 and 1 cases), while the battery utilization will begin to decrease because the battery can never be fully charged by the solar array. Table 3-4 shows the differences in battery utilization for differing demand and battery sizes.

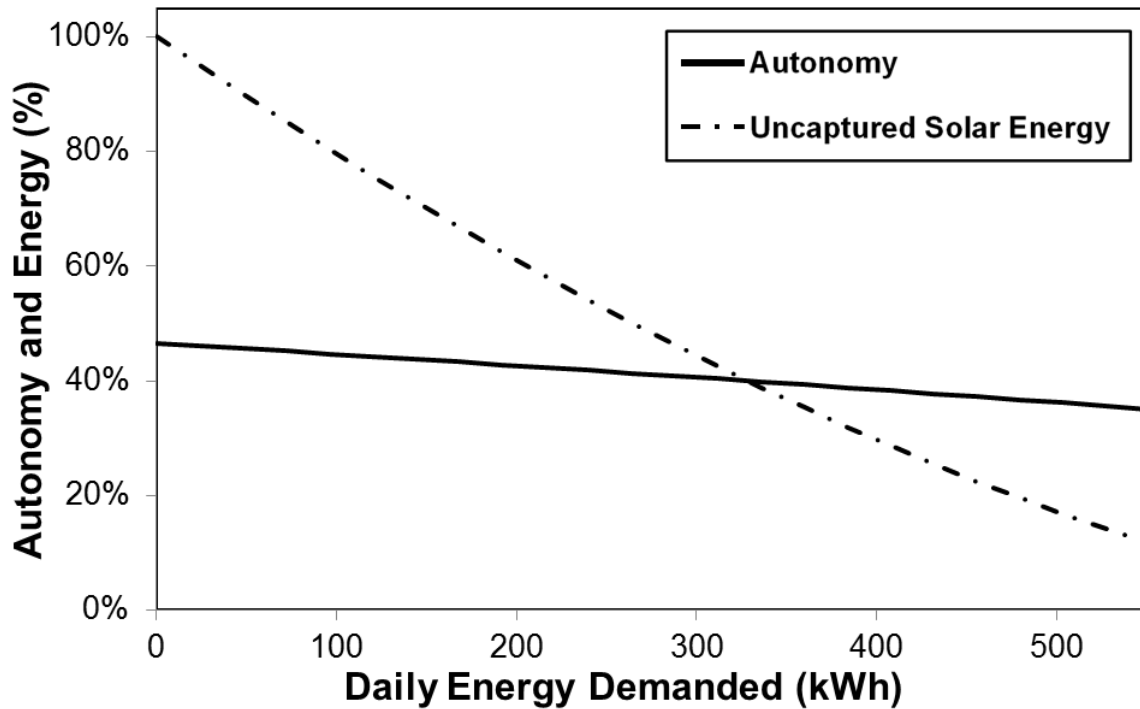


Figure 3-8: Autonomy and uncaptured solar energy for solar array with no storage and constant demand.

Table 3-4: Battery Utilization for the maximum power output demanded that still yields 100% autonomy for each of the four types of demand under three different battery sizes.

BCSC	Storage Capacity(kWh)	Constant Demand (%)	Sinusoidal Demand (%)	4hr TOU Demand (%)	4hr Parabolic Demand (%)
1.0	233.0	34.7	39.5	38.4	29.8
0.5	116.5	69.4	79.2	76.4	56.4
0.25	58.25	79.2	25.1	52.7	58.7

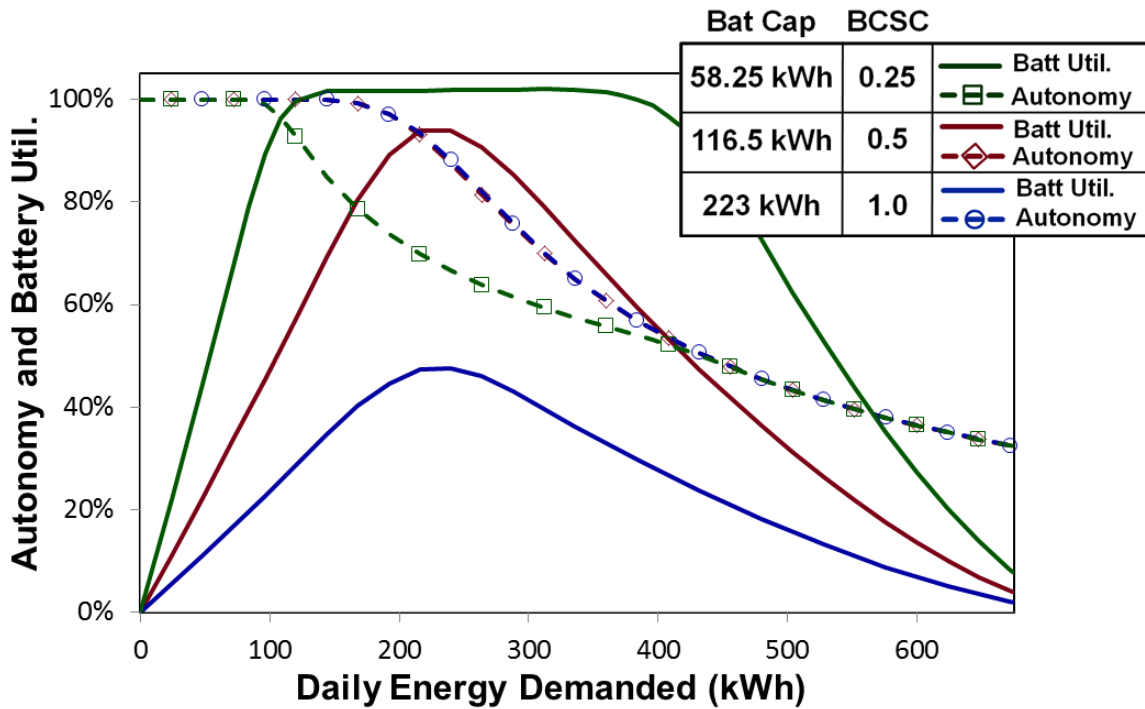


Figure 3-9: Autonomy and battery utilization of constant demand for different battery sizes.

The type of local demand also affects the autonomy and battery utilization. Figure 3-10 shows the autonomy and battery utilization for the four different types of demand curves as a function of the energy demanded. The parabolic and TOU demand shapes are 10 hours in duration centered at 3:30PM. The parabolic demand sees the lowest levels of autonomy, but its battery utilization is highest when comparing demand shapes at the same level of energy demanded. While the autonomy is affected, the demand shape has a greater effect on the battery utilization. Autonomy is more dependent on the total amount of insolation (a function of solar array size), while the battery utilization is more dependent on how much of the demanded power is not co-incident with the solar power. The TOU (Trapezoid) demand receives the lowest levels of battery utilization for daily energy demands between 100 and 300kWh because the battery cannot be fully charged by the solar array. At higher energy demands the TOU (Trapezoid) demand can still charge during the first half of the day when there is no energy demanded, but

sinusoidal and constant demands see lower battery utilization level because most of the time demand exceeds solar power meaning that the batteries will receive very little charge.

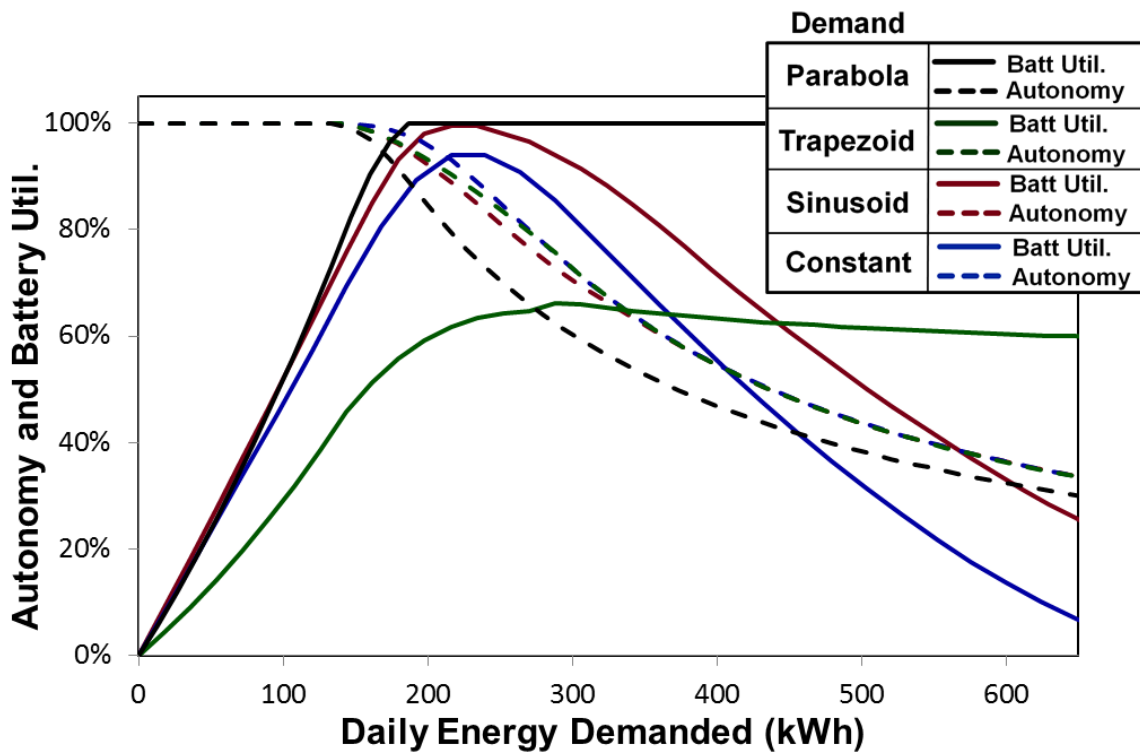


Figure 3-10: Autonomy and battery utilization of each of the four demand types under the same sized system (BCSC 0.5).

In addition to the demand shape, for the parabolic and trapezoidal demands the timing of the demand load effects system operation. Figure 3-11 shows the variation in autonomy and battery utilization for a six hour TOU demand centered at different times of a day. In Figure 3-11, the demand is always a six hour TOU demand but the timing of the load changes. The six hour TOU demand curves are centered to occur at noon, 3:30PM, 6PM, or 9PM shown in the legend as the deviation of the load timing from noon (0, 3.5, 6, and 9 hours). Since the solar insolation being used for this study is an approximation that is symmetrical, the results show the difference in the load timing between the center of the demand curve and the center of the solar insolation curve. The shape of autonomy and especially battery utilization was affected by the time of demand, with the battery utilization being more linear (as it approaches its maximum) for

demands that are not coincident with solar insolation. The closer the timing of the load is to the timing of solar insolation, the less the battery must be used to supplement power, which leads to higher levels of autonomy and lower levels of battery utilization. In some systems, certain demand loads will be dispatchable allowing them to be turned on or off at different times throughout the day. In general for these types of systems, placing loads coincident with available solar power will provide the greatest benefit.

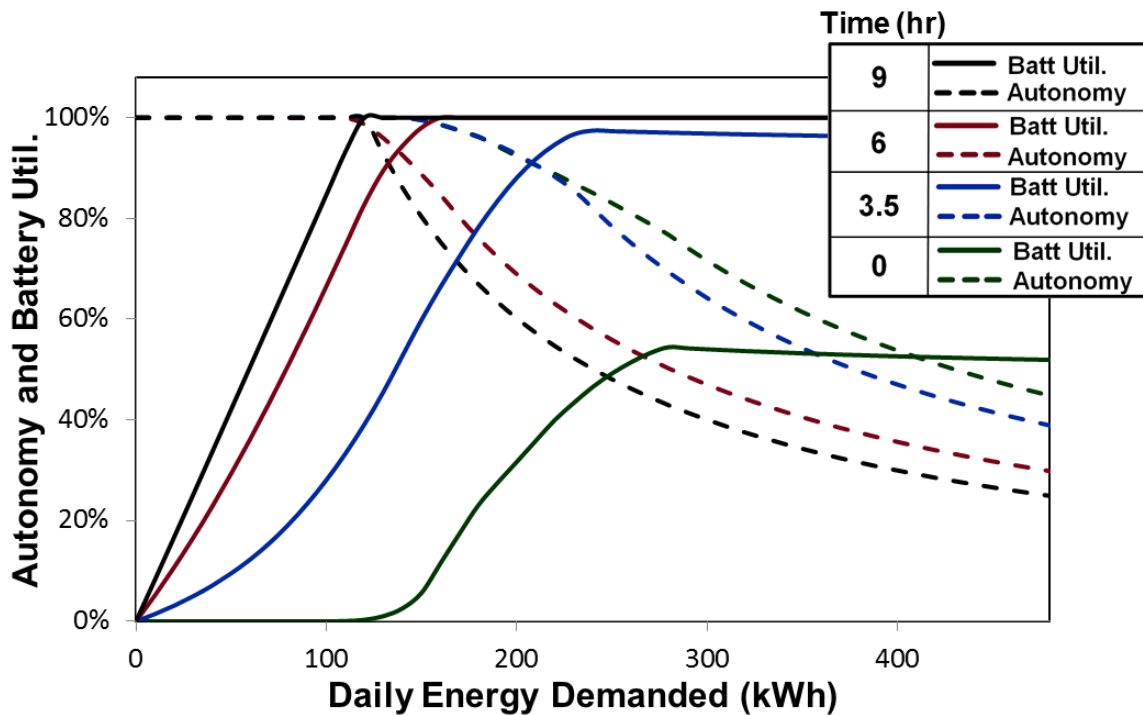


Figure 3-11: Autonomy and battery utilization based on timing of trapezoidal demand. The time represents the trapezoid’s variation from maximum solar insolation.

Figures 3-12 through 3-15 show cases that study the variation in demand length for the parabolic and TOU demand curves. Depending on the season and type of loads, the duration of peak demand could change. Three-dimensional plots of autonomy (Figure 3-12) and battery utilization (Figure 3-13) with a BCSC of 0.5 (116.5kWh capacity) for all TOU demand lengths are shown (Note a reversed x -axis [Demand] in Figure 3-13 is used to show the main contour of the battery utilization plot in three dimensions). The length of demand has a much greater effect

on battery utilization than autonomy. For a given demand value in Figure 3-12, there is not a large amount of variation across demand lengths, however, Figure 3-12 varies significantly dependent on both the amount of energy demanded (x -axis) and the length of demand (y -axis)

Similar effects are present in the case of parabolic demand curves. Three dimensional plots of autonomy (Figure 3-14) and battery utilization (Figure 3-15) for all parabolic demand lengths are shown (Note a reversed x -axis [Demand] in Figure 3-15 is used to show the main contour of the battery utilization plot in three dimensions). The major difference between the trapezoid and parabolic demand is that the parabolic demand is thinner than the equivalent trapezoid demand resulting in slightly higher levels of autonomy and battery utilization shown in Figures 3-14 and 3-15 for comparative points.

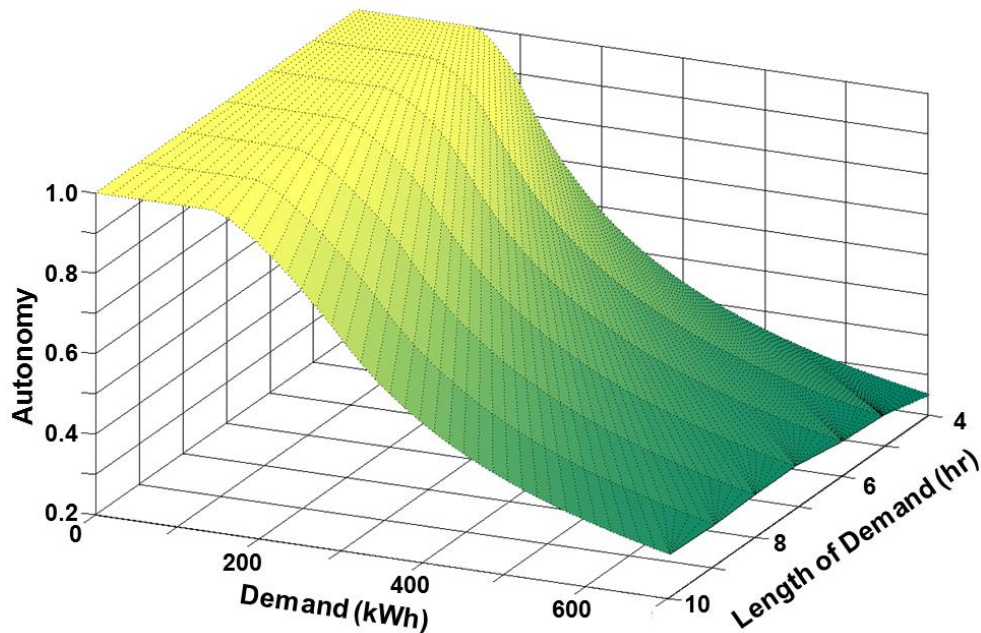


Figure 3-12: Autonomy for TOU demand shape with different amounts of daily demanded energy and length of TOU demand. Solar array of 30.5kW and battery of 116.5kWh.

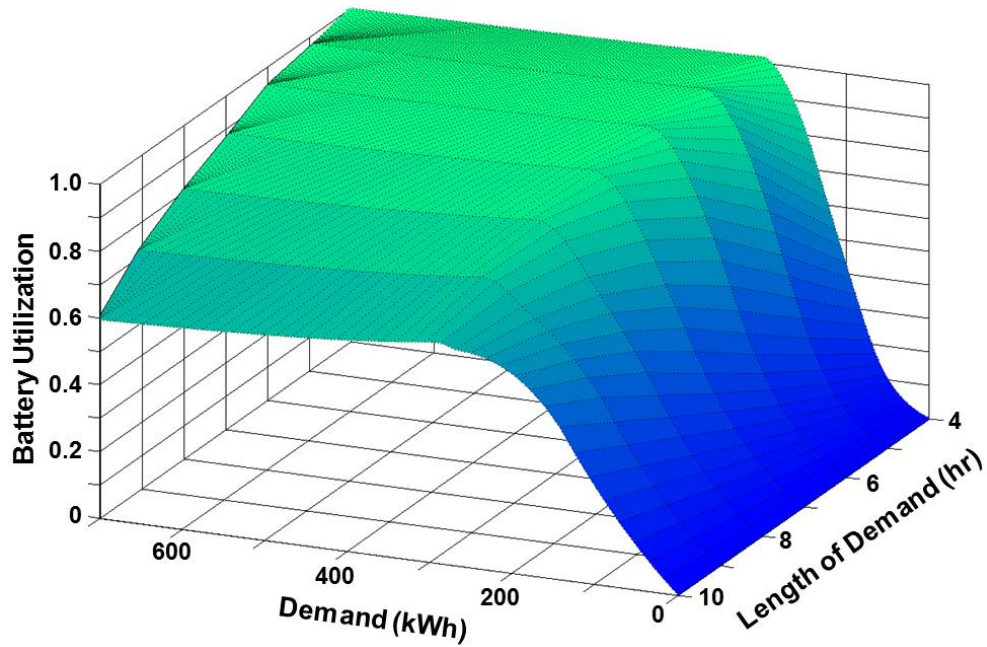


Figure 3-13: Battery Utilization for TOU demand shape with different amounts of daily demanded energy and length of TOU demand. Solar array of 30.5kW and battery of 116.5kWh. Note the reversed x-axis (demand) for highlighting the plot's contours.

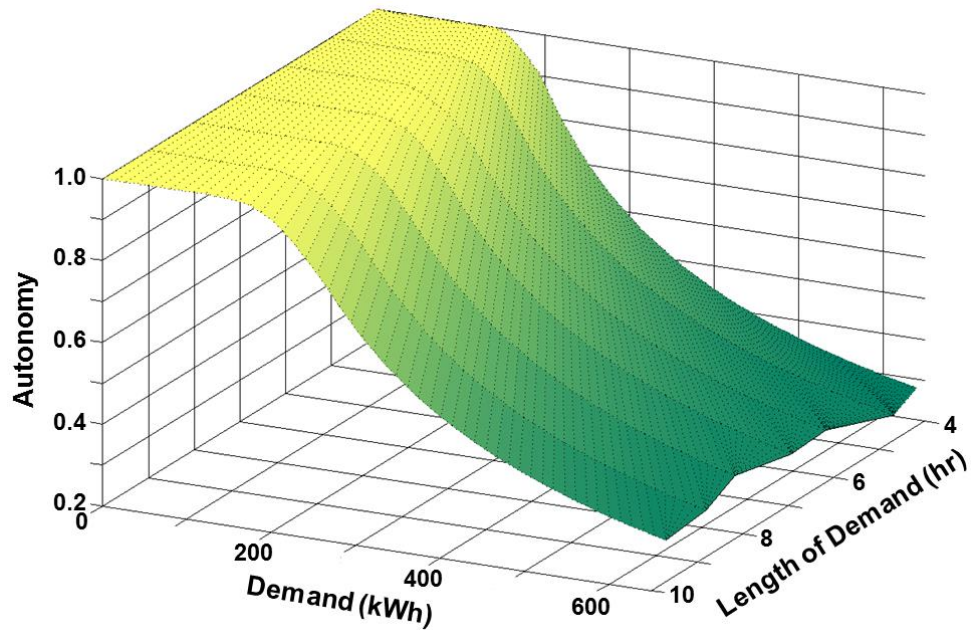


Figure 3-14: Autonomy for parabolic demand shape with different amounts of daily demanded energy and length of parabolic demand. Solar array of 30.5kW and battery of 116.5kWh.

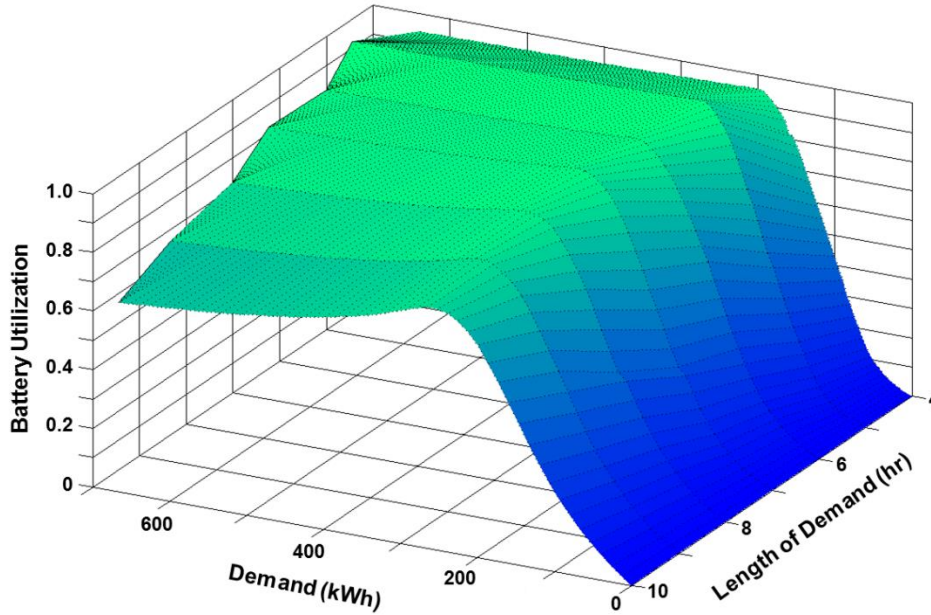


Figure 3-15: Battery Utilization for parabolic demand shape with different amounts of daily demanded energy and length of parabolic demand. Solar array of 30.5kW and battery of 116.5kWh. Note the reversed x-axis (demand) for highlighting the plot's contours.

3.7.3 Discussion from Study A

When determining the best possible size and use of a solar-battery hybrid system, many individual factors about the site and desired uses within the local grid environment must be taken into account. No single solution will fit all the cases. Study A offers an outline of how to approach best determining a system's size and operational characteristics by establishing the model for determining the relationship between a system's autonomy and the battery utilization associated with different applications. Autonomy and battery utilization cannot be maximized simultaneously in most cases. Rather a balance which best fits the consumer's needs and the site must be reached between both metrics. Study B will focus on applying the model to specific site-based inputs.

One assumption of Study A is that increased battery utilization is always beneficial in the lifetime effectiveness of a battery system. Changes in DOD will affect the cycle life of a

battery.¹³³ The relationship between DOD and cycle life is not well understood. However some cases have shown that lower levels of DOD can increase the nominal cycle life of the battery when accounting for lifetime energy storage.^{29, 134} Operating a battery at lower DOD will increase the cycle life, but will require a larger initial battery capacity and therefore higher upfront cost. Assuming a linear increase in nominal cycle life with a decrease in DOD, in order to see any economic benefit from installing a larger capacity battery and operating at lower DOD, nominal cycle life would need to increase at a rate of at least one percentage point for every percentage point decrease in DOD. Figure 3-16 shows the relationship of system cost in respect to average DOD and rate of nominal cycle life increase. The nominal cycle life slope is a measure of how much the battery's nominal cycle life will increase due to lowered DOD. At a slope of one, there would be no gain in nominal lifetime. The battery would output the same amount of energy over its lifetime (For example: 1000 cycles at 100% DOD or 2000 cycles at 50% DOD). For any slope greater than one, the total energy the battery can discharge during its lifetime will be greater at lower DOD. The slope is a relative measure of how much additional energy output can be gained from operating at a lower DOD. However, these increases can be partially offset by the need for a larger initial battery. The normalized lifetime cost measured in Figure 3-16, accounts for both the increase in battery lifetime from the nominal cycle life slope and the increased initial battery capacity needed to operate at lower DOD and is normalized to the cost per kWh supplied (over the entire lifetime) for a battery operating at 100%DOD.

$$\text{Lifetime Cost} = \frac{\text{Initial Battery Cost}}{\text{Total Energy Provided}} \quad (3.14)$$

While small gains in lifetime cost can be seen at small DOD reductions and low nominal cycle life slopes, the types of nominal cycle life increases required to see economic benefits are

greater than those from experimental studies for Li-ion batteries and therefore attempting to achieve the highest battery utilization is beneficial for system economics.^{29, 133, 134}

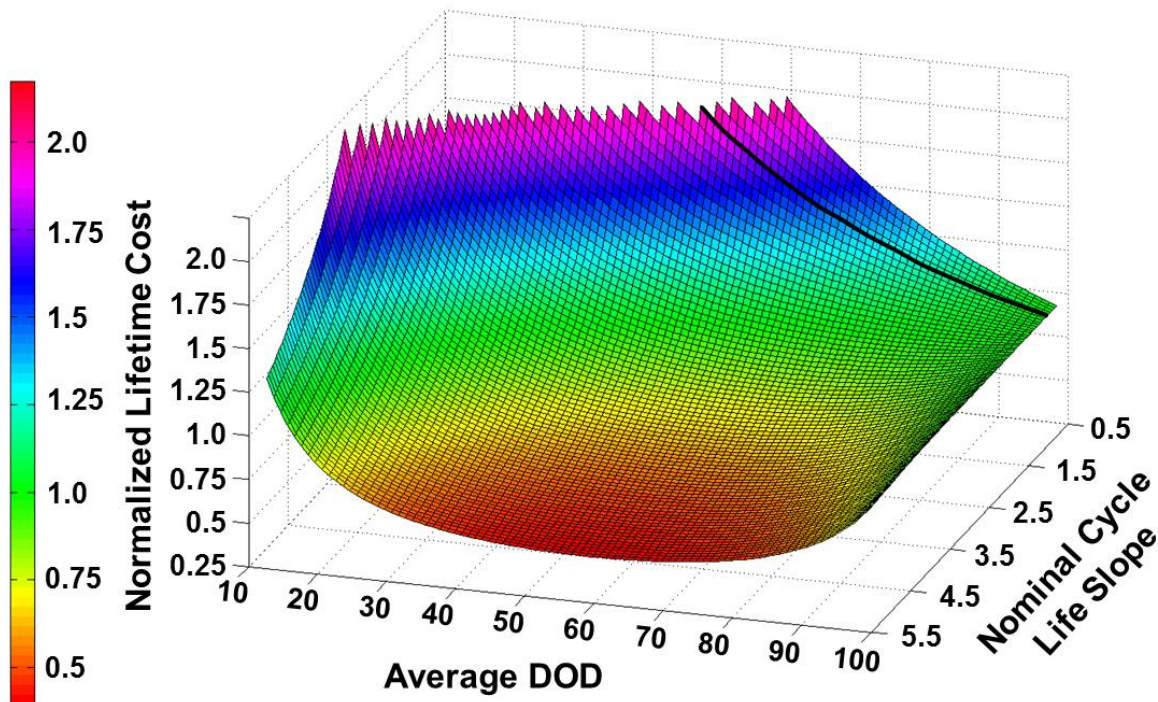


Figure 3-16: Normalized battery lifetime cost as a function of average DOD and increase in nominal life due to shallower DOD (shown as nominal cycle life slope). All costs are normalized to the cost of a 100% DOD system. The black line represents no change in nominal cycle life due to shallower DOD (Nominal Cycle Life Slope=1). Assumes a linear approximation of nominal cycle life as a function of DOD.

3.7.4 Conclusions from Study A

During the course of the year, the variation in solar insolation and demand make it difficult to determine the best system components for meeting specific demand requirements. Consumers often have to choose between maximizing autonomy or battery utilization. This study outlines a model for determining system autonomy and battery utilization based on application demand and system size. This model can be used to establish the best possible solar array and battery storage for a desired application. Under the demand types tested, demand shape and timing affect the system autonomy and battery utilization. When studying autonomy, the solar array size had a greater effect, while the battery size had a greater effect on battery utilization.

Use of the SPM allowed for greater accuracy when studying the SOC, DOD, and battery utilization for batteries operating in conjunction with intermittent renewable generation when compared with empirical battery estimates. The model allowed for fast and accurate simulation of the combined systems and enhances the system's ability to control energy storage while maintaining safety and performance.

As more microgrids and distributed energy resources enter the grid, tighter control and monitoring of a regional network of grids will be important in fully utilizing the available power capacity. The next study will use real solar insolation patterns from regional sites in order to better assess how individual systems will function and to determine how similar systems placed in different locations (experience differing solar insolation and weather patterns) will affect the system's autonomy and battery utilization.

3.8 Results from Study B

3.8.1 Solar Irradiance Data

Data was obtained for 10 sites between the years 2010 and 2014 from NREL's MIDC database. The site locations are shown on the map in Figure 3-17. Solar irradiance data was fed into the solar array component of the model to produce the solar array output. When using NREL's MIDC database, some data was incomplete or missing. Only data sets that had uninterrupted data for a complete calendar year were used in the study. Prior to obtaining data from the MIDC database, NREL's Solar and Wind Energy Resource Assessment database was used to estimate the global horizontal irradiance (GHI) at each site using SUNY's High Resolution model.¹³⁵ Daily insolation from the satellite-based and ground-based measurements at each site as well as other site-based characteristics are shown in Table 3-5. Sites are distributed geographically to study different irradiance patterns. The sites experience differing day lengths

based on latitude. Sites further north will experience longer summer days and shorter winter days compared to more southern sites. In Phoenix, AZ (the most southern site) the longest day of the year is only 14 hours and 22 minutes and the shortest day of the year is 9 hours and 56 minutes, while in Arcata, CA (the most northern site) the longest day is 15 hours and 6 minutes and the shortest day of the year is 9 hours and 14 minutes. Sites with a larger variation in day length will receive a greater portion of their total insolation in the summer months.

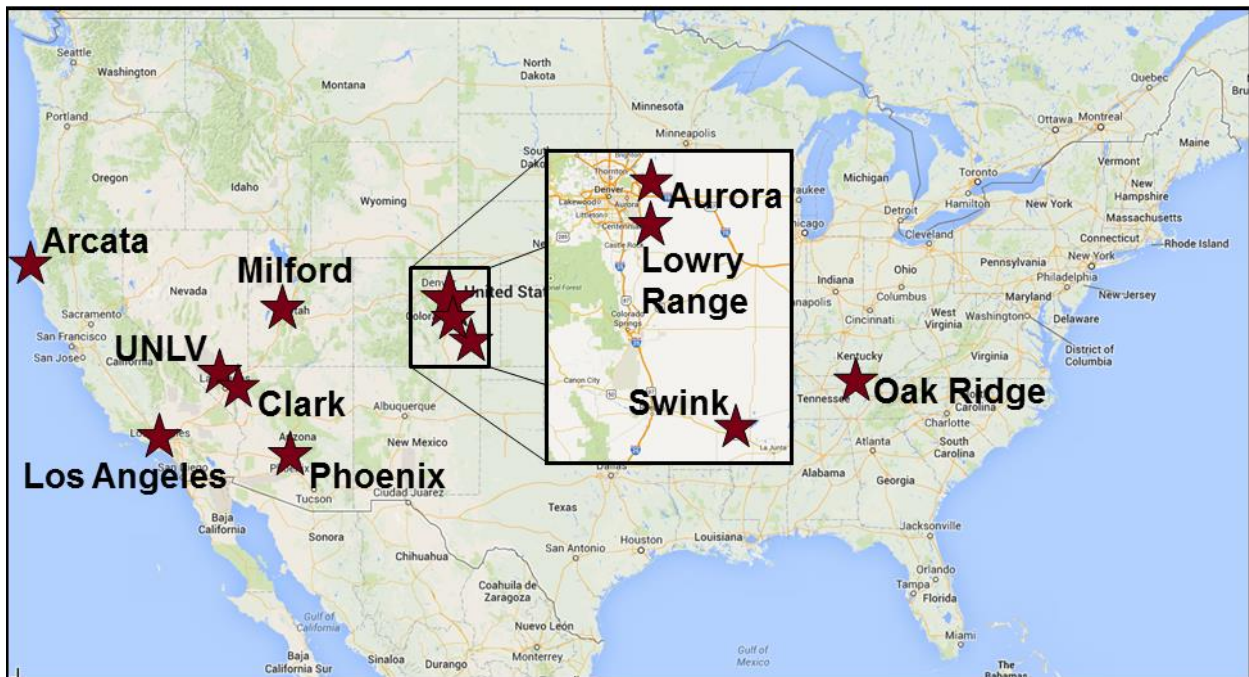


Figure 3-17: Map of sites from Study B.

In addition to the length of day, a site’s irradiance will fluctuate based on its local weather patterns. These short scale variations are one reason why average values for insolation such as those from the SUNY database do not tell the entire story of a site’s solar resource. Even very solar rich areas, see wide fluctuations in their irradiance on a day-to-day basis. Figure 3-18 shows the variation of solar irradiance during July 2012 for the Phoenix, AZ site. The site receives an average insolation of 7.92kWh/m^2 per day (satellite based) in July, but Figure 3-18 shows the large variation in irradiance on a day to day basis. Figure 3-18 shows the irradiance

levels during sunlight hours broken into quartiles. In July, 25% of the irradiance values fell into the blue region, 25% fell in the green region and 50% fell in the red region. Additionally, satellite based average values have been shown to be inaccurate at many sites especially for locations near the coast.^{136, 137} When compared to ground-based data obtained from NREL's MIDC, low insolation areas tended have higher satellite-based estimates and high insolation areas tended to have lower satellite based estimates. Figure 3-19 shows a mild, but statistically significant (p -value=0.006) correlation for the difference between the average ground-based data and GHI SUNY satellite-based data as a function of average ground-based insolation for all sites with at least two years of complete data.

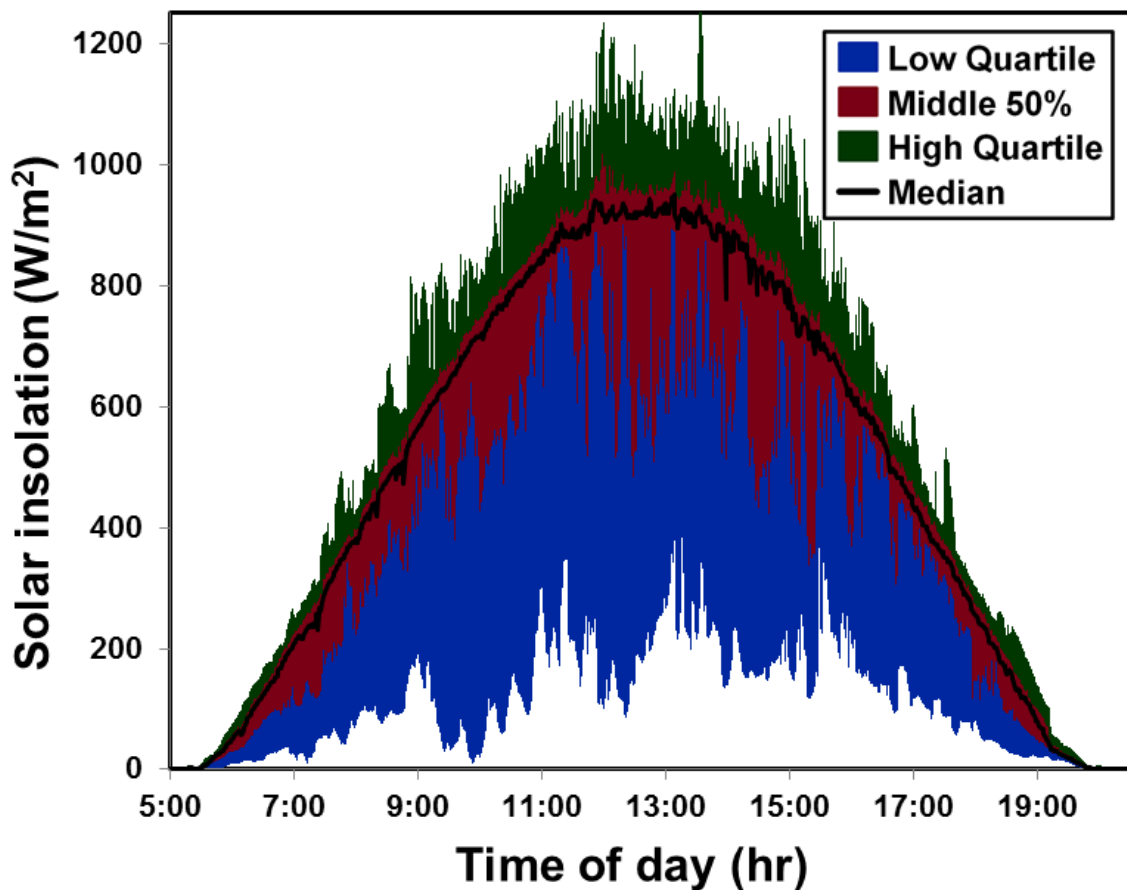


Figure 3-18: Variation in irradiance patterns for Phoenix in July 2012.

Table 3-5: Site information for each site studied. Autonomy values are averaged over all years of data for each site and the w/ Storage values include 116.5kWh of battery storage capacity.

Site Name	State	Lat.	Long.	Yrs. of Data	GHI SUNY Annual Avg.	MIDC Annual Avg.	MIDC Dec. Avg.	MIDC June Avg.	30.5kW of solar panels and 100kWh of Demand	
									Autonomy w/o Storage	Autonomy w/ Storage
Arcata	CA	40.88N	124.08W	5	3.915	3.839	1.510	6.262	35.23	74.07
Oak Ridge	TN	35.93N	84.31W	5	4.167	4.069	1.655	5.966	35.53	78.70
La Ola	HI	20.77N	156.92W	2	N/A	4.705	3.783	5.043	41.22	97.53
NREL	CO	39.74N	105.18W	1	4.638	4.687	2.606	7.131	38.62	87.71
Edinburg	TX	26.49N	98.17W	2	4.853	4.780	2.330	6.875	39.72	87.59
Rancho Cordova	CA	38.55N	121.24W	1	4.871	4.464	2.484	7.200	40.57	83.42
Lowry Range	CO	39.61N	104.58W	4	4.801	4.898	2.383	7.278	40.52	89.04
Aurora	CO	39.76N	104.62W	3	4.763	5.030	2.399	7.639	40.29	89.26
Swink	CO	38.01N	103.62W	4	5.093	5.218	2.536	7.688	41.56	90.99
Los Angeles	CA	33.97N	118.42W	3	4.905	5.232	2.877	6.671	42.19	93.58
Milford	UT	38.41N	113.03W	2	5.114	5.248	2.266	8.556	43.04	89.93
UNLV	NV	36.06N	115.08W	4	5.495	5.727	2.544	8.764	43.15	93.33
Clark	NV	36.09N	115.05W	2	5.495	5.716	2.812	8.779	42.15	94.08
NELHA	HI	19.73N	156.06W	2	N/A	5.850	4.525	6.758	44.38	99.41
Phoenix	AZ	33.43N	112.03W	2	5.617	5.824	3.101	8.442	46.10	96.59

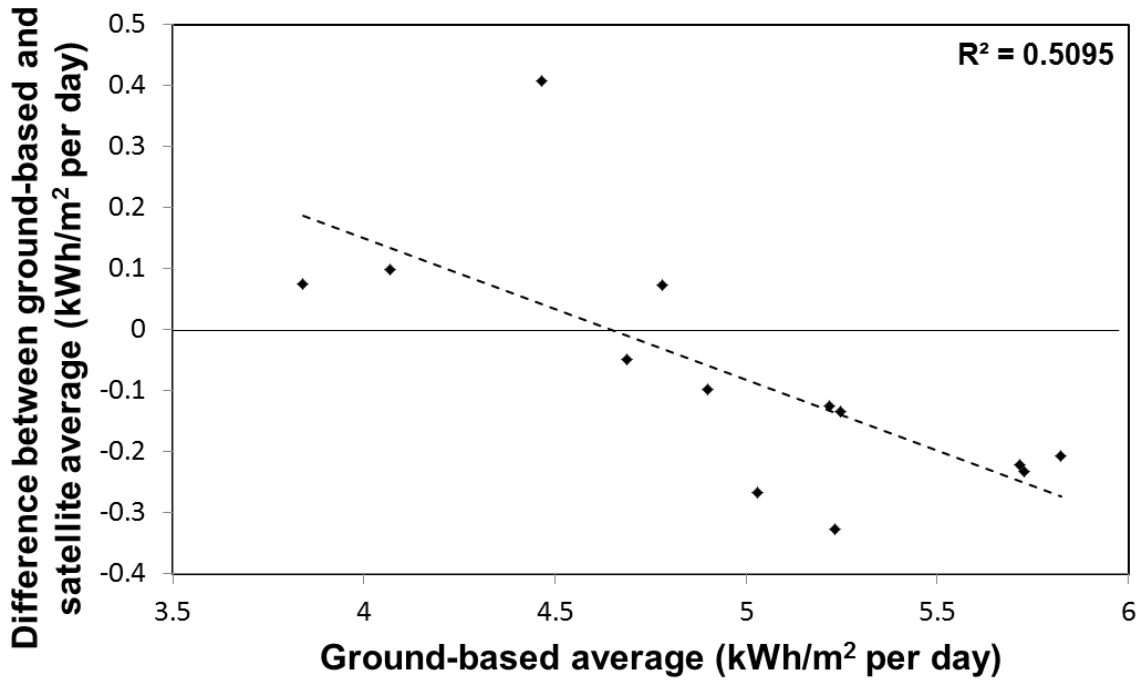


Figure 3-19: Difference between satellite and ground-based insolation yearly average by site as a function of ground based yearly insolation average, showing a mild but statistically significant (p-value=0.006) correlation.

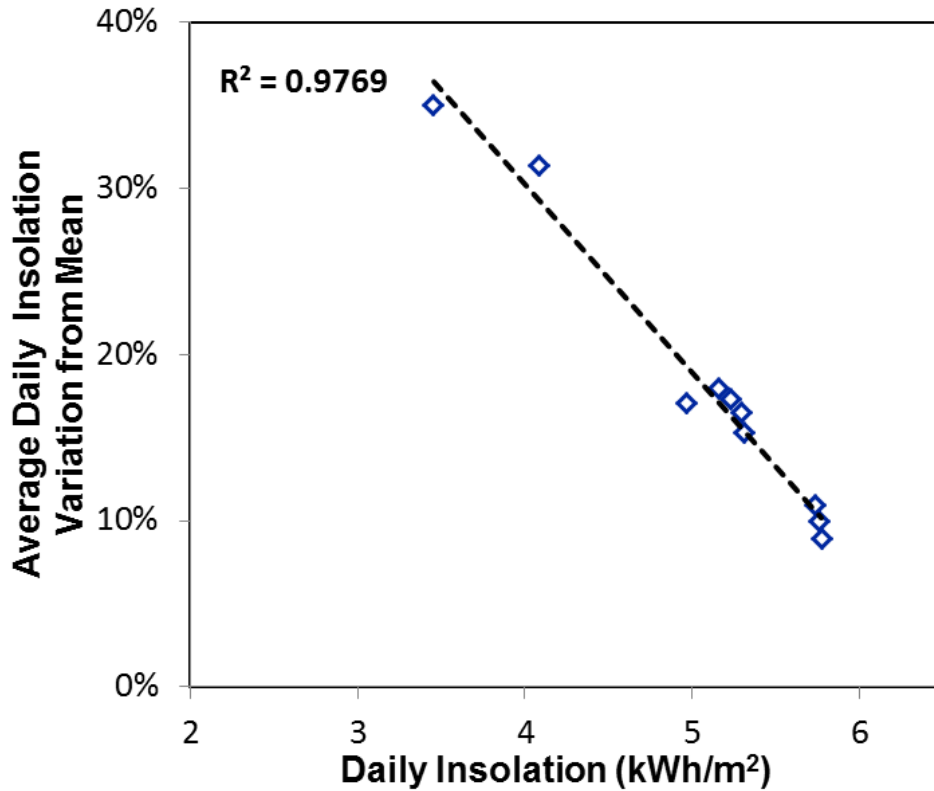


Figure 3-20: Strong inverse correlation between average daily insolation and average daily variation of irradiance.

In order to quantify weather based irradiance differences at each site, an irradiance variation metric was created. A moving average for daily insolation was calculated for each day of the year by averaging the nearest 30 days insolation values. Then the percentage of deviation from the moving average was calculated for each day and summed to create the site's "total variation" value. This metric correlated strongly with total insolation at each site (see Figure 3-20). The sites that received the highest insolation values were also the sites that had the lowest levels of daily variation in insolation. This result shows that sites that are considered to have a greater solar resource also have a more consistent solar resource on a day-to-day basis.

The combination of seasonal and daily variation can cause significant differences in the irradiance patterns that two sites with similar insolation values experience. Figure 3-21 shows Swink and LA yearly irradiance patterns in 2012. Both figures show that cloud cover has a significant effect at both sites, shown in the dark lines and spots that cut through the normal irradiance patterns. Looking at the summer months, Swink has longer days than LA, but in the winter, Swink has shorter days. Additionally, during LA's summer months, the peak daily values for irradiance are higher than Swink's, shown by the brighter center spot in Figure 3-21 A. Keep in mind that although Figure 3-21 shows differing levels of irradiance throughout the year, the total amount of insolation delivered at both sites varies by only 1.48%. Although both sites had similar levels of "total variation" the images show that there are still major differences in the individual site irradiance patterns. Using these different irradiance inputs in the solar-battery model, the effects on the battery will be monitored.

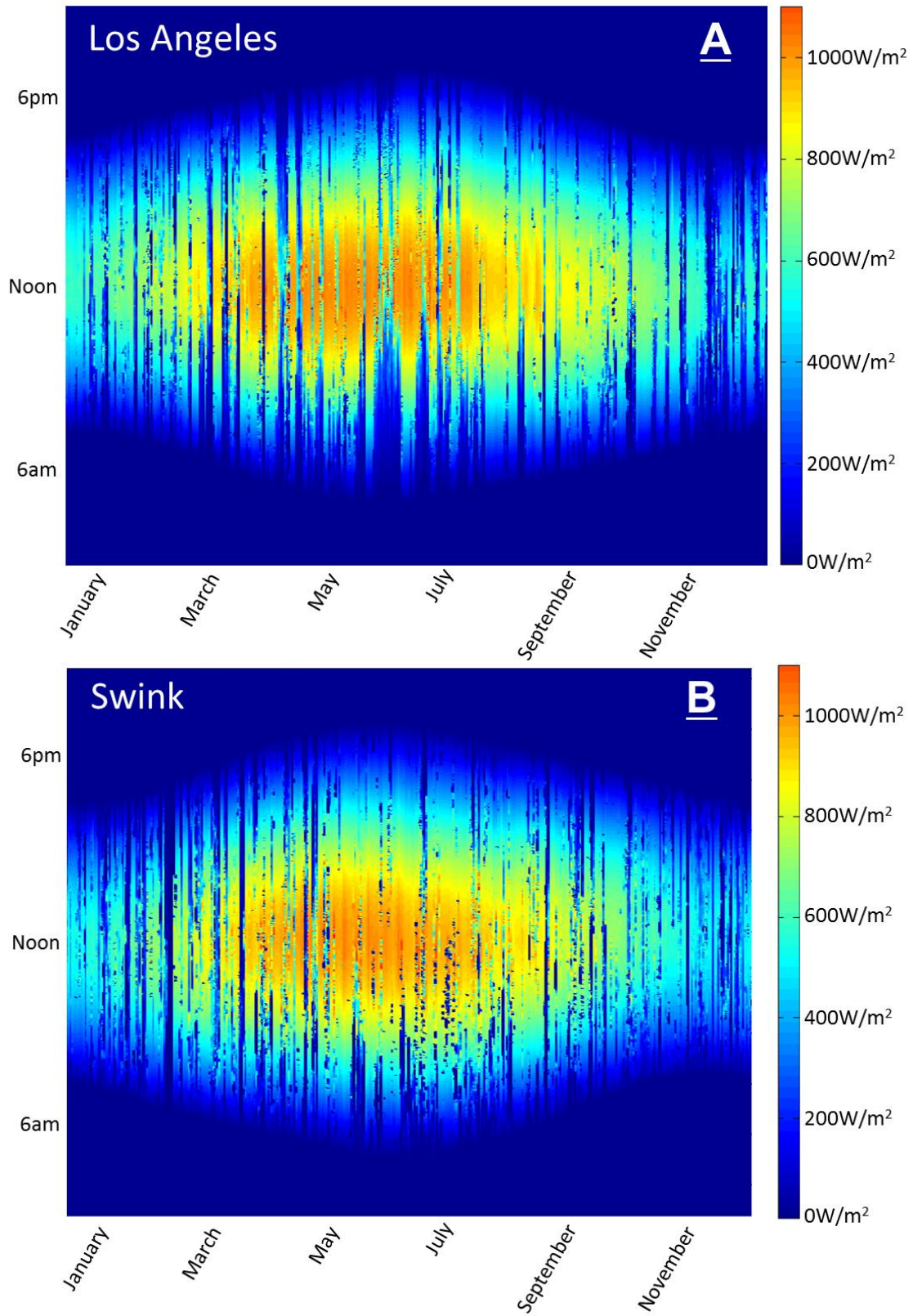


Figure 3-21: Los Angeles (A) and Swink (B) Irradiance patterns for 2012.

3.8.2 Irradiance Resolution Comparison

Many models use stochastic approaches for modeling a region's solar irradiance.¹³⁸ This method allows for a probability based assessment for a regional site, but does not account for individual weather events or daily variations in irradiance patterns and can underestimate times of operational failure. Other methods include using historical time series values, but often the resolution of these time series is hourly to daily.¹³⁹ Data at these resolutions misses important fluctuations in irradiance and induces error into measurements of autonomy, battery utilization, and capacity fade. Figure 3-22 shows the irradiance pattern for July 7th, 2011 in Los Angeles at three different resolution scales: 1-minute, 1-hour, and daily average. Both 1-minute and 1-hour data use a first derivative interpolation to connect the discrete points. The daily average finds the total insolation from a day and creates a half sine curve with the same total insolation that begins at sunrise and finishes at sunset for the site. The hour and day irradiance curve reduce the amount of fluctuations a solar-battery system will encounter during a day. Not accounting for these fluctuations will induce error into the model.

Two sites were studied with both minute and hour resolution irradiance data for the 2011 year: Los Angeles and Oak Ridge. Table 3-6 shows the difference in simulation results for the two data sets as well as the percent error of the hour resolution results as compared to the minute resolution results. Battery Utilization values show percent errors of 2.81% and 4.77% for Los Angeles and Oak Ridge respectively. This error means that the hour resolution data caused the energy throughput of the battery in the standard case to be underestimated by 523kWh (4.5 full cycles) and 748kWh (6.4 full cycles) at Los Angeles and Oak Ridge respectively over the course of 2011. While this is only a few cycles per year, over the lifetime of the battery this error could over estimate battery life by more than a year depending on nominal cycle life.

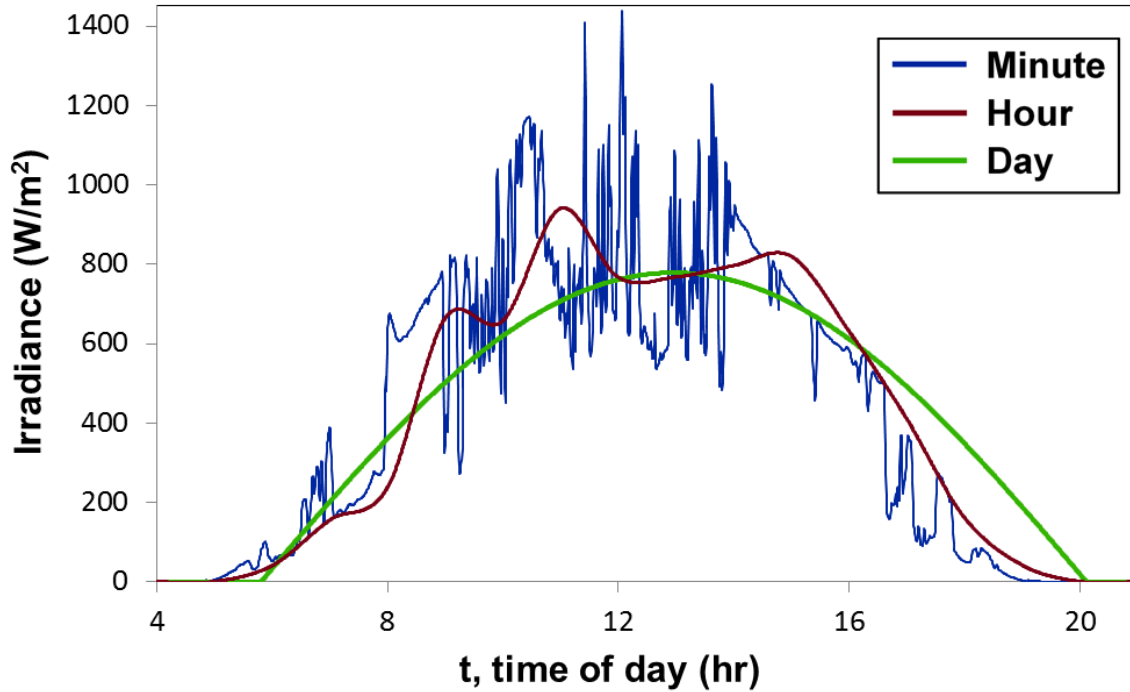


Figure 3-22: Irradiance data from LA on July 7th, 2011 for minute, hour, and daily resolution.

Table 3-6: Results of standard case simulations for Los Angeles and Oak Ridge in 2011 using 1-minute and 1-hour resolution irradiance patterns.

Los Angeles	1-min. input	1-hr. input	% Error
Battery Utilization	43.75%	42.52%	-2.81%
Autonomy	93.38%	92.98%	-0.43%
Percent Supplied by Battery	54.94%	53.64%	-2.37%
SEI growth (nm)	75.72	75.59	-0.17%
Oak Ridge	1-min. input	1-hr. input	% Error
Battery Utilization	36.86%	35.10%	-4.77%
Autonomy	78.66%	78.10%	-0.71%
Percent Supplied by Battery	54.79%	52.58%	-4.03%
SEI growth (nm)	55.88	57.04	2.08%

SEI growth is loosely correlated to the amount of battery utilization, but using hour resolution data didn't add as much error to the total SEI growth as it did to the battery utilization values over the course of the year with Los Angeles seeing only 0.17% error and Oak Ridge 2.08% error. SEI growth was calculated based on the equations from Section 3.2.3 in the SPM model. When looking at the SEI growth over monthly intervals rather than the complete year, the error is larger for the individual months. Table 3-7 shows the SEI growth from Oak Ridge every

month in 2011 for both minute and hour resolution data. On average (using weighted average of the absolute value of percent error) the monthly percent error for using hour resolution data is 3.94%, much larger than the yearly error of 2.08% (see Table 3-6). One reason for this is that the SEI values are overestimated by the hour resolution simulations in the high insolation summer months (April to September) and underestimated in the low resolution winter months (October to March). These two trends partially cancel each other out over the course of the entire year for SEI growth. More study is needed to understand why this variation between summer and winter occurs.

For studies seeking a high level of accuracy in modeling solar-battery systems, minute resolution irradiance data is favorable over hour resolution data. However, in cases where minute resolution data may not be available, hour resolution data can be used to produce close estimates.

Table 3-7: Comparison of monthly SEI growth for 1-minute and 1-hour resolution for Oak Ridge in 2011.

Month	Oak Ridge		% Error
	1-min. input (nm)	1-hr. input (nm)	
January	0.533	0.520	-2.44%
February	1.704	1.388	-18.54%
March	3.658	3.623	-0.96%
April	5.942	6.368	7.17%
May	6.158	6.471	5.08%
June	6.614	6.825	3.19%
July	7.883	8.252	4.68%
August	8.805	8.967	1.84%
September	5.438	5.646	3.82%
October	6.612	6.542	-1.06%
November	1.627	1.601	-1.60%
December	0.912	0.837	-8.22%

3.8.3 Technical Benefit of Energy Storage

Without energy storage, local demand can only be met during day light hours. If we assume the case of 100kWh of daily sinusoidal local demand and 30.5kW solar array, the

amount of demand met without energy storage by the solar panels ranges from only 35.2% in Arcata, CA up to a maximum of 46.1% Phoenix, AZ. The amount of autonomy met without any storage correlated strongly with the total amount of insolation received at the site (see Figure 3-23). Additionally, large amounts of solar power go unused in these scenarios because the solar power generated is often much higher the power demanded. All of the systems will benefit from including energy storage to store excess solar energy and use it to increase autonomy.

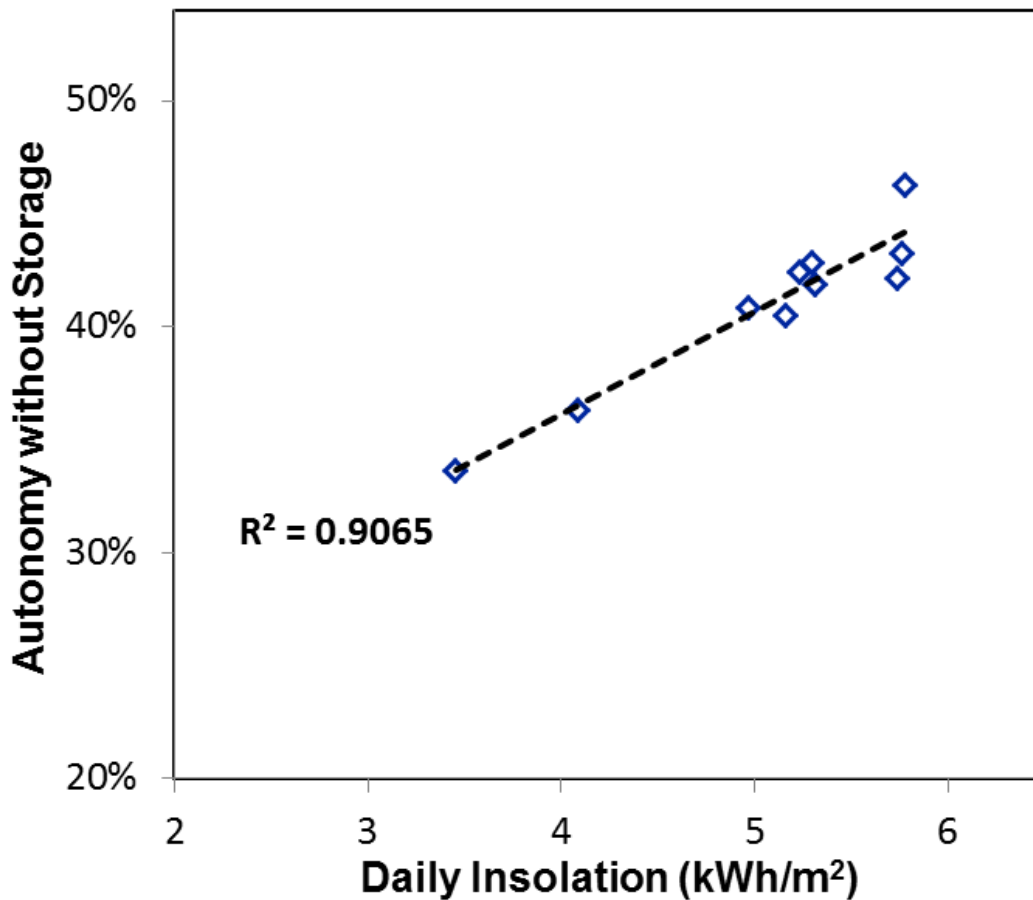


Figure 3-23: Strong correlation between average daily insolation and site autonomy without storage.

In the case of Milford in 2012, under the no storage condition with a 30.5kW solar array and 100kWh of sinusoidal demand the autonomy of the system is 42.8%. Adding only 15kWh of storage capacity will increase the autonomy to 57.2%, while adding 50kWh of storage will

increase the autonomy to 84.3%. When small amounts of storage capacity are added to the system, all of the capacity is used almost every day of the year to help supply some demand required overnight. Figure 3-24 shows the autonomy increasing with an increase in storage capacity. However, the rate of autonomy increase from added storage will decrease as more energy storage is added to the site.

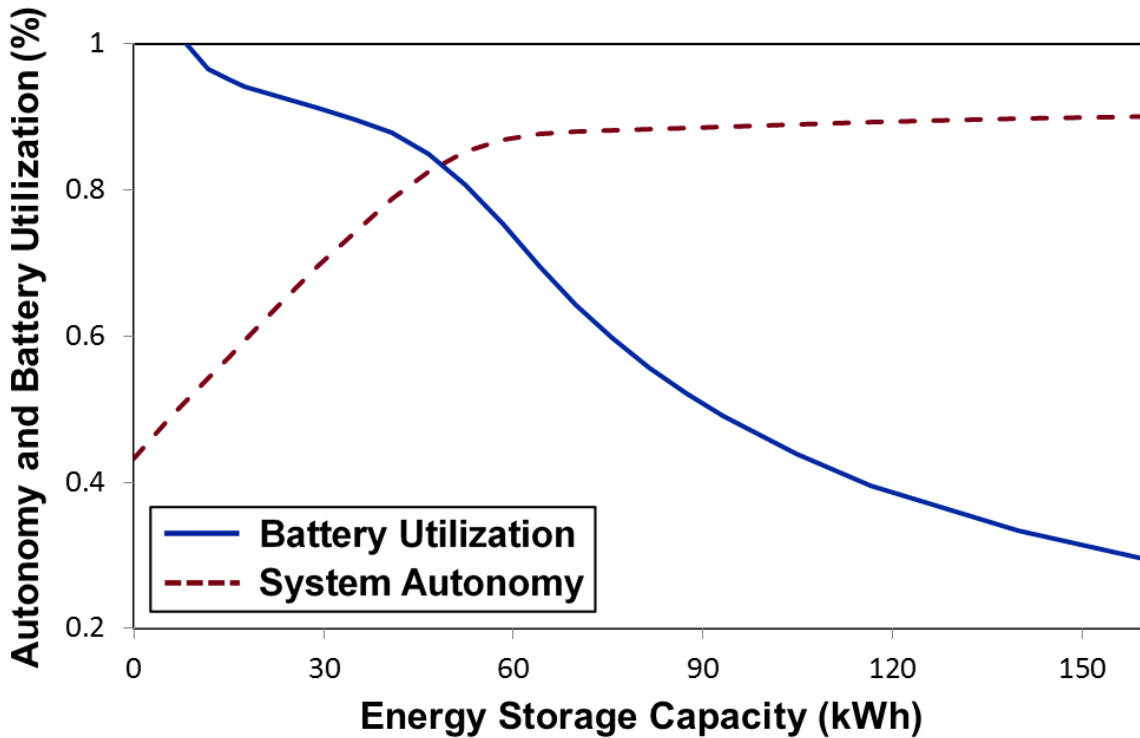


Figure 3-24: Autonomy and battery utilization as a function of battery energy storage capacity for Milford in 2012 with a 30.5kW solar array and a sinusoidal demand of 100kWh of daily energy.

In general, sites experienced two regimes of for the rate of autonomy increase: 1) an initial regime where the autonomy quickly increases for small amounts of added storage and 2) a diminishing returns regime (occurring beyond 60kWh in Figure 3-24) where adding more storage only provides small gains in autonomy. The switch between regimes is caused when storage is large enough to meet overnight demand throughout most of the year. However, 100% autonomy is not yet reached because of poor insolation during the winter months and long

periods of low insolation caused by cloud cover. To show how cloud cover can affect autonomy, Figure 3-25 shows a closer look at a seven day period in March 2012 for Milford.

Figure 3-25 shows the low insolation days of March 16th-18th in Milford depleting the battery until midway through the 18th when the SOC hits zero and the system can no longer meet demand (leading to decreased autonomy). The figure also shows that multiple days of high insolation can lead to unused solar generated energy (in the case of a grid-tied system, this energy would be sold externally). March 14th, 15th, and 20th all show days when the battery becomes fully charged around mid-day (battery is considered fully charged before SOC reaches 100% for protective purposes). With the battery fully charged and the solar power exceeding the power demanded (the standard case has a max demand of 5.56 kW), the excess solar power will go unused. These two cases of too much or too little solar power occurring over multiple days show why the amount of insolation is not always completely an accurate indicator of system autonomy.

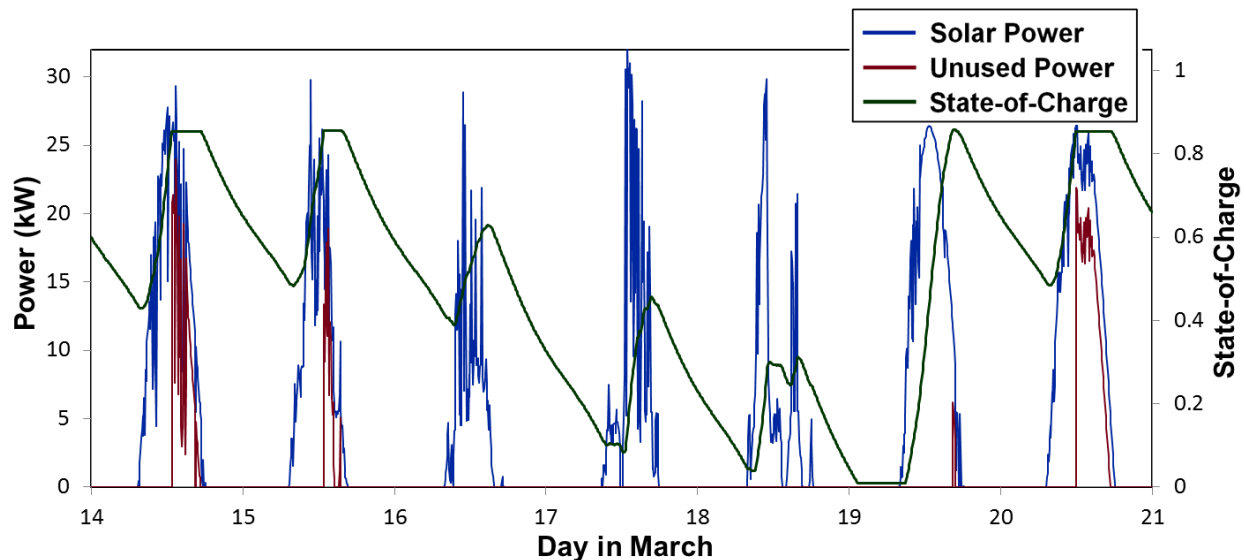


Figure 3-25: Solar power generated, solar power unused by system, and battery SOC during March 14-21, 2012 at the Milford site under the standard case.

As the battery capacity is increased, less solar power will go unused during high insolation times and fewer periods of low insolation will lead to completely depleted batteries. However, reaching 100% levels of autonomy will be very difficult because of low insolation levels during winter months. For the Milford site, each square meter of ground received an average insolation of only 2.23kWh/day in December which leads to a power output of only 45.2kWh per day from the 30.5kW solar array. Regardless of the size of the battery, without seasonal energy storage 100% autonomy will not be possible. For seasonal storage, some of the excess energy from summer month would need to be stored until the winter. In the summer Milford received 8.96kWh/m²/day in June, which equated to 256.2kWh of energy generated per day. Note that some of the variation between summer and winter insolation can be reduced by adjusting the tilt of solar panels. In order to meet 100% autonomy and overcome poor winter insolation levels, the battery would require 1,745kWh of storage capacity at Milford. A battery of this size would be cost prohibitive and Li-ion systems do not perform well for seasonal storage. Additionally, only a 3.3% of the battery's capacity would be used on any given day. Determining the optimal system size that creates the ideal balance between high levels of autonomy and battery utilization can be difficult because of the high seasonal variation in insolation levels. But the battery utilization varies significantly by month. Figure 3-26 shows the monthly variation of battery utilization for Milford 2012 under the standard case and is representative of the general trend at all sites. The lowest levels of utilization come during months of low insolation (December) which leads to depleted batteries and low levels of autonomy. Another local minimum comes during peak insolation months (June) when the days are longer and batteries are not needed for as long of a period overnight (even though autonomy measures are high). The peak utilizations come during times just before the monthly autonomy

reaches 100% (March in Figure 3-26) and just after the monthly autonomy decreases from 100% (October in Figure 3-26). This trend depends on the battery size, but shows that monthly battery utilization is affected by the length of day and amount of insolation.

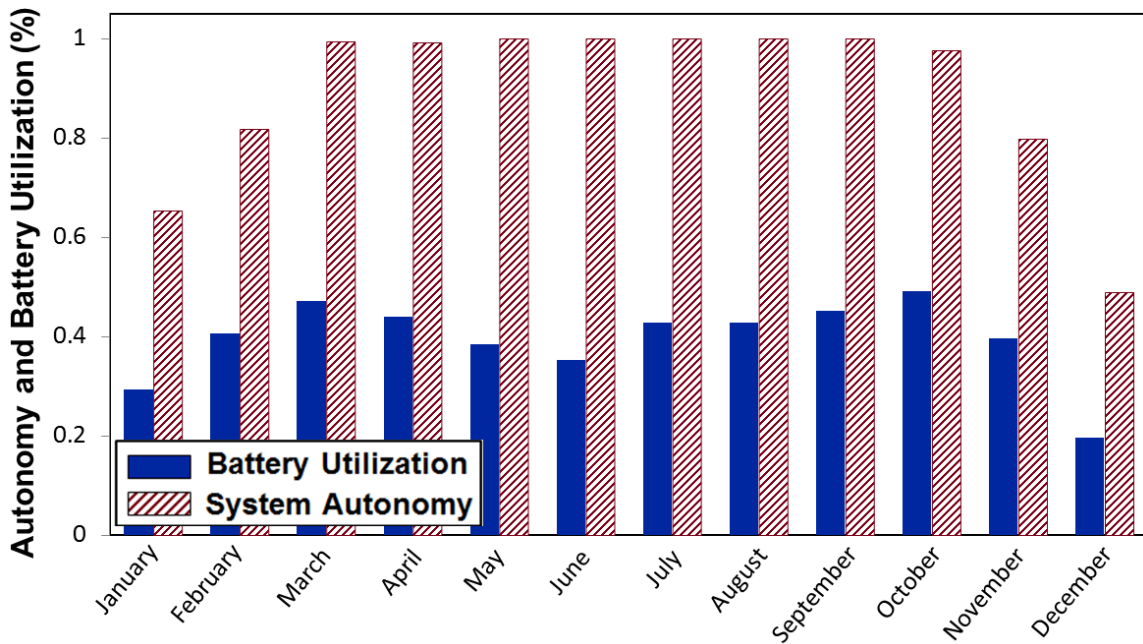


Figure 3-26: Monthly autonomy and battery utilization for Milford 2012 under the standard case.

As the size of the battery capacity increases the battery utilization will decrease and autonomy will increase as shown in Figure 3-24 for Milford. Figure 3-24 shows two regimes for how autonomy is affected by additional energy storage. For all sites, simulations were run for two battery capacities to see if sites experienced similar increase in autonomy in both regimes. To measure the initial rate of autonomy increase from storage, the increase in autonomy from 0kWh of storage to 50kWh of storage was calculated by running simulations with 50kWh of battery storage. The increased autonomy values ranged from only a 28.6% increase at Arcata, CA to 45.6% at Clark, NV. The added value from 50kWh of storage showed a strong correlation

to the site's total insolation (see Figure 3-27) similar to the correlation shown without any energy storage.

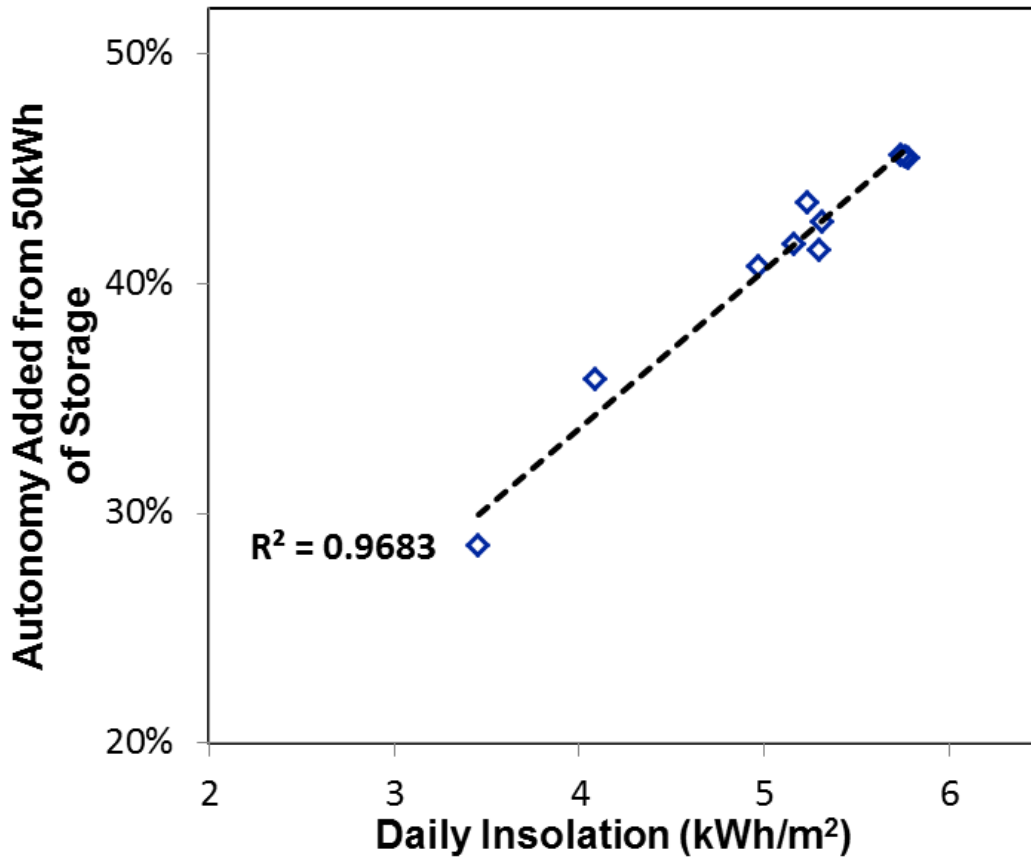


Figure 3-27: Strong correlation between average daily insolation and added autonomy from 50kWh of battery storage.

To study at what level the autonomy begins to level off (in the second regime), simulation with 116.5kWh of battery storage were conducted at each site. In addition to just data from 2012, for this study all available site data between 2010 and 2014 was simulated and autonomy and battery utilization values were determined. Figure 3-28 shows the simulation results for all sites and years. The autonomy again showed a strong correlation to the total site insolation. Figure 3-29, shows this correlation for all of the data points taken between 2010-2014. Battery utilization also shows a correlation only slightly weaker than the autonomy correlation.

These correlation results show that simulation using detailed irradiance data is not important at sites unless extremely accurate results are desired. In most cases, a site's total average insolation will offer a good determination of the relationship between system autonomy and energy storage at a site. This is only for long time-periods, if shorter time-period, such as individual weeks or months are being studied, the importance of detailed irradiance simulation becomes greater.

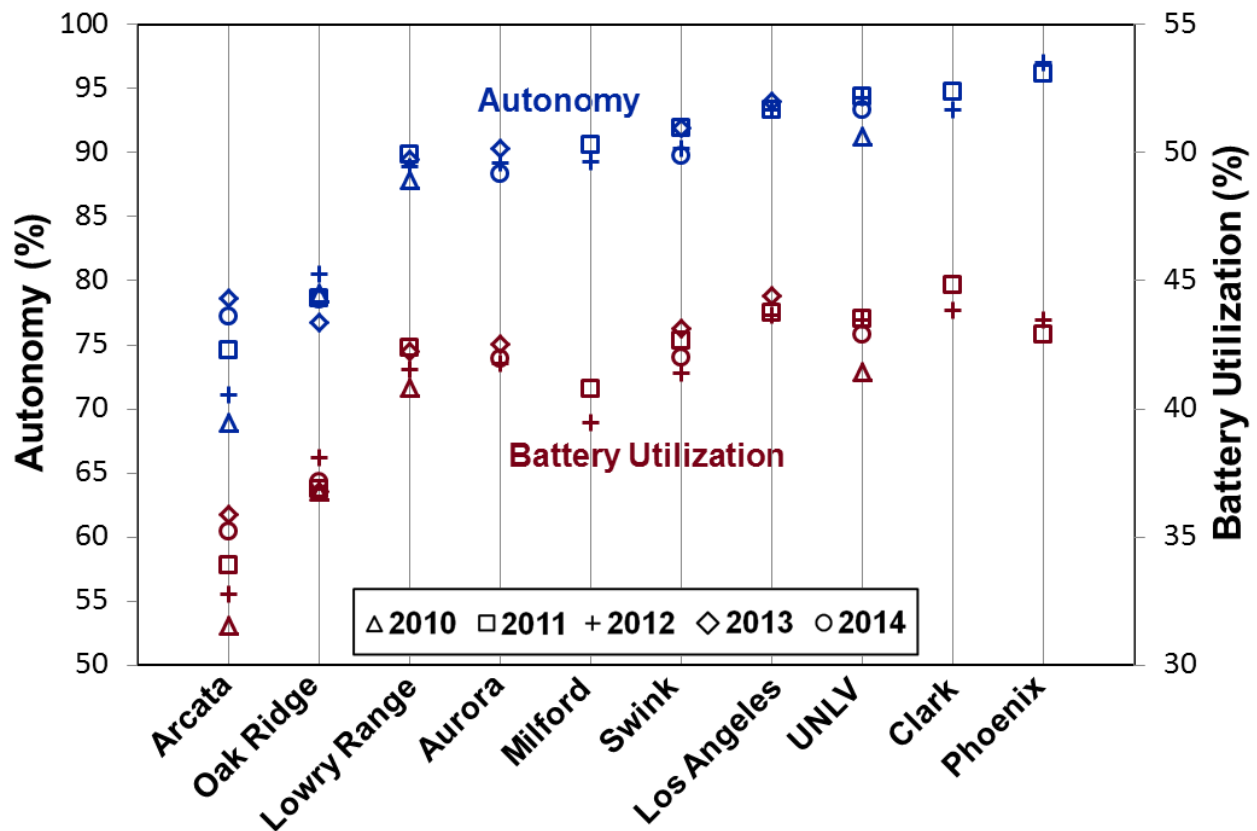


Figure 3-28: Autonomy and battery utilization values for all sites under the standard case.

While the previous section showed that insolation values could be used to determine average site characteristics such as autonomy, insolation values were shown not to be nearly as good of a predictor when studying economic value (based on time-of-use scenarios) of a system or when studying the degradation occurring within a battery at different sites.

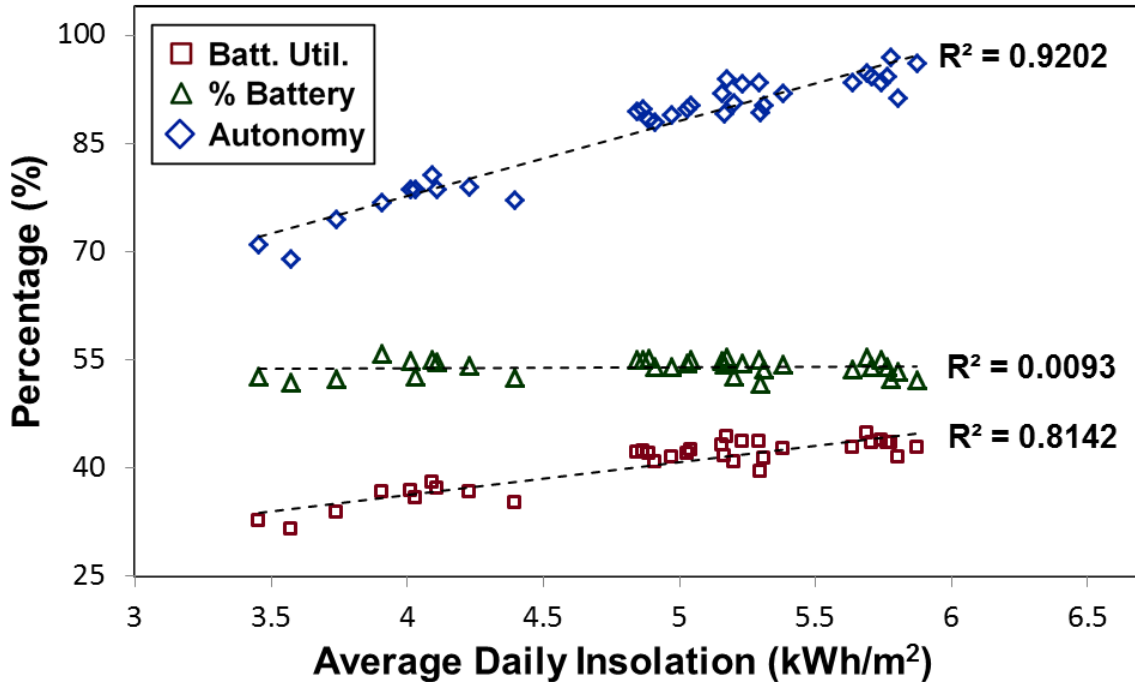


Figure 3-29: Yearly site autonomy, battery utilization, and percentage of energy supplied from battery as a function of ground-based average daily insolation for all sites.

3.8.4 Economic Value of Energy Storage

The economic benefits of the battery were considered under a two-tier TOU pricing scenario. Off-peak prices were set at \$0.10/kWh and On-peak prices were set at \$0.20/kWh. The on-peak pricing period was between 12:30pm and 6:30pm every day of the week (see Figure 3-30). First, all of the sites were considered with only solar panels (30.5kW) and no storage element. Any solar power generated during off-peak hours was worth \$0.10/kWh and any energy generated during on-peak hours was worth \$0.20/kWh. Each site’s solar array value is shown in Figure 3-31. Note, it was assumed that all power generated from the solar panels could be used locally and therefore is valued at the market utility price. Additionally, a maximum of 100kWh of peak hour demand was allowed daily with a maximum instantaneous power demand of 20kW because it was assumed that only power that could be used locally would be valued at market prices and any additional power generation beyond local demand that would need to be sold externally would only be valued at off-peak prices.

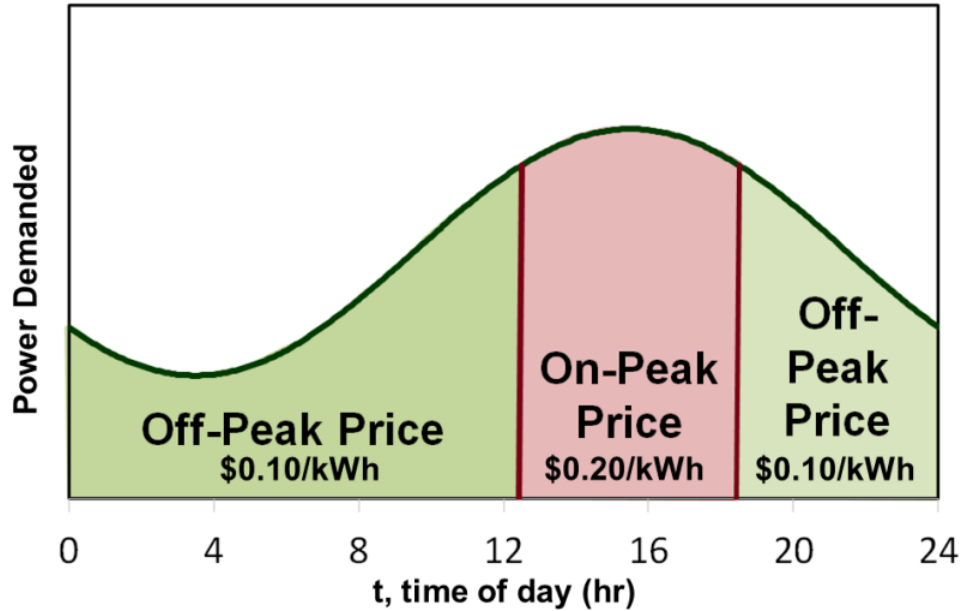


Figure 3-30: Diagram of time-of-use pricing setup.

Economic benefit from the solar panels alone (for 2012) ranged from \$138.60 per installed kW at Arcata, CA to \$263.63 per installed kW in Phoenix, AZ. When considering only the solar panels, the economic value on the panels based on TOU pricing correlated strongly with the average insolation that a site received. The sites with more yearly insolation received more economic value from the solar panels (see Fig 3-32).

To measure the benefits of battery storage in addition to the solar panels, a 116.5kWh battery was added to the system to try to store some of the solar energy produced during off-peak periods to be used during on-peak periods and therefore be used at a higher value. 116.5kWh of storage was used because it can store approximately one half of energy generated from a 12-hour summer day approximated by a half sine curve when 30.5kW of solar panels are present. The batteries generate value at each site ranging from an additional \$44.32 of value per installed kW at Arcata, CA to \$62.54 of value per installed kW at Clark, NV. The additional value gained by including the battery system did not correlated with the amount of insolation a site received (see Figure 3-32). In fact, Phoenix which received the most insolation during 2012 had the second

lowest amount of value added from a battery at only \$44.39 per installed kW. Note that all values reported here are in terms of solar array size and will be affected by changing the capacity of the installed battery.

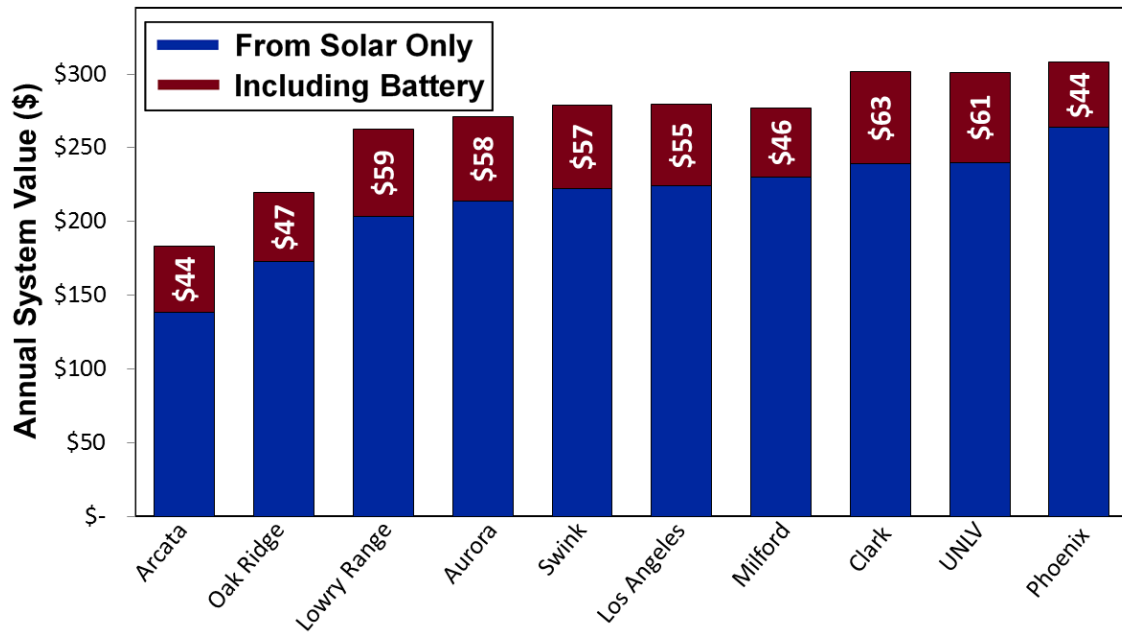


Figure 3-31: Economic value under TOU pricing in 2012 for all sites.

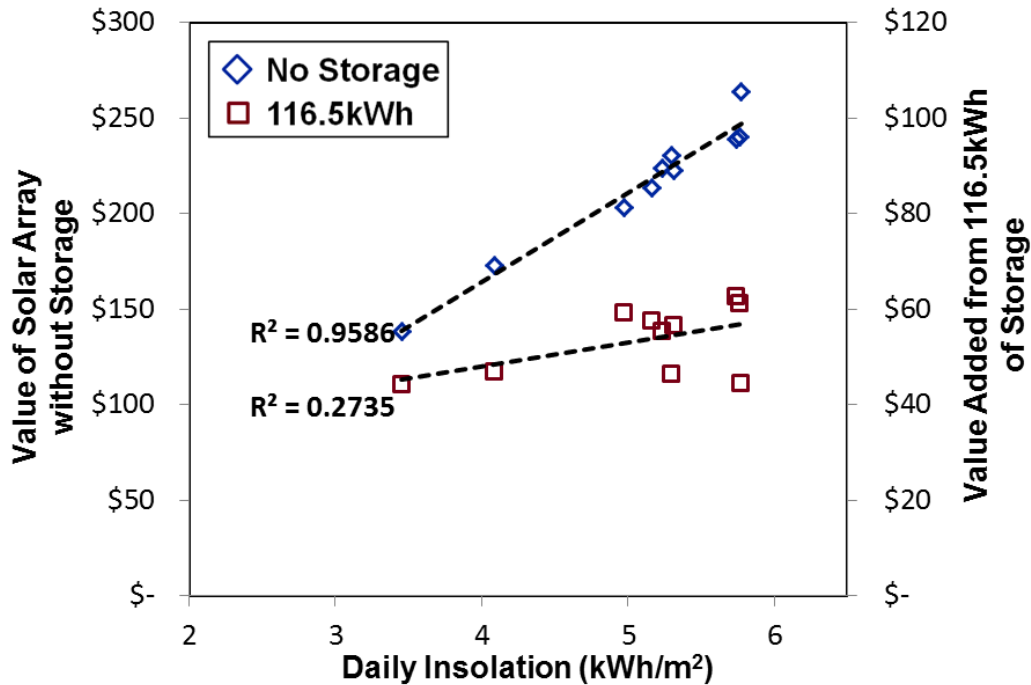


Figure 3-32: Strong correlation between average daily insolation and the economic value under TOU pricing without storage and no statistically significant correlation between average daily insolation and economic value from 50kWh of added storage.

When determining the economic value from TOU pricing for an added battery, the amount of irradiance that is coincident with the time of peak demand also had no correlation to the absolute economic value derived from the system. But when the added economic value was instead considered as the relative gain compared to the initial value of the solar array without storage (taking the absolute value gained from the battery and dividing it by the amount of economic value of the solar array without the battery system), there was a very strong inverse correlation between the amount of irradiance coincident with the on peak periods as shown in Figure 3-33.

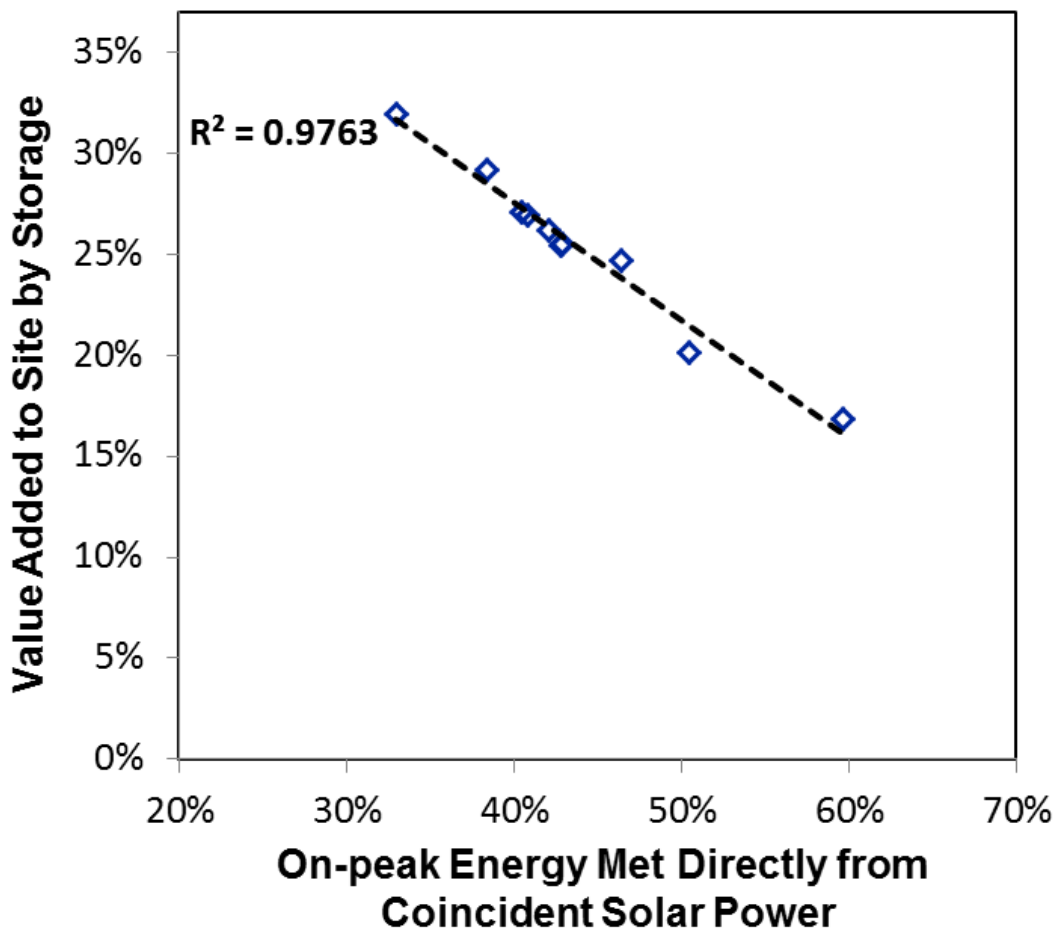


Figure 3-33: Strong correlation between the amount of solar power generated coincident with on-peak demand and relative value added from storage.

For example, Swink, CO and Milford, UT received 5.31kWh/m²/day and 5.30kWh/m²/day of insolation respectively in 2012, but a battery at Swink increased value by 25.4% (\$56.57 per installed kW) while Milford's value was only increased by 20.2% (\$46.43 per installed kW). Milford produced an average of 50.5kWh of energy during on-peak hour per day (out of 100kWh demand), while Swink produced only 42.8kWh of energy during on-peak hours per day on average. The exact reason for why Milford produced more coincident power was not obvious. The amount of daily variation between sites is similar and both sites sit at similar latitudes (38.0N and 38.4N) and therefore experience similar length of days. One possible explanation for the discrepancy could be that the two sites sit at opposite ends of the same time zone and therefore, although the day lengths are similar, the time of sunset is much earlier for Swink than for Milford. More study is needed to determine the effects of time zones on TOU pricing scenarios.

3.8.5 SEI Effects of Cycling on Battery Life

Adding a battery to the solar array at any site will increase system autonomy and will add some economic benefit to the system, however aggressive cycling will reduce the life of the battery. Sites that use the battery more frequently will shorten the life of the battery. But not all cycles will affect the life of the battery equally. In order to measure the effects of cycling on the life of the battery, SEI layer growth is tracked at all of the sites under the TOU pricing scenario. The amount of SEI layer growth shows a mild correlation to the value added by the battery (see Figure 3-34), which itself is a strong indicator of the amount of battery utilization. However there is still significant discrepancy on the amount of SEI layer growth at similar sites. Comparing three sites that received similar insolation shows how differences in the SEI layer growth can lead to changes in how the lifetime value of a battery system is perceived.

Looking at Swink, CO and Milford, UT under the TOU pricing scenario, the battery provides a 22.0% greater economic (\$56.57 per kW of solar) benefit at Swink than at Milford. However, in order to achieve that higher economic gain, the battery at Swink was cycled more. By tracking Battery Utilization, the Swink site was shown to have discharged 23.1% more energy in 2012. By comparing the SEI layer growth at the two sites, we can study how the additional cycling affected the batteries at each site. SEI layer will experience growth each cycle during charging and the layer will slowly build up over the course of the year. Figure 3-35 tracks the growth of the both Swink and Milford and shows that the SEI layer growth at Swink in 2012 was 21.7% greater than growth at the Milford. So while the same capacity battery may be more valuable over a single year at Swink, most of that value is wiped out over the battery's entire lifetime because the battery at the Milford will last longer and be able to recoup most of the economic difference. Note that there are many degradation mechanisms beyond just SEI layer growth that will affect the life of the battery, but that this mechanism offers a good relative view of degradation occurring based on cycling at individual sites. Other factors, such as different temperature conditions at sites, were not considered in this analysis.

When applying the same comparison between the Milford and LA sites, LA is economically 19.1% more valuable in 2012 and cycles 20.7% more energy than Milford. However, as shown in Figure 3-35, LA experiences 38.4% more SEI layer growth. With that much SEI layer growth, although the economic gain from a single year is greater at LA, the lifetime economic value of the battery will be higher at Milford. This type of capacity fade analysis is imperative to determining the lifetime benefit of storage at differing sites.

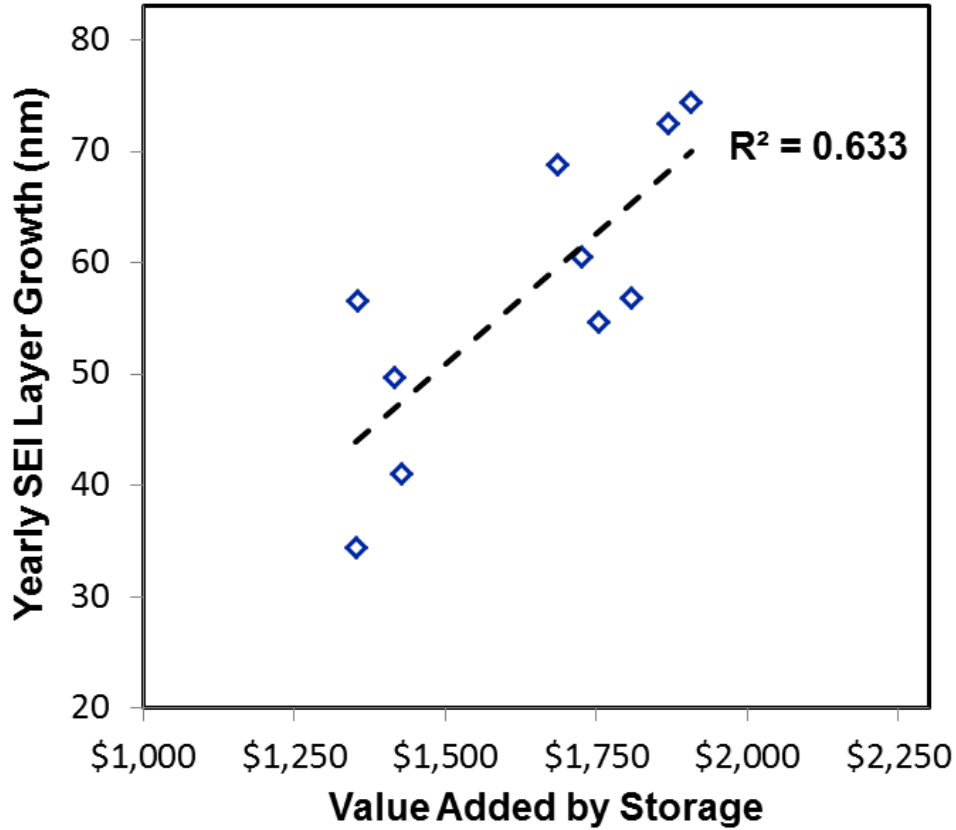


Figure 3-34: Mild correlation between absolute value added from storage and the amount of SEI layer growth.

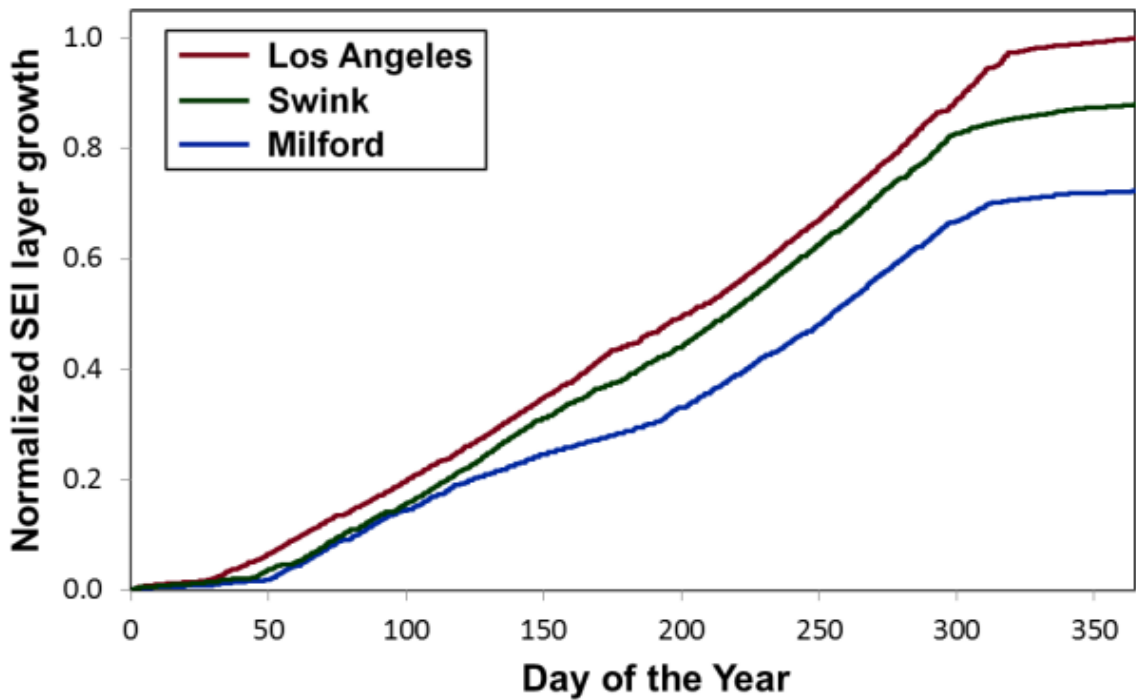


Figure 3-35: SEI layer growth for three sites in 2012 under TOU pricing scenario. SEI layer growth is normalized to the amount of growth experience by LA.

3.8.6 Demand Size and Type Effects

Similar to changing the battery size of the system, altering the size of the demand will also affect the operation of the solar-battery hybrid system. So far in the results section, the daily energy demand was always 100kWh. Altering that demand will affect both the autonomy and battery utilization. Figure 3-36 shows the battery utilization and autonomy as a function of demand size at Lowry Range in 2011 (the solar array is 30.5kW, battery capacity is 116.5 kWh and the demand type in sinusoidal). The shape of the demand remains sinusoidal, but the magnitude of the demand will change. For example, when daily energy demand is 200kWh instead of 100kWh (as in the standard case) the maximum power demand would be 11.12 kW and the minimum power demand would be 5.56 kW (maintaining the 2:1 ratio).

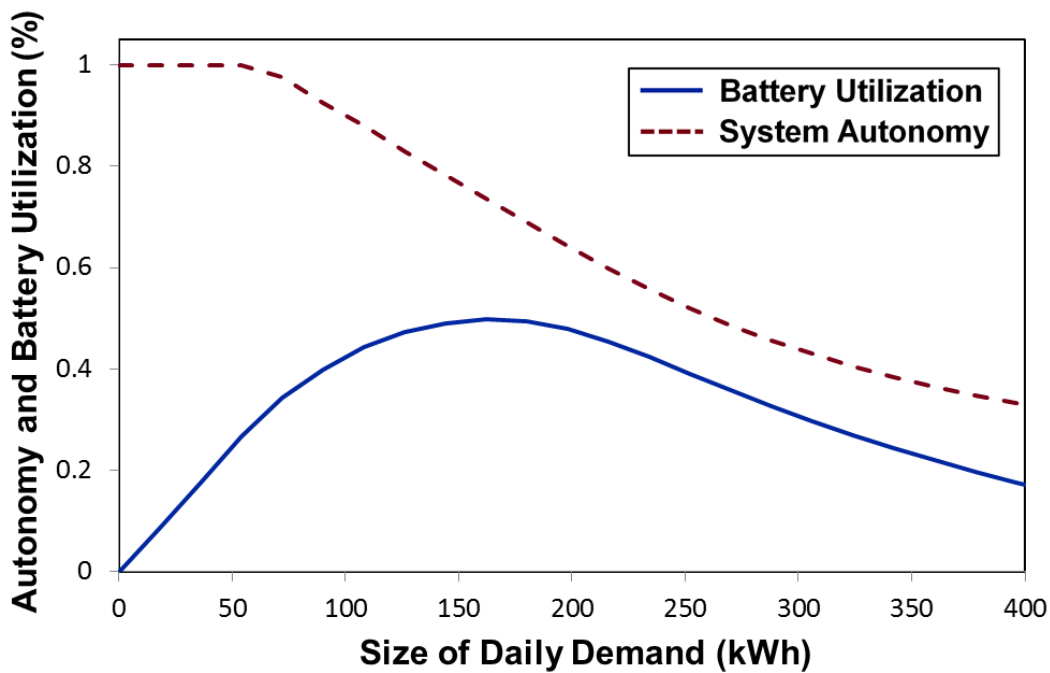


Figure 3-36: Autonomy and battery utilization demand as a function of total daily demanded energy for a system of 30.5kW solar array and 116.5kWh battery at Lowry Range in 2011 with Sinusoidal demand.

For low levels of demand, the autonomy will be 100% and as demand increases the autonomy will decrease. At the high levels of demand there is no way to supply the amount of

energy demanded with the available solar cells. In 2011, Lowery Range averages 127.81kWh of energy produced by its solar array per day, so demands above this amount could not reach 100% autonomy even with the largest batteries.

Battery utilization follows a different trend. The utilization values begin very small when only a few kWhs of energy is demanded because the amount of energy capacity required to supply the total demand is only a small percentage of its total capacity. As the demand size increases, the battery utilization rises, but it will reach a maximum and then begin to decrease. At the low demand sizes, the amount of energy required does not deplete the battery resulting in low DOD cycles. But for the high demand sizes, the battery is completely depleted overnight and the energy demanded during the day is much higher than the solar energy and therefore the battery cannot be fully charged and remains at low levels of SOC throughout the year. For Lowry 2011 with a 116.5kWh battery, the battery utilization peaks at just below 50% around 160kWh of sinusoidal demand.

The timing/shape (sinusoid versus TOU) of demand will also affect the battery utilization. TOU demand was also studied at varying sizes for autonomy and battery utilization at Lowry Range in 2011. This type of study is relevant for systems that are already in place that may be adding additional loads to maximize solar energy value. Figure 3-37 shows the autonomy and battery utilization as a function of demand size for TOU demand at Lowry Range in 2011. The autonomy values for TOU demand are very similar to those of sinusoidal demand shape because when sufficient amounts of energy storage are available, autonomy is driven heavily by the total amount of solar insolation (see discussion). At low levels of demand size, the TOU demand shows similar autonomy and battery utilization values to the sinusoidal demand (see Figure 3-37). However, beyond 100kWh of demand size, the battery utilization values begin to

diverge when comparing TOU and sinusoidal demand. As mentioned previously, for the sinusoidal demand beyond 100kWh, the battery is not able to be fully charged during the day. But for TOU demand, since no power is demanded before 12:30PM, the battery will always be able to charge in the morning. This charging allows higher levels of battery utilization to be reached and instead of peaking then decreasing, battery utilization for the TOU demand case remains high because of the ability for the battery to be charged every morning regardless of the amount of energy demanded. Note that autonomy values will still continue to decrease.

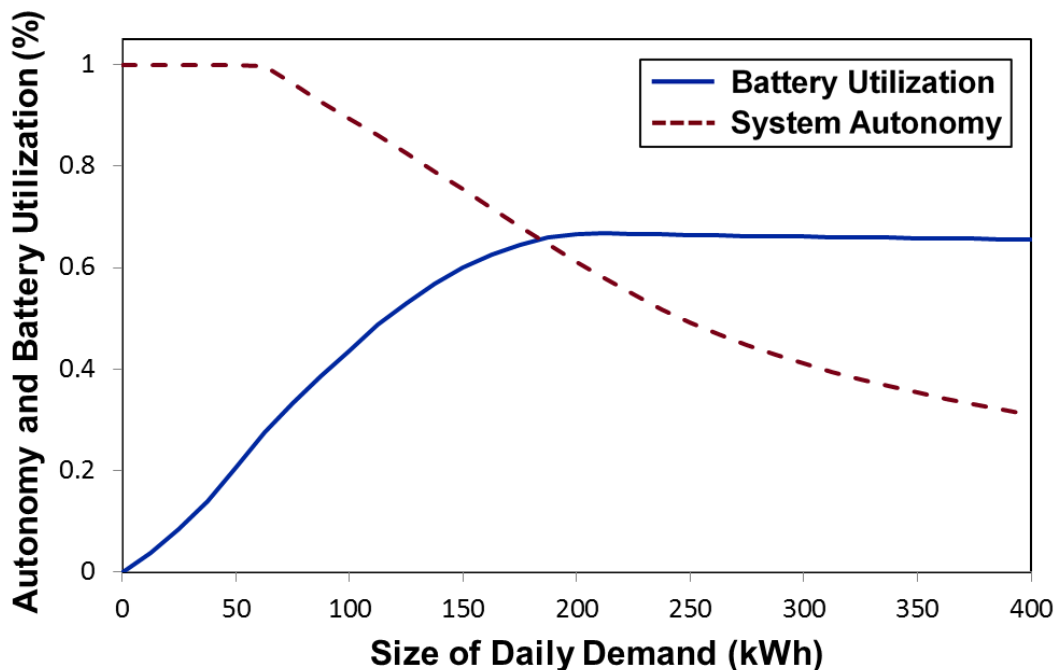


Figure 3-37: Autonomy and battery utilization demand as a function of total daily demanded energy for a system of 30.5kW solar array and 116.5kWh battery at Lowry Range in 2011 with TOU demand.

Figures 3-38 and 3-39 shows the battery SOC during the first 10 days of April at Lowry Range in 2011 for both TOU and sinusoidal demands at two different demand sizes. The figures show the trend that daily DODs are more similar for the 100kWh of daily demand than the 200kWh of daily demand. At 200kWh of daily demand, the sine demand restricts the battery from reaching as high of SOC levels as the battery in the TOU demand scenario during daily charging which leads to lower battery utilization for the sine demand shape simulations.

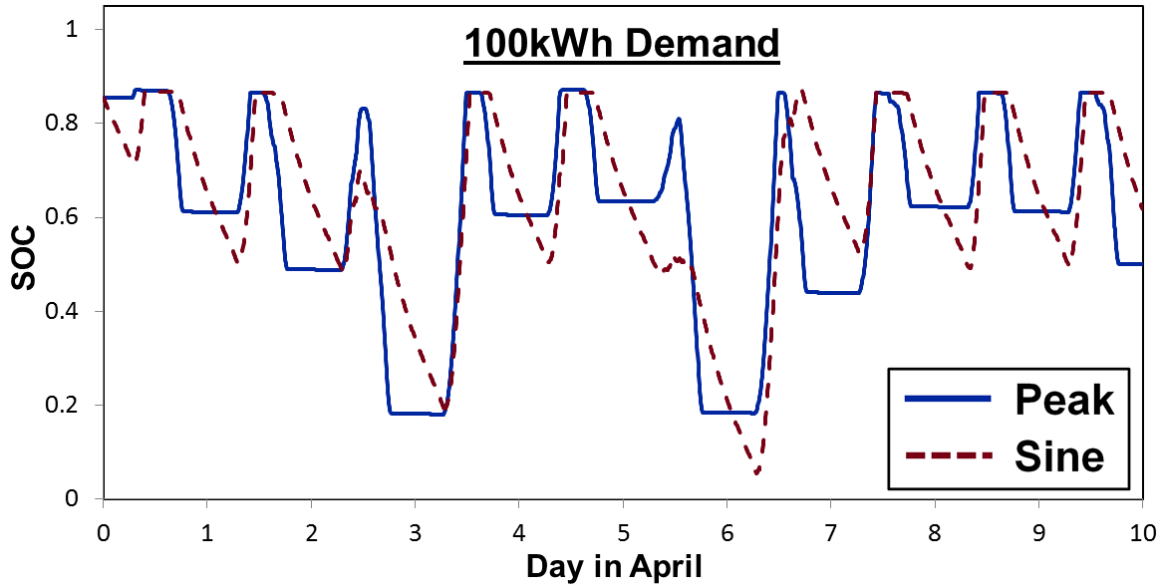


Figure 3-38: SOC values for TOU and sine demand from April 1-10, 2011 at Lowry Range with battery energy capacity was 116.5kWh and solar array was 30.5kW and 100kWh of energy demanded.

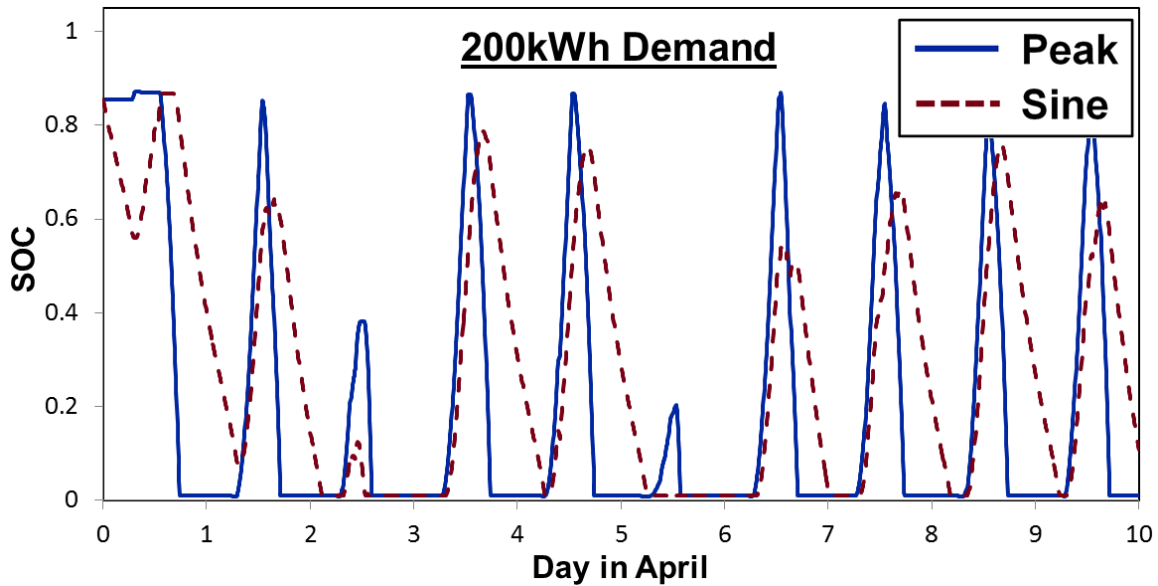


Figure 3-39: SOC values for TOU and sine demand from April 1-10, 2011 at Lowry Range with battery energy capacity was 116.5kWh and solar array was 30.5kW and 200kWh of energy demanded.

Comparing the SEI layer growth between the sinusoidal demand type and the TOU demand type, the SEI growth at low daily energy demands (<150kWh) is larger for the sinusoidal demand, but for high daily energy demands the SEI growth is larger for TOU demand. SEI growth is dependent on SOC, charging time, and battery voltage.¹⁴⁰ For the lower demands

when battery utilization between sine demand shape and TOU demand shape is similar, the duration of charging for the sinusoidal demand battery is slightly longer while SOC and voltage ranges are similar to the TOU demand battery (see Figure 3-38) which leads to larger SEI growth in sinusoidal demand. But at high demands, in addition to having lower battery utilization, the SOC and battery voltage remains lower for the sinusoidal demand battery (see Figure 3-39). The SEI reaction is less likely to occur at low SOC and therefore less SEI growth occurs for the sinusoidal demand shape at high levels of demand.¹⁴¹ For 100kWh of energy demanded the SEI growth was 16.8% higher in the sinusoidal demand battery than in the TOU demand battery, but for 200kWh of energy demanded the SEI growth was 10.7% lower in sinusoidal demand battery than the TOU demand battery.

3.8.7 Discussion of Study B with Lifetime Economic Value

Within each site there is a small variation in the results each year. When comparing the variation in autonomy and battery utilization results for individual sites, the average standard deviation for year-to-year variation was 1.27% (1.27kWh of demand met per day) for system autonomy and 0.69% (2.5 cycles full cycles per year) for battery utilization (see Figure 3-29). These values were calculated only for sites with at least three year of data. Results from simulations run for any one year of data will be accurate for following years.

While the single-year economic benefit from adding battery storage to a site was affected by both battery and demand size (see section 3.8.3), the lifetime economic value was not very sensitive to these two variables. Single year economic benefit correlated strongly with battery utilization because the added economic benefit was tied directly to the amount of energy throughput. However increased battery utilization will lead to short lifetimes in terms of years before a battery must be replaced.

When installing a battery system, the amount of savings over the lifetime of the battery should exceed the total costs in order to be economically viable. The maximum installation price per kWh of storage capacity will be based on the TOU price structure (which will determine the annual savings), and the battery life. The equation below is used to determine the maximum allowable installation price for a battery system to be economically beneficial during its lifetime:

$$\text{Price}_{\text{per kWh}} = \frac{(Value_{\text{BatteryCase}} - Value_{\text{BaseCase}})(Lifetime_{\text{Battery}})}{Capacity_{\text{Battery}}} \quad (3.15)$$

where lifetime of the battery is measured in years. For example, at Lowry Range using 2011 data (with 30.5kW solar array and 116.5kWh battery) and a peak to off-peak price difference of \$0.15 (e.g. P_{Off}=\$0.10 and P_{On}=\$0.25), the base case will provide \$6,712 in savings per year and the battery case will provide \$9,557 in savings based on simulation. Assuming a 10 year battery life, the total lifetime savings will be \$28,450 ([\$9,557-\$6,712] x 10 years) from the addition of the battery. Dividing by the 116.5kWh of capacity will yield a maximum allowable installation price of \$244 per kWh. Any installation price cheaper than \$244 per kWh will yield an economic benefit over the life of the battery.

The maximum allowable installation price is highly dependent on the TOU price structure and the battery lifetime. Figure 3-40 shows how this price will change based on the peak to off-peak price difference and the battery life. The previous example of a 10 year battery life and \$0.15 peak to off-peak difference is shown by the black dot in Figure 3-40. Increasing the TOU price difference or the battery lifetime will allow for higher installation prices that still produce economic benefits. If installation costs are \$300/kWh for an energy storage system, any point on the surface above the \$300 line would represent an economically beneficial case to install batteries. Note that this analysis focuses only on energy capacity. The nature of the

surface plot will vary based on the site and year of the data chosen, but will follow a similar trend shape.

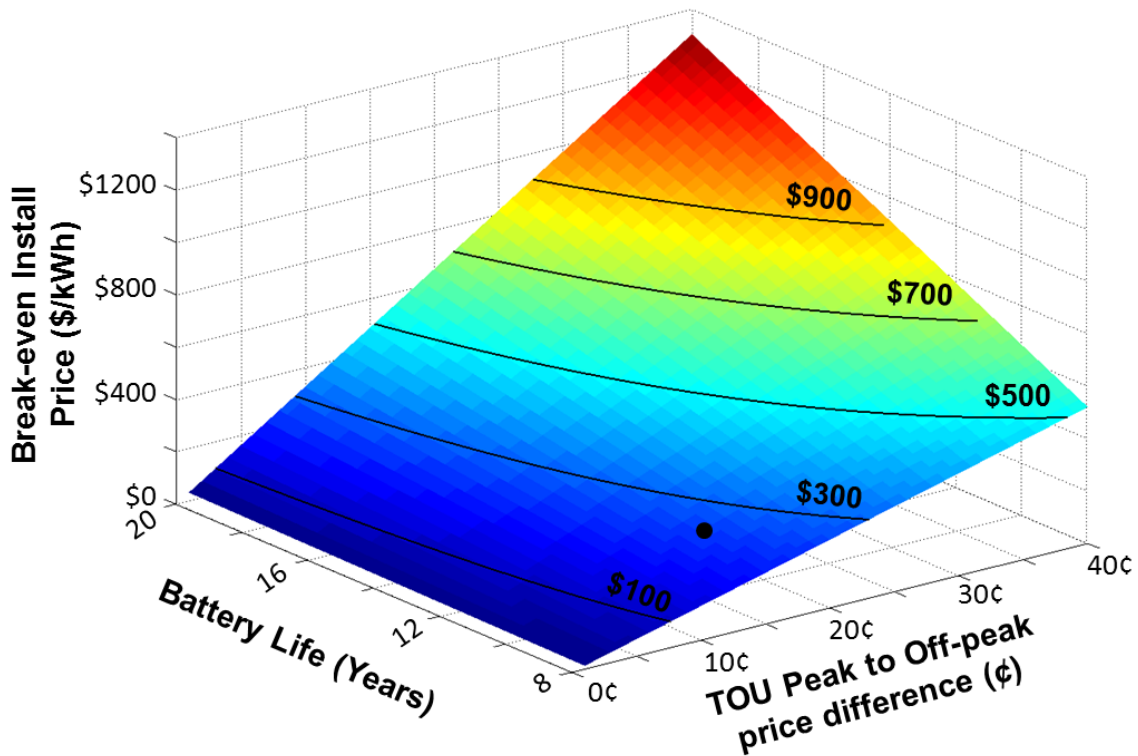


Figure 3-40: Break even battery installation prices for Lowry Range (using 2011 data) as a function of two-tiered TOU price difference and nominal battery cycle life.

3.8.8 Conclusions from Study B

A systems level model for coupling battery storage to a solar array was studied for 10 sites in the US over a five year period (2010-2014). The model allowed for much faster analysis of these sites than implementation of individual experimental setup at each site and year long study. Site based data from 2012 was analyzed to show that daily amounts of cloud variation at each site correlated strongly with the total site insolation. The total site insolation was a strong indicator for site performance. The site autonomy both without storage and with storage correlated strongly with total site insolation and the total economic value produced by a site's solar array without storage (based on a TOU pricing scenario) also correlated to the site's total insolation. In order to obtain these simple metrics, detailed irradiance time-series simulations

(such as the model presented here) are not required, rather these metrics can be elucidated with more readily available average insolation values. However, the economic value of the added battery under a TOU pricing scenario did not correlate to the total insolation of a site. Instead the relative amount of value added from the battery was strongly driven by the amount of solar power at the site that was generated coincident to the on-peak demand. For this type of economic study, irradiance based models such as the one presented here are required for thorough analysis of the system.

Additionally, The SEI layer was tracked at sites to monitor the degradation caused by different cycling patterns at individual sites. SEI growth at individual sites showed only a weak correlation with the amount of economic value added at a site and therefore indicates that although some sites may benefit from battery storage more (in economic terms) over a single year, they may not generate the most benefit over the entire life of the battery due to shorter battery life from degradation caused by certain types of cycling. Again detailed modeling is required to determine the relation of economic benefit to degradation at a site.

Studies comparing the accuracy of different resolution irradiance inputs showed that 1-minute resolution showed significant difference in yearly results when compared to 1-hour resolution data. And a method outlining calculation of lifetime value and break-even installation price was presented. This type of model-based study offers a blueprint for how sites should be evaluated from both an operational standpoint and economic standpoint. The efficacy of the system level model, specifically when analyzing the effects of operation on the battery storage, enhances the study of site-based energy storage coupled to solar power.

3.9 Conclusions to Solar-Battery Hybrid Modeling

The systems level model proved adept at analyzing a wide range of applications for energy storage coupling with renewable energy. The electrochemical modeling of the battery component offered insight not only into the operation of the device, but also the degradation effects of different cycling patterns through the monitoring of SEI layer growth. The ability of the model to handle real-world inputs and run simulations for different locations and applications allowed for a wide scope of study. More information about future directions for the solar-battery hybrid model can be found in Chapter 7.

Chapter 4

Optimization of Storage in Solar-Battery Hybrid System

This chapter contains excerpts from the following journal article, reproduced here with permission from IEEE:

Lawder, Matthew T., Suthar, Bharat K., Northrop, Paul. W.C, De, Sumitava, Hoff, C.Michael, Leitermann, Olivia, Crow, Mariesa L., Santhanagopalan, Shriram, Subramanian, Venkat R. “Battery Energy Storage System (BESS) and Battery Management System (BMS) for Grid-Scale Applications” *Proceedings of the IEEE*, 102:6 (2014) A682-A692.

4.1 Battery Management Systems

While the previous chapter focused on studying areas that would benefit from battery storage, this chapter will give an overview of how battery modeling can help batteries perform optimally once the energy storage devices have been installed in a solar-battery hybrid system.

Batteries require a BMS in order to control how cells are charged and discharged. This BMS can consist of a simple charge controller or a complex algorithm monitoring many variables. For small cells that do not have strict application requirements, basic BMS systems that are cheap and robust work best. But for large applications, especially in the grid, where hundreds to thousands of individual cells make up battery energy storage systems (BESS) that undergo unpredictable cycling patterns, advanced BMS are required to obtain the greatest benefit out of these expensive battery packs.

BESS require BMS to monitor and maintain safe, optimal operation of each battery pack and for systems that have multiple sets of batteries that can be operated independently, a system supervisory control (SSC) to monitor the full system. Batteries are dynamic in nature, constantly operating outside of the equilibrium state during cycling. In addition, the situation worsens for the case of intercalation based storage systems (e.g. lithium chemistry) which operate as a closed system with very few measureable state variables making them difficult to properly monitor and maintain safe operation. Furthermore, even under normal operation the battery packs of a BESS

will degrade during cycling. This degradation can be accelerated by extreme charging patterns, increased temperature (both ambient and operating), overcharging, or undercharging. A basic BMS controls battery packs only to meet the power demand. However, smarter model-based BMS can reduce the causes of degradation and improve the performance of a system. Predictive and adaptive BMS based on models are especially important for large battery packs for applications such as EVs and grid integration.¹⁴²⁻¹⁴⁴ While there are many possible solutions to the intricate problem of BESS control, Figure 4-1 describes a general BESS-BMS structure used for implementation.

The BESS in Figure 4-1 can be used for many different objectives, such as:

- Matching peak power demand
- Load following to increase generation utilization
- Improving grid stability, power quality and balancing (e.g. frequency control)
- Reducing source intermittency

The BMS and SCC portion of Figure 4-1 can help the BESS provide these services with optimal performance by:

- Minimizing temperature gradients across the system
- Protecting the cells from internal degradation and capacity fade
- Providing optimal charging patterns
- Balancing cells throughout the stack

While these systems work in tandem, unfortunately physical measurements of the internal states of the cells are not accessible to the BMS and SCC. The only battery states that can be measured are:

- Voltage

- Current
- External Temperature

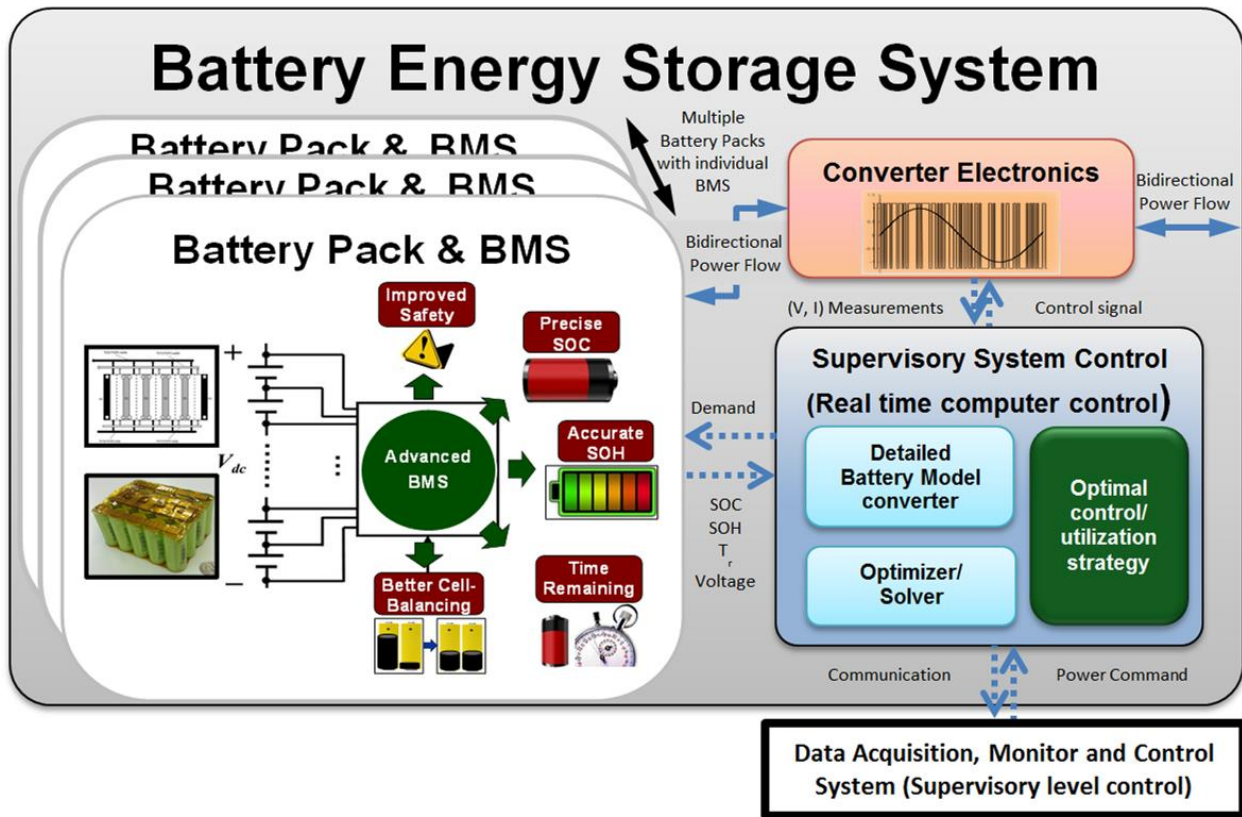


Figure 4-1: Schematic for the implementation of a battery pack and BMS into a BESS.

Other measurements are not cost practical or infeasible *in situ*. Additionally, the BMS and SCC can only control the BESS by manipulating:

- Current or Voltage
- Ambient temperature (when cooling or heating is available)

However, by utilizing physics-based models, the BMS can accurately estimate many internal variables that allow it to gain a thorough understanding of battery SOC and SOH.

A BESS will incorporate a BMS that is responsible for managing the operations of the battery. The BMS' relationship within the BESS system can be seen in Figure 4-1. The BMS is responsible for: safe operations (thermal management, operating between safe current and

voltage limits, shutdown on detection of fault etc.), state estimation (SOC determination), parameter estimation (SOH determination), time remaining (t_r) (depending on the applied load profile), and other miscellaneous functions. In addition, for Li-ion and other closed-cell systems, the BMS must also perform inter-cell charge balancing.

In large systems, many battery packs with individual BMS will be combined to create a large capacity BESS. The SSC of the BESS is the interface between the grid and the BMS. The information about battery packs are conveyed from BMS to SSC. When the grid demands power to be supplied from the batteries, the SSC chooses the optimal protocol for releasing charge while accounting for both the current state of the batteries and the grid's demand request. This SSC protocol will call power from individual packs in order to meet the final power demand.

During certain periods, the required power profiles of batteries will be more flexible and the BESS can have more control over the charging pattern. For example, in a peak-shaving application, the discharge is heavily constrained but the charging can be chosen based on the needs of the BESS. Here the individual BMS can run optimization routines to come up with the best charging profiles. These charging profiles can be communicated to the SSC which can control the power input from the grid. When determining the performance of a storage system, in addition to the BMS and the SSC, power electronics which connect these systems to each other and the grid must be taken into account. These power electronics allow for the bidirectional flow of power to and from the grid.¹⁴⁵ The way these individual pieces are structured creating a hierarchical system architecture will influence the efficiency and operation of the entire system and can aid in control.

4.2 Optimal Model-based Protocols

The model-based optimization performed in this chapter will utilize the P2D model outlined in Section 1.5.2. Using the P2D model allows the tracking of many internal states that would not be possible during operation otherwise. With better knowledge of these internal states, the cycling protocol for the battery can be optimized in order limit degradation while still meeting an application's power needs. A nonlinear dynamic optimization will be performed on the system to obtain the best possible charging pattern under the solar-battery hybrid system constraints.

Any type of control must be able to operate in real-time so that it can affect battery operation. Often when running an optimization routine, the model must be simulated hundreds of times in order to find the best possible protocol. Using techniques like reformulation and the perturbation approach outlined in Chapter 2, the optimization performed for this chapter can be conducted in real-time. An example demonstrating the advantages of a model-based optimization approach is discussed by showing three possible charging protocols for the energy storage component of a solar-battery hybrid system. For more information on the method of optimization used please see Appendix B.

Starting with a reformulated P2D model explained in Chapters 1 and 2, we included equations to model the internal temperature changes during charging and the growth of the SEI layer caused from side reactions at the anode.^{17, 146, 147} The passive SEI layer growth causes capacity fade by increasing diffusion resistance and removing lithium from the system, and can therefore be used to determine battery cycle life based on the remaining capacity.^{38, 40} For more explanation on SEI layer growth please see Section 1.6.1. While SEI growth has been shown to cause fade within Li-ion batteries, many mechanisms can cause fade to occur (see Figure 1-4).

If the only objective is storing the maximum amount of charge for the system with no time limits or additional constraints, an optimization of the P2D model leads to a constant current-constant voltage (CC-CV) charging pattern.¹⁴⁸ However, in order to guarantee long cycle life, the battery should limit the amount of SEI growth during each cycle. By adding a new constraint for the optimization model which sets a maximum allowable SEI layer, the charging pattern will deviate from the typical CC-CV charging in order to obtain the greatest amount of charge while ensuring that the SEI layer does not grow significantly. Additionally, constant current (CC) charging is not possible when using solar power due to the non-steady-state power from the solar cells.

Applying this approach to an example of a solar-battery hybrid system, we can see the effect that optimization can have on a system's performance and life. Our sample solar-battery hybrid system will be used to help satiate peak demand by providing as much power as possible between the hours of 4 to 8 PM. The solar insolation for the system is approximated by half sine curve over a 12 hour period which begins at 6AM and lasts until 6PM (Assuming full charging of the battery, the system will be able to meet a power demand 141.3% of the peak solar output over the four hour demand period). Under basic charging conditions, when power is not demanded from the system, but there is solar insolation, the solar power will go directly to charging the battery. Since some of the solar insolation will occur during the time of demand, this portion of the power will go directly to the demand load instead of battery charging. The portion of the day for which the battery can be charged will be between 6AM and 4PM and the battery will be sized so that it can capture 80% of the power supplied during that time. This percentage was chosen because many days there will not be perfect solar insolation, which can

cause underutilization of the battery. Any power generated once the battery is fully charged will be supplied to the grid at a standard rate.

A standard charging protocol (labeled “Standard Charging” in Figure 4-2) would begin charging the battery with power as soon as the power became available and continue to charge with the maximum available power until the voltage limit was reached. However, using optimization with an objective of maximizing the amount of charge stored and a constraint to limit the passive SEI growth (and therefore capacity fade) to the same level as seen in the under the standard charging protocol, the amount of charge stored would be increased (labeled “Max Stored Charge” in Figure 4-2). Note that we have not increased the amount of capacity fade, but have increased the amount of charge stored over the course of the day by altering when the battery accepts charge. The model based optimal charging protocol increases the amount of charge stored by 0.5%, and experiences the same amount of capacity fade.

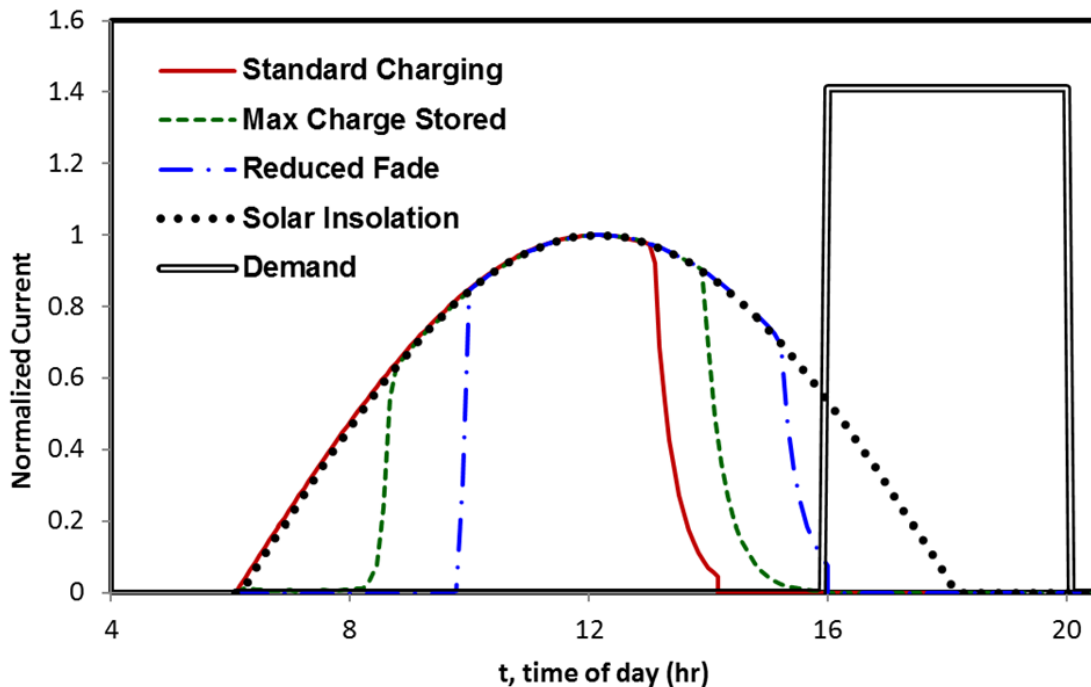


Figure 4-2: Different charging patterns for a battery powered from a solar array with different optimization objectives and constraints. The solid line (red) shows standard charging with no optimization constraints; the dashed line (green) attempts to maximize the charge stored while not increasing fade from the standard case; and the dashed-dotted line (blue) reduces capacity fade to

90% of the standard charging case while maximizing the amount of charge stored. The solar irradiance curve and demand curve are shown as well.

To further improve life, we can restrict the total amount of capacity fade which occurs in a single cycle. With the solar insolation pattern, we can limit the SEI layer growth to 90% of the standard charging protocol without losing much stored charge. The “Reduced Fade” line in Figure 4-2 shows the charging pattern with this capacity fade bound in place, which only reduces the total charge stored by 0.42%. This small decrease in single cycle capacity means we can add many additional cycles to the battery life without sacrificing performance in the short term. The reduction of SEI layer will not lead to a large reduction in charge stored until we push beyond a 10% reduction in fade. After this point, the stored charge begins to decrease significantly and further SEI layer growth reduction is prohibitive (see Figure 4-4). When comparing the three cases Figure 4-3 shows the normalized growth of the SEI layer for each charging pattern and Figure 4-4 shows the total energy gained over battery lifetime as well as the energy unutilized per cycle due to the SEI layer growth constraint.

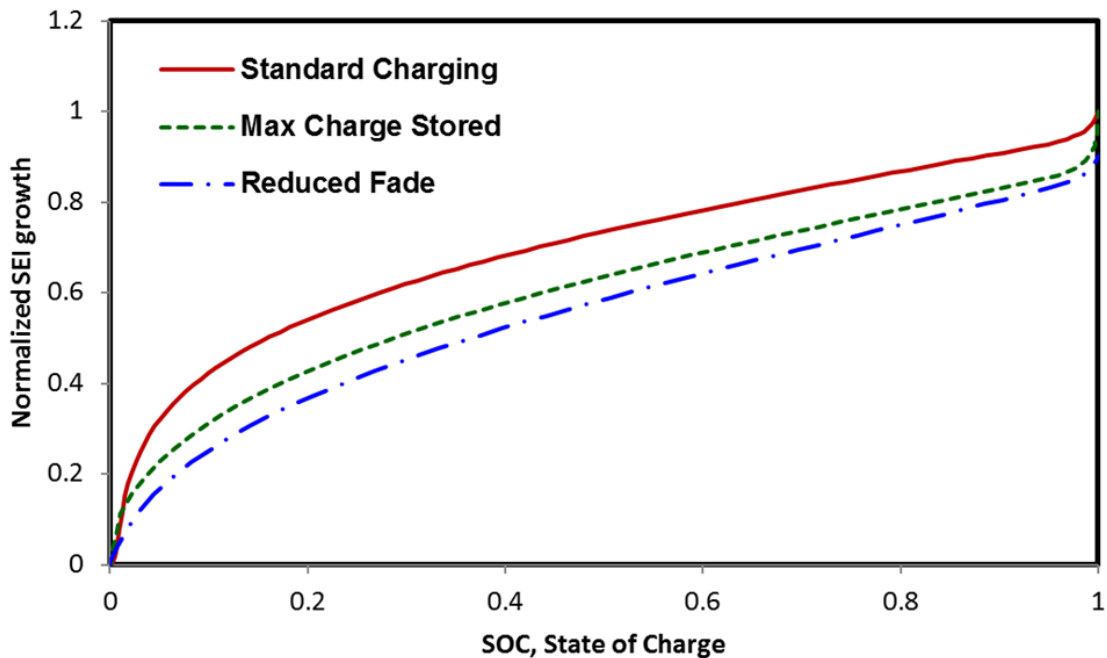


Figure 4-3: Normalized SEI layer growth as a function of SOC during the charging cycle for the three cases.

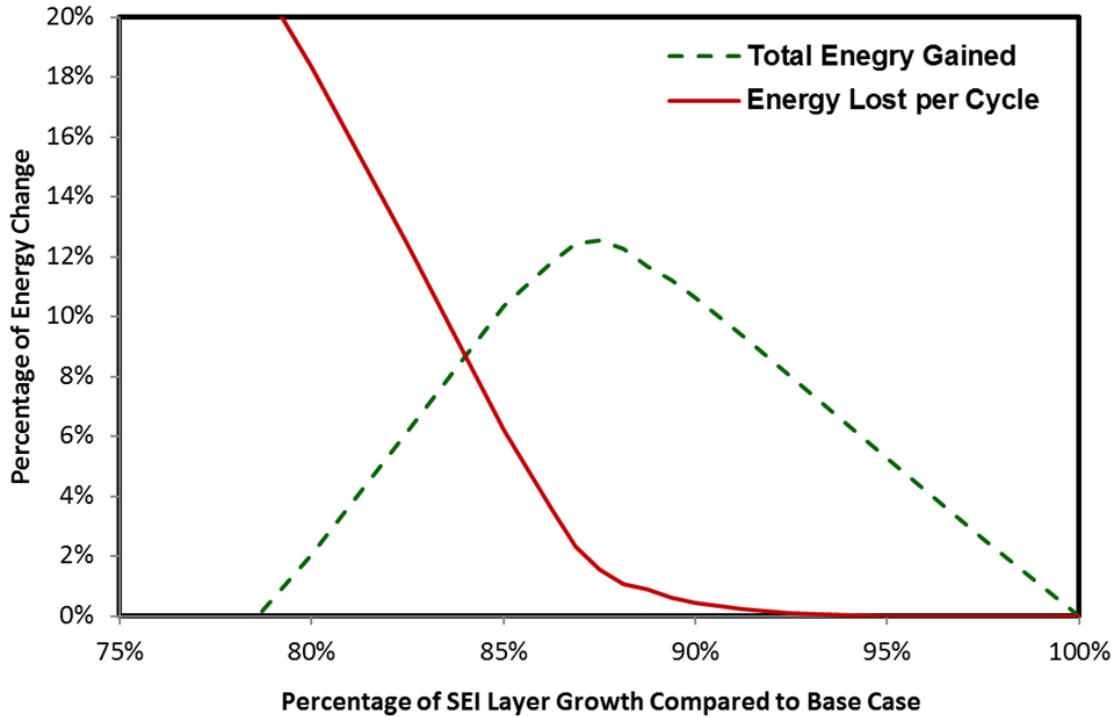


Figure 4-4: Comparison of energy benefit per cycle and over the complete life of the battery.

Restricting the capacity fade in this example will increase the cycle life by 11.1%. Although each cycle will store slightly less charge, the cumulative amount of storable energy will increase by 9.6% over the lifetime of the battery. The amount of savings will vary depending on the shape and structure of the available charge (e.g. solar insolation) within grid systems, but using adaptive optimal charging protocols gathered from model-based simulation that limit degradation effects can lead to significant improvement of energy storage systems over the lifetime of the battery.

The results given here only represent a simple case. Since insolation and demand can change on a daily basis, these types of systems will require continuous real-time optimization based on fast physics based models. These curves are presented as evidence that modeling and simulation capability for batteries have advanced to a state where one can make real-time predictions and optimize charging protocols.⁴² The objectives and constraints placed on the

battery system can be altered for many different situations and system sizes can be altered to study the effectiveness of system parameters for various sites. The real-time simulation and optimization was enabled by the advancement in model reformulation and efficient simulation of battery models.^{15, 44, 149, 150}

Chapter 5

Analysis of Batteries under Electric Vehicle Constraints

This chapter contains excerpts from the following journal article, reproduced here under the Creative Commons Open Access BY-NC-ND licenses:

Lawder, Matthew T., Northrop, Paul. W.C., Subramanian, Venkat R. “Model-Based SEI Layer Growth and Capacity Fade Analysis for EV and PHEV Batteries and Drive Cycles” *Journal of the Electrochemical Society*, 161:14 (2014) A2099-A2108.

5.1 Electric Vehicle Battery Modeling

In addition to renewable energy support, large-scale battery packs are being implemented in other applications such as EVs. While working EVs have been in existence for over a century (a lead-acid battery powered car achieved speeds of 30m/s in 1899), the price of EVs has not become competitive with their internal combustion engine (ICE) counterparts.¹⁵¹ EV sales are currently aided by subsidies ranging from \$3,000 in China to \$7,500 in the US and Western Europe to \$10,000 in Japan.¹⁵² One of the causes of the high prices of EVs is the expensive nature of the vehicle's battery pack, which is not required by ICE vehicles running entirely on gas (hybrids operate on a combination of both systems with plug-in hybrid electric vehicles (PHEV) being able to operate in an all-electric mode). Most currently available and planned EVs (and PHEVs) use a Li-ion battery chemistry. Li-ion EV battery pack costs were estimated at between \$600-\$1,200 per kWh of energy capacity in 2013.^{152, 153} This price can cause battery packs to cost in excess of \$10,000 per vehicle and account for 30-50% of total vehicle cost.¹⁵⁴ Although battery prices have decreased, they remain one of the most expensive components of an EV. Decreasing the price of the battery pack will be extremely important in making the EVs price competitive in the automobile market.

As EV and PHEVs age, their battery packs will have to be replaced due to capacity and power fade. Power fade is defined as the loss of cell power caused by increased cell impedance from aging. Capacity fade is defined as the loss of energy storage capacity due to degradation

caused by cycling.¹⁵⁵ Based on present requirements, EV batteries that have lost 20% of their initial factory capacity are no longer useful for automotive use and should be replaced.¹⁵⁶ Typically, an EV battery will last between 5 to 10 years within its automotive application depending on driving and charging patterns. Nissan estimates that the battery installed in the 2011 Nissan Leaf will contain approximately 80% of its original capacity after five years.¹⁵⁷ PHEV batteries will experience capacity fade on a similar time scale. At the end of the eight year warranty coverage for the 2013 Chevrolet Volt's battery, Chevrolet states that the battery may have degraded anywhere between 10% and 30% depending on driving patterns.¹⁵⁸ These wide variations are a byproduct of consumer's different driving and charging patterns. The charging and discharging patterns for EV and PHEVs will greatly affect the amount of capacity fade that occurs during cycling and will determine when the battery needs to be retired from automotive use. While many studies have shown capacity fade associated with SEI layer growth for galvanostatic charge and discharge conditions, few studies have looked at the SEI layer growth caused from dynamic discharge condition seen in EV and PHEVs.^{30, 41, 159}

5.1.1 P2D Model with SEI Layer Growth

For this study, the P2D model (see Section 1.5.2) is used to represent the Li-ion battery pack. An SEI layer side reaction was included with the P2D model. More info about the SEI layer can be found in Section 1.6.1. Side reactions creating the passive SEI layer can form in two steps, at contact of the lithium ion to the electrode and during the intercalation of the lithium ion into the electrode.¹⁶⁰ Additional side reactions that may cause capacity fade, but do not directly contribute to SEI growth, can also occur at these stages (see Figure 1-4). Three variations on the generally SEI reaction mechanism were tested for this study. Each of these expressions are derived from variations on Butler-Volmer kinetics for determining the amount of current flux

consumed by the reaction, but each has a different pre-exponential dependence on the lithium and solvent concentrations.^{30, 38, 40} The simplest of the three terms assumes that the variation in lithium and solvent concentration will be negligible at low to moderate rates and that neither of the concentrations will be rate limiting.³⁰ Therefore there is no concentration dependence in the flux term for SEI layer growth shown as:

$$j_{SEI} = -k_{SEI} \exp \left(\frac{\alpha F}{RT} \left(\Phi_1 - \Phi_2 - U_{SEI} - \frac{\delta_{SEI} j_n}{\kappa_{SEI}} \right) \right) \quad (5.1)$$

based on the model developed by Ramadass et al.³⁰

In Safari et al.⁴⁰, a term is included to account for the electrolyte concentration, but the equilibrium potential, U_{SEI} , is removed from the system.⁴⁰ The equilibrium potential for SEI is not well understood with values being reported in literature ranging from 0.4 to 2.0V.^{161, 162} The resulting flux equation is:

$$j_{SEI} = -k_{SEI} c_{sol} \exp \left(\frac{\alpha F}{RT} \left(\Phi_1 - \Phi_2 - \frac{\delta_{SEI} j_n}{\kappa_{SEI}} \right) \right) \quad (5.2)$$

The final expression studied includes the concentration for the electrolyte and the lithium ions at the surface as well as the equilibrium potential for the SEI. Based on the model developed by Pinson and Bazant, the resulting expression is:³⁸

$$j_{SEI} = -k_{SEI} c_{sol}^{0.5} c_{Li^+}^{0.5} \exp \left(\frac{\alpha F}{RT} \left(\Phi_1 - \Phi_2 - U_{SEI} - \frac{\delta_{SEI} j_n}{\kappa_{SEI}} \right) \right) \quad (5.3)$$

Note that with the reaction occurring at the anode the, current density flux at the anode must be split into two pieces, one intercalation term and one side reaction term, shown as:

$$j_n = j_{int} + j_{SEI} \quad (5.4)$$

At the cathode, all of the current will go to intercalation with no side reactions occurring. By including the SEI equations into the P2D model, capacity fade will be simulated throughout the cell during both charging and regenerative braking (during braking while driving the batteries will be partially charged from the force use to brake). SEI layer growth will not occur during discharging of the battery.

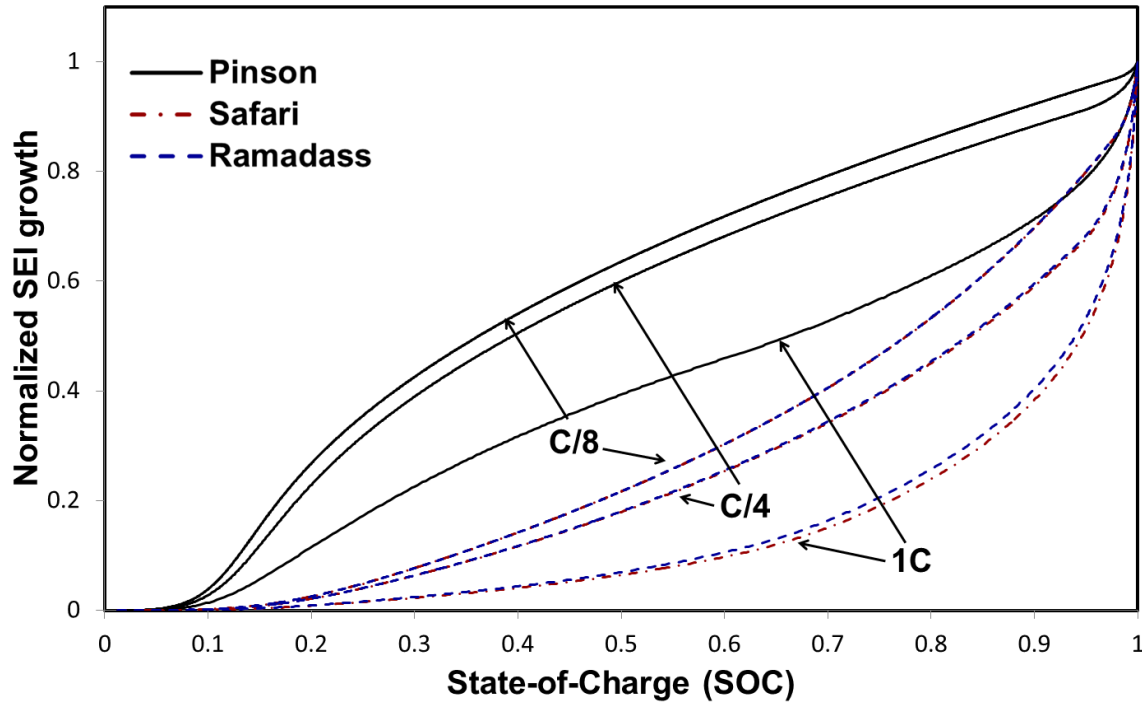


Figure 5-1: SEI growth shown for charging at 1C, C/4, and C/8 rates for three SEI growth mechanisms. SEI growth is scaled and normalized for the total growth over one charging cycle to be equal across cases.

5.2 Comparison of SEI Growth Expressions

The SEI layer growth from the three different growth expressions (Eqs. (5.1), (5.2), and (5.3)) can be seen for three charging rates (under CC-CV charging) in Figure 5-1. Figure 5-2 shows the SEI growth occurring during EV use under the DST driving cycle (regenerative charging accounts for all of the SEI growth in this case) for all three growth expressions. The kinetically limited expressions from Eqs. (5.1) and (5.2) are qualitatively similar, with both showing much greater SEI growth during the later stages of charging especially the CV portion

of charging in Figure 5-1. In Figure 5-1, as charging rates decrease the differences between the different SEI growth expressions will shrink. Additionally as the charging rates decrease, the ratio of SEI growth occurring during driving to the growth during charging decreases as seen in Table 5-1.

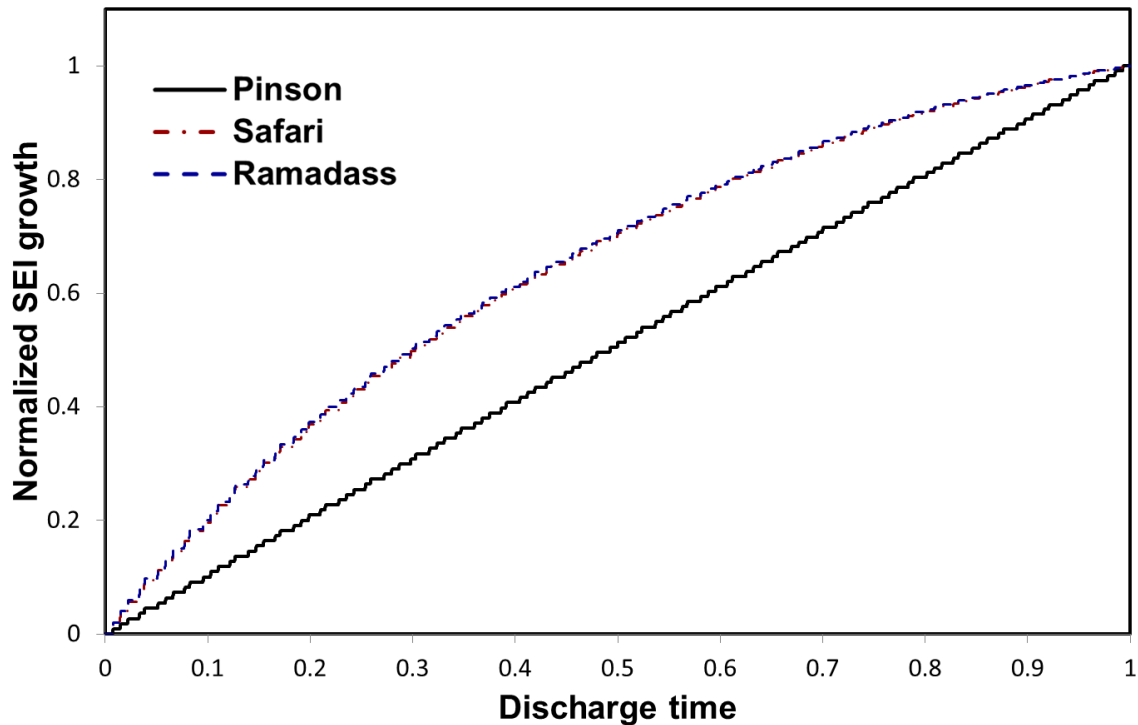


Figure 5-2: SEI layer growth during the DST driving cycle for each SEI growth mechanism over a complete discharge. Time has been scaled over the entire discharging cycle (Note: Regenerative charging will occur during the driving cycle). SEI growth is scaled and normalized for the total growth over one discharge cycle to be equal across cases.

Table 5-1: When completing a full charge-discharge cycle, the SEI growth contributed will be less than the amount contributed through CC-CV charging. This table shows the percentage of total SEI growth that the DST driving cycle contributes one a single charge-discharge cycle when charging rates are 1C, C/4, and C/8.

Charging Rate	Pinson and Bazant	Safari and Delacourt	Ramadass, et al.
1C	6.32%	8.48%	7.54%
C/4	3.07%	6.09%	5.67%
C/8	1.62%	3.60%	3.31%

During regenerative braking (see Figure 5-2) the Pinson expression shows close to linear growth of SEI layer, while the Safari et al. as well as the Ramadass expressions show growth that

is dependent on the remaining SOC of the battery. Both expressions show larger amounts of growth at high SOC levels than Pinson.

While consumers typically desire fast charging for EV applications, the majority of vehicle charging occurs at levels of 2C and below with Level 2 and home installation charging typically ranging between C/3-and C/16. The charging and discharging occurring during an EV drive cycle can vary greatly and the high rates of charging or discharging that may occur due to driving preferences may affect the dependence of certain variables on SEI layer growth. However, testing the differences between the SEI growth expressions is beyond the scope of this chapter and therefore all simulations beyond this section will utilize the Ramadass, et al. rate expression (Eq. (5.1)). When studying capacity fade over the entire life of the battery, the amount of growth each cycle is more important than the shape of the growth over a single cycle.

High rates of cycling have been shown to lead to increased capacity fade, however for the SEI growth expressions shown above, the amount of SEI growth actually increases with a decrease in the charging, mainly due to the increased charging time which allows more time for the side reaction to occur.²³ Other mechanisms can have greater effects on capacity fade during high rate charging beyond SEI growth, such as mechanical stress fractures or overcharging.²⁶ Stress induced fractures can create fresh electrode surface sites which experience greater SEI growth than portions of the electrode that already have some SEI layer covering them.^{163, 164} At lower rates of charging the contribution of SEI growth towards overall capacity fade is greater and while other fade mechanisms are present, SEI layer growth has been shown to be one of the greatest factors of capacity fade.²⁸ SEI growth remains an important fade mechanism in the large format cells that are used in EVs.^{128, 165}

5.3 EV Driving Cycles

To study the effects of driving on EV batteries, we apply different standard drive cycles to the EV battery. These cycles incorporate both discharge and regenerative braking, but will be referred as the discharge portion of battery cycling (charging will refer to only the CC-CV charging of the battery). Eight driving cycles commonly used by the US and European government were chosen. These cycles approximate different types of driving, from urban stop and go cycles to predominately highway cycles. They include: Urban Dynamometer Driving Schedule (UDDS); Federal Test Procedure (FTP-75); Highway Fuel Economy Driving Schedule (HWFET); Supplemental FTP Driving Schedule (US06); Elementary Urban Cycle (ECE-15); Extra-Urban Driving Cycle (EUDC); New European Driving Cycle (NEDC); and Dynamic Stress Test (DST) (see Appendix C see more details).¹⁶⁶ Other than the DST cycle, the remaining seven test cycles prescribes a different set of velocities and accelerations throughout the drive cycle. In order to be useful for our studies we must convert these velocity and acceleration time curves into power curves that can then be applied to the EV battery packs.

To find the power required from the battery we need to study the forces that are applied to the car which include:

$$F_{motor} = F_{drive} + F_{rr} + F_{drag} + F_g \quad (5.5)$$

$$P_{motor} = F_{motor} v \quad (5.6)$$

where F_{motor} is the force required from the motor, F_{drive} is the force required for vehicle acceleration, F_{rr} is the rolling resistance between the tires and the roadway, F_{drag} is the force from the aerodynamic drag, and F_g is the gravitational force created when the car is driving uphill or downhill. We will assume for all drive cycles that the driving surface is flat, therefore $F_g = 0$ for all cases.

The three other forces are represented as:¹⁶⁷

$$F_{drive} = m \frac{dv}{dt} \quad (5.7)$$

$$F_{rr} = k_r m g \cos(\theta) \quad (5.8)$$

$$F_{drag} = \frac{1}{2} \rho C_D A_f (v - v_w)^2 \quad (5.9)$$

where m is the vehicle mass, k_r is the rolling resistance coefficient, ρ is the density of air, C_D is the drag force coefficient, A_f is the 2-D projected vehicle area, v_w is the wind velocity (assumed to be zero), and θ is the roadway gradient (also assumed to be 0). Using these conversions we can take any of the normal velocity drive cycles and convert them to power cycles (The only drive cycle that did not need to be converted was the DST cycle, which was developed for EV testing and provides a direct power curve). The vehicle and roadway parameters used to convert vehicle velocity into power are shown in Table 5-2.^{168, 169} Driving cycles range from the simple ECE-15 seen in Figure 5.3 to the more reality based UDDS seen in Figure 5.4.^{170, 171}

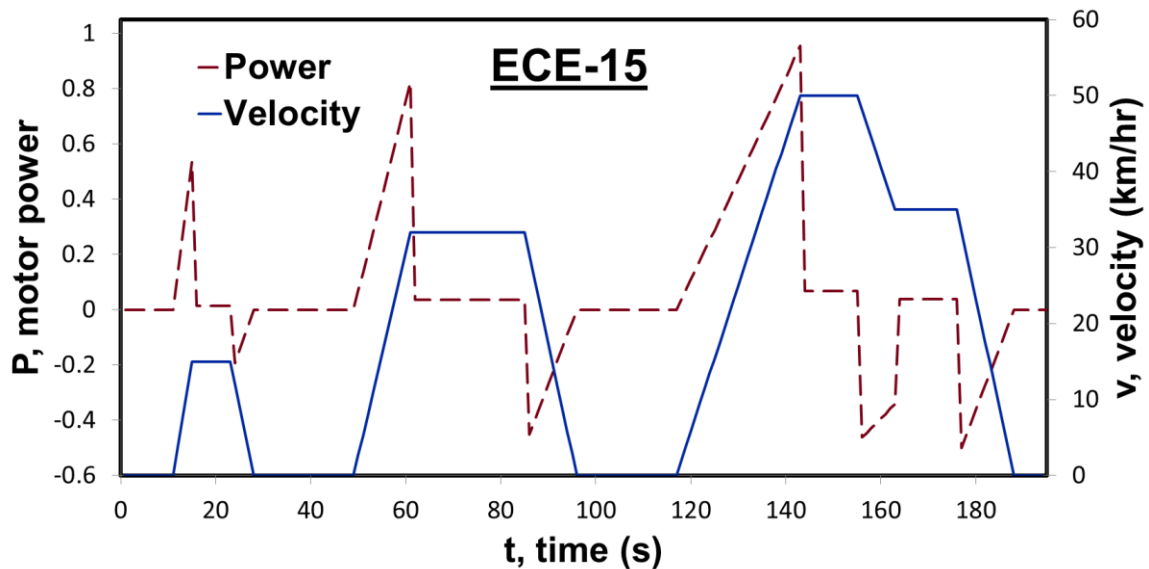


Figure 5-3: The power and velocity seen under vehicle conditions shown in Table 5-2 for the ECE-15 drive cycle.

Table 5-2: Parameters used for converting velocity profiles into power profiles for use in electric batteries.^{168, 169}

Vehicle Characteristics	
Mass	1500 kg
Coefficient of Drag	0.34
Frontal Area	1.75m ²
Regenerative Efficiency	0.6
Tire rolling drag coefficient	0.01

The duration and distance of each driving cycle varies. The driving cycles were repeated multiple times until the battery was 100% discharged. When applying cycles to the battery model with SEI growth, each was scaled so that the battery capacity would allow for 150 km of driving distance, which is a range typical of many available EVs, in order to provide a fair comparison. Therefore the number of individual driving cycles that a battery went through in one discharge varied based on the cycle. The same scaling factor was applied when conducting tests on different DOD (DOD was calculated based on SOC and anode lithium concentration).

$$SOC = \frac{C_n^s}{C_{max,n}^s} \tag{5.10}$$

$$DOD = SOC_{initial} - SOC_{final} \tag{5.11}$$

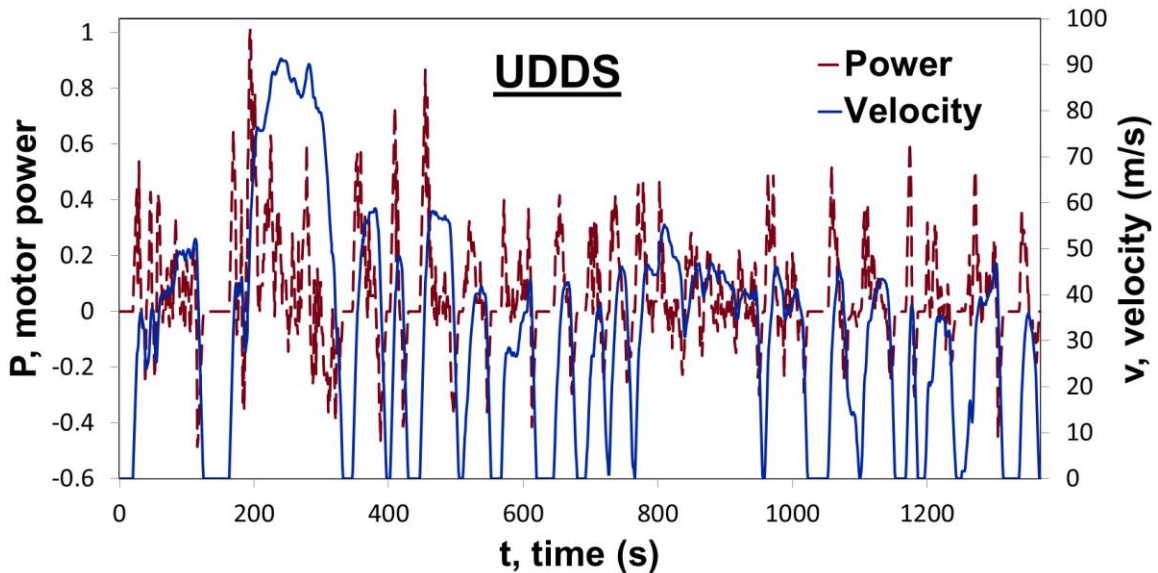


Figure 5-4: The power and velocity seen under vehicle conditions shown in Table 5-2 for the UDDS drive cycle.

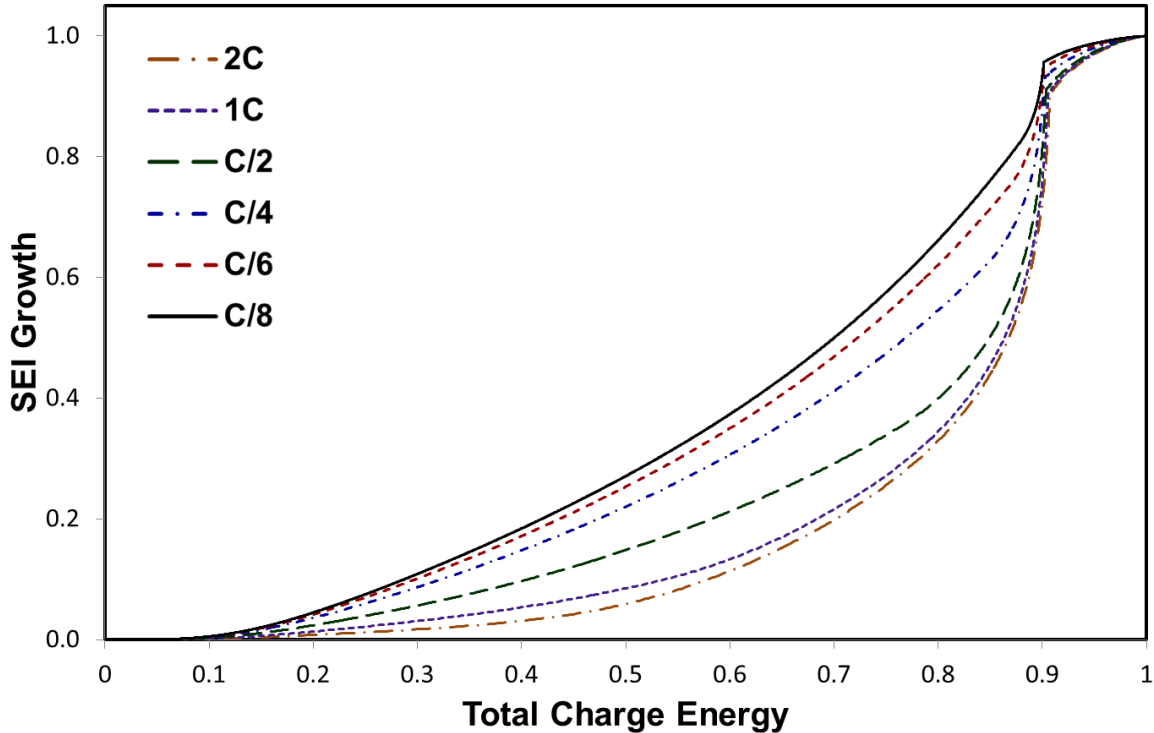


Figure 5-5: SEI growth over a single charge-discharge cycle, for six different rates of CC-CV charging. The discharge cycle in all cases was the standard DST driving cycle. “Total Charge Energy” is scaled based on the total amount of energy used to charge the battery (including regenerative charging during the discharge cycle). SEI growth is scaled and normalized for the total growth over one charge-discharge cycle to be equal across cases.

5.4 EV Charging Characteristics

While fast charging is desired for most EV and PHEVs, a typical EV will see a wide range of different charging patterns over the course of its lifetime. Charging rates for EVs are categorized into three levels: Level 1; Level 2; and Level 3. Level 1 charging operates through the standard residential outlet plug (120V AC) and EVs will have the charging equipment built in to the vehicle. This type of charging will only add a few miles of charge per hour. Therefore, it can take over ten hours to fully charge a vehicle depending on the battery size and is typically only used for residential overnight charging. Level 2 charging occurs at mid-range voltages (208V and 240V (AC) are common levels) and requires off-board charging equipment for most vehicles. This level of charging is prominent in public charging stations or can be installed in homes. Charging at Level 2 takes between 2-8 hours. Level 3 encompasses charging rates that

can fully charge a battery in even less time through use of DC often at 480V (Note that the AC/DC refers only to the charging source, the battery must be charged through DC). These charging stations require extensive off-board equipment, but offer the ability to regain close to a full charge in a half hour. Note that all charging times are dependent on battery size. The range of rates that typical EV batteries experience is between C/8-2C. Figure 5-5 shows the differing SEI growth over one cycle of charging followed by the EV DST cycle at these differing charging rates. Vehicle charging will lead to the majority of growth over the life of battery.

5.5 Results and Discussion

Most charging applications apply a CC-CV. While this protocol maximizes the amount of charge stored for a single cycle, the CV portion of charging greatly increases the charging time while adding stored charge at a diminishing rate. The increased charging time will lead to increased SEI growth. CV charging only occurs during the end of the charging cycle and at high levels of SOC. Figure 5-1 shows that during the CV portion of charging the rate of SEI growth with respect to charge stored increases for all cases. Previous experimental studies have shown that increasing the portion of CV charging can lead to increased capacity fade.¹⁷² In cases where a EV owner is willing to forego the additional charge stored from CV charging (less than 10% in most cases), they will see a benefit over the life of the battery by reducing the SEI growth. Other degradation effects may negate the benefit of CC only charging.

An overview of several EV and PHEVs available to the public in 2013 is shown in Table 5-3. This table includes all EVs and PHEVs that sold at least 550 units in the US during 2013. For the two types of vehicles reviewed here (EV and PHEV), the charge/discharge patterns vary. PHEVs can operate in several modes depending on how the driver wishes to use the available capacity. In a charge depleting mode, the PHEV battery will experience deep DOD cycles

because the battery will be completely depleted as the vehicle operates in an all electric mode until the battery is out of energy and then switches to the ICE. A more commonly used mode for PHEVs is a charge sustaining mode which will keep the battery capacity at an average capacity during driving through sparingly using the electric motor in combination with the ICE. The vehicle will only operate in all-electric mode for a portion of its battery capacity before switching to a balance between the ICE and battery.

Many PHEV batteries are optimally sized so that a consumer's average driving cycle will use the entire battery capacity while only briefly needing the ICE. The DOD patterns of PHEVs will often experience deeper DOD than EVs because of their smaller battery size (although charge sustaining operation for PHEVs will limit the DOD). An EVs' battery is sized to allow for cushion or buffer capacity beyond the consumer's typical driving cycle so that a driver is not stranded on the road. This overhead capacity is rarely used, but does alleviate some of the consumer's range anxiety (fear that the vehicle will not be able to travel to a desired destination and back on a single charge) which is one of the primary customer concerns when purchasing an EV.¹⁷³⁻¹⁷⁵

For PHEVs, battery sizing is based on capturing the optimal amount of vehicle miles. Vehicle manufactures differ on what is viewed as optimal size shown in the variance in battery capacity present among PHEVs in Table 5-3. The Department of Transportation determined that the average trip distance for a US vehicle in 2009 was 9.72 miles and the average daily vehicle miles traveled (VMT) per driver was 28.97 miles.¹⁷⁶ Figure 5-6 shows the percentage of miles covered in all electric mode for several of the PHEVs for average US driving characteristics and Figure 5-7 shows the breakdown of daily VMT for US vehicles.^{177, 178}

Table 5-3: Characteristics of 2013 production EV batteries.^{158, 179-187} *The Prius-Plug-in energy capacity is an estimated amount. *The Honda Fit EV is only available to lease.

Car Type	Make	Model	Energy Capacity(kWh)	Range (miles)	MPGe	Peak Power (kW)	MSRP(\$)
EV	Fiat	500e	24	87	108	83	31800
	Ford	Focus EV	23	76	105	107	39200
	Honda	Fit EV	20	82	118	100	374152*
	Mitsubishi	i-MiEV	16	62	112	49	29975
	Nissan	Leaf	24	75	115	80	28800
	Smart	ED	17.6	68	107	55	25000
	Tesla	Model S	60/85	208/265	95/89	270/270	69900/79900
	Toyota	Rav4 EV	41.8	103	76	115	49800
PHEV	Chevy	Volt	16.5	38	98	111	39145
	Ford	Fusion Energi	7.6	21	100	88	35525
	Ford	C-max Energi	7.6	21	100	88	33745
	Toyota	Prius Plug-in	4.4*	11	95	60	32000

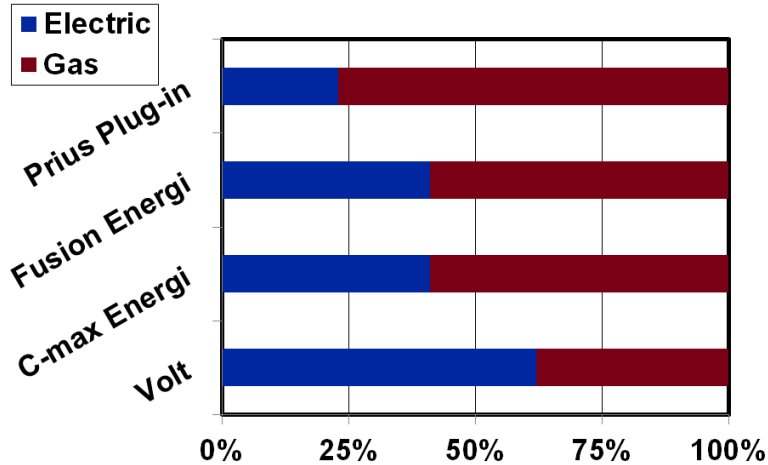


Figure 5-6: Percentage of total VMT driven using the all-electric mode for different PHEV (assuming charge depletion).

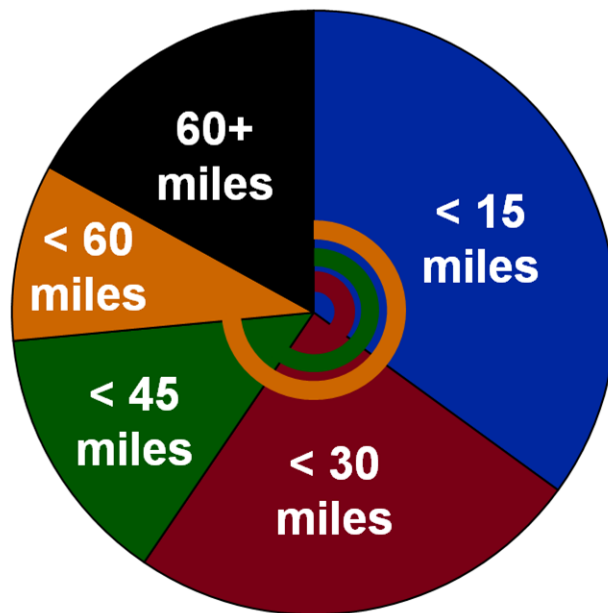


Figure 5-7: Amount of daily VMT for American vehicles. Blue represents all vehicles drive less than 15 miles per day. Blue and Red represent all vehicles driven less than 30 miles per day, etc.

The daily driving cycles will affect the DOD experienced by EVs and PHEVs. Assuming operation in all electric mode for the entire battery capacity (no charge sustaining mode or re-charging), a battery with a 10 mile all-electric range will experience 100% DOD during 96% of an average driver’s daily travel cycles, while a battery with a 40 mile all-electric range will experience full discharge in only 69% of daily travel cycles. Variation in DOD cycles creates more difficulty for vehicle manufactures who try to implement a BMS to optimally control the

battery.¹⁸⁸ While PHEVs will experience deep discharge more frequently, EVs will still utilize a larger absolute amount of battery energy due to the greater size of their battery and the requirement that all VMT are driven by electric power. The nature of an individual’s driving cycles and the amount of regenerative braking that occur during a cycle will also affect the vehicle’s all electric range and the battery’s experienced DOD.

5.5.1 SEI Growth Results

We applied each of the driving cycle power curves to the P2D Li-ion battery model with SEI layer growth to study the effects of different driving patterns and different levels of regenerative braking on the SEI layer growth within the battery. Figures 5-8 and 5-9 show the SEI layer growth during the first two hours of driving and the first 30 km of distance covered, respectively. The SEI growth in these figures has been normalized relative to the amount of growth experienced under the NEDC driving cycle during the same periods. The absolute values of SEI layer growth are on the order of nanometers as only one cycle was simulated.^{189, 190}

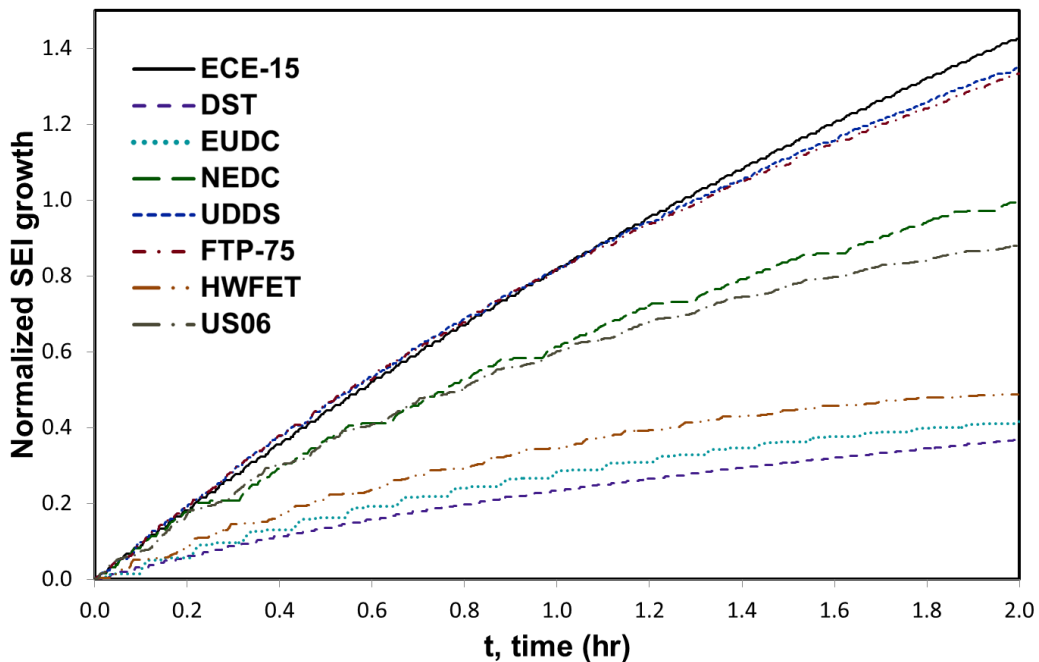


Figure 5-8: SEI growth for all 8 driving cycles for two hours of driving. The SEI growth was scaled to the amount of growth from the NEDC case over two hours in order to show a relative comparison among the driving cycles.

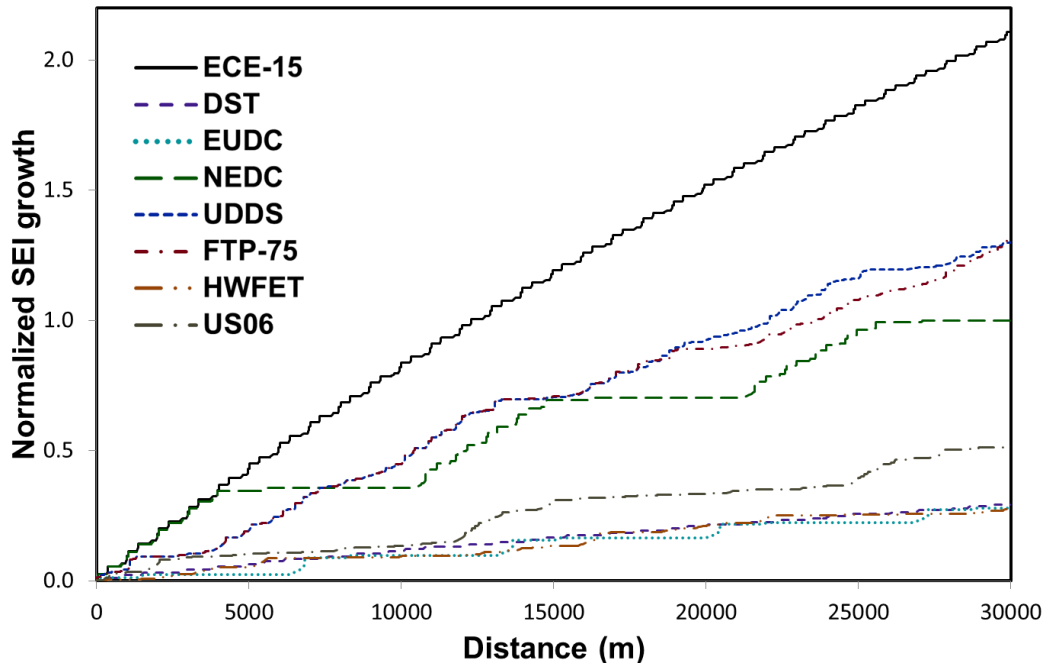


Figure 5-9: SEI growth for all 8 driving cycles for 30km of driving. The SEI growth was scaled to the amount of growth from the NEDC case over 30 km in order to show a relative comparison among the driving cycles.

The results show that the drive cycles that averaged faster speeds and had lower ratios of braking power to propulsion power (R-P ratio) also had lower amounts of growth during the driving cycle. This trend held for both SEI growth measured over distance traveled and over travel time. The distribution among rates was much greater for the rate per distance traveled than it was from time. Results for the amount of growth per unit distance and per unit time of each cycle are shown in Table 5-4. For each drive cycle the duration and magnitude of the acceleration and deceleration period were the predominant factors in determining the ratio of regenerative power that could be captured (shown Table 5-4). Stretches of constant velocity did not affect the power, but did increase the distance traveled greatly with less growth of the SEI layer. Cycles such as the HWFET cycle which maintains a high constant velocity without much acceleration, travels longer distances without gaining as much SEI layer growth as other cycles. In general, the cycles that approximate lower speed, urban driving patterns experienced more

Table 5-4: Characteristics for the eight drive cycles studied. Average velocity, duration, distance, and R-P Ratio are the characteristic for one driving cycle (not repeated unless end of discharge) while the remaining categories show values for drive cycles repeated unless battery has reach 100% DOD. Regen Energy Added is the percentage of energy gained during the driving cycle, compared to the amount from a full charge. Regen SEI Added is the percentage of SEI layer thickness gained during the driving cycle, compare to the amount from a full charge cycle. R-P Ratio is the ratio of regenerative energy during a driving cycle to the amount of energy used for vehicle propulsion during a driving cycle. SEI growth/ min and SEI growth/ km are scaled to the amount of SEI growth/min and SEI growth/ km of the NEDC cycle. These value represent a relative comparison of how much growth each driving cycle will accumulate per min or km. *DST characteristic were back calculated from Power curve.

EV Cycle	<i>DST*</i>	<i>NEDC</i>	<i>ECE-15</i>	<i>EUDC</i>	<i>UDDS</i>	<i>FTP-75</i>	<i>HWFET</i>	<i>US06</i>
Average Velocity (km/h)	46.3	33.6	18.4	62.6	31.5	34.2	77.7	77.9
Duration (min)	6.0	19.7	3.3	6.7	22.8	31.2	12.8	9.9
Distance (km)	4.63	11.02	1.00	6.96	11.99	17.79	16.45	12.89
Regen Energy Added	18.1%	18.2%	66.6%	15.9%	49.1%	41.0%	27.1%	50.0%
Regen SEI Added	11.7%	39.0%	82.9%	11.3%	54.2%	51.2%	12.8%	23.1%
R-P Ratio	0.052	0.183	0.423	0.143	0.363	0.357	0.171	0.303
SEI growth/min	0.37	1.00	1.38	0.43	1.38	1.39	0.54	0.97
SEI growth/km	0.29	1.00	2.14	0.29	1.43	1.37	0.32	0.58

SEI growth during an entire discharge cycle, but also had the greatest amount of regenerative braking (which is the main cause for SEI growth during driving) and therefore would typically require a smaller battery pack in order to achieve the distances studied. Additionally, when driving between points, utilizing driving patterns similar to the DST or EUDC cycles (which experience the lowest growth rates per km) would be most beneficial for reducing SEI growth.

When focusing on how the regenerative nature of the driving cycle affects the amount of SEI growth, we found the percentage of additional energy output from the battery and the amount of additional SEI layer growth during a single discharge cycle caused from using regenerative braking instead of conventional brakes (see Table 5-4). While the regenerative braking caused some SEI formation for all the drive cycles, the cycles that experienced the greatest amount of additional energy benefit also experienced the greatest rate of SEI growth. For the ECE-15, UDDS, FTP-75, and NEDC cycles, the percentage of additional SEI growth exceeded the additional energy gained. If SEI growth was the only fade mechanism occurring during driving, then the use of regenerative braking during these cycles would be prohibitive over the entire life of the battery because even though additional energy is being gained during a single cycle, the fade that occurs will result in a net total energy loss over the life of the battery due to the decrease in cycle life. For the DST, EUDC, HWFET, US06 cycles the additional percentage of energy gained is greater than the additional SEI layer growth meaning that the use of regenerative braking in these cycles is beneficial over both a single cycle and the entire life of the battery.

Many real-world driving cycles do not deplete the battery to 100% DOD before recharging. We looked at the SEI growth of cycling at different DOD levels for each of the

driving cycles. The results for SEI growth at 4 different DOD levels is shown in Figure 5-10 for the HWFET cycle and Figure 5-11 for the UDDS cycle.

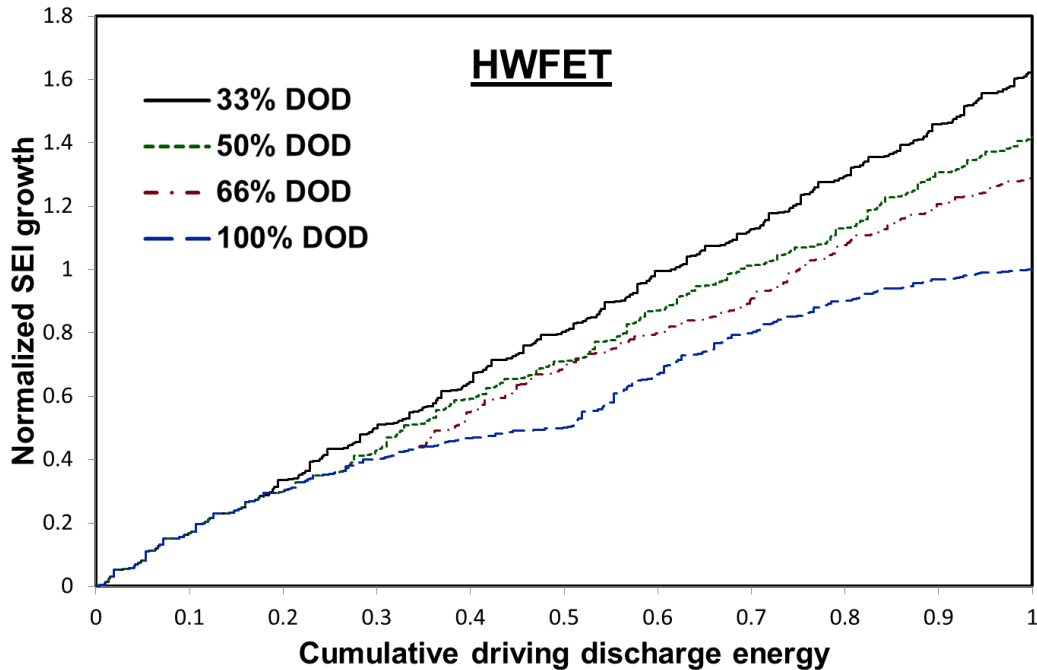


Figure 5-10: SEI growth over multiple driving cycles using the HWFET driving cycle for differing DOD. Only SEI growth during discharging is shown (no charging growth). The SEI growth is measured in comparison to the amount of discharged energy since more energy will be discharged during a deeper DOD (and we would expect more SEI layer growth). This method allows for comparison between cases even though they stored different amounts of energy during a single cycle. The discharge energy and SEI growth is scaled to the amount seen during two cycles of 100% DOD. For all cases discharge will begin at 100% SOC.

Table 5-5: Summary of the ratio of SEI layer growth for different DOD in comparison to 100% DOD for all eight driving cycles beginning at 100% SOC for all cases.

Driving Cycle	66% DOD	50% DOD	33% DOD
DST	1.30	1.45	1.68
NEDC	1.31	1.47	1.69
ECE-15 (UDC)	1.30	1.46	1.68
EUDC	1.29	1.47	1.64
UDDS	1.27	1.42	1.62
FTP-75	1.23	1.36	1.54
HWFET	1.29	1.42	1.64
US06	1.22	1.36	1.52

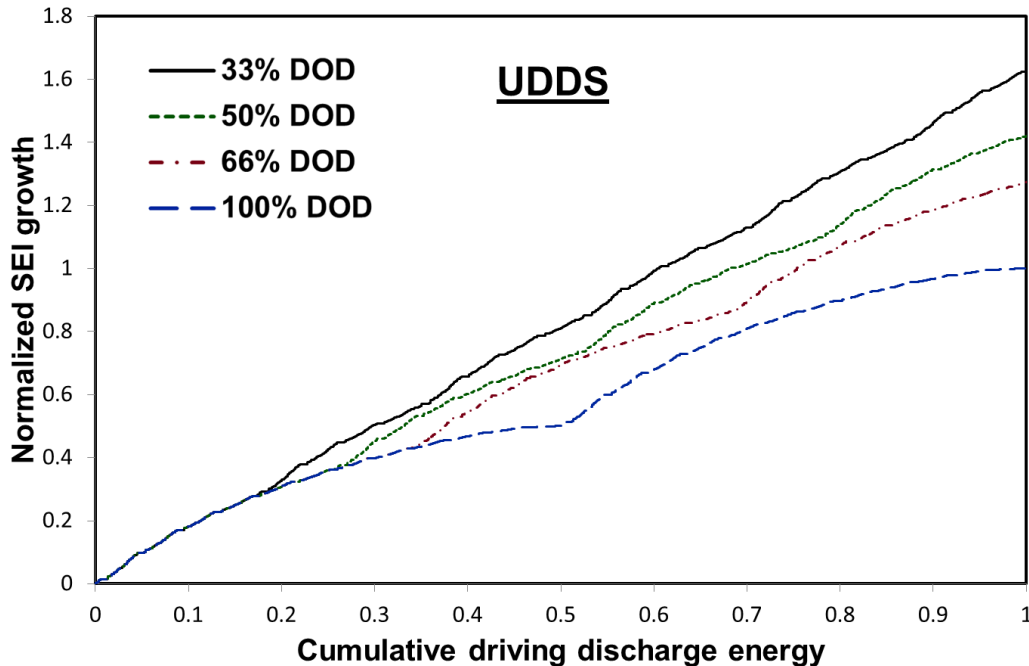


Figure 5-11: SEI growth over multiple driving cycles using the UDDS driving cycle for differing DOD. Only SEI growth during discharging is shown (no charging growth). The SEI growth is measured in comparison to the amount of discharged energy since more energy will be discharged during a deeper DOD (and we would expect more SEI layer growth). This method allows for comparison between cases even though they stored different amounts of energy during a single cycle. The discharge energy and SEI growth is scaled to the amount seen during two cycles of 100% DOD. For all cases discharge will begin at 100% SOC.

The figures show only SEI growth during the driving cycles (additional growth will occur during charging). Table 5-5 summarizes the relative SEI layer growth for all the driving cycles based on varying DOD where the amount of usable energy from the batteries is normalized to the amount of energy utilized during two 100% DOD discharges. The SEI growth is greater for cycling at lower DOD for all of the driving cycles. Part of this higher growth rate is due to the higher potential of the battery during cycling for small DOD cycles because lower potentials correlate to the lower states of charge. Figures 5-10 and 5-11 and Table 5-5 have measured DOD starting from 100% SOC, however we can also start the driving cycle at a lower SOC. For example, instead of beginning a 33% DOD at 100% SOC and driving until 67% SOC, the driving cycle can begin at 33% SOC and end at 0% SOC. Changing the range of SOC experienced during driving will change the potential of the battery during the cycle. Results for

the same 4 DOD for the UDDS cycle are again shown in Figure 5-12, however now the SOC range will always go to 0% SOC (eg. 0-33% SOC, 0-50% SOC, 0-67% SOC). Because of the lower potential during the driving cycles the SEI growth is actually lowest for the 100% DOD case on a growth per km driven basis. Since the EV cycles apply a desired power to the battery, the current applied by the cycles will be higher during the operation at low SOC. However, Figure 5-12 shows that the potential is more important for the SEI growth than the applied current. Experimental studies have shown increased side reactions at the SEI layer for high potentials.¹⁹¹

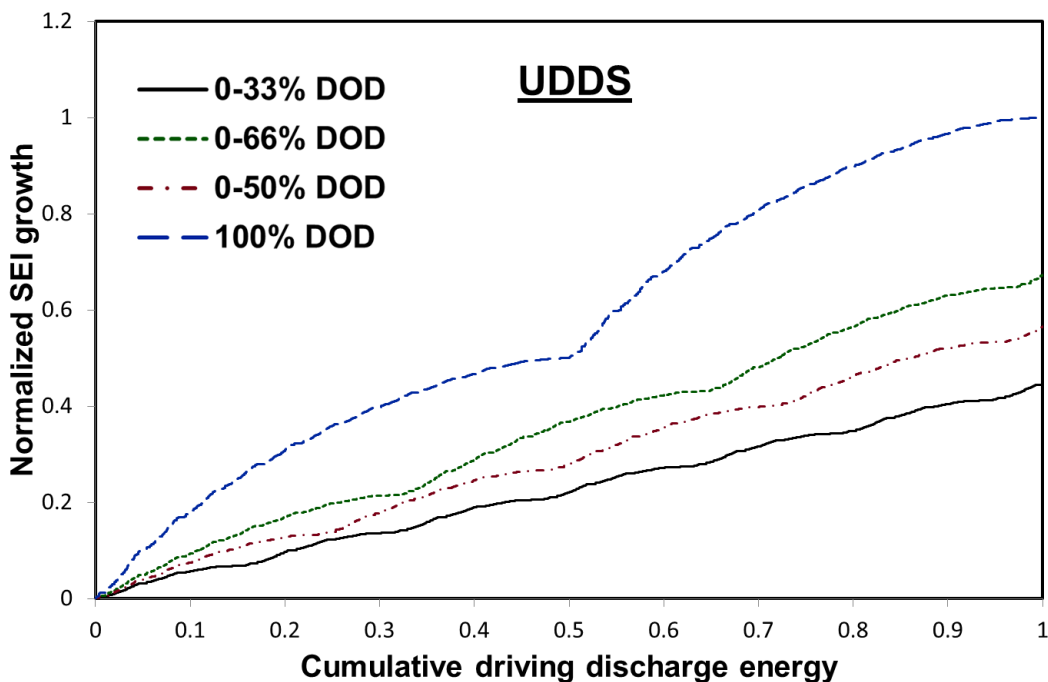


Figure 5-12: SEI growth over multiple driving cycles using the UDDS driving cycle for differing DOD. Only SEI growth during discharging is shown (no charging growth). The SEI growth is measured in comparison to the amount of discharged energy since more energy will be discharged during a deeper DOD (and we would expect more SEI layer growth). This method allows for comparison between cases even though they stored different amounts of energy during a single cycle. The discharge energy and SEI growth is scaled to the amount seen during two cycles of 100% DOD. For all cases discharge will end at 0% SOC.

Although operating the battery at lower SOC will reduce the SEI growth, it has several other undesirable affects. Along with increases in the current required to meet power requirements, low SOC operation does not utilize the full capacity of the battery. In most EV

cases, drivers will begin the day with a full charge at 100% SOC and therefore cycling beginning at low SOC level would not be commonly seen in EV usage.

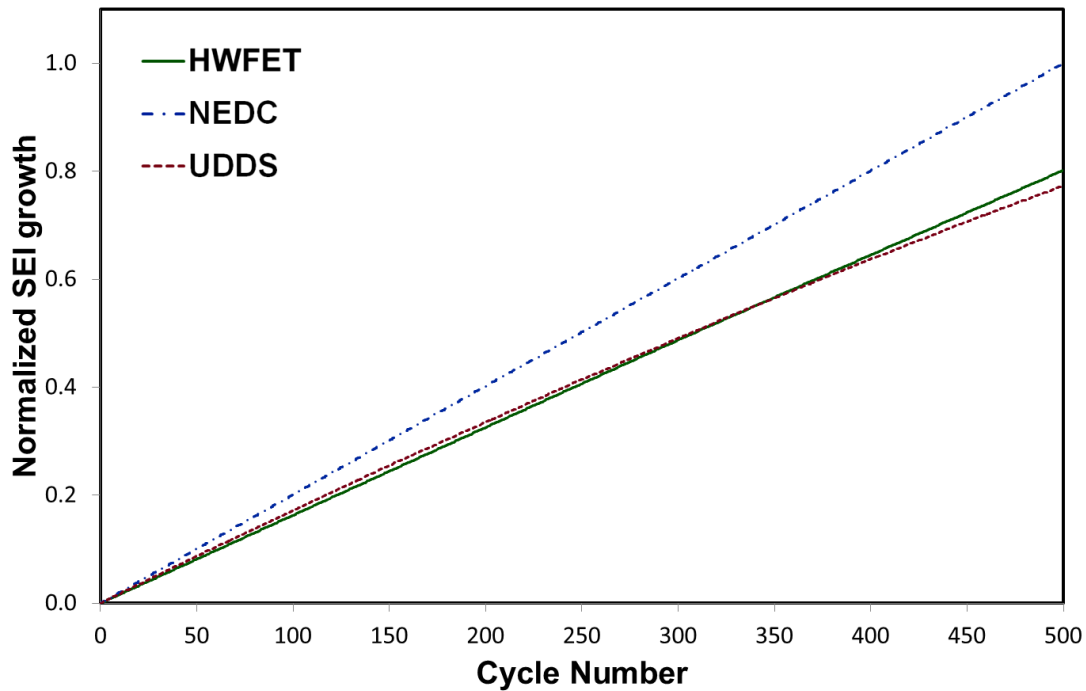


Figure 5-13: SEI growth over 500 charge-discharge cycles (100% DOD) for the HWFET, NEDC, and UDDS driving cycles. The SEI growth was scaled to the amount of growth from the NEDC case over 500 cycles in order to show a relative comparison among the driving cycles.

When studying the complete lifetime of the battery, simulations will need to include multiple years of driving cycles and run until the end of automotive life. These simulations must include hundreds to thousands of cycles. Although studying the end of life characteristics of batteries is beyond the scope of this chapter, Figure 5-13 shows the ability of the reformulated P2D model to approach these types of problems. Figure 5-13 shows the SEI layer growth for 500 charge/discharge cycles for the HWFET, NEDC, and UDDS driving cycles. These simulations required 6.54, 4.56, and 7.49 hours respectively to complete 500 cycles. Without using the reformulated model each of these cases would have required multiple days to weeks for running a single simulation. The use of the reformulated P2D model enhances the efficiency for solving stiff computational problems such as EV driving. Figure 5-13 also shows that continuing to drive

under the NEDC driving cycle will lead to more total SEI layer growth than driving under the HWFET or UDDS over 500 cycles.

5.6 Conclusions

Passive SEI layer growth is a major contributor to capacity fade in Li-ion batteries used for EV and PHEV applications. The majority of SEI layer growth will occur during charging. While fast charging creates undesired stress and temperature affects among other degradation problems, it will limit the amount of direct SEI layer growth in comparison to slow rates. Additionally, CC-CV charging will increase the amount of charge stored within a battery for a single cycle, but over the entire cycle life of the battery will decrease the total amount of usable energy from the battery for drive cycle cases.

The driving cycle will add to the SEI layer growth mainly during the regenerative braking portion of the drive cycles. For start and stop traffic, where most driving occurs at low speeds, the negative effect of SEI layer growth on cycle life exceeds the benefit of increased energy available to the driver during a single cycle. If regenerative braking is used in these cases, the total amount of usable energy over the life of the battery will decrease. For driving cycles that have higher, more constant speeds, and briefer (sharper) levels of deceleration, the SEI layer grows at a slower rate than the amount of energy added, which results in benefits over both a single cycle and the lifetime of the battery.

During daily cycling most EVs do not experience a 100% DOD of their batteries. Cycling at smaller DOD from 100% SOC will increase the amount of SEI growth per mile driven compared to 100% DOD cycling. However, cycling at small DOD at lower starting SOC (eg. starting at 50% SOC and cycling to 0% SOC for a 50% DOD) will decrease the amount of SEI layer growth when compared to 100% DOD mainly due to the lower battery potential during

cycling. While cycling at lower SOC may be beneficial for reducing SEI growth, it is not advisable for actual EV and PHEV use because it causes underutilization of the battery capacity over each cycle.

Chapter 6

Experimental Analysis of Capacity Fade

This chapter contains excerpts from the following journal article, reproduced here with permission from M.A.P.L.E. group:

Lawder, Matthew T. and Subramanian, Venkat R. “Extending Battery Life of LiFePO₄ Cells through Secondary Applications” *In review in the Journal of the Electrochemical Society*.

6.1 Value of LiFePO₄ cells

Applications using Li-ion batteries for power and energy demands continue to increase. With many of these new applications, predicting battery cycle life can be difficult because the life will be dependent on the charging and discharging protocols as well as the SOC window of operation for an application.¹⁹² While commercial cells are tested under galvanostatic cycling conditions to determine factory rated cycle life, an application’s constraints will often create varying cycling demands causing the actual cycle life to deviate from the factory rated cycle life. For batteries used under the same type of application, many cells experience very different cycling patterns. Batteries used for EVs will have a cycling pattern based on a consumer’s driving habits and a battery used for grid storage will experience a cycling pattern based on the localized needs of the grid.¹⁹³ With so much variation, a better understanding of capacity fade is required for more accurately predicting battery life within an application.

In this chapter, we focus on experimental cycling of Li-ion LiFePO₄ battery cells to examine capacity fade occurring for different cycling patterns. Additionally, protocols for altering cycling patterns to extend battery life are tested. Since first being realized as an advantageous cathode chemistry for batteries in the late 1990’s, LiFePO₄ cells have become popular for their stability and resistance to capacity fade.¹⁹⁴ While they operate at a slightly lower voltage than other Li-ion chemistries, reducing their energy density, LiFePO₄ cells have a very flat voltage curve during cycling and have shown low rates of degradation.³³ Degradation in

cells is caused by many different mechanisms but has been shown to vary based on cycling rate.^{31, 195-197} Higher rates generally lead to shorter battery life. Wang et al. experimentally showed that the cycle life of LiFePO₄ batteries is affected by the cycling rate.²⁹

One way to reduce the rate of capacity fade is to cycle the battery at a lower rate. In addition to measuring capacity fade, several experiments in this chapter focus on slowing the rate of capacity fade in the later portions of a battery's life by altering the cycling protocol of the battery to lower rates. The value of a battery over a single cycle depends on the available amount of energy to discharge and the value of that energy to an application. The cost of a single cycle will be dependent on the amount of degradation that occurs over a cycle and the total cell cost. By analyzing the ratio between benefit and cost, the value of any individual cycle within an application can be determined:

$$\text{Value Ratio} = \frac{(\text{Energy}_{\text{Discharged}})(\text{Value}_{\text{Application}})}{(\text{Degradation})(\text{Cost}_{\text{Battery}})} \quad (6.1)$$

Note that the units in the equation above will be [kWh] for Energy_{discharged}, [\$/kWh] for Value_{application}, [%] for Degradation (degradation will be calculated based on 100% degradation at end-of-life (EOL) conditions of 80% initial capacity), [\$] for Cost_{battery}. If the Value Ratio is greater than 1, the economic value of a cycle will outweigh the cost. For example, if a battery can discharge 10kWh for one cycle valued at \$0.50/kWh and degradation occurring during this cycle was 0.02% with a total battery cost of \$5,000, then the value ratio would be 5 and battery would create substantial value from that cycle. To have a battery be economically viable over its entire lifetime, the average Value Ratio for all of the cycles would need to be above 1.

Unfortunately, determining the exact amount of degradation occurring during a single cycle is not a straightforward task. Additionally, the amount of degradation per cycle will change

throughout a battery's life and the amount of energy discharged per cycle will be affected by degradation. The experiments in this chapter focus on better measuring the amount of degradation occurring over the life of the battery and testing methods for decreasing degradation later in life in order to increase the Value Ratio during later-in-life cycles, thereby increasing the total value of a battery during its lifetime.

6.2 Methods

6.2.1 Equipment

Two different battery testing systems were used to perform experimental cycle tests. The majority of the tests were performed by a 16-channel Arbin BT 2000. Additional tests were conducted using an 8-channel Maccor 4300. The batteries studied were LiFePO₄ 18650 cells (1.1Ah). While LiFePO₄ is classified as a Li-ion electrode, it has several differences from traditional LI-ion cells. LiFePO₄ cells operate at a lower voltage range (2.0V-3.6V) than many other Li-ion ion cells. Additionally, the intercalation process may behave differently for LiFePO₄ cells. While lithium ions will typically intercalate homogeneously throughout the cathodes of most Li-ion chemistries such as LiCoO₂, LiFePO₄ electrodes have shown intercalation occurring heterogeneously with lithium rich and lithium poor regions developing within the electrodes.¹⁹⁸ This heterogeneous intercalation will enhance certain capacity fade mechanism (such as those associated with particle stress), but LiFePO₄ batteries have shown great resilience even for high power applications leading some researchers to question if the difference in intercalation has much of an effect on capacity.¹⁹⁹ Another difference is the amount of lithium that can be extracted from different cathode chemistries during charging. LiCoO₂ can only stably extract half of the lithium from the cathode during charging, while LiFePO₄ can extract much more.²⁰⁰ The anode for the cells is graphite.

6.2.2 Procedure

For all tests, charging was conducted using a CC-CV protocol. The battery was charged at the specified rate until the voltage limit (3.6V) was reached at which point the current would be continuously reduced to maintain a constant voltage of 3.6V. The battery would continue to receive charge until the current dropped below 10% of the original charge rate. For all tests, discharging was conducted using a CC protocol. The battery was discharged at a specified rate until the voltage limit (2.0V) was reached.

A total of 21 cells were tested under a range of conditions. Seven cells were tested under control conditions, meaning that they experienced the same rate for both charging and discharging and were cycled at the same rate throughout their entire lifetime. Cycling rates for these cells varied between 1C and 4C. Table 6-1 provides more information about individual tests. Four cells were tested with different rates for charging and discharging. Tests 8 and 9 from Table 6-1 were charged at 1C and discharged at 4C, while tests 10 and 11 were charged at 4C and discharged at 1C. The rates remained the same throughout the entire test. Ten cells were tested by switching the cycling rate prior to EOL conditions being reached. Tests 12-16 were charged at either 4C or 3C for 2,000 cycles and then switched to rates between C/2 and 2C until EOL. Tests 17-21 were charged at either 4C or 3C until they began experiencing *accelerated fade* (See section 6.3.2) at which time they were switched to a 1C cycling rate. All tests were conducted at room temperature (23C).

Under most applications EOL refers to when the battery reach 80% of initial usable capacity. For this chapter some studies continued beyond EOL to examine fade later in the batteries life.

Table 6-1: Summary of Tests.

Test Number	Primary Cycling Rate		Secondary Cycling Rate	Test Type
	Charge Rate	Discharge Rate		
1	1C	1C	N/A	Control
2	1C	1C	N/A	Control
3	2C	2C	N/A	Control
4	2C	2C	N/A	Control
5	3C	3C	N/A	Control
6	4C	4C	N/A	Control
7	4C	4C	N/A	Control
8	4C	1C	N/A	Fast Charging
9	4C	1C	N/A	Fast Charging
10	1C	4C	N/A	Fast Discharging
11	1C	4C	N/A	Fast Discharging
12	4C	4C	2C	Secondary App after 2,000 cycles
13	4C	4C	1C	Secondary App after 2,000 cycles
14	3C	3C	2C	Secondary App after 2,000 cycles
15	3C	3C	1C	Secondary App after 2,000 cycles
16	3C	3C	C/2	Secondary App after 2,000 cycles
17	4C	4C	1C	Secondary App based on slope
18	4C	4C	1C	Secondary App based on slope
19	3C	3C	1C	Secondary App based on slope
20	3C	3C	1C	Secondary App based on slope
21	3C	3C	1C	Secondary App based on slope

6.3 Experimental Cycling Results

Although manufactures rate cycle life to be the same for all batteries of a single type, there will be variability among individual cell capacity even for cells manufactured within the same batch.^{201, 202} The variability will become enhanced as cells are cycled (even when cells are cycled under the same conditions) and can lead to large discrepancies in cycle life for equivalently rated cells operated under the same constraints. For the seven cells studied under 3C cycling conditions (Tests 5, 14-16, and 19-21), the initial capacity (as measured by the average Ah stored during charging of the first 25 cycles of the battery) ranged between 1.009Ah-1.032Ah with a standard deviation of 8.8mAh. In this chapter *capacity* will refer to Ah stored and *usable energy capacity* will refer to the amount of Wh discharged during a battery cycle. For the seven

cells studied under 3C cycling conditions, the initial usable energy capacity ranged between 3.139Wh-3.249Wh with a standard deviation of 0.038 Wh.

When the batteries are cycled, tracking the percentage of capacity fade in comparison to their initial capacity is more important than comparing their absolute capacity. For the first thousand cycles, the variation between the batteries grows, but is still relatively small with all the cells experiencing between 3.36%-4.85% capacity fade from their initial capacity. At 1,000 cycles the standard deviation of the capacity fade for the seven cells is 0.6%. However, as the cells age more, the variation in capacity fade increases. At 2,000 cycles, the capacity fade ranges from 7.50%-15.58% and the standard deviation increases to 2.7%. Figure 6-1 shows the capacity (compared to their initial capacity) for the seven cells cycled at a rate of 3C for 2,000 cycles along with the standard deviation of the set.

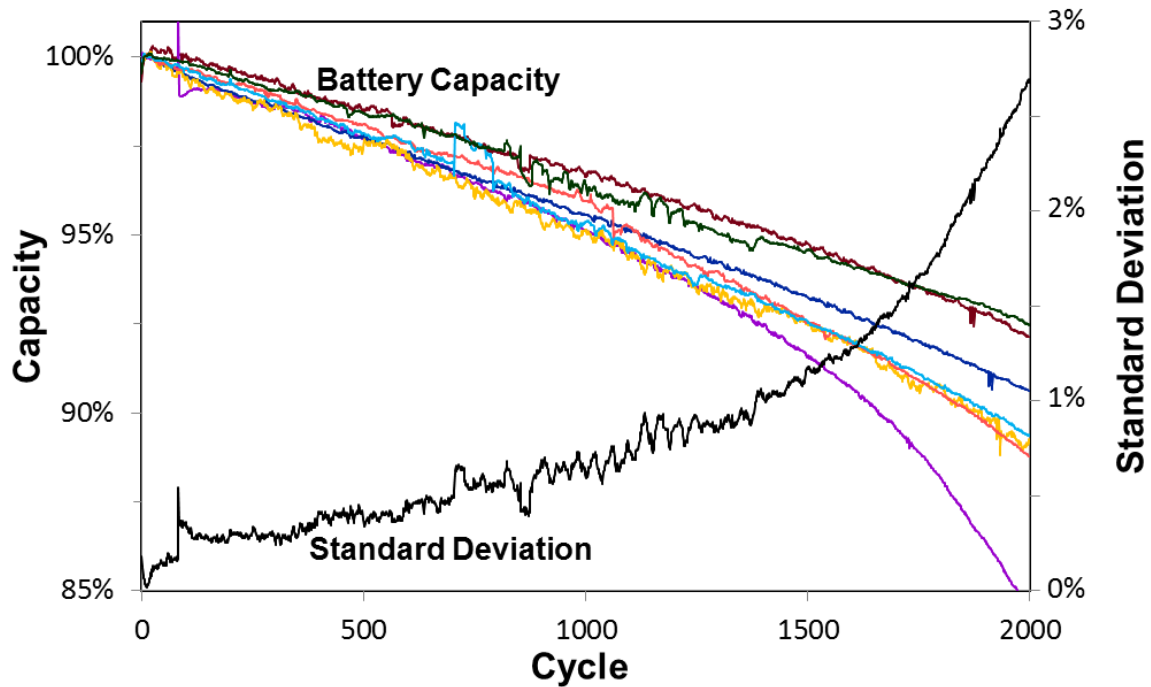


Figure 6-1: Variability of Capacity for cells cycled at 3C (Tests 5, 14-16, and 19-21).

The absolute initial capacity of a cell is a poor predictor of how it will experience fade showing almost no correlation to capacity fade. Figure 6-2 shows the R^2 values for the initial Ah capacity correlation to both absolute (Ah) and relative (percentage of initial) fade. The correlation between the absolute capacity fade and initial absolute capacity weakens with increasing cycles, so there is almost no correlation by EOL. The correlation between relative capacity fade and initial absolute capacity never exists. A better predictor of lifetime capacity fade is important to be able to prepare for battery replacement and cell balancing purposes later in life.

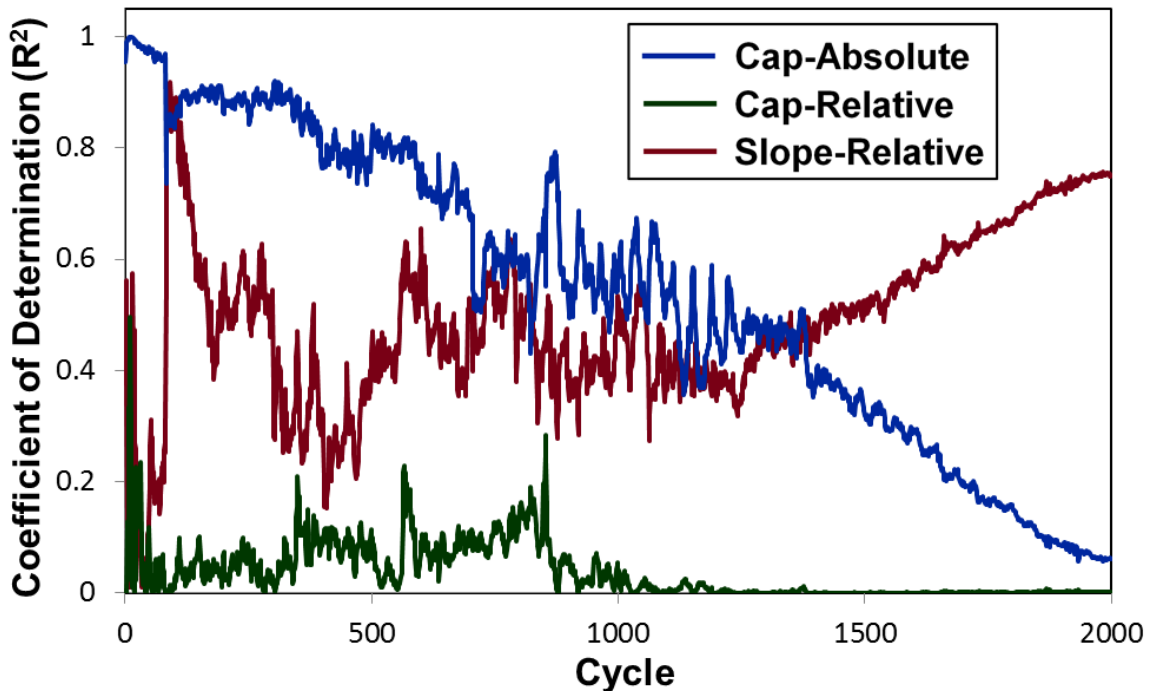


Figure 6-2: Correlation between the capacity fade and initial capacity or first 100 cycle slope.

The slope calculated from a cell's first 100 cycles (after the initial 25 cycles used to calculate initial capacity) was found to be a better indicator of remaining capacity after 2,000 cycles. The correlation between first 100 cycle slope and remaining capacity over 2,000 cycles is also shown in Figure 6-2. The correlation between these values strengthens as the cells move towards EOL. The cells that experience faster fade over their first 100 cycles are more likely to

reach their accelerate fade regime sooner and therefore this method helps to produce a more accurate life estimate early in a cell's life. Basically, the rate of capacity fade tends to only increase throughout life, so if a cell is degrading more than others early in its life, the cell is unlikely to slow that fade later in life. Note that the results for the correlation between initial capacity slope and remaining capacity only became statistically significant (<0.05 p-value) beyond 1,650 cycles. More cycling tests are required to increase the significance and verify these results.

6.3.1 Initial Fade Rate as a Function of Cycling Rate

While there will be variation in the capacity fade of cells cycled under the same constraints, the rate of cycling will have a greater effect on the capacity fade. Other studies have shown that for Li-ion batteries^{22, 203} and LiFePO₄ cells²⁹ in particular, prior to their accelerated fade regime (see section 6.3.2), capacity fade exhibits a power law relationship. However, our results show cells exhibiting linear or slightly accelerating fade.

In order to measure the rate of capacity fade occurring throughout the batteries life, the slope of the capacity fade curve was calculated at each cycle. Figure 6-3 shows the slope of the capacity curve for Test 6 which cycles at 4C. The instantaneous slope is calculated by measuring the linear fit over the previous 150 cycles and the following 150 cycles (therefore the instantaneous slope has a 150 cycle lag). The dashed line in Figure 6-3 represents when 80% of initial capacity was reached. After reaching this level of remaining capacity the cells will need to be replaced. The slope (and therefore the rate of capacity fade) remains mostly flat during the first 1,000 cycles of operation. After this time the slope begins to rapidly increase. This acceleration continues beyond EOL until plateauing once the battery reaches around 60% of initial capacity. The only time the slope decrease is when the remaining capacity reaches levels

approaching only 40% of remaining capacity well beyond what is considered the useful life of the battery.

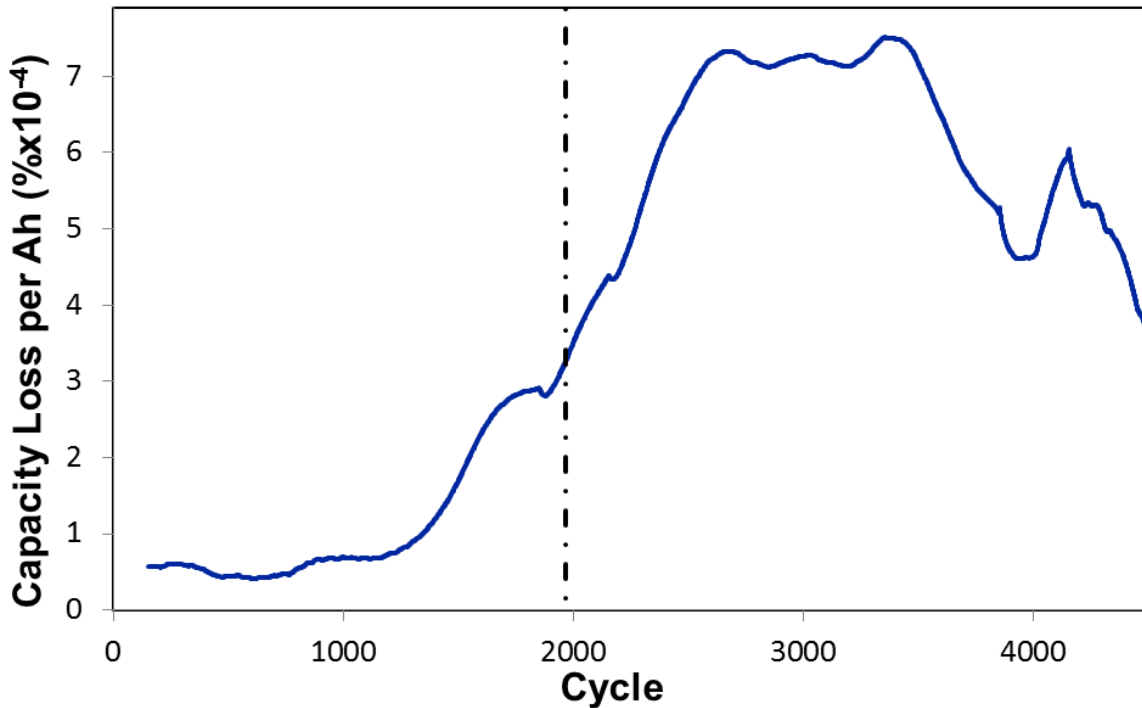


Figure 6-3: Capacity loss per cycle for Test 6.

Using our slope calculation method, the instantaneous slope was measured during the first 1,000 cycles of operation for all 17 tests that used the same charging and discharging rate during their first 1,000 cycles. The capacity fade rates fluctuated over the first thousand cycles, but they retained mostly flat or slightly accelerating trends for all the tests. The average slopes over the first thousand cycles were calculated for the 17 tests and are shown in Figure 6-4 as a function of their cycling rate. Figure 6-4 shows a strong correlation between increased cycling rate and increased capacity fade during the linear regime. Figure 6-5 shows the slope measurements for 4 tests each with a different cycling rate. These figures show that the higher cycling rate will lead to increased capacity fade beginning on the first cycle of operation.

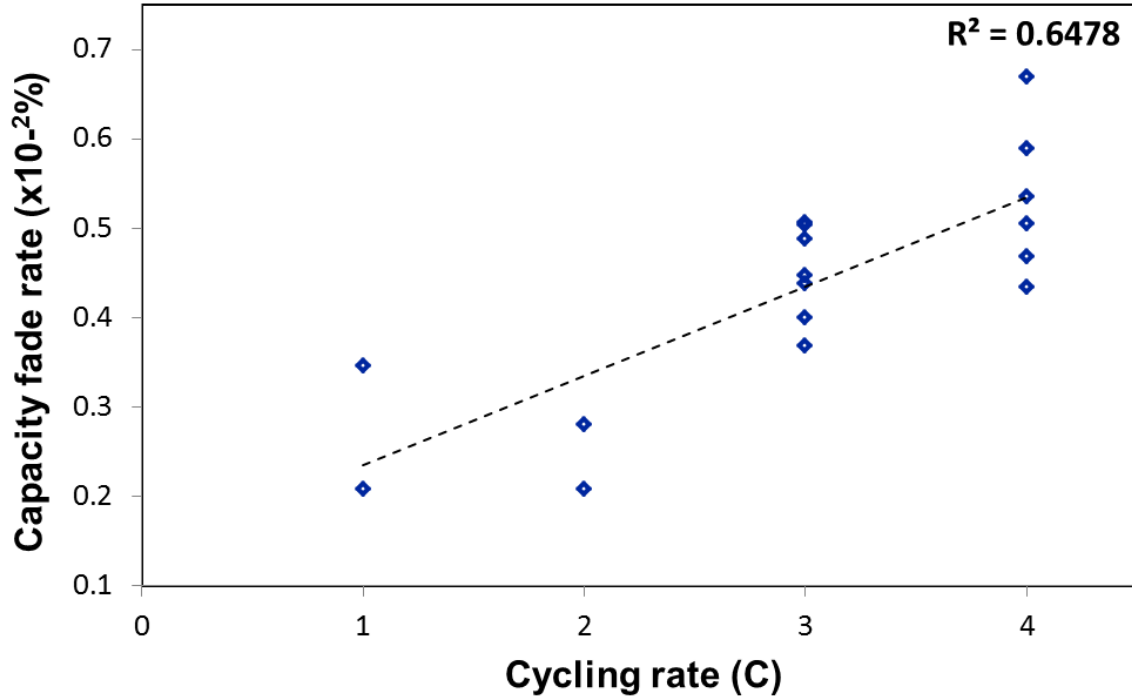


Figure 6-4: The average capacity fade per cycle for the first 1,000 cycles of operation for all tests as a function of cycling rate.

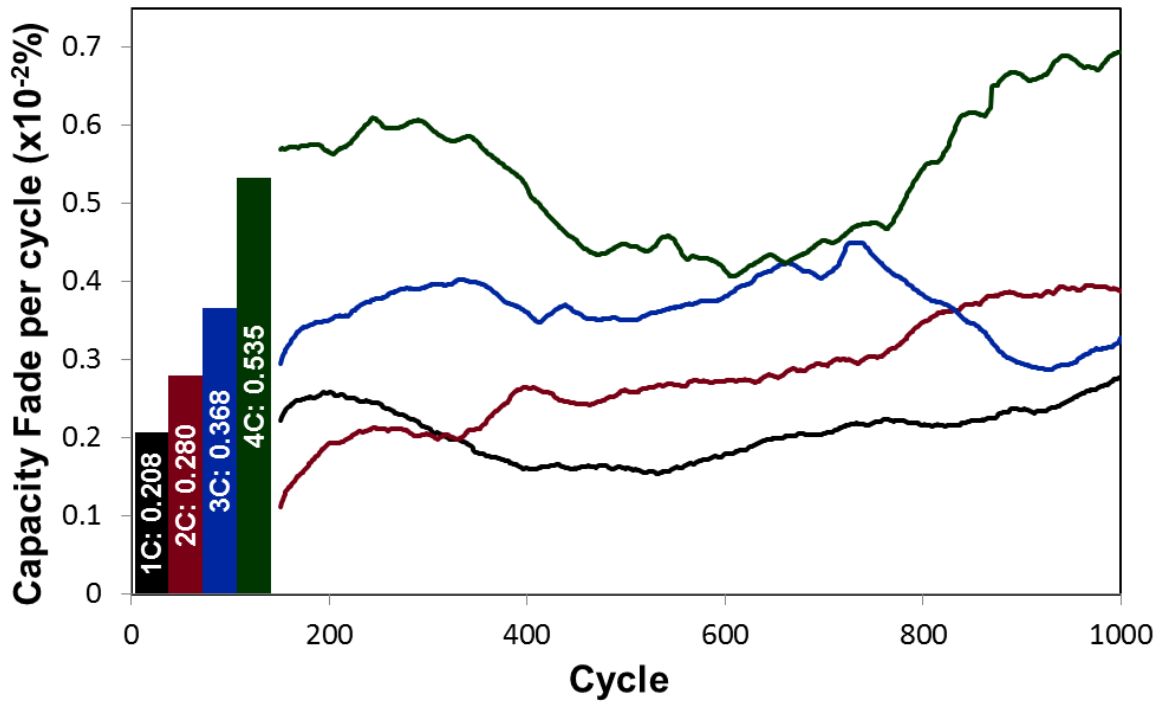


Figure 6-5: The capacity fade per cycle for the first 1,000 cycles for different rates (Test 2, 3, 5, and 6).

Additionally higher rate cycling will lead to accelerated fade beginning at a higher remaining capacity. The four tests cycling at 4C began accelerated fade (as described in Section 6.3.3) at an average remaining capacity of 91.4% while the four tests cycling at 3C began accelerated fade at an average remaining capacity of 88.6% and the two tests cycling at 2C began accelerated fade at an average remaining capacity of 83.4%. Ongoing tests of 1C will be studied to verify this trend.

6.3.2 Analyzing Fade Characteristics

Most studies of capacity fade are interested in the first 20% of capacity fade before traditional EOL occurs for a cell. Several studies of Li-ion batteries have shown a power law decrease in capacity fade occurring during early cycling.²⁰³⁻²⁰⁵ Wang et al. presented a capacity loss model based on a power law fitting of experimental data for LiFePO₄ cells.²⁹ While power law models could predict the measured capacity fade for small losses. The power law models failed to accurately measure capacity fade beyond the first few hundred cycles. The power law model assumes that the amount of capacity fade per Ah throughput decreases throughout the battery's life. Our results found the opposite to be true, specifically for high rate cycling. Decreases in the capacity fade stay mostly constant during early operation until reaching an inflection point where the capacity fade begins to increase with each Ah of capacity used. Only when the battery begins to reach very low levels of remaining capacity (well beyond the 80% EOL) does the battery experience a reduction in capacity lost per Ah of throughput.

Figure 6-6 shows the remaining battery capacity for cells cycled continuously at the same rate (1C-4C). The shape of the capacity curve at each rate is similar, with the batteries experiencing a steady rate of declining capacity during early cycling and then entering a phase where capacity fade rapidly accelerates. The initial rate of fade and the point at which the

acceleration in fade begins will vary depending on the rate of cycling (see Section 6.3.1). Smith et al. shows data that exhibits the same “knee joint” where fade accelerates rapidly.²⁰⁶ Cell capacity data extended from the original Wang et al. study is shown in Smith et al. to also exhibit the accelerated fade regime. Smith et al. proposes that the cell experiences power law fade until reaching the knee joint and then additional mechanisms such as stress related site loss begin to greatly contribute to capacity fade causing a rapid shift in the rate of capacity fade. Zhang and White proposed a model for LiNiCoO₂ cells that showed an accelerated regime of fade caused by a shift in the limiting electrode from the anode to cathode.²⁰⁷ Spotnitz showed that accelerated fade occurred late in a batteries life, but that this region often occurred after 80% EOL had been reached and therefore was not often reported on in literature.³⁴ However, with improvements in overall battery life, many batteries will reach the accelerated fade regime before EOL. Therefore better understanding of the accelerated fade regime is important for extending battery life later in life especially for batteries experiencing high rates (>1C).

The cycle life is affected greatly by when the accelerated fade begins. Table 2 shows characteristics for the control batteries (2C-4C) before and after accelerated fade begins to occur. The beginning of the accelerated fade regime is defined as when the instantaneous capacity fade (as defined by the slope) reaches 0.01% per cycle and EOL is 80% of initial capacity. For the Test 6 shown in Figure 6-3, the cell experienced 1,344 cycles before reaching the accelerated fade regime at which point it had lost 7.60% of its initial capacity. The cell lasted another 622 cycles before reaching EOL. The rate of capacity loss after the knee joint was 3.5 times the rate of capacity fade loss before the knee joint. The cost of continuing to cycle the cell under the same constraints greatly increases after the accelerated fade begins because each cycle will do a much greater amount of damage to the battery. If the amount of fade increases enough the cost of

using the battery in the application may outweigh the benefits of using the battery for some other purpose. Finding a different application where the remaining capacity would provide a better Value Ratio may be preferable to continuing to operate the cell under the same conditions.

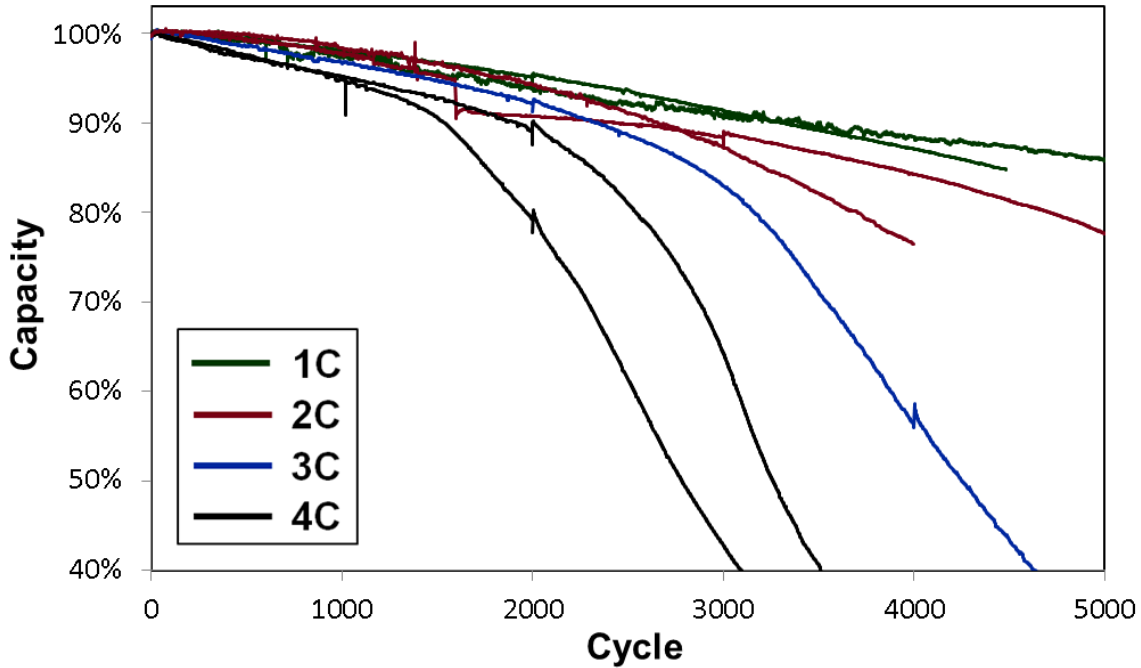


Figure 6-6: The Capacity fade for all control cycles. (Tests 1-7).

Table 6-2: Characteristics of capacity fade before (pre-) and in accelerated fade regime. Test 1-4 currently under continued cycling to verify the result.

Test #	Cycle Rate	Cycles Pre-Accel	Fade Pre-Accel	Cycles in Accel	Fade in Accel	Ratio of Fade
4	2C	2956	12.28%	760	7.72%	2.45
5	3C	2576	11.94%	585	8.06%	2.97
6	4C	1344	7.60%	622	12.40%	3.52
7	4C	2002	9.86%	539	10.14%	3.82

6.3.3 Extending Battery Life through Secondary Applications

Two sets of battery cycling studies focused on trying to increase the value of the battery once accelerated fade has begun by changing the cycling rate for the cell. Altering the cycling rate (in effect removing the cell from its primary application and moving into a secondary

application) can change the rate at which capacity fade is occurring and extend the total energy throughput of the cell before EOL.

The first test assumed that no real-time monitoring of the battery would be available for informing when to switch applications in the cell. Therefore, cells were cycled for a prescribed number of cycles (2,000) before being removed from their primary application and switched into a secondary operation. In Tests 12 and 13, cells were cycled for 2,000 cycles at a 4C rate. After 2,000 cycles, one cell (Test 13) was switched to 1C cycling and the other (Test 12) to 2C cycling. In Tests 14-16, cells were cycled for 2,000 cycles at a 3C rate. After 2,000 cycles, one cell (Test 14) switched to 2C cycling, one cell (Test 15) was switched to 1C cycling and one cell (Test 16) was switched to C/2 cycling.

After 2,000 cycles none of the cells had reached EOL, but the 4C cells were already beginning to experience accelerated fade and two of the 3C cells showed slight signs (approaching 0.01% fade per cycle) of entering the accelerate fade regime. By changing the cycling rate, we were able to arrest the fade and obtain more energy throughput for the battery before reaching EOL conditions. An empirical fade model was used to simulate what the capacity fade data would be if the cells had continued being cycled at 4C. The experimental data was compared to the simulated data to measure how much additional energy the cells were able to store because of the altered cycling conditions.

For the empirical model, the slope during the first two thousand cycles was calculated in the same manner shown in Figure 6-3. From the slope values an exponential curve was fit from cycles 1700-1850 (because the slope calculation uses 150 cycles of both sides of a point, cycle 1,850 is the last usable slope value). The model follows the empirical equation:

$$Slope_{sim} = Slope_{1700} \exp\left(A\left(N_{cycle} - 1700\right)\right) \quad (6.2)$$

where $Slope_{1700}$ is the calculated slope value from cycle 1,700 and N_{cycle} is the cycle number. The A coefficient is calculated so that the sum of the squared error between the simulated slope and the experimental slope from cycles 1,700-1,850 is minimized.

The exponential slope model fits well for cells that have begun to experience accelerated fade. To calculate the simulated capacity beyond 2,000 cycles, the simulated slope values were used to subtract capacity until EOL. For cells in the earliest stages of accelerated fade, the model slightly underestimated the slope values simulating slower capacity fade than the experimental controls. Therefore the simulated results are considered the best case results for battery lifetime if the cells continue to be cycled in their primary applications. Figure 6-7 shows the experimental slope values along with the simulated values for Tests 12 and 13. Figure 6-8 shows the experimental remaining capacity and the simulated remaining capacity for the same two tests. Not only will the slope of the capacity fade for a cell decrease when the application is switched, but also the absolute capacity may show a slight increase because the slower charging rate will allow for more storage before reaching charging cut-off (See Section 6.4.1).

In Figure 6-8, a qualitative measure of a cell's lifetime utility can be seen by the size of the area under its capacity fade curve. A larger area under the curve will represent greater Ah throughput during a battery's lifetime. Table 6-3 shows the increase in the Ah throughput for switching applications when compared to the simulated data at EOL. In Test 12, the cell switched to 2C rate after 2,000 cycles added 27.6% more Ah to its life than if the cell had remained at a 4C rate. Results for Tests 12-16 are shown in Table 3. For Test 16, the cell did not exhibit accelerated fade (or approaching accelerated fade) by 2,000 cycles and therefore the simulated capacity used a constant slope consistent with cycles 1,700-1,850.

Because of the variability of cells, monitoring the battery throughout cycling and switching cycling conditions at the first sign of accelerated fade can be more effective than using an arbitrary cycle cutoff. Tests 17-21 were conducted where the slope of the cell capacity was monitored continuously to allow for an accurate measure of the rate of capacity fade. When the rate of capacity fade reached 0.01% per cycle the cell was deemed to be in the accelerated fade regime and was switched to a different cycling rate.

The rate of capacity fade prior to the accelerated regime is a function of cycling rate (see section 6.3.2), but will show variability even between cells cycled under the same conditions. For example the six tests cycled at 4C experienced between $4.68 \times 10^{-3}\%$ and $5.89 \times 10^{-3}\%$ fade per cycle over their first 1,000 cycles (all prior to the accelerated regime). Because of cell variability, the cycle number at which accelerated fade begins to occur will vary. The capacity fade is also affected by the cycling rate, so different rates will reach the accelerate regime at different time. The monitoring and switch method allows for each cell to be switched when accelerated fade begins rather than at an arbitrary cycle number.

Tests 17-21 all monitored capacity fade by calculating the slope for each cycle. During their first 1,000 cycles, the slope showed some variation within each cell, but the average capacity fade rates were $4.38 \times 10^{-3}\%$, $5.06 \times 10^{-3}\%$, and $4.00 \times 10^{-3}\%$ for the 3C cells and $4.34 \times 10^{-3}\%$ and $6.69 \times 10^{-3}\%$ for the 4C cells. Once 0.01% fade per cycle was measured, the cells were switched to 1C cycling (Test 17 waited until $1.25 \times 10^{-2}\%$ fade was reached before switching rates). To simulate continued use under primary cycling conditions, an empirical exponential fit of the previous 100 cycles was used. Only 100 cycles were used instead of 150 because the cells had only just begun to enter the accelerated regime. The additional energy gained for switching cycling rates is shown in Table 6-3.

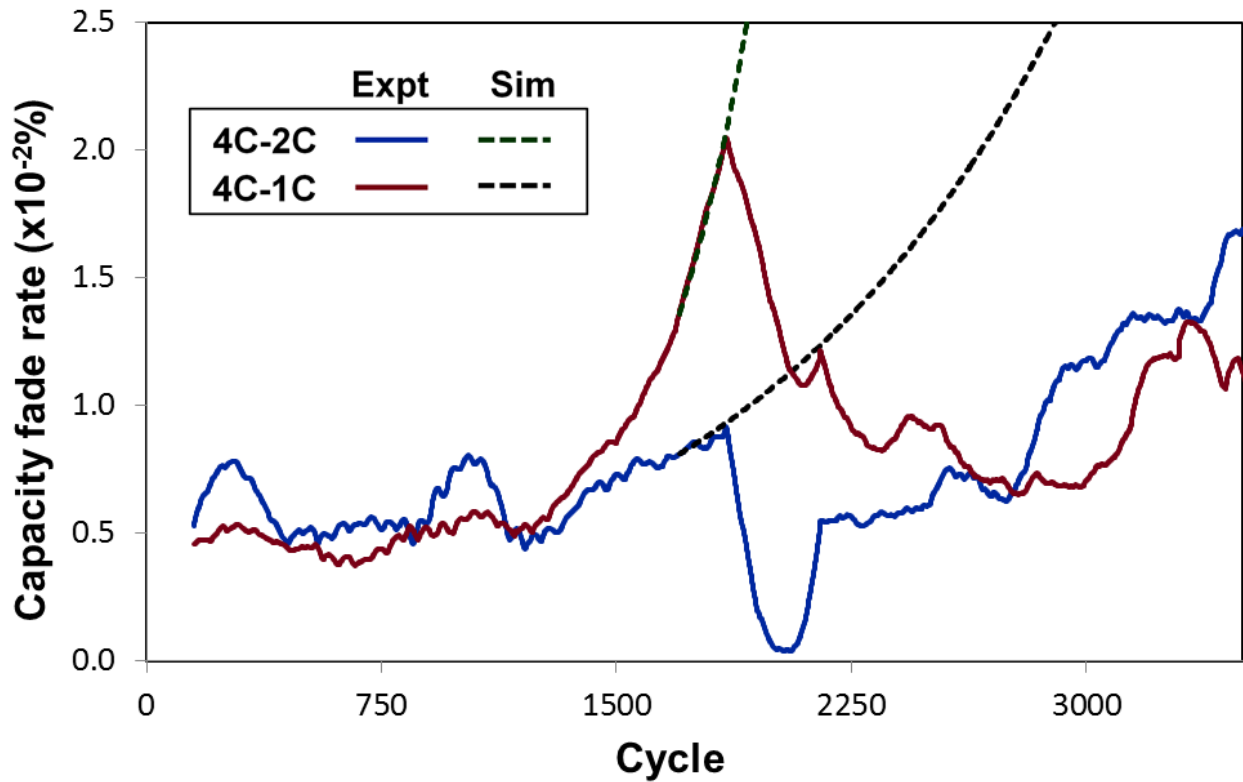


Figure 6-7: Simulated and Experimental capacity fade rates for tests 12 and 13.

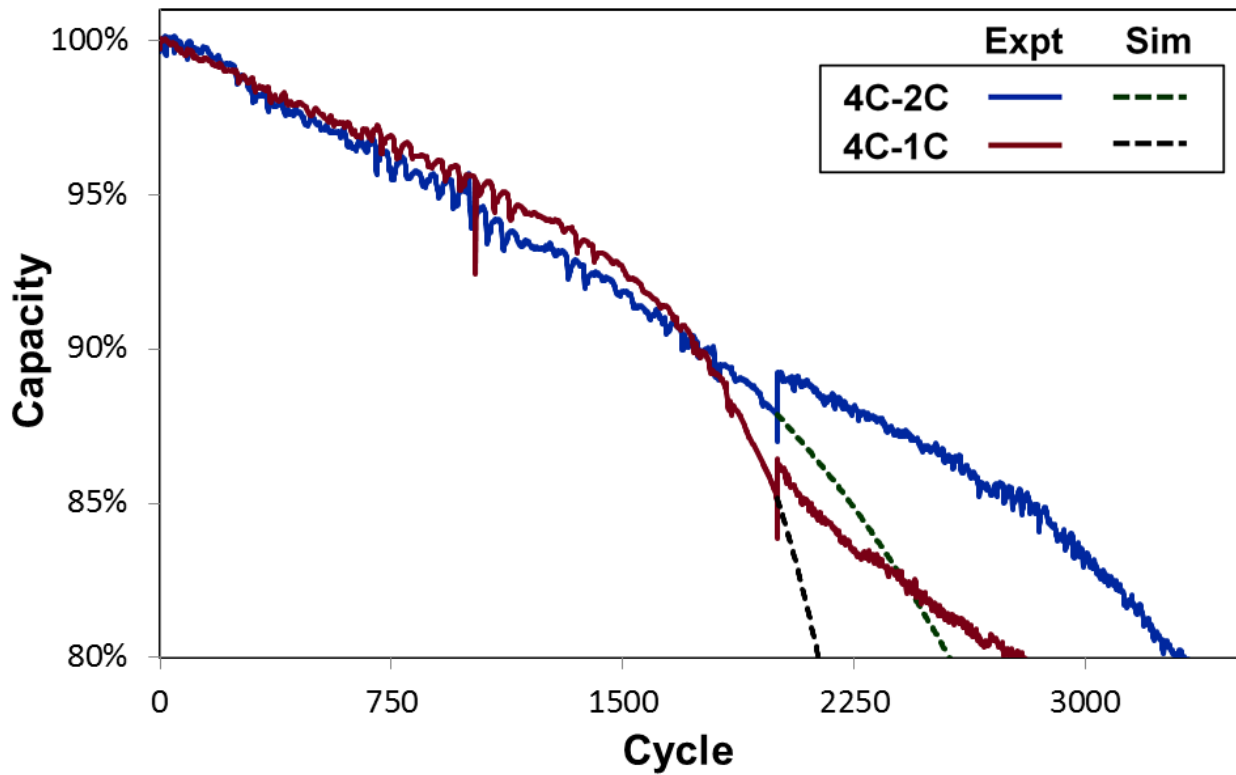


Figure 6-8: Simulated and Experimental Capacity for tests 12 and 13.

Table 6-3: Lifetime Energy added by switching application.

Primary Cycling Rate	Cycles in Primary Rate	Secondary Cycling Rate	Energy Gained from App. Switch	% Increase in Storable Energy
4C	2000	2C	667.8Ah	27.6%
4C	2000	1C	545.9Ah	27.2%
3C	2000	2C	203.3Ah	10.0%
3C	2000	1C	1143.3Ah	39.6%
3C	2000	C/2	1630.7Ah	53.8%
4C	2089*	1C	724.9Ah	31.8%
4C	1393	1C	563.1Ah	30.7%
3C	2148	1C	837.3Ah	36.8%
3C	2273	1C	1051.1Ah	45.3%
3C	2899	1C	845.8Ah	26.8%

6.3.4 Effect of Charge and Discharge on Capacity Fade

The overall capacity fade rate has been shown to increase with cycling rate. For Tests 1-7 and 12-21 the rate remained the same for both charging and discharging. Other studies of Li-ion chemistries have shown that individually, higher charging¹⁹⁵ or discharging²³ rates will also lead to increased capacity fade. To help quantify the relative degradation of faster charging and faster discharging, four more tests were conducted. In Tests 8 and 9, cells were charged at a 4C rate and discharged at a 1C rate and in Tests 10 and 11, cells were charged at a 1C rate and discharged at a 4C rate. Tests 1, 2, 6, and 7 were used as controls for this study. Our hypothesis that the capacity fade from the new test cells would fall between the capacity fade for the 1C and 4C control tests was proven wrong. Figure 6-9 shows the remaining capacity for the four experimental cells and the four control cells.

All of Tests 8-11 (those that experienced fast charging only or fast discharging only) exhibited much quicker capacity fade than the control cells. Cells from Tests 8 and 9 faded extremely quickly reaching EOL after only 284 and 373 cycles respectively. The cells from Tests 10 and 11 fared better reaching EOL at 1,064 and 1,103 cycles respectively. This fade was much faster than for both 4C and 1C control cycling.

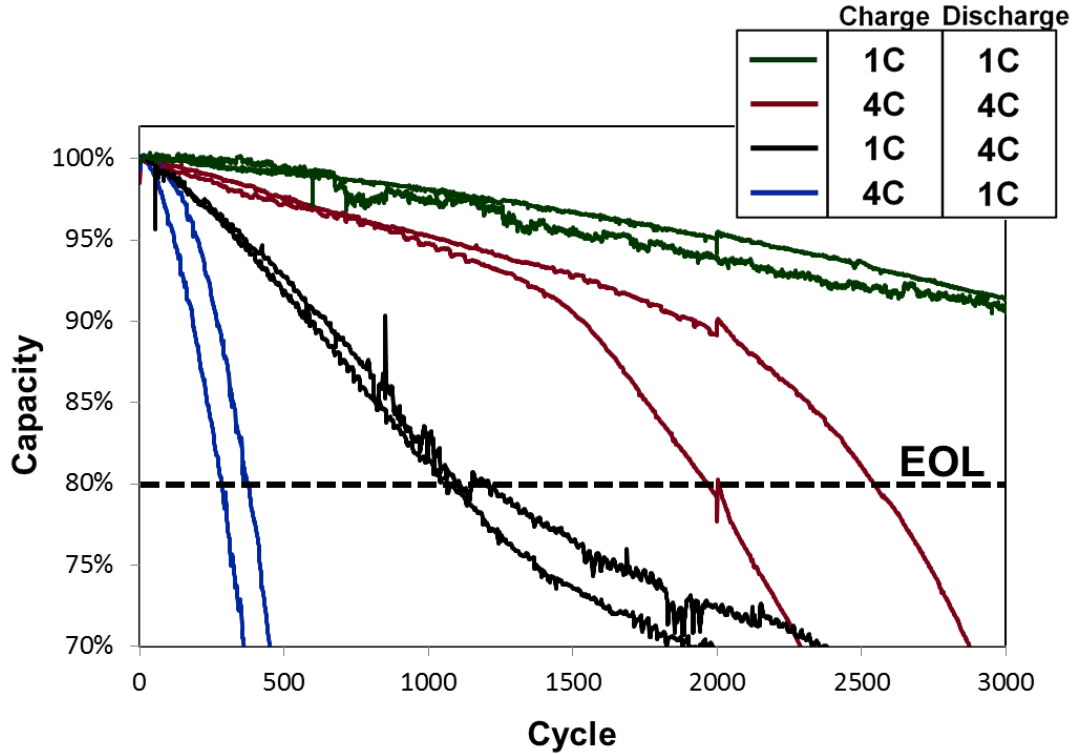


Figure 6-9: Capacity for Tests 1, 2, and 6-11.

6.4 Discussion

The internal resistance (R_{int}) is increasing much faster in Tests 8 and 9 than any of the other cycling tests. The internal resistance can be measured by studying the voltage curves of the cells. Operating voltage will be based on the open circuit voltage (V_{OC}) of the system, applied current and internal resistance shown in Ohm's law as²³:

$$V = V_{OC} - I_{app} R_{int} \quad (6.3)$$

The V_{OC} curve should not be affected by capacity fade, so if the applied current remains the same during cycling, changes in the operating voltage can be attributed to increased internal resistance. Figure 6-10 and 6-11 show the voltage discharge curves over the first 500 cycles for Test 9 and Test 11, respectively. For Test 9 and Test 11 the operating voltage decreases as the cycles increase and the discharging time becomes much shorter. The trend is more pronounced in

Test 9 which experiences faster capacity fade. An increased internal resistance can be caused by many different factors and does not show the cause for capacity fade.

Lui et al. showed that most degradation within LiFePO_4 cells occurs at the anode and often involves irreversibly removing active lithium and physical degradation of graphite.²⁰⁸ Models for LiFePO_4 capacity fade were developed by Deshpande et al. that focus on modeling the removal of active lithium through SEI film growth.²⁰⁹ Diffusion induced stress and electrode cracking are also cited as major reasons for capacity fade. Assuming most degradation is occurring at the anode, Tests 8-11 reveal that high rate intercalation of lithium into the anode does more damage to the battery than high rate deintercalation. However, the fact that both Tests 8 and 9 as well as Tests 10 and 11 show much more degradation than the 4C control tests shows that the discrepancy between the charging and discharging rates is also a major cause of degradation.

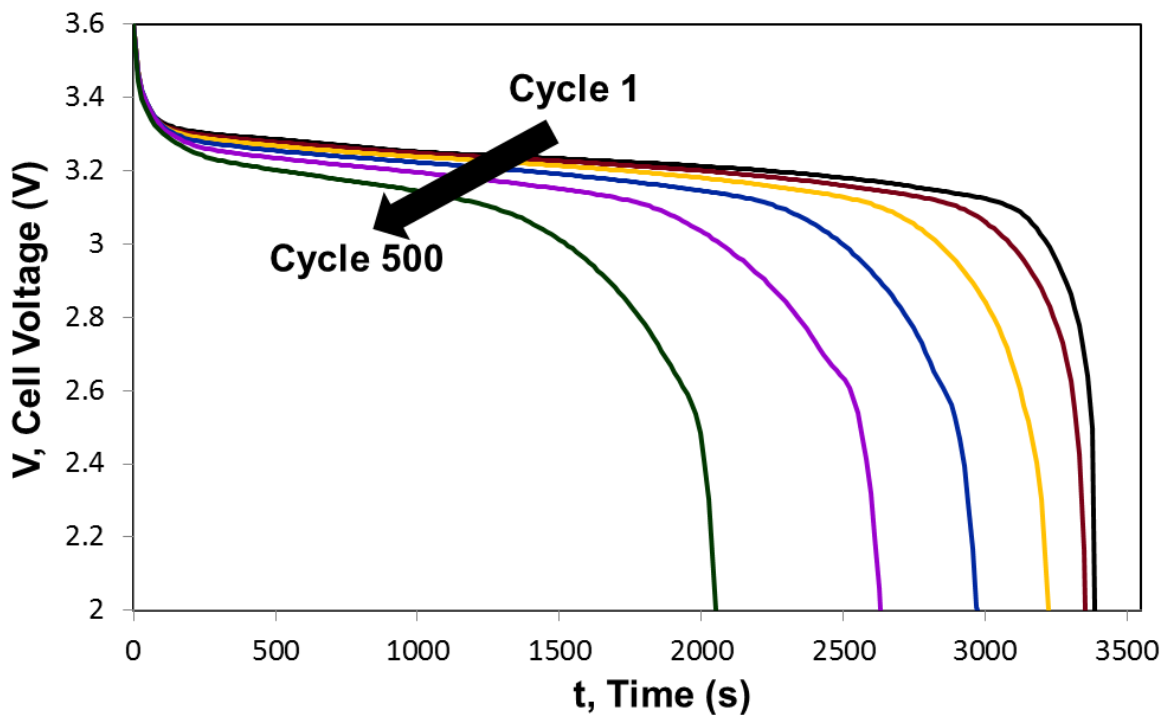


Figure 6-10: Voltage discharge curves for first 500 cycles of test 9.

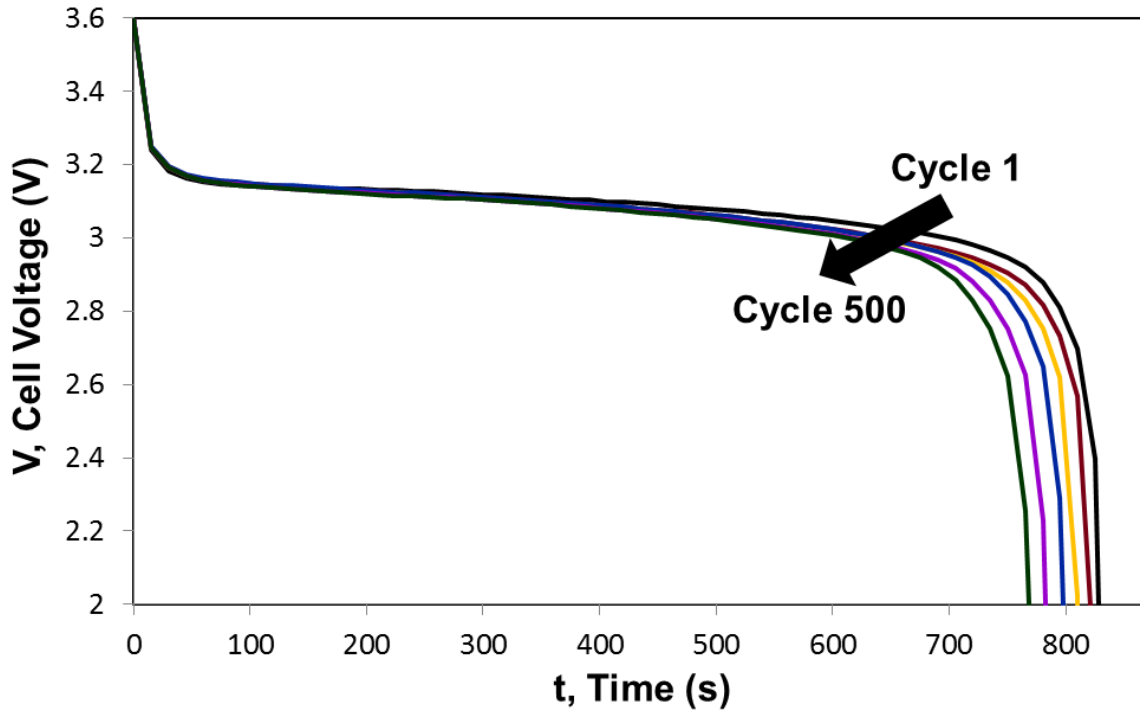


Figure 6-11: Voltage discharge curves for first 500 cycles of test 11.

6.4.1 Energy Capacity Increases through Application Switching

While the charging pattern cannot reverse internal resistance buildup in the battery, lowering the cycling current can actually increase the usable energy capacity of the battery later in life. The amount of physically storable charge will remain the same when switching applications, but because the applied current will be lower the internal resistance will have less of an effect on the voltage deviation from the open circuit voltage (see Eq. (6.3)). When discharging at a lower applied current, the operating voltage will be higher which leads to an increase in energy discharged per cycle.

Figure 6-12 shows the voltage discharge curves from Test 16 at cycle 1,990 when discharge is occurring at 3C and at cycle 2,010 when discharge is occurring at C/2. Before the switch the charge capacity for the 3C cycling is 0.915Ah and after switching to C/2 charging the charge capacity is only 0.884Ah. But the energy discharged from the cell goes from 2.89Wh at 3C discharge to 3.13Wh at C/2 discharge, an increase of 8.5%. All values were averaged over ten

cycles before or after the switch. In Figure 6-12 the C/2 discharge curve remains at a much higher voltage throughout which leads to overall more energy discharged from the system. Table 6-4 shows the values of energy discharged per cycle before and after switching applications.

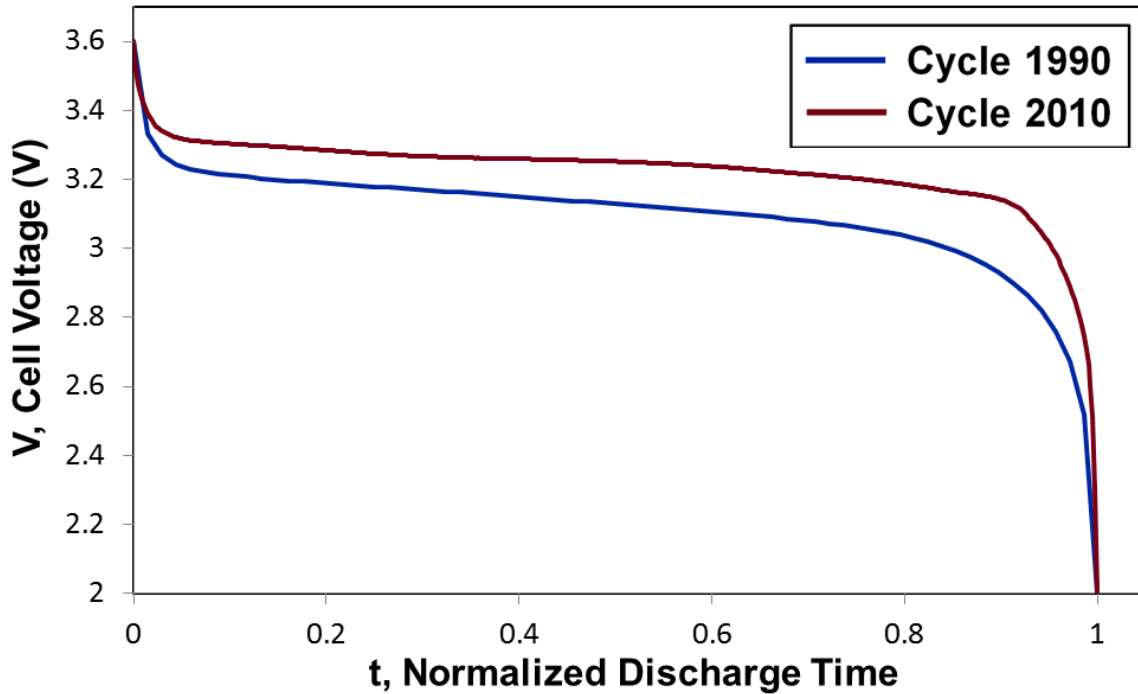


Figure 6-12: Voltage curve before and after switch.

Table 6-4: Summary of increase in discharged energy after switching applications.

Primary Cycle Rate	Secondary Cycle Rate	Switch Cycle	Discharge Energy pre-switch	Discharge Energy post-switch	Percentage Increase
4C	2C	2000	2.764	2.888	4.49%
4C	1C	2000	2.624	2.784	6.11%
4C	1C	2090	2.696	2.838	5.27%
4C	1C	1394	2.679	2.979	11.20%
3C	2C	2000	2.673	2.727	2.01%
3C	1C	2000	2.890	2.989	3.43%
3C	1C	2148	2.710	2.812	3.76%
3C	1C	2273	2.754	2.857	3.75%
3C	1C	2899	2.684	2.777	3.44%
3C	C/2	2000	2.887	3.132	8.50%

6.4.2 Added Lifetime Value

An extension of battery life has been shown in Section 6-3, but the ultimate value of the battery depends on the application in which it is being used. If the secondary application places a

low economic value on the energy storage then extending a battery's life through a secondary application may not make economic sense. In order to show how the economic value of a battery application will affect the determination of continuing in a primary application or switching to a secondary application, sample application values are chosen for a case study.

Assuming a battery cost of \$800/kWh (about \$3 for a single 1.1Ah 18650 cell) and primary storage value of \$0.40/kWh, the Value Ratio for Test 6 is shown in Figure 6-13. The average Value Ratio during the life of the battery is 1.17 meaning that the battery produced a value at just over the cost during its lifetime (\$3.25 value versus \$2.88 cost) and therefore was a good economic decision. However, the highest Value Ratios occur early in cycling and will begin to decrease as the battery ages, especially after accelerated fade begins. Switching applications can help to increase the average value ratio. But the secondary application's value of energy storage will also affect the Value Ratio.

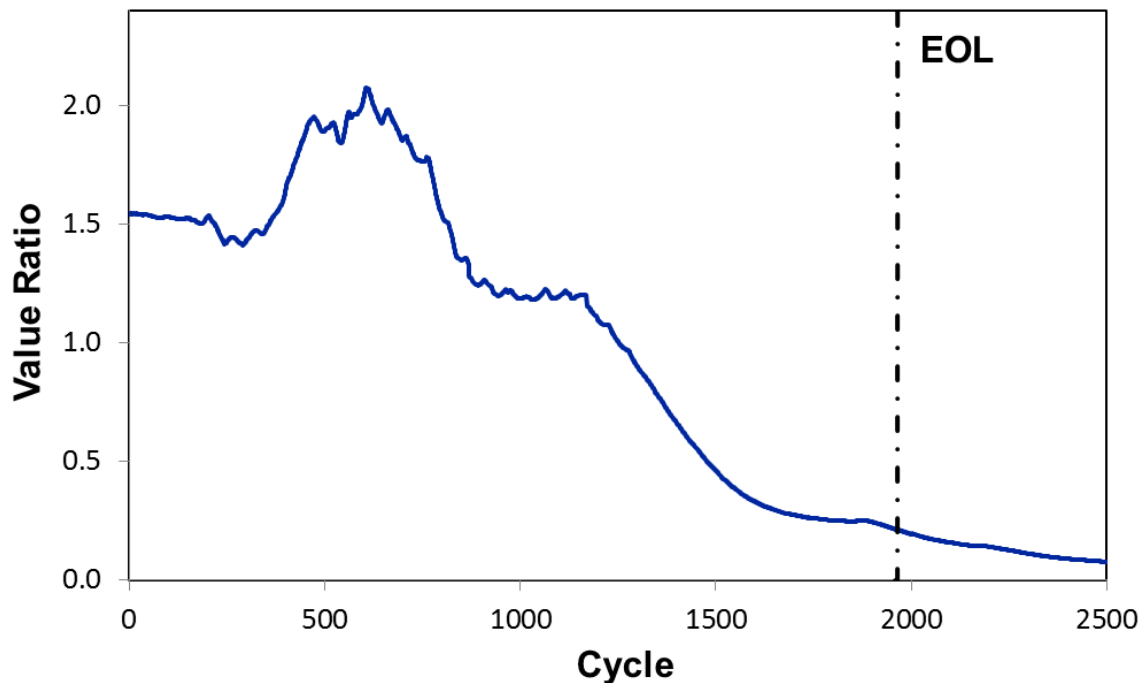


Figure 6-13: Value Ratio for Test 6.

Consider again a battery cost of \$800/kWh and a primary storage value of \$0.40/kWh for Test 12. During the first 2,000 cycles (4C) the average Value Ratio is 1.33 (see Figure 6-14). At this point Test 12 switches to its secondary cycle protocol (2C). Using the simulated data (see Section 6.3.3), a prediction can be made for what the Value Ratio would be if the battery remained in its primary application. After 2,000 cycles, if the battery remained under the primary cycling rate the average Value Ratio until the EOL would be 0.54 and EOL would be reached at cycle 2,558. If the battery is switched into a secondary application with a storage value of \$0.25/kWh the average Value Ratio from cycle 2,000 to cycle 2,558 would be 0.88 (see Figure 6-14).

Comparing the two cases, switching the battery into a secondary application offered less economic value between cycles 2,000-2,558 (\$0.40 versus \$0.59) because of the lower value of storage, but it produced much less capacity fade thereby boosting its value ratio. While the cell that remained in the primary cycling rate reached EOL at 2,558, the cell that switched to a secondary application did not reach EOL until cycle 3,314. The lifetime cost of the battery was the same at \$2.88, but the value accumulated was \$2.98 for the cell that continued its primary rate and \$3.09 for the cell switched to a secondary application, a 3.7% increase in value. Note that ultimate lifetime value produced is very sensitive to the storage value and the cycling protocol of the battery in the secondary application. Figure 6-14 shows the Value Ratio for three different storage values in the secondary application. When a suitable application with high enough storage value and a lower charging rate can be found, switching applications for the battery will be beneficial to both the battery life and system economics. Note that the cost of physically moving the battery between systems is not considered here. An example of a possible switching application would be moving used electric car batteries into stationary grid storage

before the cells have reached EOL. For the EV battery owner, selling the battery with life remaining and purchasing a new battery may be more beneficial economically than continuing to use the battery at low levels of life.

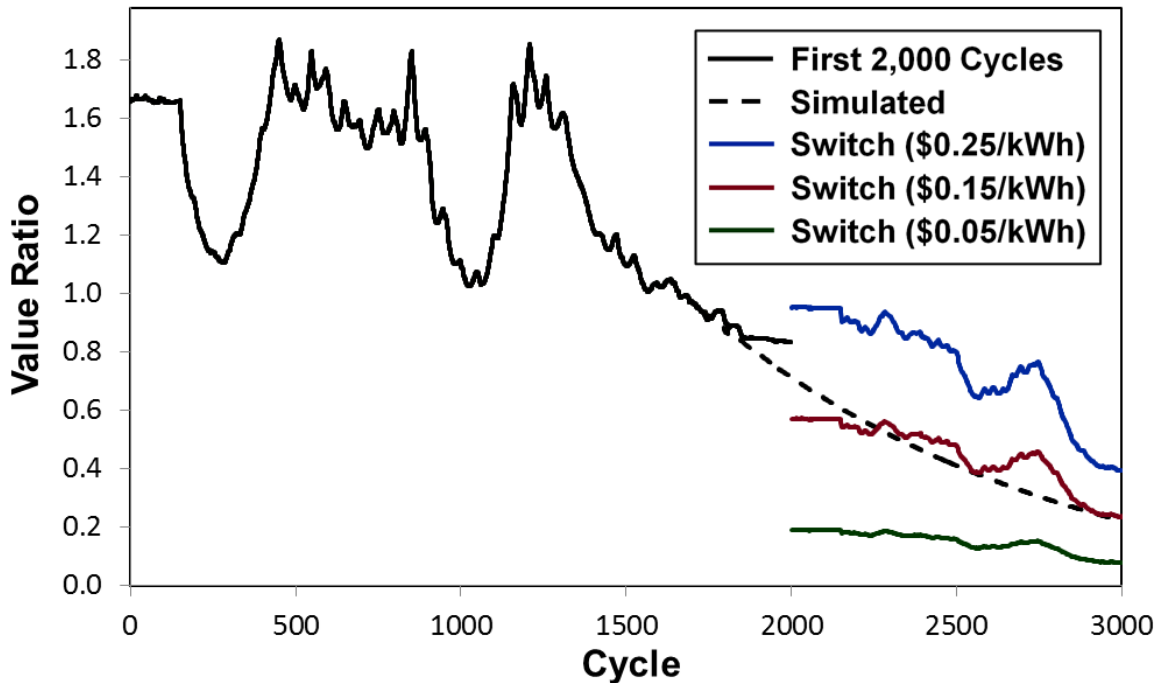


Figure 6-14: Value Ratio for Test 12 (Primary storage value of \$0.40/kWh and Battery cost of \$800/kWh) with three different secondary storage values (\$0.25/kWh, \$0.15/kWh, and \$0.05/kWh) as well as the value ratio for the cell simulated remaining in primary storage (\$0.40/kWh).

6.5 Conclusions

Through experimental cycling of LiFePO_4 cells, the capacity fade was analyzed at different cycling rates. The cells experienced linear fade until reaching an inflection point where they will begin to see accelerated fade. The rate of linear fade will be dependent on the rate of cycling. However, even for similarly rated cells that undergo the same cycling patterns, there will be significant variation in the amount of fade they experience and when they transition into the accelerated fade regime.

The onset of accelerated fade is the deciding factor in determining EOL for a cell. This onset can be prolonged by altering the cycling conditions of the battery. By reducing the cycling

rate for a cell, the increase in the rate of capacity fade can be slowed or even temporarily reversed allowing for an increase in lifetime energy throughput for the cell. By moving the battery to a secondary cycling pattern, we showed that cells originally cycling under 3C and 4C rates could increase their lifetime Ah throughput by up to 50%.

Additionally, tests for fast (4C) charging with regular (1C) discharge as well as tests for regular (1C) charging and fast discharging (4C) revealed that fast charging did more damage. But both cases reach EOL much faster than when rates remained the same during charging and discharging. Cells charged and discharged at 4C (and 1C) lasted much longer.

The cycling protocol of a battery greatly affects the battery's life. Through active monitoring and proactive application of battery protocol switching, the overall value of the battery can be increased by raising the battery's lifetime storage throughput.

Chapter 7

Conclusions and Future Directions

7.1 Efficient Simulation of Battery Models

Since the MAPLE lab was founded, a major objective of the lab's ongoing work has been to increase computational efficiency for the models being studied. This has included model reduction under certain assumptions as well as reformulation of models as outlined in Chapter 2. Work in this dissertation added to the model efficiency by describing the perturbation and switch single-step method for solving systems of DAEs. All of these techniques have allowed for battery models to be simulated across a wide set of conditions and parameters at some of the fastest speed reported in literature.¹²⁶ While these techniques greatly enhance the speed of simulation, they always seek to minimize any error added to the system.

The implementation of the perturbation and switch single-step approach has advanced the group's ability to simulate and analyze systems of DAEs by allowing for easier system set up and execution of the solver. The increased range of allowable ICs greatly reduces the need to know exact ICs prior to simulating a system. The combination of the perturbation method with the actual simulation of the system also enhances the robustness of the solvers and increased solving speed.

Work in the MAPLE lab will continue to focus on increasing efficiency of simulation while increasing the level of detail within the model. While most work in this dissertation looked at capacity fade through a single mechanism, the SEI layer growth, additional mechanisms that contribute to fade in battery are being studied. Work by Suthar et al.¹⁴⁸ has studied stress effects during charging and Northrop et al.²¹⁰ has included thermal effects. With the inclusion more

intricate mechanisms for capacity fade, the models strive to become more predictive of actual fade occurring within the battery.

The fast, accurate models developed within the lab, allowed for many of the simulations in this dissertation to be performed in a timely manner. Simulation of year long periods of minute resolution data in Chapter 3, required robust models that could handle very dynamic charge discharge patterns over long periods of time without crashing. Additionally, to be able to study the many varying levels of demanded power and battery size, hundreds of individual simulations needed to be run for each site. In order to study all of the cases required for a thorough analysis, a fast model was required. The optimization of solar-battery operation in Chapter 4 required hundreds to thousands of iterations of the P2D model to be run in order to determine the best scenario. Without a model that could solve an individual iteration on the order of milliseconds, this type of optimization would become much slower and more difficult to implement. The need for robust models was also present in the study of EVs in Chapter 5.

The ability to study the effects of application on Li-ion batteries was only enabled by first having an accurate, robust, fast model to implement within these systems. And as the models become even better in the future, more intricate applications can be studied for a wider range of variables.

7.2 Advances to the Solar-Battery Hybrid Model

By using electrochemically based Li-ion battery models within systems level models, the ability to understand how the battery functions within specific applications has been enhanced and allowed greater understanding of Li-ion batteries in a wide range of systems not previously studied within our group. And while applications, such as connection to a solar array, have been modeled for Li-ion batteries before, the models has never been as extensive as those used in the

studies from Chapter 3 and have not given the insight into battery operation seen in this dissertation.

The solar-battery hybrid model allowed for the battery model to be tested under a wide range of constraints, most notably variation in irradiance patterns and variation in demand patterns. This systems level model was the first implementation by the M.A.P.L.E. group allowing for continuously changing current from real data to be studied over multiple cycles of a battery in a single simulation. The ability to easily read in high resolution real world data and simulate over long periods of time allowed for a much more thorough understanding of the battery throughout its lifetime. Most previous studies within the group focused only on one or a few cycles of operation and used constant or simplified approximation of varying current or power demands. Incorporating the battery into a MAPLESim system level model allowed for long duration studies with varying current or power demands to become viable. The speed of simulation of the solar-battery hybrid model allowed for many real world cases to be studied.

Another benefit of the solar-battery hybrid model was that it was developed modularly to be able to connect other individual components that could enhance the accuracy of the simulation. The main components of the solar-battery hybrid model are: the battery, the solar array, and the demand load. In addition to these components, power flow was control through a series of components that measured incoming power, battery SOC, and demand load and made decisions about how to route power. The modular approach allowed for more versatility during studies by allowing easily changeable control structures.

This approach to modeling allows for new additional components to be added or for multiple solar arrays or batteries to be simulated together and analyzed individually. The solar battery model has been run with battery stacks in place of the individual cell. Simple cases were

run with 16 independent SPM model strung together (4 parallel strings of 4 cells in series) in order to study cell variation within a battery pack. Each individual cell could be given different parameters to analyze how small variations between cells within a larger pack can effect operation. Again, the modular approach to create this systems level model made analyzing different sized packs much simpler by allowing for easier implementation of additional components.

Future work within the MAPLE lab will include continuing to study battery packs in connection to utility generation sources. Degradation mechanisms within battery packs will also be studied to see how SEI layer growth may vary between cells. The ability to model many cells within an individual pack has been aided by the efficiency of the model, as battery packs are scaled up for study, the system of equations for simulation increases, slowing the ability of the computer to simulate and analyze. The fast solving methods developed in the MAPLE have been important in allowing modeling to move from individual cells into true battery packs with cell variation.

While the work outlined in this dissertation has dealt exclusively with Li-ion battery models, redox-flow battery models have also been studied. Redox-flow batteries have been an area of interest in recent years because of their ability to store large amounts energy with a single cell because they decouple the power and energy capacity of the battery. A CSTR (continuous stir-tank reactor) model of a vanadium redox-flow battery was studied within the solar-battery hybrid model in place of the Li-ion component. Future work undertaken by the MAPLE group will include studying how redox-flow battery operations may differ from a Li-ion battery under the same constraints. Additionally, combinations of redox-flow cells and Li-ion cells within a larger system could be tested together. Along with multiple battery models, a true microgrid

system with multiple generation sources, individualized demand and storage devices can be built using this model as a basis. Creating complex system level models like the one described here, offer the greatest ability to truly be able to analyze real working systems through modeling.

7.3 Advances to the EV Battery Model

The EV battery model and the solar-battery model share similarities in that they were both developed as system level models to study Li-ion batteries in specific applications. However, the EV model had different constraints than the solar-battery hybrid model. The discharging rates were much higher for the EVs and PHEV driving cycles than they were for the solar-battery application. EV batteries were being cycled on the order of hours instead of days and EV could see rate spikes over 1C for short periods of time. Additionally if the EV required fast charging, the rates for charging would be much higher for the EV model than for the solar-battery application. Therefore, the P2D model which does a better job of handling the higher rates was chosen for the battery component in the EV model. The P2D model also offered tracking of more internal variables and more points at which those variables could be tracked within the system. Since most of the simulation were only over one or a few cycles for this study, the more information about internal states was beneficial without greatly reducing the computational time.

The charging pattern for the EV model was the normal CC-CV charging pattern used for most battery charging applications, but the discharge required deriving the power requirements necessary in order to achieve different driving cycles. The variation from these cycles was made easier to work with through the same modular approach outlined in section 7.2. The addition of the SEI layer growth mechanism allowed for a thorough analysis of how regenerative braking will affect the life of battery. Other types of degradation will occur during normal EV operation,

but the analysis of the SEI layer growth offered a first basis of how variation in regenerative braking based on driving patterns will affect the battery.

Work within the M.A.P.L.E. lab has included studying additional capacity fade mechanisms such as stress and temperature affects. Including these effects into the EV model would allow for a more thorough analysis of degradation caused from driving. It will be difficult however, to get more than generalized results because the charging patterns seen within EV will be highly dependent on the owner of the vehicle's driving patterns. Additionally the size and type of batteries within EV is continually changing as models are upgraded or new models become available.

The EV study for this work standardized the vehicle and battery and focused only on the driving patterns. More work could analyze specific battery and car characteristic so that individual vehicle models could be compared among each other. However, this would require an extensive amount of simulation for each model and knowledge of each model that is sometime proprietary, such as the exact chemistry of the battery being used.

Any future work on this system should also include an analysis of how pack variation may affect operation similar to the analysis that has begun in the MAPLE lab for the solar-battery hybrid application. Variation among cells within EV battery packs offers many possible areas of study.

7.4 Advances to Model-based Optimization

Model-based optimization has been an advancing area of research for the MAPLE lab for the past several years. Because the speed and robustness of the battery models used within the lab has increased greatly, optimization of these models has become possible. There are many

applications in which optimization can greatly enhance understanding of operation and help lead to more advanced control methods that are predictive in nature instead of reactive.

Optimization of a solar-battery model was undertaken to better understand how charge could be best stored within the battery being charged solely by the sun. For optimization of the solar-battery model to be useful for model-based control accurate solar forecasts must be available. Optimization of the system requires that we know the possible available current for the battery during the complete day, only then can the best charging current profile be chosen. The accuracy of the solar forecast will influence the accuracy of the model-based optimization. While the MAPLE group has not previously looked into solar forecasting, a better understanding of the possible limitations of solar forecasting for model-based control would be useful.

For the optimization presented in Chapter 4 approximate solar curve were used with a simple demand structure. Using real world irradiance curves with more dynamic demand would show how optimization could be implemented beyond a proof of concept and dig deeper into the important aspect of how control of a system would work. Additionally, as stated in section 7.3, additional mechanisms could be added that would allow additional variable constraints to be included in the optimization of the battery.

Our model analysis of the system focused on two important objectives, maximizing charge stored over a given day and maximizing the life of the battery. Many additional objectives could be used to study the system including reduced temperature rise of the system, maximizing solar power utilized locally, etc. While Chapter 4 only shows a simple case of how optimization could be performed on a system, with the method in place and validated, many additional studies can be undertaken using the framework outline in Chapter 4. The MAPLE group continues to

study optimization specifically for battery control purposes for both EV applications and grid scale storage.

7.5 Experimental Cycling

Cycling cells experimentally, helped to gain a much more thorough understanding of the advantages of attempting lifetime modeling of batteries and applications as well as the limitation of such models. The duration of experimental cycling is time prohibitive. In order to test a battery rated to last 5,000 cycles at 1C, you would need 417 days of continuous cycling. Accelerated testing, where rates are higher or the temperature is increased can shorten the required time needed to experimentally reveal fade occurring, but it is difficult to extrapolate those findings to other cases. Especially for applications like solar power shifting or EVs that experience different cycling patterns every day, this type of extrapolation results in a great amount of uncertainty in life estimates. Modeling can be performed on a much shorter time scale for many more cases.

While our experimental studies were limited by the bandwidth of our testing facilities and the amount of cycles it took to degrade the individual cells, for the cases that were studied, the experiments provided vital information to inform our understanding. For example, the most interesting case from our exponential study was the high charge or high discharge experiments where a cell was either charged fast and discharged slowly or charged slowly and discharged fast. Both cases degraded extremely fast. Both faded faster than the control cells cycling at 4C for both charge and discharge. Normally slower cycling reduces battery fade, but performing half of a cycle at a slow rate did not slow the fade, and actually increased it! The mechanism that causes this behavior is not included in the model and is currently unknown.

While the model can be useful to simulate known processes within the battery, there are still many cases of cycling that require independent validation in order to verify results. For the studies in this dissertation capacity fade is measured through only a few variables, most often SEI layer growth. While this mechanism has shown to be a good predictor of capacity fade, there remain many cases such as the fast charge slow discharge case, where the SEI layer mechanism alone cannot explain the fade seen in the experimental studies. It remains important not to lose sight of experimental studies of cycling to help inform future models. These models should not just use the information gained to add empirical corrections to a model, but rather should seek to better understand the physics and mechanisms causing the variations between simulated results and experimental results.

References

1. R. Schmid and C. Pillot, "Introduction to Energy Storage with Market Analysis and Outlook," in *1st International Freiberg Conference on Electrochemical Storage Materials*, Freiberg, Germany, 2014, pp. 3-13.
2. B. Scrosati, "History of lithium batteries", *Journal of Solid State Electrochemistry*, **15**, (2011).
3. J. M. Tarascon and M. Armand, "Issues and challenges facing rechargeable lithium batteries", *Nature*, **414**, (2001).
4. M. Endo, C. Kim, K. Nishimura, T. Fujino, and K. Miyashita, "Recent development of carbon materials for Li ion batteries", *Carbon*, **38**, (2000).
5. M. Winter and R. J. Brodd, "What are batteries, fuel cells, and supercapacitors?", *Chemical Reviews*, **104**, (2004).
6. A.-I. Stan, M. Swiercaynski, D.-I. Stroe, R. Teodorescu, and S. J. Andreasen, "Lithium ion battery chemistries from renewable energy storage to automotive and back-up power applications-An overview," presented at the 2014 International Conference on Optimization of Electrical and Electronic Equipment (OPTIM), Brasov, Romania, 2014.
7. K. Mizushima, P. C. Jones, P. J. Wiseman, and J. B. Goodenough, "LiCoO₂ (0 < x <= 1) - a New Cathode Material for Batteries of High-Energy Density", *Materials Research Bulletin*, **15**, (1980).
8. S. Santhanagopalan, K. Smith, J. Neubauer, G.-H. Kim, M. Keyser, and A. Pesaran, *Design and Analysis of Large Lithium-Ion Battery Systems*. Boston: Artech House, 2015.
9. K. C. Kam and M. M. Doeff, "Electrode Materials for Lithium Ion Batteries", *Material Matters*, **7**, 56 (2012).
10. M. S. Whittingham, "Role of Ternary Phases in Cathode Reactions", *Journal of the Electrochemical Society*, **123**, (1976).
11. W. J. Zhang, "A review of the electrochemical performance of alloy anodes for lithium-ion batteries", *Journal of Power Sources*, **196**, (2011).
12. Z. Li, J. Huang, B. Y. Liaw, V. Metzler, and J. B. Zhang, "A review of lithium deposition in lithium-ion and lithium metal secondary batteries", *Journal of Power Sources*, **254**, (2014).
13. G. G. Botte, V. R. Subramanian, and R. E. White, "Mathematical modeling of secondary lithium batteries", *Electrochimica Acta*, **45**, 2595 (2000).
14. G. Ning and B. N. Popov, "Cycle life modeling of lithium-ion batteries", *Journal of the Electrochemical Society*, **151**, (2004).
15. V. R. Subramanian, V. D. Diwakar, and D. Tapriyal, "Efficient macro-micro scale coupled modeling of batteries", *Journal of the Electrochemical Society*, **152**, (2005).
16. C. Y. Wang, W. B. Gu, and B. Y. Liaw, "Micro-macroscopic coupled modeling of batteries and fuel cells - I. Model development", *Journal of the Electrochemical Society*, **145**, (1998).
17. S. Santhanagopalan, Q. Z. Guo, P. Ramadass, and R. E. White, "Review of models for predicting the cycling performance of lithium ion batteries", *Journal of Power Sources*, **156**, 620 (2006).
18. M. Doyle, T. F. Fuller, and J. Newman, "Modeling of Galvanostatic Charge and Discharge of the Lithium Polymer Insertion Cell", *Journal of the Electrochemical Society*, **140**, 1526 (1993).

19. R. C. Kroeze and P. T. Krein, "Electrical battery model for use in dynamic electric vehicle simulations," in *Power Electronics Specialists Conference, 2008. PESC 2008. IEEE*, 2008, pp. 1336-1342.
20. R. N. Methekar, P. W. C. Northrop, K. J. Chen, R. D. Braatz, and V. R. Subramanian, "Kinetic Monte Carlo Simulation of Surface Heterogeneity in Graphite Anodes for Lithium-Ion Batteries: Passive Layer Formation", *Journal of the Electrochemical Society*, **158**, A363 (2011).
21. M. Broussely, S. Herreyre, P. Biensan, P. Kasztejna, K. Nechev, and R. J. Staniewicz, "Aging mechanism in Li ion cells and calendar life predictions", *Journal of Power Sources*, **97-8**, 13 (2001).
22. I. Bloom, B. W. Cole, J. J. Sohn, S. A. Jones, E. G. Polzin, V. S. Battaglia, *et al.*, "An accelerated calendar and cycle life study of Li-ion cells", *Journal of Power Sources*, **101**, 238 (2001).
23. G. Ning, B. Haran, and B. N. Popov, "Capacity fade study of lithium-ion batteries cycled at high discharge rates", *Journal of Power Sources*, **117**, 160 (2003).
24. Y. Hamon, T. Brousse, F. Jousse, P. Topart, P. Buvat, and D. M. Schleich, "Aluminum negative electrode in lithium ion batteries", *Journal of Power Sources*, **97-8**, 185 (2001).
25. I. Kim, G. E. Blomgren, and P. N. Kumta, "Nanostructured Si/TiB₂ composite anodes for Li-ion batteries", *Electrochemical and Solid State Letters*, **6**, A157 (2003).
26. P. Arora, White, R. E., and Doyle, M., "Capacity Fade Mechanisms and Side Reactions in Lithium ion Batteries", *Journal of the Electrochemical Society* **145-10**, 3647 (1998).
27. V. Ramadesigan, K. J. Chen, N. A. Burns, V. Boovaragavan, R. D. Braatz, and V. R. Subramanian, "Parameter Estimation and Capacity Fade Analysis of Lithium-Ion Batteries Using Reformulated Models", *Journal of the Electrochemical Society*, **158**, A1048 (2011).
28. M. Broussely, P. Biensan, F. Bonhomme, P. Blanchard, S. Herreyre, K. Nechev, *et al.*, "Main aging mechanisms in Li ion batteries", *Journal of Power Sources*, **146**, 90 (2005).
29. J. Wang, P. Liu, J. Hicks-Garner, E. Sherman, S. Soukiazian, M. Verbrugge, *et al.*, "Cycle-life model for graphite-LiFePO(4) cells", *Journal of Power Sources*, **196**, (2011).
30. P. Ramadass, B. Haran, P. M. Gomadam, R. White, and B. N. Popov, "Development of first principles capacity fade model for Li-ion cells", *Journal of the Electrochemical Society*, **151**, A196 (2004).
31. J. Vetter, P. Novak, M. R. Wagner, C. Veit, K. C. Moller, J. O. Besenhard, *et al.*, "Ageing mechanisms in lithium-ion batteries", *Journal of Power Sources*, **147**, 269 (2005).
32. D. Zhang, B. S. Haran, A. Durairajan, R. E. White, Y. Podrazhansky, and B. N. Popov, "Studies on capacity fade of lithium-ion batteries", *Journal of Power Sources*, **91**, (2000).
33. V. Etacheri, R. Marom, R. Elazari, G. Salitra, and D. Aurbach, "Challenges in the development of advanced Li-ion batteries: a review", *Energy & Environmental Science*, **4**, 3243 (2011).
34. R. Spotnitz, "Simulation of capacity fade in lithium-ion batteries", *Journal of Power Sources*, **113**, 72 (2003).
35. S. Bashash, S. J. Moura, J. C. Forman, and H. K. Fathy, "Plug-in hybrid electric vehicle charge pattern optimization for energy cost and battery longevity", *Journal of Power Sources*, **196**, 541 (2011).

36. E. Prada, D. Di Domenico, Y. Creff, J. Bernard, V. Sauvant-Moynot, and F. Huet, "A Simplified Electrochemical and Thermal Aging Model of LiFePO₄-Graphite Li-ion Batteries: Power and Capacity Fade Simulations", *Journal of the Electrochemical Society*, **160**, (2013).
37. K. Tasaki, A. Goldberg, J. J. Lian, M. Walker, A. Timmons, and S. J. Harris, "Solubility of Lithium Salts Formed on the Lithium-Ion Battery Negative Electrode Surface in Organic Solvents", *Journal of the Electrochemical Society*, **156**, (2009).
38. M. B. Pinson and M. Z. Bazant, "Theory of SEI Formation in Rechargeable Batteries: Capacity Fade, Accelerated Aging and Lifetime Prediction", *Journal of the Electrochemical Society*, **160**, A243 (2013).
39. A. V. Randall, R. D. Perkins, X. C. Zhang, and G. L. Plett, "Controls oriented reduced order modeling of solid-electrolyte interphase layer growth", *Journal of Power Sources*, **209**, 282 (2012).
40. M. Safari, M. Morcrette, A. Teyssot, and C. Delacourt, "Multimodal Physics-Based Aging Model for Life Prediction of Li-Ion Batteries", *Journal of the Electrochemical Society*, **156**, A145 (2009).
41. P. Ramadass, B. Haran, R. White, and B. N. Popov, "Mathematical modeling of the capacity fade of Li-ion cells", *Journal of Power Sources*, **123**, 230 (2003).
42. V. Ramadesigan, P. W. C. Northrop, S. De, S. Santhanagopalan, R. D. Braatz, and V. R. Subramanian, "Modeling and Simulation of Lithium-Ion Batteries from a Systems Engineering Perspective (vol 159, pg R31, 2012)", *Journal of the Electrochemical Society*, **159**, S12 (2012).
43. J. C. Forman, S. Bashash, J. L. Stein, and H. K. Fathy, "Reduction of an Electrochemistry-Based Li-Ion Battery Model via Quasi-Linearization and Pade Approximation", *Journal of the Electrochemical Society*, **158**, (2011).
44. P. W. C. Northrop, V. Ramadesigan, S. De, and V. R. Subramanian, "Coordinate Transformation, Orthogonal Collocation, Model Reformulation and Simulation of Electrochemical-Thermal Behavior of Lithium-Ion Battery Stacks", *Journal of the Electrochemical Society*, **158**, A1461 (2011).
45. E. Hairer and G. Wanner, *Solving Ordinary Differential Equations II: Stiff and Differential-Algebraic Problems*, 2nd ed. vol. 14: Springer, 1996.
46. L. R. Petzold, "A Description of DASSL: A Differential/Algebraic System Solver," Sandia National Lab SAND82-8637, September, 1982 1982.
47. J. J. B. de Swart, W. M. Lioen, and W. A. van der Veen, "Specification of PSIDE," National Research Institute for Mathematics and Computer Science (CWI) (The Netherlands), Amsterdam, NL MAS-R9833, December, 1998 1998.
48. P. E. VanKeken, D. A. Yuen, and L. R. Petzold, "DASPK: A new high order and adaptive time-integration technique with applications to mantle convection with strongly temperature- and pressure-dependent rheology", *Geophysical and Astrophysical Fluid Dynamics*, **80**, (1995).
49. Maplesoft. (Accessed: June, 2015). *Maple dsolve*. Available at: <http://www.maplesoft.com/support/help/maple/view.aspx?path=dsolve>
50. Mathworks. (Accessed: June, 2015). *Matlab ODE15s*. Available at: <http://www.mathworks.com/help/matlab/ref/ode15s.html>

51. M. Berzins, P. M. Dew, and R. M. Furzeland, "Developing Software for Time-Dependent Problems Using the Method of Lines and Differential-Algebraic Integrators", *Applied Numerical Mathematics*, **5**, (1989).
52. A. C. Hindmarsh, "LSODE and LSODI, two new initial value ordinary differential equation solvers", *ACM SIGNUM Newletters*, **15**, 10 (1980).
53. Wolfram. (Accessed: November, 2014). *NDSolve*. Available at: <http://reference.wolfram.com/language/ref/NDSolve.html>
54. J. R. Cash, "Efficient numerical methods for the solution of stiff initial-value problems and differential algebraic equations", *Proceedings of the Royal Society a-Mathematical Physical and Engineering Sciences*, **459**, (2003).
55. F. E. Cellier and E. Kofman, *Continuous System Simulation*: Springer US, 2006.
56. R. N. Methekar, V. Ramadesigan, J. C. Pirkle, and V. R. Subramanian, "A perturbation approach for consistent initialization of index-1 explicit differential-algebraic equations arising from battery model simulations", *Computers & Chemical Engineering*, **35**, (2011).
57. P. N. Brown, A. C. Hindmarsh, and L. R. Petzold, "Using Krylov Methods in the Solution of Large-Scale Differential-Algebraic Systems", *Siam Journal on Scientific Computing*, **15**, (1994).
58. P. N. Brown, A. C. Hindmarsh, and L. R. Petzold, "Consistent initial condition calculation for differential-algebraic systems", *Siam Journal on Scientific Computing*, **19**, (1998).
59. E. Hairer and G. Wanner, "Stiff differential equations solved by Radau methods", *Journal of Computational and Applied Mathematics*, **111**, (1999).
60. D. Schwalbe, H. Kooijman, and R. Taylor, "Solving stiff differential equations and differential algebraic systems with Maple V", *Mapletech*, **3**, (1996).
61. M. L. Michelsen, "Application of Semi-Implicit Runge-Kutta Methods for Integration of Ordinary and Partial-Differential Equations", *Chemical Engineering Journal and the Biochemical Engineering Journal*, **14**, (1977).
62. R. Taylor, "Engineering Computing with Maple: Solution of PDEs via the Method of Lines", *CACHE News*, **49**, 5 (1999).
63. Maplesoft. (Accessed: Jan. 2015). *Maple*. Available at: <http://www.maplesoft.com/products/maple/>
64. Dassault Systems. (Accessed: Jan. 2015). *DYMOLA*. Available at: <http://www.3ds.com/products-services/catia/capabilities/modelica-systems-simulation-info/dymola>
65. B. Leimkuhler, L. R. Petzold, and C. W. Gear, "Approximation Methods for the Consistent Initialization of Differential-Algebraic Equations", *Siam Journal on Numerical Analysis*, **28**, (1991).
66. L. Petzold, "Differential-Algebraic Equations Are Not Odes", *Siam Journal on Scientific and Statistical Computing*, **3**, (1982).
67. R. Lamour and F. Mazzia, "Computation of consistent initial values for properly stated index 3 DAEs", *Bit Numerical Mathematics*, **49**, (2009).
68. V. Gopal and L. T. Biegler, "A successive linear programming approach for initialization and reinitialization after discontinuities of differential-algebraic equations", *Siam Journal on Scientific Computing*, **20**, (1998).

69. G. Reissig, H. Boche, and P. I. Barton, "On inconsistent initial conditions for linear time-invariant differential-algebraic equations", *Ieee Transactions on Circuits and Systems I-Fundamental Theory and Applications*, **49**, (2002).
70. J. A. G. Garcia, "A singlar Perturbation Approach to Modeling Closed Kinematic Chains," Rice University, Houston, TX, 2000.
71. M. T. Lawder, V. Ramadesigan, B. Suthar, and V. R. Subramanian, "Extending explicit and linearly implicit ODE solavers for index-1 DAEs", *Computers and Chemical Engineering*, **82**, 283 (2015).
72. V. Boovaragavan, V. Ramadesigan, M. V. Panchagnula, and V. R. Subramanian, "Continuum Representation for Simulating Discrete Events of Battery Operation", *Journal of the Electrochemical Society*, **157**, (2010).
73. C. Schneider, "Rosenbrock-Type Methods Adapted to Differential-Algebraic Systems", *Mathematics of Computation*, **56**, (1991).
74. D. Manz, R. Walling, N. Miller, B. LaRose, R. D'Aquila, and B. Daryanian, "The Grid of the Future", *Ieee Power & Energy Magazine*, **12**, (2014).
75. GE Energy, "Western Wind and Solar Integreation Study," National Renewable Energy Laboratory, Golden, COMay, 2010 2010.
76. J. A. Wood and B. F. Wollenberg, *Power Generation, Operationnd Contol*. New York: John Wiley & Sons, Inc., 1996.
77. A. M. Gopstein, "Energy Storage & the Grid-From Characteristics to Impact", *Proceedings of the IEEE*, **100**, (2012).
78. B. Yang, Y. Makarov, J. Desteese, V. Viswanathan, P. Nyeng, B. McManus, *et al.*, "On the use of energy storage technologies for regulation services in electric power systems with significant penetration of wind energy," in *5th International Conference on the European Electricity Market*, Lisbon, Portugal, 2008, p. 6.
79. R. M. Dell and D. A. J. Rand, "Energy storage - a key technology for global energy sustainability", *Journal of Power Sources*, **100**, (2001).
80. J. M. Guerrero, J. C. Vasquez, J. Matas, L. G. de Vicuna, and M. Castilla, "Hierarchical Control of Droop-Controlled AC and DC Microgrids-A General Approach Toward Standardization", *Ieee Transactions on Industrial Electronics*, **58**, (2011).
81. A. Mishra, D. Irwin, P. Shenoy, J. Kurose, and T. Zhu, "SmartCharge: cutting the electric bill in smart homes with energy storage," in *3rd Interntional Conference on Future Energy Systems*, Madrid, Spain, 2012, p. 10.
82. J. A. P. Lopes, C. L. Moreira, and A. G. Madureira, "Defining control strategies for microgrids islanded operation", *Ieee Transactions on Power Systems*, **21**, (2006).
83. N. Hatziargyriou, H. Asano, R. Iravani, and C. Marnay, "Microgrids", *Ieee Power & Energy Magazine*, **5**, (2007).
84. M. A. Pedrasa and T. Spooner, "A survey of techniques used to control microgrid generationand storage during island operation", *Proceedings of the Austrailian Universities Power Engineering Conference*, (2006).
85. C. H. Lo and M. D. Anderson, "Economic dispatch and optimal sizing of battery energy storage systems in utility load-leveling operations", *Ieee Transactions on Energy Conversion*, **14**, (1999).
86. T. K. A. Brekken, A. Yokochi, A. von Jouanne, Z. Z. Yen, H. M. Hapke, and D. A. Halamay, "Optimal Energy Storage Sizing and Control for Wind Power Applications", *Ieee Transactions on Sustainable Energy*, **2**, (2011).

87. S. Teleke, M. E. Baran, A. Q. Huang, S. Bhattacharya, and L. Anderson, "Control Strategies for Battery Energy Storage for Wind Farm Dispatching", *Ieee Transactions on Energy Conversion*, **24**, (2009).
88. W. X. Shen, "Optimally sizing of solar array and battery in a standalone photovoltaic system in Malaysia", *Renewable Energy*, **34**, (2009).
89. S. Teleke, M. E. Baran, S. Bhattacharya, and A. Q. Huang, "Rule-Based Control of Battery Energy Storage for Dispatching Intermittent Renewable Sources", *Ieee Transactions on Sustainable Energy*, **1**, (2010).
90. C. Protopogeropoulos, B. J. Brinkworth, and R. H. Marshall, "Sizing and techno-economical optimization for hybrid solar photovoltaic wind power systems with battery storage", *International Journal of Energy Research*, **21**, (1997).
91. H. X. Yang, L. Lu, and W. Zhou, "A novel optimization sizing model for hybrid solar-wind power generation system", *Solar Energy*, **81**, (2007).
92. B. Borowy and Z. Salameh, "Methodology for optimally sizing the combination of a battery bank and PV array in a Wind/PV hybrid system - Reply", *Ieee Transactions on Energy Conversion*, **11**, (1996).
93. R. Chedid and S. Rahman, "Unit sizing and control of hybrid wind-solar power systems", *Ieee Transactions on Energy Conversion*, **12**, (1997).
94. H. S. V. S. K. Nunna and S. Doolla, "Energy Management in Microgrids Using Demand Response and Distributed Storage-A Multiagent Approach", *Ieee Transactions on Power Delivery*, **28**, (2013).
95. H. X. Yang, W. Zhou, L. Lu, and Z. H. Fang, "Optimal sizing method for stand-alone hybrid solar-wind system with LPSP technology by using genetic algorithm", *Solar Energy*, **82**, (2008).
96. S. H. Madaeni, R. Sioshansi, and P. Denholm, "Comparison of Capacity Value Methods for Photovoltaics in the Western United States," National Renewable Energy Laboratory, Golden, CO July, 2012 2012.
97. J. A. Gow and C. D. Manning, "Development of a photovoltaic array model for use in power-electronics simulation studies", *Ieee Proceedings-Electric Power Applications*, **146**, (1999).
98. M. G. Villalva, J. R. Gazoli, and E. Ruppert, "Comprehensive Approach to Modeling and Simulation of Photovoltaic Arrays", *Ieee Transactions on Power Electronics*, **24**, (2009).
99. A. Chambers, *Distributed generation: a nontechnical guide*. Tulsa, OK: PennWell, 2001.
100. A. G. Tsikalakis and N. D. Hatziargyriou, "Operation of microgrids with demand side bidding and continuity of supply for critical loads", *European Transactions on Electrical Power*, **21**, (2011).
101. C. A. Hill, M. C. Such, D. M. Chen, J. Gonzalez, and W. M. Grady, "Battery Energy Storage for Enabling Integration of Distributed Solar Power Generation", *Ieee Transactions on Smart Grid*, **3**, (2012).
102. G. Notton, M. Muselli, and A. Louche, "Autonomous hybrid photovoltaic power plant using a back-up generator: A case study in a mediterranean island", *Renewable Energy*, **7**, (1996).
103. G. Notton, M. Muselli, P. Poggi, and A. Louche, "Autonomous photovoltaic systems: Influences of some parameters on the sizing: Simulation timestep, input and output power profile", *Renewable Energy*, **7**, (1996).

104. P. Nema, R. K. Nema, and S. Rangnekar, "A current and future state of art development of hybrid energy system using wind and PV-solar: A review", *Renewable & Sustainable Energy Reviews*, **13**, (2009).
105. B. S. Borowy and Z. M. Salameh, "Methodology for optimally sizing the combination of a battery bank and PV array in a Wind/PV hybrid system", *Ieee Transactions on Energy Conversion*, **11**, (1996).
106. T. Lambert, P. Gilman, and P. Lilienthal, "Micropower system modeling with homer," in *Integration of Alternative Source of Energy*, F. A. Farret and M. G. Simoes, Eds., ed: John Wiley & Sons, Inc., 2006, p. 39.
107. S. M. Shaahid and M. A. Elhadidy, "Economic analysis of hybrid photovoltaic-diesel-battery power systems for residential loads in hot regions - A step to clean future", *Renewable & Sustainable Energy Reviews*, **12**, (2008).
108. G. B. Shrestha and L. Goel, "A study on optimal sizing of stand-alone photovoltaic stations", *Ieee Transactions on Energy Conversion*, **13**, (1998).
109. H. X. Yang, L. Lu, and J. Burnett, "Weather data and probability analysis of hybrid photovoltaic-wind power generation systems in Hong Kong", *Renewable Energy*, **28**, (2003).
110. J. P. Fossati, A. Galarza, A. Martin-Villate, and L. Fontan, "A method for optimal sizing energy storage systems for microgrids", *Renewable Energy*, **77**, 539 (2015).
111. H. J. Khasawneh and M. S. Illindala, "Battery cycle life balancing in a microgrid through flexible distribution of energy and storage resources", *Journal of Power Sources*, **261**, (2014).
112. P. M. Gomadam, J. W. Weidner, R. A. Dougal, and R. E. White, "Mathematical modeling of lithium-ion and nickel battery systems", *Journal of Power Sources*, **110**, (2002).
113. M. Chen and G. A. Rincon-Mora, "Accurate electrical battery model capable of predicting, runtime and I-V performance", *Ieee Transactions on Energy Conversion*, **21**, (2006).
114. C. Truchot, M. Dubarry, and B. Y. Liaw, "State-of-charge estimation and uncertainty for lithium-ion battery strings", *Applied Energy*, **119**, (2014).
115. S. K. Rahimian, S. Rayman, and R. E. White, "Extension of physics-based single particle model for higher charge-discharge rates", *Journal of Power Sources*, **224**, (2013).
116. T. F. Fuller, M. Doyle, and J. Newman, "Simulation and Optimization of the Dual Lithium Ion Insertion Cell", *Journal of the Electrochemical Society*, **141**, (1994).
117. C. Budischak, D. Sewell, H. Thomson, L. Mach, D. E. Veron, and W. Kempton, "Cost-minimized combinations of wind power, solar power and electrochemical storage, powering the grid up to 99.9% of the time (vol 225, pg 60, 2013)", *Journal of Power Sources*, **232**, (2013).
118. V. Ramadesigan, P. W. C. Northrop, S. De, S. Santhanagopalan, R. D. Braatz, and V. R. Subramanian, "Modeling and Simulation of Lithium-Ion Batteries from a Systems Engineering Perspective", *Journal of the Electrochemical Society*, **159**, (2012).
119. X. S. Hu, S. B. Li, and H. Peng, "A comparative study of equivalent circuit models for Li-ion batteries", *Journal of Power Sources*, **198**, (2012).
120. H. W. He, R. Xiong, and J. X. Fan, "Evaluation of Lithium-Ion Battery Equivalent Circuit Models for State of Charge Estimation by an Experimental Approach", *Energies*, **4**, (2011).

121. S. Cho, H. Jeong, C. Han, S. Jin, J. H. Lim, and J. Oh, "State-of-charge estimation for lithium-ion batteries under various operating conditions using an equivalent circuit model", *Computers & Chemical Engineering*, **41**, (2012).
122. T. Kim and W. Qiao, "A Hybrid Battery Model Capable of Capturing Dynamic Circuit Characteristics and Nonlinear Capacity Effects", *Ieee Transactions on Energy Conversion*, **26**, (2011).
123. T. K. Dong, A. Kirchev, F. Mattera, J. Kowal, and Y. Bultel, "Dynamic Modeling of Li-Ion Batteries Using an Equivalent Electrical Circuit", *Journal of the Electrochemical Society*, **158**, (2011).
124. M. G. Ouyang, G. M. Liu, L. G. Lu, J. Q. Li, and X. B. Han, "Enhancing the estimation accuracy in low state-of-charge area: A novel onboard battery model through surface state of charge determination", *Journal of Power Sources*, **270**, (2014).
125. G. Liu, L. Lu, H. Fu, J. Hua, J. Li, M. Ouyange, *et al.*, "A comparative study of equivalent circuit models and enhanced equivalent circuit models of lithium-ion batteries with different model structures," presented at the Transportation Electrification Asia-Pacific, 2014 IEEE Conference and Expo, Beijing, China, 2014.
126. P. W. C. Northrop, B. Suthar, V. Ramadesigan, S. Santhanagopalan, R. D. Braatz, and V. R. Subramanian, "Efficient Simulation and reformulation of Lithium-Ion Battery Models for enabling electric transportation", *Journal of the Electrochemical Society*, **161**, E3149 (2014).
127. Y. H. Chiang, W. Y. Sean, and J. C. Ke, "Online estimation of internal resistance and open-circuit voltage of lithium-ion batteries in electric vehicles", *Journal of Power Sources*, **196**, (2011).
128. M. Dubarry, B. Y. Liaw, M. S. Chen, S. S. Chyan, K. C. Han, W. T. Sie, *et al.*, "Identifying battery aging mechanisms in large format Li ion cells", *Journal of Power Sources*, **196**, 3420 (2011).
129. G. L. Plett, "Extended Kalman filtering for battery management systems of LiPB-based HEV battery packs - Part 2. Modeling and identification", *Journal of Power Sources*, **134**, (2004).
130. T. Huria, M. Ceraolo, J. Gazzarri, and R. Jackey, "High Fidelity Electrical Model with Thermal Dependence for Characterization and Simulation of High Power Lithium Battery Cells," presented at the IEEE International Electric Vehicle Conference, Greenville, SC, 2012.
131. A. Rahmoun and H. Biechl, "Modelling of Li-ion batteries using equivalent circuit diagrams", *Przeglad Elektrotechniczny*, **88**, (2012).
132. National Renewable Energy Laboratory. (Accessed: 2014). *Measurement and Instrumentation Data Center (NREL)*. Available at: <http://www.nrel.gov/midc/>
133. C. J. Rydh and B. A. Sanden, "Energy analysis of batteries in photovoltaic systems. Part I: Performance and energy requirements", *Energy Conversion and Management*, **46**, (2005).
134. J. D. Dogger, B. Roossien, and F. D. J. Nieuwenhout, "Characterization of Li-Ion Batteries for Intelligent Management of Distributed Grid-Connected Storage", *Ieee Transactions on Energy Conversion*, **26**, (2011).
135. National Renewable Energy Laboratory. (Accessed: 2014). *Solar and Wind Energy Resource Assessment*. Available at:

- http://maps.nrel.gov/swera?visible=swera_dni_nasa_lo_res&opacity=50&extent=-179.14,18.92,-65.57,71.41
136. A. Nottrott and J. Kleissl, "Validation of the NSRDB-SUNY global horizontal irradiance in California", *Solar Energy*, **84**, (2010).
 137. R. Perez, J. Schlemmer, D. Renne, S. Cowlin, R. George, and B. Bandyopadhyay, "Validation of the SUNY satellite model in a meteosat environment," in *ASES Annual Conference*, Buffalo, New York, 2009, p. 6.
 138. W. Zhou, C. Z. Lou, Z. S. Li, L. Lu, and H. X. Yang, "Current status of research on optimum sizing of stand-alone hybrid solar-wind power generation systems", *Applied Energy*, **87**, (2010).
 139. T. Markvart, A. Fragaki, and J. N. Ross, "PV system sizing using observed time series of solar radiation", *Solar Energy*, **80**, (2006).
 140. H. Ekstrom and G. Lindbergh, "A Model for Predicting Capacity Fade due to SEI Formation in a Commercial Graphite/LiFePO₄ Cell", *Journal of the Electrochemical Society*, **162**, A1003 (2015).
 141. M. T. Lawder, P. W. C. Northrop, and V. R. Subramanian, "Model-based SEI Layer Growth and Capacity Fade Analysis for EV and PHEV Batteries and Drive Cycles", *Journal of the Electrochemical Society*, **161**, A2099 (2014).
 142. M. W. Verbrugge, "Adaptive Characterization and Modeling of Electrochemical Energy Storage Devices for Hybrid Vehicle Applications," in *Modern Aspects of Electrochemistry no.43*, M. Schlesinger, Ed., ed New York: Springer, 2009.
 143. M. Verbrugge and B. Koch, "Generalized recursive algorithm for adaptive multiparameter regression - Application to lead acid, nickel metal hydride, and lithium-ion batteries", *Journal of the Electrochemical Society*, **153**, (2006).
 144. M. W. Verbrugge and R. S. Conell, "Electrochemical and thermal characterization of battery modules commensurate with electric vehicle integration", *Journal of the Electrochemical Society*, **149**, (2002).
 145. P. F. Ribeiro, B. K. Johnson, M. L. Crow, A. Arsoy, and Y. L. Liu, "Energy storage systems for advanced power applications", *Proceedings of the IEEE*, **89**, (2001).
 146. D. Bernardi, E. Pawlikowski, and J. Newman, "A General Energy-Balance for Battery Systems", *Journal of the Electrochemical Society*, **132**, (1985).
 147. C. R. Pals and J. Newman, "Thermal Modeling of the Lithium/Polymer Battery .2. Temperature Profiles in a Cell Stack", *Journal of the Electrochemical Society*, **142**, (1995).
 148. B. Suthar, V. Ramadesigan, S. De, R. D. Braatz, and V. R. Subramanian, "Optimal charging profiles for mechanically constrained lithium-ion batteries", *Physical Chemistry Chemical Physics*, **16**, (2014).
 149. V. R. Subramanian, V. Boovaragavan, V. Ramadesigan, and M. Arabandi, "Mathematical Model Reformulation for Lithium-Ion Battery Simulations: Galvanostatic Boundary Conditions", *Journal of the Electrochemical Society*, **156**, A260 (2009).
 150. V. Ramadesigan, V. Boovaragavan, J. C. Pirkle, and V. R. Subramanian, "Efficient Reformulation of Solid-Phase Diffusion in Physics-Based Lithium-Ion Battery Models", *Journal of the Electrochemical Society*, **157**, (2010).
 151. M. Armand and J. M. Tarascon, "Building better batteries", *Nature*, **451**, 652 (2008).

152. A. Dinger, R. Martin, X. Mosquet, M. Rabl, D. Rizoulis, M. Russo, *et al.*, "Batteries for Electric Cars: Challenges, Opportunities, and the Outlook to 2020," Boston Consulting Group 2010.
153. J. Nuebauer, Brooker, A., and Wood, E., "Sensitivity of battery electric vehicle economics to drive patterns, vehicle range, and charge strategies", *Journal of Power Sources* 209, 269 (2012).
154. R. Allen, "Electric and Hybrid Vehicle Technologies Charge Ahead", *Electronic Design* 3/26, 26 (2010).
155. B. Pattipati, C. Sankavaram, and K. R. Pattipati, "System Identification and Estimation Framework for Pivotal Automotive Battery Management System Characteristics", *Ieee Transactions on Systems Man and Cybernetics Part C-Applications and Reviews*, **41**, 869 (2011).
156. E. Cready, J. Lippert, J. Pihl, I. Weinstock, P. Symons, and R. G. Jungst, "Technical and economic feasibility of applying used EV batteries in stationary applications," Sandia National Labs 2003.
157. Nissan. (2011, March). 2011 Leaf Owner's Manual. *Nissanusa.com*. Available: nissan-techinfo.com/refgh0v/og/leaf/2011-nissan-leaf.pdf
158. Chevrolet. (Accessed: May). *Chevrolet*. Available at: www.chevrolet.com
159. A. P. Schmidt, M. Bitzer, A. W. Imnre, and L. Guzzella, "Model-based distinction and quantification of capacity loss and rate capability fade in Li-ion batteries", *Journal of Power Sources*, **195**, 7634 (2010).
160. S. S. Zhang, "A review on electrolyte additives for lithium-ion batteries", *Journal of Power Sources*, **162**, (2006).
161. G. Sikha, B. N. Popov, and R. E. White, "Effect of porosity on the capacity fade of a lithium-ion battery - Theory", *Journal of the Electrochemical Society*, **151**, A1104 (2004).
162. P. Verma, P. Maire, and P. Novak, "A review of the features and analyses of the solid electrolyte interphase in Li-ion batteries", *Electrochimica Acta*, **55**, (2010).
163. S. Bhattacharya, A. R. Riahi, and A. T. Alpas, "A transmission electron microscopy study of crack formation and propagation in electrochemically cycled graphite electrode in lithium-ion cells", *Journal of Power Sources*, **196**, 8719 (2011).
164. J. Christensen, "Modeling Diffusion-Induced Stress in Li-Ion Cells with Porous Electrodes", *Journal of the Electrochemical Society*, **157**, A366 (2010).
165. Y. C. Zhang, C. Y. Wang, and X. D. Tang, "Cycling degradation of an automotive LiFePO(4) lithium-ion battery", *Journal of Power Sources*, **196**, (2011).
166. Environmental Protection Agency. (Accessed). *Dynamometer Drive Schedules*. Available at: <http://www.epa.gov/nvfel/testing/dynamometer.htm>
167. R. V. N. Melnik, N. Song, and P. Sandholdt, "Dynamics of torque-speed profiles for electric vehicles and nonlinear models based on differential-algebraic equations," in *Proceedings of the Fourth International Conference on Dynamical Systems and Differential Equations*, Wilmington, NC, USA, 2002.
168. Committee for the national Tire Efficiency Study, "Tires and Passenger Fuel Economy: Improving Consumers, Improving Performance," National Research Council of the National Academies 2006 2006.

169. Y. Gao, L. Chu, and M. Ehsani, "Design and control principles of hybrid braking system for EV and FCV," presented at the Vehicle Power and Propulsion Conference, Arlington, TX, 2007.
170. Environmental Protection Agency. (Accessed). *Dynamometer Drive Schedules*. Available at: <http://www.epa.gov/nvfel/testing/dynamometer.htm>
171. T. J. Barlow, S. LAtham, I. S. McCrae, and P. G. Boulter. (2009). *A reference book of driving cycles for use in the measurement of road vehicle emissions*.
172. G. Sikha, P. Ramadass, B. S. Haran, R. E. White, and B. N. Popov, "Comparison of the capacity fade of Sony US 18650 cells charged with different protocols", *Journal of Power Sources*, **122**, 67 (2003).
173. M. K. Hidrue, G. R. Parsons, W. Kempton, and M. P. Gardner, "Willingness to pay for electric vehicles and their attributes", *Resource and Energy Economics*, **33**, 686 (2011).
174. International Energy Agency, Electric Vehicles Initiative, and C. E. Ministerial, "Global EV Outlook: Understanding the Electric Vehicle Landscape to 2020," International Energy Agency April, 2013 2013.
175. J. Nuebauer and E. Wood, "The impact of range anxiety and home, workplace, and public charging infrastructure on simulated battery electric vehicle lifetime utility", *Journal of Power Sources*, **257**, 12 (2014).
176. A. Santos, N. McGuckin, H. Y. Nakamoto, D. Gray, and S. Liss, "Summary of Travel Trends 2009 National Household Travel Survey," 2011.
177. A. Vyas and D. Santini, "Use of National Surveys for Estimating "Full" PHEV Potential for oil use reduction," presented at the PLUG-IN 2008 Conference, San Jose, CA, 2008.
178. NHTS. (2012, *National Household Travel Survey*. Available: nhts.ornl.gov
179. Honda Motor Company. (Accessed: May). *Honda Motor Company*. Available at: www.honda.com
180. Mitsubishi Motors Company. (Accessed: May). *Mitsubishi Motors Company*. Available at: <http://www.mitsubishicars.com/MMNA/jsp/index.do>
181. Nissan Automotive Company. (Accessed: May). *Nissan USA*. Available at: <http://www.nissanusa.com/>
182. Smart USA. (Accessed: May). *Smart USA*. Available at: <http://www.smartusa.com/>
183. Tesla Motors. (Accessed: May). *Tesla Motors*. Available at: <http://www.teslamotors.com/>
184. Toyota Motor Corporation. (Accessed: May). *Toyota Motor Corporation*. Available at: www.toyota.com
185. Fisker Automotive. (Accessed: May). *Fisker Automotive*. Available at: www.fiskerautomotive.com
186. Fiat USA. (Accessed: May). *Fiat*. Available at: www.fiatusa.com
187. Ford Motor Company. (Accessed: May). *Ford Motor Company*. Available at: <http://www.ford.com/>
188. A. Vyas and D. Santini, "Use of National Surveys for Estimating "Full" PHEV Potential for oil use reduction", *PLUG-IN 2008 Conference, San Jose, CA*, (2008).
189. W. Choi, J. Y. Lee, B. H. Jung, and H. S. Lim, "Microstructure and electrochemical properties of a nanometer-scale tin anode for lithium secondary batteries", *Journal of Power Sources*, **136**, 154 (2004).
190. F. F. Cao, Y. G. Guo, S. F. Zheng, X. L. Wu, L. Y. Jiang, R. R. Bi, *et al.*, "Symbiotic Coaxial Nanocables: Facile Synthesis and an Efficient and Elegant Morphological Solution to the Lithium Storage Problem", *Chemistry of Materials*, **22**, 1908 (2010).

191. G. Q. Liu, L. Wen, and Y. M. Liu, "Spinel $\text{LiNi}_{0.5}\text{Mn}_{1.5}\text{O}_4$ and its derivatives as cathodes for high-voltage Li-ion batteries", *Journal of Solid State Electrochemistry*, **14**, 2191 (2010).
192. M. Dubarry, V. Svoboda, R. Hwu, and B. Y. Liaw, "Capacity loss in rechargeable lithium cells during cycle life testing: The importance of determining state-of-charge", *Journal of Power Sources*, **174**, (2007).
193. C. K. Zhou, K. J. Qian, M. Allan, and W. J. Zhou, "Modeling of the Cost of EV Battery Wear Due to V2G Application in Power Systems", *Ieee Transactions on Energy Conversion*, **26**, (2011).
194. A. K. Padhi, K. S. Nanjundaswamy, and J. B. Goodenough, "Phospho-olivines as positive-electrode materials for rechargeable lithium batteries", *Journal of the Electrochemical Society*, **144**, (1997).
195. S. S. Choi and H. S. Lim, "Factors that affect cycle-life and possible degradation mechanisms of a Li-ion cell based on LiCoO_2 ", *Journal of Power Sources*, **111**, (2002).
196. S. K. Rahimian, S. C. Rayman, and R. E. White, "Maximizing the Life of a Lithium-Ion Cell by Optimization of Charging Rates", *Journal of the Electrochemical Society*, **157**, (2010).
197. S. S. Zhang, "The effect of the charging protocol on the cycle life of a Li-ion battery", *Journal of Power Sources*, **161**, (2006).
198. M. Z. Bazant, "Theory of Chemical Kinetics and Charge Transfer based on Nonequilibrium Thermodynamics", *Accounts of Chemical Research*, **46**, (2013).
199. P. Bai, D. A. Cogswell, and M. Z. Bazant, "Suppression of Phase Separation in LiFePO_4 Nanoparticles During Battery Discharge", *Nano Letters*, **11**, (2011).
200. S. Santhanagopalan, K. Smith, J. Nuebauer, G.-H. Kim, M. Keyser, and A. Pesaran, *Design and Analysis of Large Lithium-Ion Battery Systems*. USA: Artech House, 2015.
201. D. Shin, M. Poncino, E. Macii, and N. Chang, "A Statistical Model-Based Cell-to-Cell Variability Management of Li-ion Battery Pack", *Ieee Transactions on Computer-Aided Design of Integrated Circuits and Systems*, **34**, (2015).
202. M. Dubarry, N. Vuillaume, and B. Y. Liaw, "Origins and accommodation of cell variations in Li-ion battery pack modeling", *International Journal of Energy Research*, **34**, (2010).
203. J. Schmalstieg, S. Kabitz, M. Ecker, and D. U. Sauer, "A holistic aging model for $\text{Li}(\text{NiMnCo})\text{O}_2$ based 18650 lithium-ion batteries", *Journal of Power Sources*, **257**, (2014).
204. M. Ecker, N. Nieto, S. Kabitz, J. Schmalstieg, H. Blanke, A. Warnecke, *et al.*, "Calendar and cycle life study of $\text{Li}(\text{NiMnCo})\text{O}_2$ -based 18650 lithiumion batteries", *Journal of Power Sources*, **248**, (2014).
205. J. Li, E. Murphy, J. Winnick, and P. A. Kohl, "Studies on the cycle life of commercial lithium ion batteries during rapid charge-discharge cycling", *Journal of Power Sources*, **102**, (2001).
206. K. Smith, E. Wood, S. Santhanagopalan, G.-H. Kim, J. Neubauer, and A. Pesaran, "Models for Battery Reliability and Lifetime," presented at the Battery Congress 2013, Ann Arbor, MI, 2014.
207. Q. Zhang and R. E. White, "Capacity fade analysis of a lithium ion cell", *Journal of Power Sources*, **179**, (2008).

208. P. Liu, J. Wang, J. Hicks-Garner, E. Sherman, S. Soukiazian, M. Verbrugge, *et al.*, "Aging Mechanisms of LiFePO₄ Batteries Deduced by Electrochemical and Structural Analyses", *Journal of the Electrochemical Society*, **157**, (2010).
209. R. Deshpande, M. Verbrugge, Y. T. Cheng, J. Wang, and P. Liu, "Battery Cycle Life Prediction with Coupled Chemical Degradation and Fatigue Mechanics", *Journal of the Electrochemical Society*, **159**, (2012).
210. P. W. C. Northrop, M. Pathak, D. Rife, S. De, S. Santhanagopalan, and V. R. Subramanian, "Efficient Simulation and Model Reformulation of Two-Dimensional Electrochemical Thermal Behavior of Lithium-Ion Batteries", *Journal of the Electrochemical Society*, **162**, (2015).
211. B. Wu and R. E. White, "An initialization subroutine for DAEs solvers: DAEIS", *Computers & Chemical Engineering*, **25**, (2001).
212. Mathworks. (Accessed: June, 2015). *Matlab ODE15i*. Available at: <http://www.mathworks.com/help/matlab/ref/ode15i.html>
213. Lawrence Berkeley National Lab. (Accessed: November, 2014). *Sundials IDA*. Available at: https://computation.llnl.gov/casc/sundials/description/description.html#descr_ida
214. R. E. S. White, Venkat R., *Computational Methods in Chemical Engineering with Maple*. Berlin: Springer-Verlag, 2010.
215. L. T. Biegler, "An overview of simultaneous strategies for dynamic optimization", *Chemical Engineering and Processing*, **46**, (2007).
216. A. Wachter and L. T. Biegler, "On the implementation of an interior-point filter line-search algorithm for large-scale nonlinear programming", *Mathematical Programming*, **106**, (2006).
217. B. Suthar, P. W. C. Northrop, R. D. Braatz, and V. R. Subramanian, "Optimal Charging Profiles with Minimal Intercalation-Induced Stresses for Lithium-Ion Batteries Using Reformulated Pseudo 2-Dimensional Models", *Journal of the Electrochemical Society*, **161**, (2014).
218. B. Suthar, P. W. C. Northrop, D. Rife, and V. R. Subramanian, "Effect of Porosity, Thickness and Tortuosity on Capacity Fade of Anode", *Journal of the Electrochemical Society*, **162**, (2015).

Appendix A: Additional Examples of the Perturbation and Switch Method

This chapter contains excerpts from the following journal article, reproduced here with permission from Elsevier:

Lawder, Matthew T., Ramadesigan, Venkat, Suthar, Bharat K., Subramanian, Venkat R. "Extending explicit and linearly implicit ODE solvers for index-1 DAEs" *Computers and Chemical Engineering*, 82(2015) 283-292

A.1: Wu and White Problem

An example of a two equation system representing a thin film nickel hydroxide electrode described in Wu and White²¹¹ is studied during the charging process. This system can cause difficulty in determining consistent ICs. The system is represented by the equations:⁵⁶

$$\frac{\rho V}{W} \frac{dy(t)}{dt} = \frac{j_1}{F} \quad (8.1)$$

$$j_1 + j_2 - i_{app} = 0 \quad (8.2)$$

where:

$$j_1 = i_{o,1} \left[2(1 - y(t)) \exp\left(\frac{(z(t) - \phi_1)F}{2RT}\right) - 2y(t) \exp\left(-\frac{(z(t) - \phi_1)F}{2RT}\right) \right] \quad (8.3)$$

$$j_2 = i_{o,2} \left[\exp\left(\frac{(z(t) - \phi_2)F}{RT}\right) - \exp\left(-\frac{(z(t) - \phi_2)F}{RT}\right) \right] \quad (8.4)$$

The parameters of the system are given in Table A-1. The differential variable y represents the nickel hydroxide mole fraction and the algebraic variable z represents the potential difference at the solid liquid interface. In a discharged state, the mole fraction of the nickel hydroxide is estimated to be:

$$y(0) = 0.05 \quad (8.5)$$

under the algebraic constraint, the consistent IC for the potential must be:

$$z(0) \approx 0.350236 \quad (8.6)$$

Table A-1: Parameters for Nickel Hydroxide Electrode.

Symbol	Parameter	Value	Units
F	Faraday Constant	96487	C/mol
R	Gas Constant	8.3143	J/(mol K)
T	Temperature	303.15	K
ϕ_1	Equilibrium potential	0.420	V
ϕ_2	Equilibrium potential	0.303	V
W	Mass of active material	92.7	g
V	Volume	1x10 ⁻⁵	m ³
i_{o1}	Exchange current density	1x10 ⁻⁴	A/cm ²
i_{o2}	Exchange current density	1x10 ⁻¹⁰	A/cm ²
i_{app}	Applied current	1x10 ⁻⁵	A/cm ²
ρ	Density	3.4	g/cm ³

(Several imaginary roots are solutions to the algebraic constraint, but these are non-physical solutions, so they are not useful for the electrode equations shown here).

When deviating from the consistent ICs, many initialization routines and solvers fail to obtain a solution. Table A-2 shows the range of possible ICs for the algebraic variable that provide a solution for different solvers and approaches including the proposed single-step approach. Under normal conditions (no initialization), these solvers require initial guesses that are very close to the consistent values. The proposed single-step approach greatly widens the possible range of ICs. The solution for a full charge of the electrode is shown in Figure A-1 (with an initial guess $z(0)=0.7$). For systems where the ICs are not easily available or obvious from the physical system, the expanded range of possible initial guesses is important for obtaining a solution. As mentioned in Chapter 2, a compiled single procedure can be obtained for a nonlinear DAE system with this approach just like a procedure for ODEs. This helps improve the efficiency and robustness for inverse optimization problems (optimal control and parameter/state estimation).

Table A-2: Comparison of working ranges of initial algebraic guess for Example 2 using different solvers. The Maple dsolve approach uses Maple’s rkf45 method. ^{49, 50, 212, 213}

Solver	Algebraic Range
Maple dsolve	$z(0)=0.3502359$, Exact conditions required
MATLAB ode15i	$0.342 \leq z(0) \leq 0.365$
MATLAB ode15s	$0.271 \leq z(0) \leq 0.474$
SUNDIALS IDA	$-1.27 \leq z(0) \leq 1.87$
Proposed Approach Maple dsolve	$-9.13 \leq z(0) \leq 9.85$

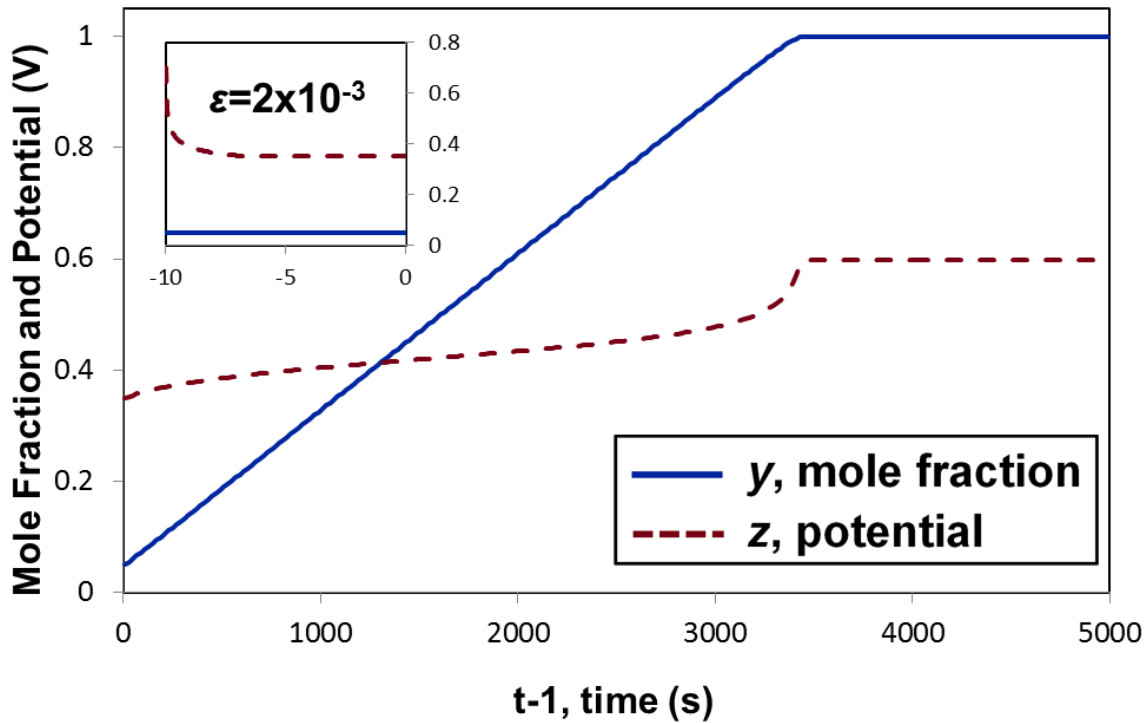


Figure A-1: Solution to Example 1.

A.2: Implicit ODE converted to DAE solved with Explicit Solver

The proposed approach can also be used to solve implicit ODEs. Consider the implicit ODE:

$$\left(\frac{dy(t)}{dt}\right)^2 + \left(\frac{dy(t)}{dt}\right)(y(t) + 1) + y(t) = \cos\left(\frac{dy(t)}{dt}\right) \quad (8.7)$$

This problem cannot be directly solved using explicit solvers. When attempted, Maple states that IC for dy/dt is not known or the system cannot be converted to explicit ODE form.

However, including a substitution:

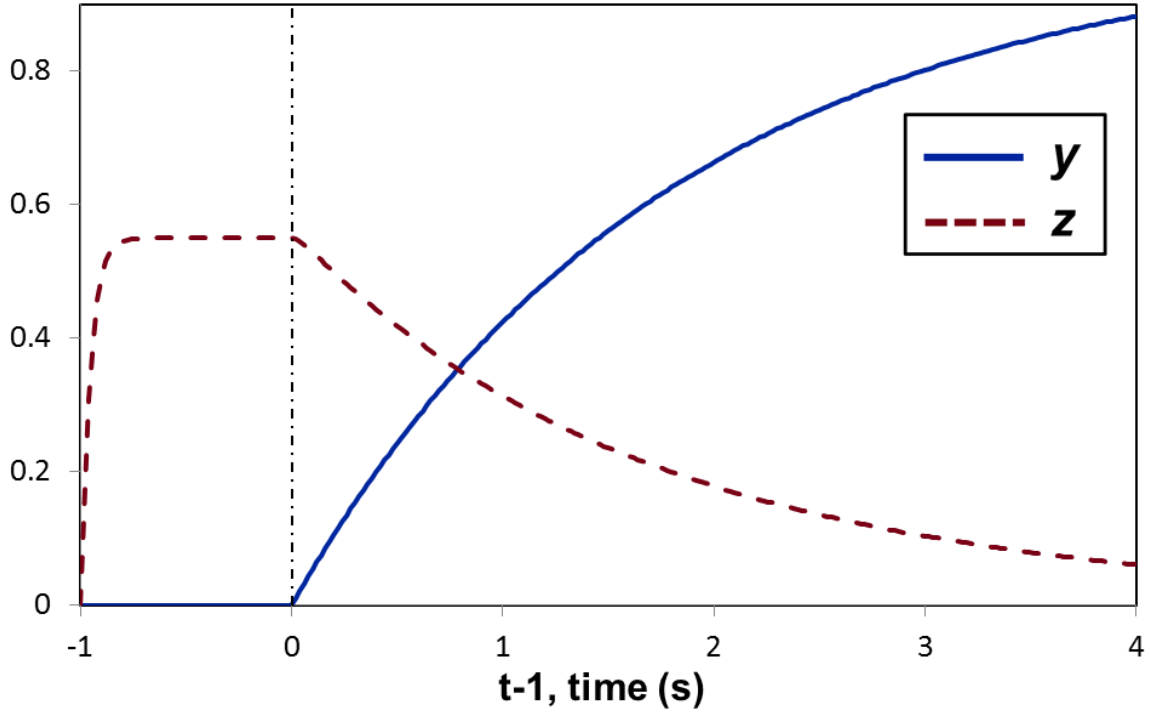


Figure A-2: Solution to Example 2.

$$\frac{dy(t)}{dt} = z(t) \tag{8.8}$$

converts Eq. (8.7) into:

$$z(t)^2 + z(t)(y(t) + 1) + y(t) = \cos(z(t)) \tag{8.9}$$

This adds a variable z , allowing the proposed approach to be used. The proposed approach is applied to Eqs. (8.8) and (8.9) leading to:

$$\varepsilon \left(2z(t) \frac{dz(t)}{dt} + \frac{dz(t)}{dt} (y(t) + 1) + z(t) \frac{dy(t)}{dt} + \frac{dy(t)}{dt} + \sin(z(t)) \frac{dz(t)}{dt} \right) = z(t)^2 + z(t)(y(t) + 1) + y(t) - \cos(z(t)) \tag{8.10}$$

$$\frac{dy(t)}{dt} = z(t) \left(\frac{1}{2} + \frac{1}{2} \tanh(1000(t-1)) \right) \quad (8.11)$$

where $q=1000$ and $t_j=1$ for the switch function. The results for both initialization and simulation are shown in Figure A-2 for the system solved using $\varepsilon = 0.1$ with ICs of:

$$y(0) = 0 \quad z(0) = 0 \quad (8.12)$$

The converged value for $z(0)$ from the initialization portion of the solver is 0.550.

A.3: Partial Differential Equation Discretized to DAEs

When PDEs are discretized they can create a system of DAEs. Many of these systems consist of variables with explicit time derivatives (like concentration) and static variables (like potential which may not consist of time derivatives, but still change with time because other variables in the system change with time). Consider the following set of PDEs:

$$\frac{\partial y}{\partial t} = \frac{\partial^2 y}{\partial x^2} - y(1+z) \quad (8.13)$$

$$\frac{\partial^2 z}{\partial x^2} = (1-y^2) \exp(-z) \quad (8.14)$$

with the boundary conditions:

$$\left. \frac{\partial y}{\partial x} \right|_{x=0} = 0 \quad y|_{x=1} = 1 \quad (8.15)$$

$$\left. \frac{\partial z}{\partial x} \right|_{x=0} = 0 \quad z|_{x=1} = 0 \quad (8.16)$$

Though $\partial z/\partial t$ is not present in the system, z changes with time as y changes with time. The model can be solved using numerical method of lines²¹⁴ which will discretize the spatial derivatives over a series of node points between the system's boundaries. When discretizing for the spatial variable the system becomes:

$$\frac{dy_i}{dt} = \frac{1}{h^2}(y_{i+1} - 2y_i + y_{i-1}) - y_i(1 + z_i) \quad (8.17)$$

$$\frac{1}{h^2}(z_{i+1} - 2z_i + z_{i-1}) = (1 - y_i^2) \exp(-z_i) \quad (8.18)$$

where h is the length between node points. And the boundary conditions become:

$$\frac{1}{2h}(3y_0 - 4y_1 + y_2) = 0 \quad y_{N+1} = 1 \quad (8.19)$$

$$\frac{1}{2h}(3z_0 - 4z_1 + z_2) = 0 \quad z_{N+1} = 0 \quad (8.20)$$

where N is the number of interior node points of the system. Converting to the proposed approach the system equations become:

$$\frac{dy_i}{dt} = \left[\frac{1}{h^2}(y_{i+1} - 2y_i + y_{i-1}) - y_i(1 + z_i) \right] \left(\frac{1}{2} + \frac{1}{2} \tanh(1000(t-1)) \right) \quad (8.21)$$

$$\begin{aligned} & \frac{-\varepsilon}{h^2} \left[\frac{dz_{i+1}}{dt} - 2 \frac{dz_i}{dt} + \frac{dz_{i-1}}{dt} + 2y_i \frac{dy_i}{dt} \exp(-z_i) + (1 - y_i^2) \frac{dz_i}{dt} \exp(-z_i) \right] \\ & = (1 - y_i^2) \exp(-z_i) - \frac{1}{h^2}(z_{i+1} - 2z_i + z_{i-1}) \end{aligned} \quad (8.22)$$

And the boundary equations are:

$$\frac{-\varepsilon}{2h} \left[3 \frac{dy_0}{dt} - 4 \frac{dy_1}{dt} + \frac{dy_2}{dt} \right] = \frac{1}{2h}(3y_0 - 4y_1 + y_2) \quad -\varepsilon \frac{dy_{N+1}}{dt} = y_{N+1} - 1 \quad (8.23)$$

$$\frac{-\varepsilon}{2h} \left[3 \frac{dz_0}{dt} - 4 \frac{dz_1}{dt} + \frac{dz_2}{dt} \right] = \frac{1}{2h}(3z_0 - 4z_1 + z_2) \quad -\varepsilon \frac{dz_{N+1}}{dt} = z_{N+1} \quad (8.24)$$

For standard solvers the system cannot be solved for a large number N using explicit solvers (*i.e.*, one cannot convert this system of DAEs to explicit ODEs of the form $dy/dt = f$. Maple's `dsolve`, even with consistent ICs ($y_i(0)=1$ and $z_i(0)=0$), cannot solve the system for N greater than 5. Maple aims to convert the DAE system to an explicit ODE system of the form $dy/dt = f$ and fails for larger values of N . However using the single step proposed approach

loosens the restrictions on the number of interior node points and increases the solving speed in Maple without having to use solvers involving Newton type iterations. Larger values of N may be required for higher accuracy and better convergence. Figure A-3 shows the value of y at $x=0, 1/3, 2/3,$ and 1 for $N=2$ and $N=11$ with $\varepsilon=1 \times 10^{-5}$). The values at $N=11$ have converged to more accurate values, especially for values closer to $x=0$. Consistent ICs ($y_i(0)=1$ and $z_i(0)=0$) were used for Figure A-3. The proposed approach can use the standard Maple dsolve approach to solve for more internal node points, without having to use direct DAE solvers that use Newton-Raphson type iterations. Even at lower number of node points, the proposed approach is faster than standard simulation techniques as it provides Maple with an approximate ODE that it can solve directly. At $N=5$ the proposed approach solves in 159ms using Maple dsolve, over an order of magnitude faster than the standard techniques inbuilt in Maple.

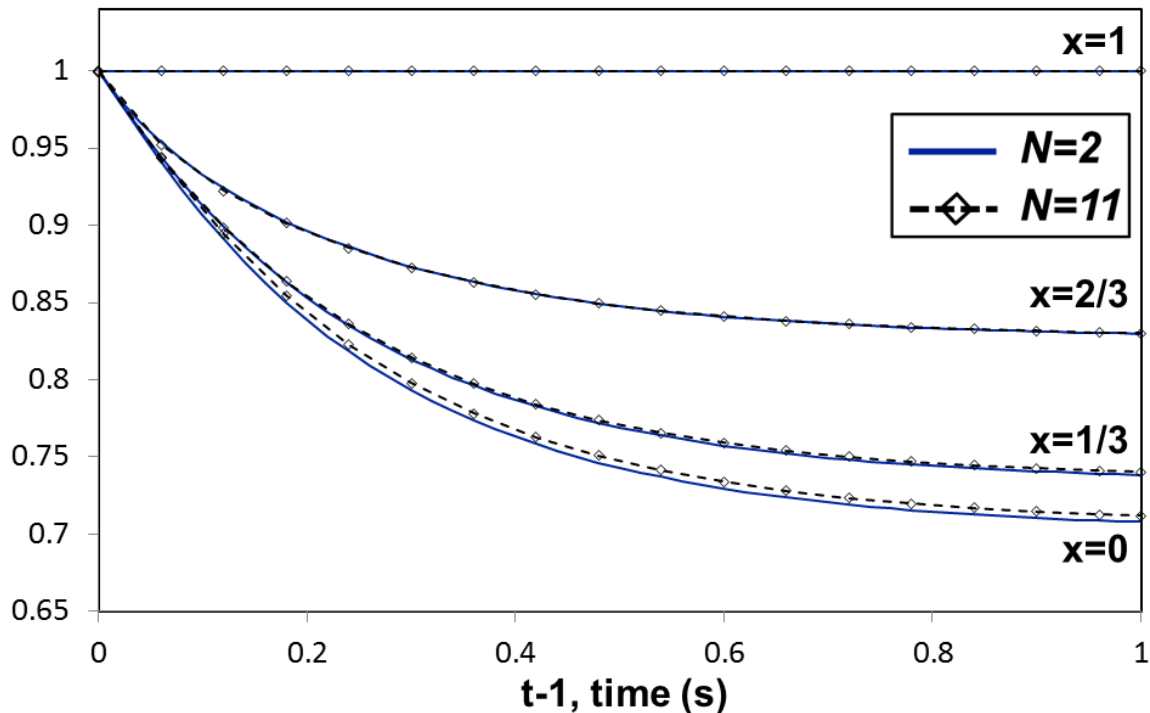


Figure A-3: Solution to Example 3 for $N=2$ and $N=11$ at four different x -values.

Appendix B: Methods for Optimization

B.1 Optimization Simulation: Objectives and Constraints

The goal of the battery optimization in Chapter 4 is to find the charging protocol that will maximize the amount of charge stored in a given time period while limiting the negative effects of the charging protocol. There are many different methods for optimization simulation, but the type of optimization being performed in this work is simultaneous nonlinear programming optimization.²¹⁵ In order to perform the optimization, the battery model equations are first spatially discretized and then temporally discretized in order to create a set of nonlinear algebraic equations. An objective function and path constraints are then applied to the system resulting in a large nonlinear program which is then solved using IPOPT (a nonlinear programming solver).²¹⁶ IPOPT will iterate solutions within the bounds until finding a solution with the maximum value of the objective function. Note that in practice, the IPOPT code objective function will find the minimum of the objective function, therefore in the cases stated, the objective function contains the negative of the stored. The optimization performed in Chapter 4 will be outlined below.

The objective function for maximizing charge stored will be:

$$\max Q = \int_0^{t_f} i_{app}(t) dt \quad (9.1)$$

where Q is the charge stored and i_{app} is the current applied to the battery. In the case outlined in Chapter 4, the i_{app} can only come from the solar array and therefore there will be a constraint such that:

$$0 \leq i_{app}(t) \leq i_{max}(t) \quad (9.2)$$

where:

$$i_{max}(t) = i_o \sin \left(\frac{(t-6)\pi}{12} \right) \quad (9.3)$$

with t in hours. Additionally the Voltage of the system is constrained by the safe limits of operation such that:

$$2.8 \leq V(t) \leq 4.15 \quad (9.4)$$

Under the standard charging scenario (see Figure 4.3), optimization is not performed and the i_{app} follows the maximum charge until reaching the maximum voltage at which time the battery is considered fully charged. Under this scenario the SEI layer growth is tracked. The amount of growth to the SEI layer from the base case is represented by δ_{SEI}^{base} . When optimization is performed to maximize Q , Eq. (9.1) will be used as the objective function.

This optimization will increase the amount of charge stored by utilizing a different charging protocol which allows slightly more charge to be stored before reaching the voltage cut-off of 4.15. In addition to increasing the charge stored, the SEI layer growth will be restricted so that it does not increase from the base case. For further optimization, the growth of the SEI layer will seek to be limited without greatly reducing the amount of charge stored. In order to limit the amount of SEI layer growth, an additional constraint to the system is included shown as:

$$0 \leq \delta_{SEI} \leq 0.9 \delta_{SEI}^{base} \quad (9.5)$$

Since the SEI layer only grows and cannot shrink under our assumptions, this constraint will only affect the SEI at the final simulation time.

This constraint limits the SEI layer growth of the system to only 90% of the SEI layer growth in the base case. Assuming the SEI layer growth is the predominant form of capacity, reducing growth per cycle by 10% will increase total cycle life of the battery by 11.1%. The final case that reduces fade still includes the objective function to maximize the amount of charge

stored. For results of these cases see Chapter 4. Using both the objective function and constraints allows for controlling multiple variables within the simulation.

The M.A.P.L.E lab has worked on optimization of Li-ion battery models for different applications, targeting a variety of internal states for constraints. These topics include finding the best charging profiles for mechanically constrained systems¹⁴⁸ and high stress systems²¹⁷ as well as analyzing design characteristics such as electrode porosity, thickness, and tortuosity.²¹⁸

B.2 Graphical User Interface for Battery Optimization

In order to provide easier access and demonstration of the M.A.P.L.E. group's battery optimization models, a graphical user interface (GUI) was developed in Excel and VBA to allow for users outside the lab to utilize the optimization simulation. For faster solving, the optimization code, which was developed in Maple (software), was converted into an executable C file. This executable file used text files as inputs to allow for changing of parameters such as simulation time, or constraints such as maximum allowable charging current. The output of the executable file is also placed into a text file. The GUI was created to allow easy manipulation of the input text files and running of the executable. Additionally, once the executable has finished running and outputs the results, the GUI aggregates the results into a viewer panel with important charts and metrics of the optimization simulation. The GUI runs a full optimization simulation of the system through the executable file just as the original code would.

The GUI home window is shown in Figure B-1. The home window allows users to set the allowable charging time (30min; 45min; 1hour) and set upper bounds for temperature, T_{max} , (310K; 315K; 320K; Unbounded), maximum allowable current, i_{max} (1C; 1.5C; 2C), and lower bound for cycle life (500 cycles; 750 cycles; 1000cycles). The objective function will try to maximize the charge stored in all cases and the voltage will be limited to operation between 2.8V

and 4.1V. The set of objectives and constraints for the system based on user input can be shown as:

$$\max Q = \int_0^{t_f} i_{app}(t) dt \quad (9.6)$$

$$0 \leq i_{app}(t) \leq i_{max} \quad (9.7)$$

$$2.8 \leq V \leq 4.1 \quad (9.8)$$

$$0 \leq T(t) \leq T_{max} \quad (9.9)$$

$$0 \leq \delta_{SEI} \leq \delta_{SEI}^{max} \quad (9.10)$$

The SEI layer growth is used to determine the cycle life of the battery. When the minimum cycle life of the battery is required to be 1,000 cycles, the maximum allowable SEI layer growth, δ_{SEI}^{max} , will be half of the value allowed for the 500 cycle life case.

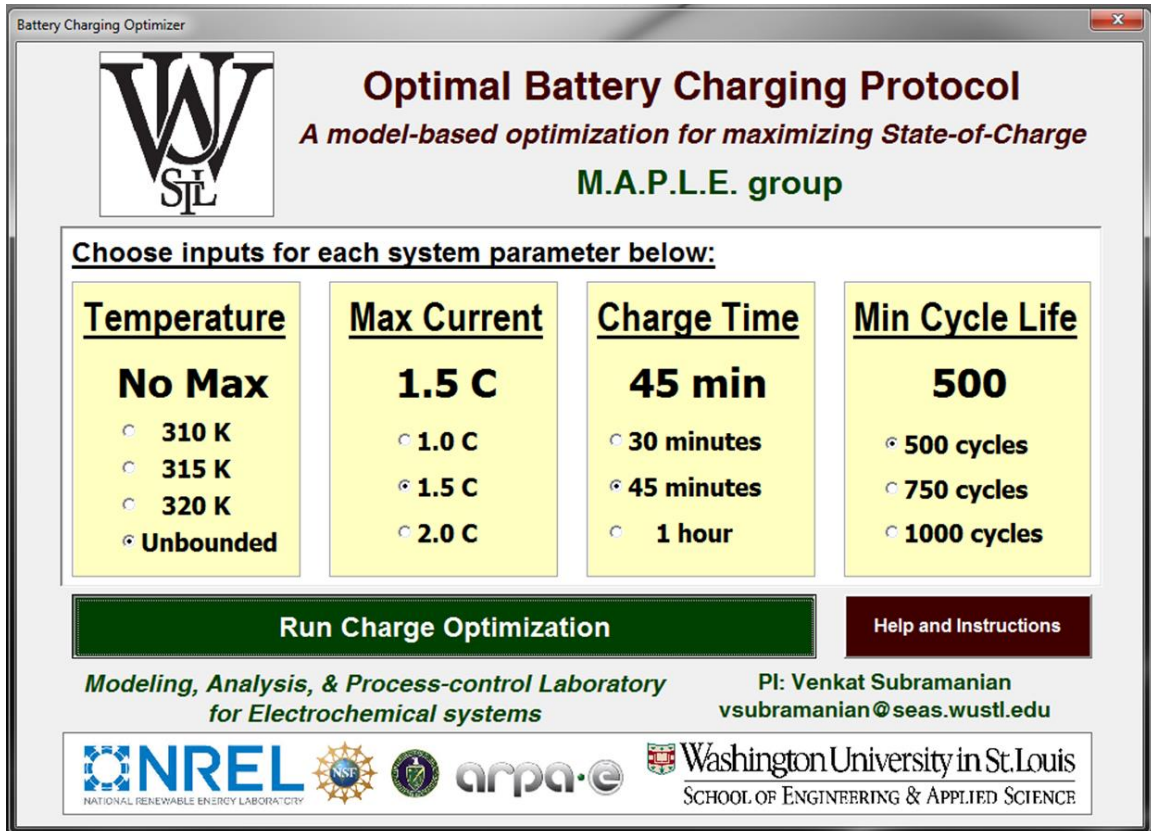


Figure B-1: GUI for battery optimization.

After running the optimization executable and obtaining the optimal charge protocol, the GUI will create charts from the results of the applied current, voltage, temperature and SOC of the battery with respect to time. Note, the SOC is measured as the amount of lithium in the anode divided by the maximum amount of lithium allowed in the anode. Additionally, the GUI will report the input bounds and simulation time as well as the final SOC. A view of the results window from the GUI is shown in Figure B-2.

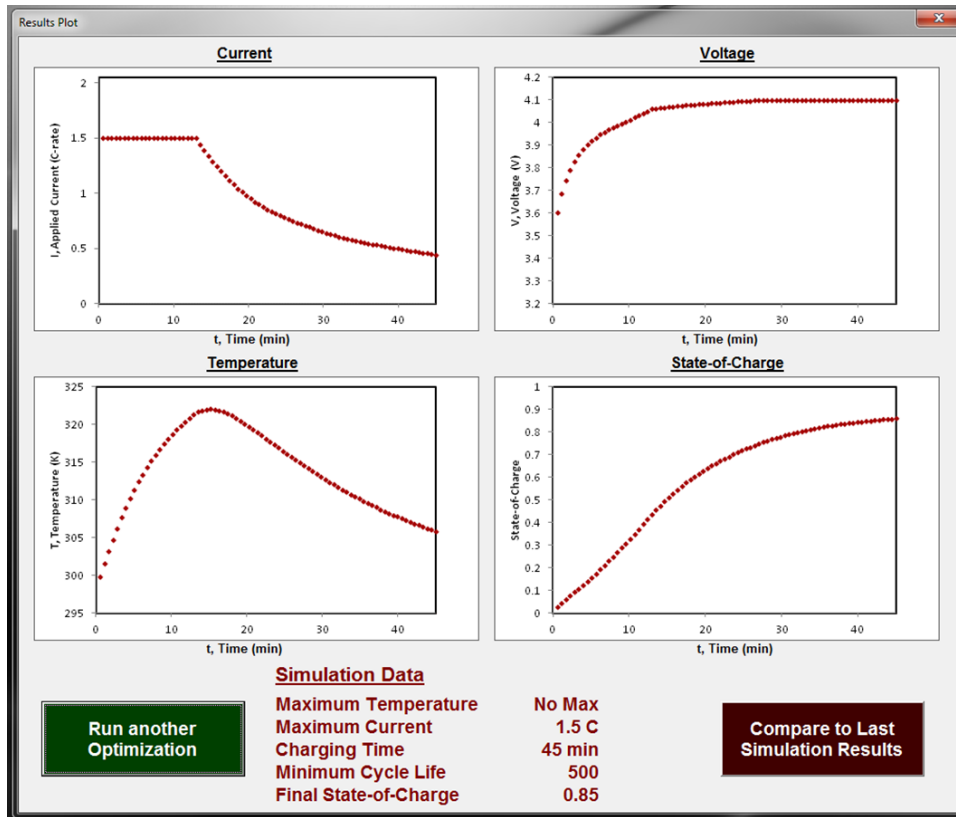


Figure B-2: Results from the GUI.

A comparison between two successive simulations can be done as well. Figure B-3 shows comparisons of two different cases. The GUI allows for any user to access many different cases to test battery optimization without the need for intimate knowledge of the battery model, optimization methods, or the coding language (in this case Maple and C) that the original optimization code was written in. This type of interface greatly lowers the barrier for someone

new to understand how the battery optimization works and view customized results. A video tutorial of the GUI that walks the user through several cases is available on the M.A.P.L.E group's website at http://depts.washington.edu/maple/Batteryopt_new.html.

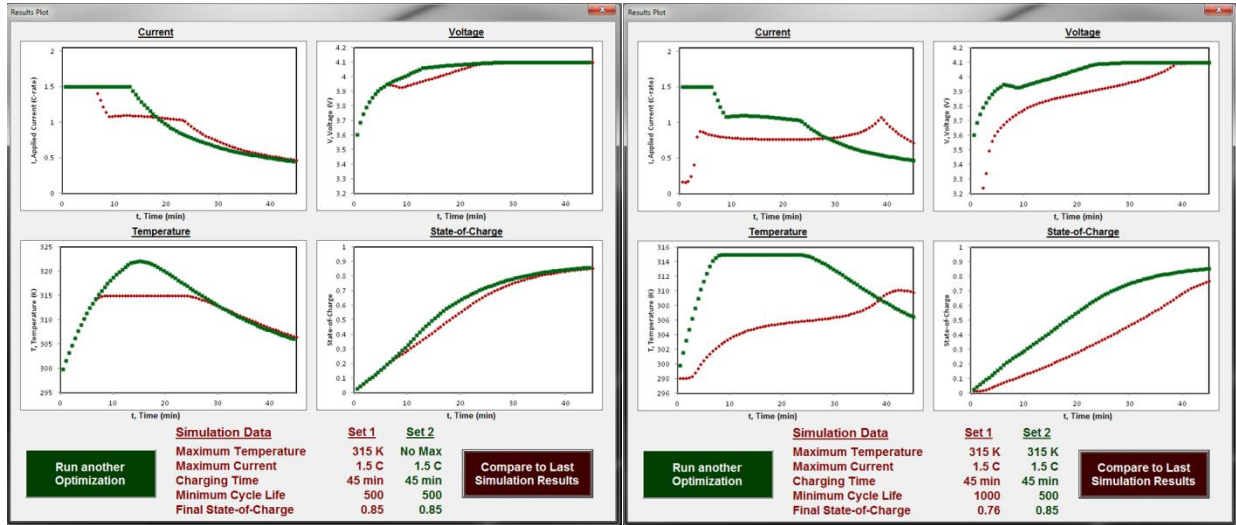


Figure B-3 Two comparisons of different cases.

Appendix C: Drive Cycles

DST: Dynamic Stress Test

Duration: 360s

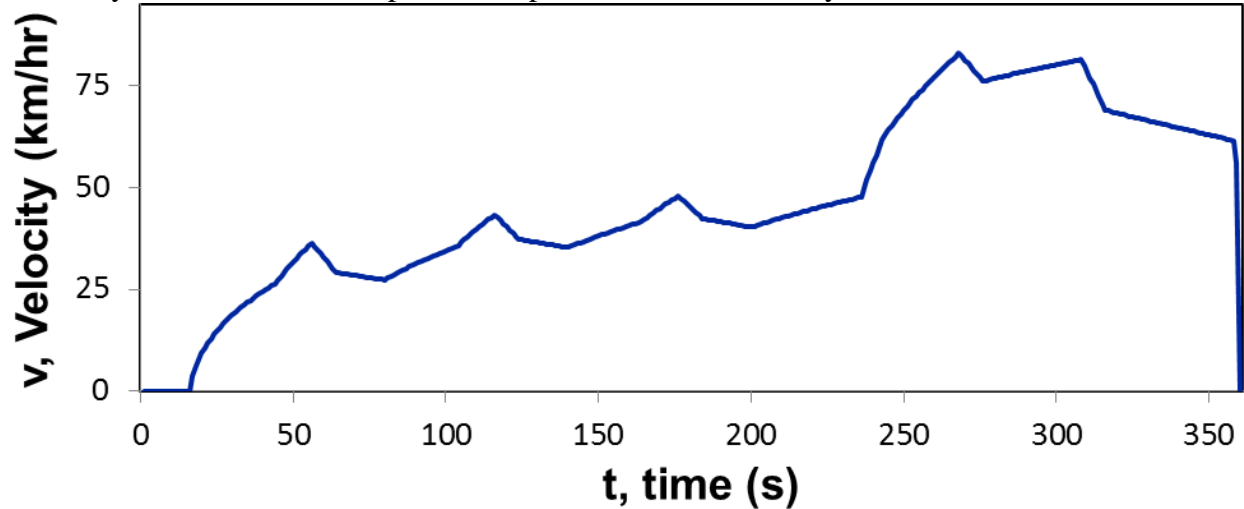
Distance: 4.63km

Average Velocity: 46.3km/h

Max Velocity: 83km/h

Regenerative Braking to Propulsion Power Ratio: 0.052

*Velocity curve derived from prescribed power curve for DST cycle



NEDC: New European Driving Cycle

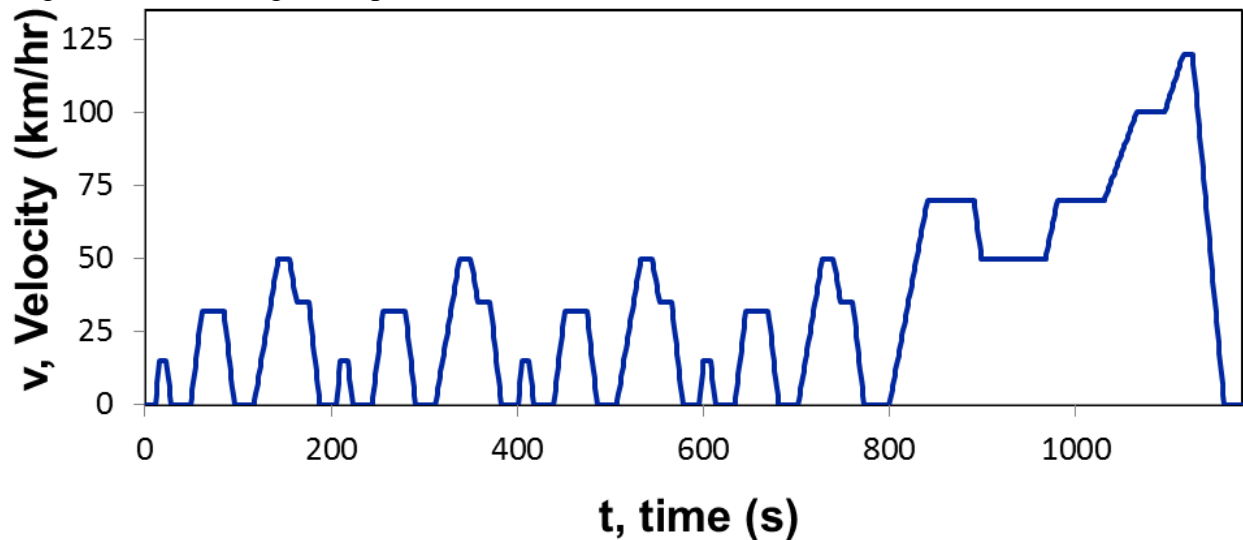
Duration: 1180s

Distance: 11.02km

Average Velocity: 33.6km/h

Max Velocity: 120km/h

Regenerative Braking to Propulsion Power Ratio: 0.183



ECE-15: Elementary Urban Cycle

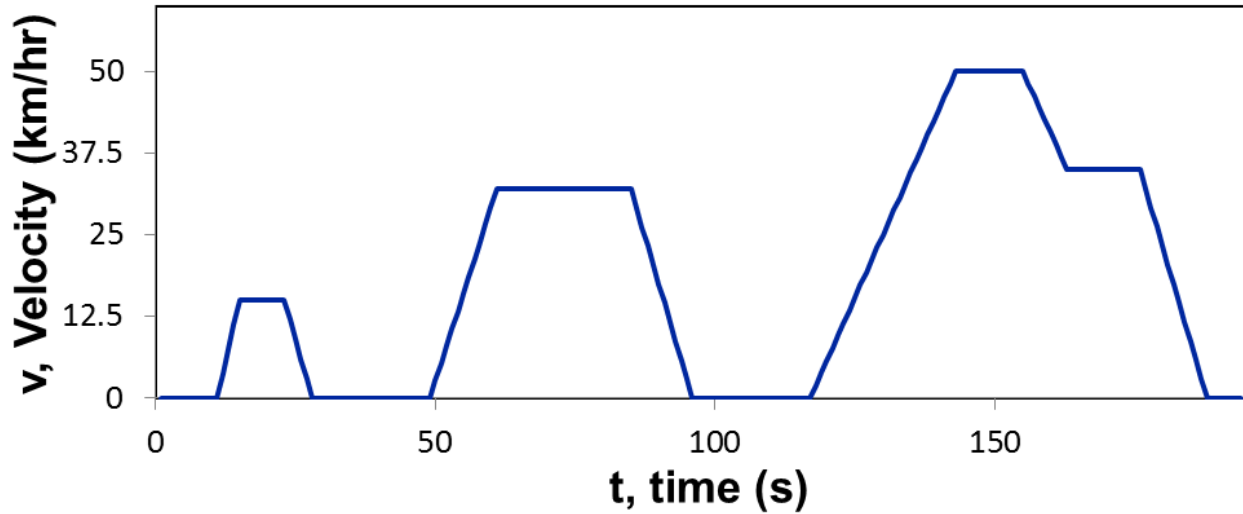
Duration: 195s

Distance: 1.00km

Average Velocity: 18.4km/h

Max Velocity: 50km/h

Regenerative Braking to Propulsion Power Ratio: 0.423



EUDC: Extra-Urban Driving Cycle

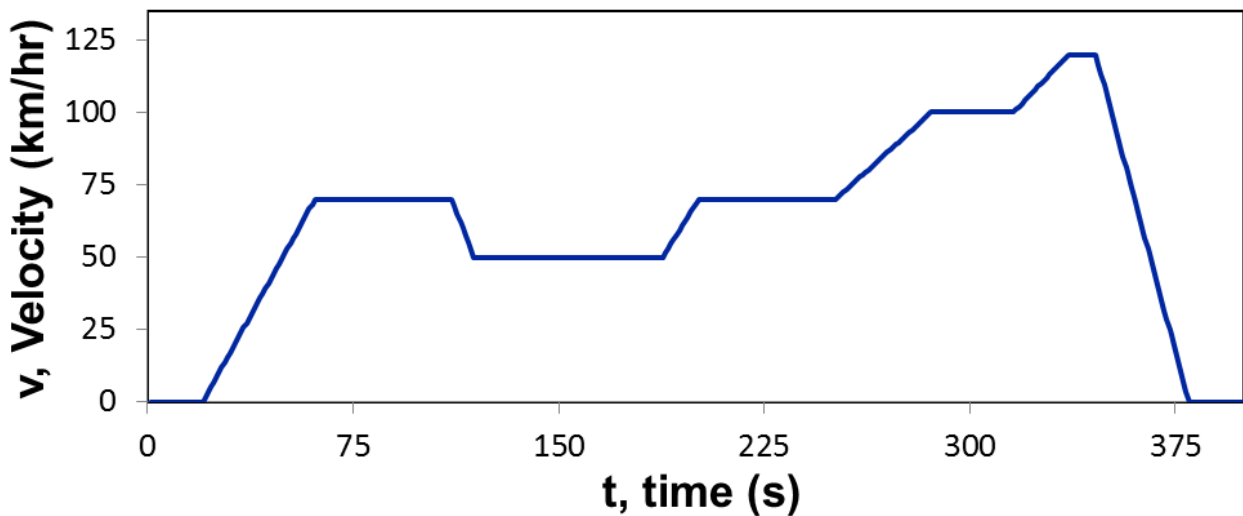
Duration: 400s

Distance: 6.96km

Average Velocity: 62.6km/h

Max Velocity: 120km/h

Regenerative Braking to Propulsion Power Ratio: 0.143



UUDS: Urban Dynamometer Driving Schedule

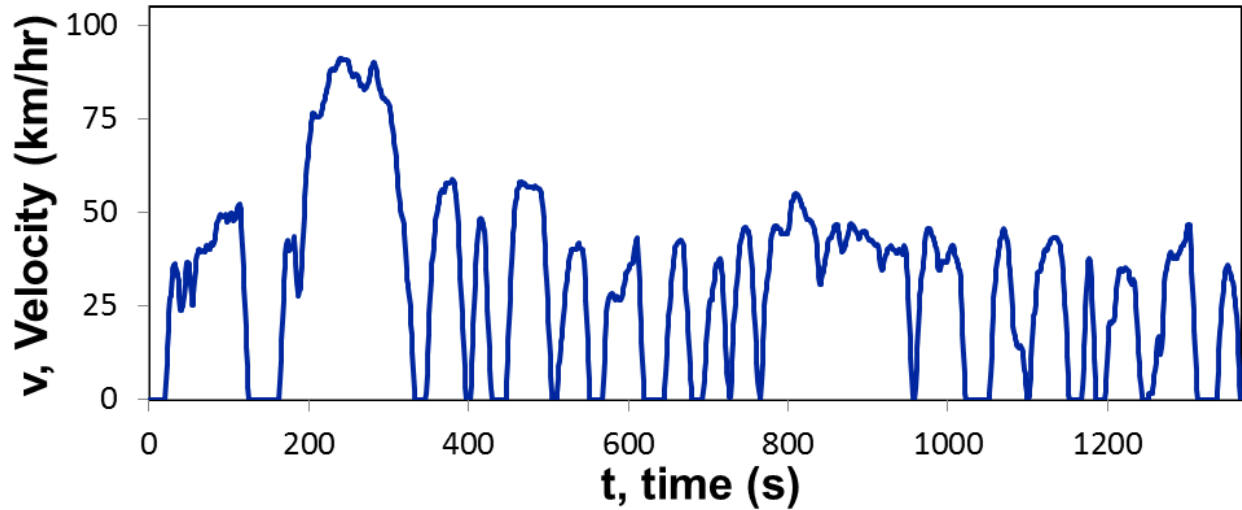
Duration: 1370s

Distance: 11.99km

Average Velocity: 31.5km/h

Max Velocity: 91km/h

Regenerative Braking to Propulsion Power Ratio: 0.363



FTP-75: Federal Test Procedure

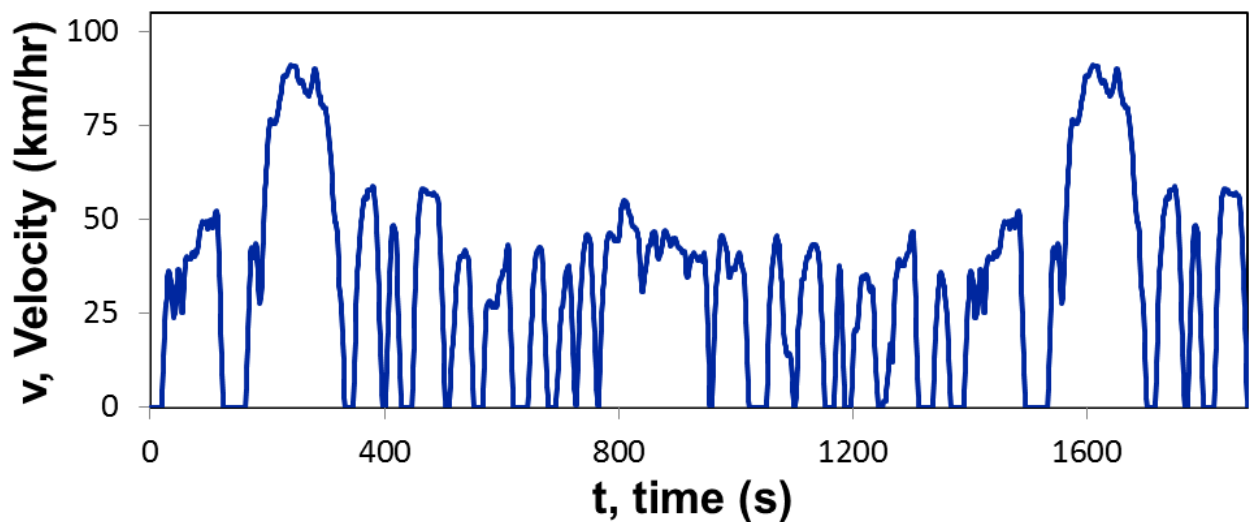
Duration: 1875s

Distance: 17.79km

Average Velocity: 34.2km/h

Max Velocity: 91km/h

Regenerative Braking to Propulsion Power Ratio: 0.357



HWFET: Highway Fuel Economy Driving Schedule

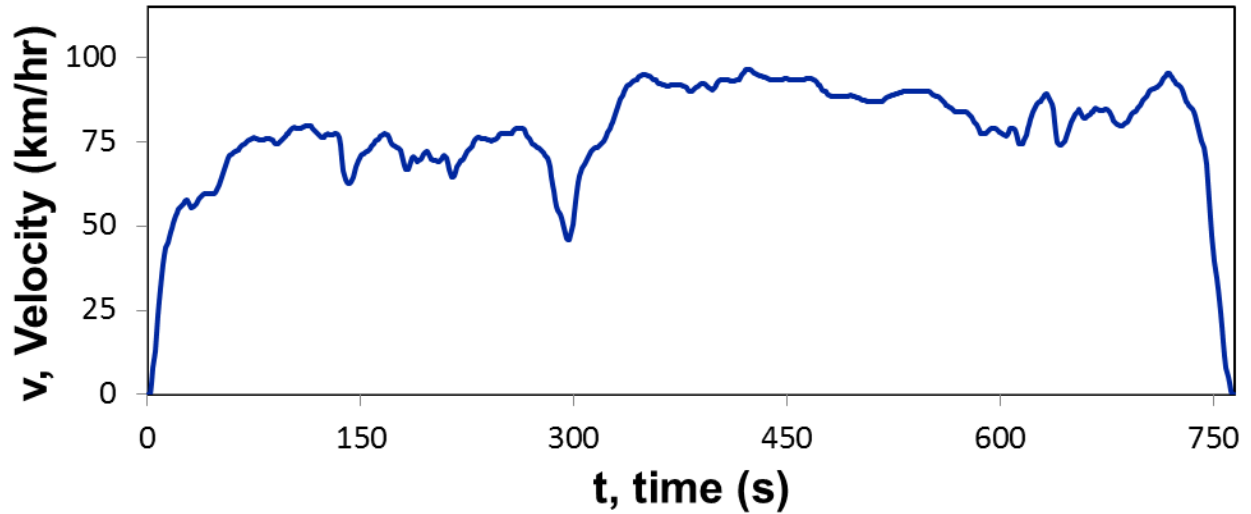
Duration: 765s

Distance: 16.45km

Average Velocity: 77.7km/h

Max Velocity: 96km/h

Regenerative Braking to Propulsion Power Ratio: 0.171



US06: Supplemental FTP Driving Schedule

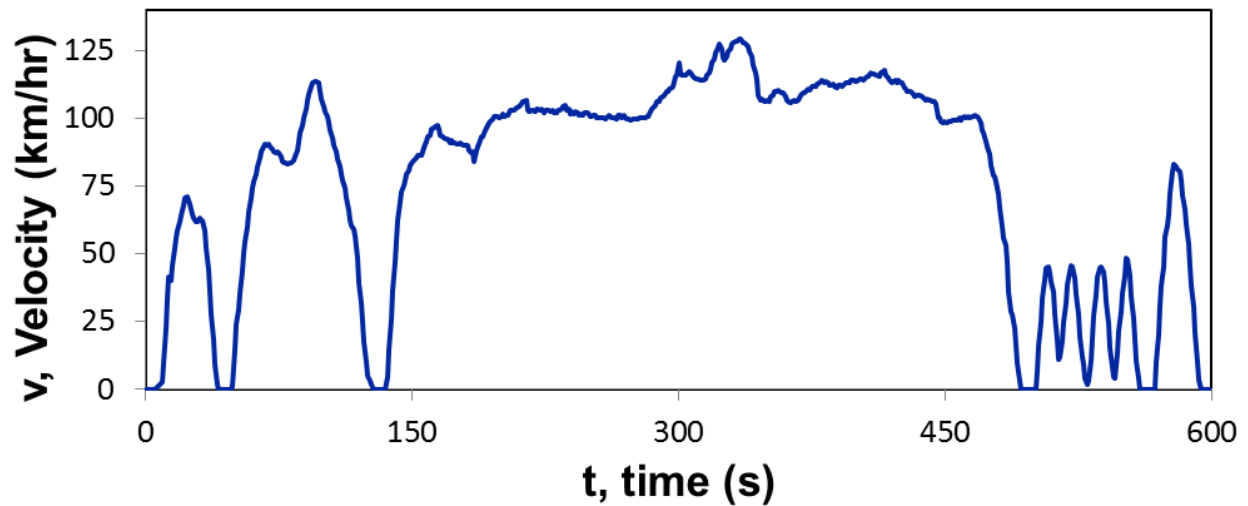
Duration: 600s

Distance: 12.89km

Average Velocity: 77.9km/h

Max Velocity: 129km/h

Regenerative Braking to Propulsion Power Ratio: 0.303



Appendix D: List of Abbreviations & Variables

Abbreviations

AE	Algebraic Equation
BCSC	Battery Capacity to Solar daily Capacity ratio
BESS	Battery Energy Storage System
BMS	Battery Management System
CC	Constant Current
CC-CV	Constant Current, Constant Voltage
DAE	Differential Algebraic Equation
DOD	Depth-of-Discharge
DST	Dynamic Stress Test
ECE-15	Elementary Urban Cycle
ECM	Equivalent-Circuit Model (battery)
EOL	End-of-Life
EUDC	Extra-Urban Driving Cycle
EV	Electric Vehicle
FD	Finite Difference
FTP-75	Federal Test Procedure
GHI	Global Horizontal Irradiance
HWFET	Highway Fuel Economy Driving Schedule
IC	Initial Conditions
ICE	Internal Combustion Engine
KMC	Kinetic Monte Carlo Model
Li-ion	Lithium ion
LPSP	Loss of Power Supply Probability
MIDC	Measurement and Instrumentation Data Center
NEDC	New European Driving Cycle
Ni-Cd	Nickel Cadmium
NiMH	Nickel Metal Hydride
NREL	National Renewable Energy Lab
ODE	Ordinary Differential Equations
P2D	Porous electrode Pseudo Two Dimensional model
PHEV	Plug-in Hybrid Electric Vehicle
RK	Runge-Kutta
R-P	Regenerative braking power to propulsion power
SCC	System Supervisory Control
SEI	Solid-Electrolyte Interface
SOC	State-of-Charge
SPM	Single Particle Model
TOU	Time-of-Use
UDDS	Urban Dynamometer Driving Schedule
US06	Supplemental FTP Driving Schedule
VMT	Vehicle Miles Traveled

Variables and parameters

α	SEI constant
a	Specific surface area
b	Diode ideality constant
A	Empirical coefficient
A_f	Projected 2D vehicle area
c	Liquid-phase lithium concentration
c^{avg}	Average solid-phase lithium concentration
c_e	Electrolyte concentration
c^s	Solid-phase lithium concentration
c_{max}^s	Maximum lithium concentration
c_{surf}^s	Lithium surface concentration
C_C	Capacitance
C_D	Drag coefficient
δ_{SEI}	SEI layer thickness
D_{eff}	Effective diffusion coefficient
D_s	Solid-phase diffusion coefficient
ε	Perturbation (Ch. 2 only)
ε_i	Porosity
F	Faraday's constant
F_{drag}	Aerodynamic drag force
F_{drive}	Driving acceleration force
F_g	Gravity force
F_{motor}	Motor force
F_{rr}	Rolling resistance force
i_{app}	Applied current
i_{int}	Intercalation current
i_{SEI}	SEI reaction current
I	Solar output current
I_0	Saturation current
I_{PV}	Photovoltaic current
j	Pore wall flux
κ_{eff}	Liquid-phase effective conductivity
k	Reaction rate constant
k_r	Rolling resistance coefficient
k_{SEI}	SEI reaction rate constant
l	Length of electrode
m	Vehicle mass
M	Molecular weight
N_{cycle}	Cycle number
Φ_1	Solid-phase potential
Φ_2	Liquid-phase potential
P_D	Power demanded
P_G	Power generated
P_{motor}	Motor power
q	Switch function weighting factor
Q	Charge stored

Variables and parameters (cont.)

ρ	Density
R	Gas constant
R_0	Ohmic resistance
R_{int}	Internal resistance
R_C	Capacitor parallel resistance
R^p	Particle radius
R_p	Parallel resistance
R_s	Series resistance
σ_{eff}	Solid-phase effective conductivity
θ	Roadway gradient (Ch. 5)
t_+	Transfer number
t_j	Perturbation time
T	Temperature
T_H	Switch function
U	Open circuit potential
v	Vehicle velocity
v_w	Wind velocity
V	Solar output voltage
V_b	Battery voltage
V_C	Capacitance voltage
V_{OC}	Open circuit voltage
V_t	Thermal voltage

Curriculum Vitae

MATTHEW T. LAWDER

Telephone: 314-920-2619
E-mail: mtlawder@gmail.com

4161 Laclede Ave.
St. Louis, MO 63108

PROFESSIONAL PROFILE

Completing Ph.D. in Energy, Environmental, and Chemical Engineering with experience in modeling, efficient simulation, and techno-economic analysis based on fundamental chemical engineering principles. Developed system-level models for coupling battery energy storage in large-scale applications including: electric vehicles, renewable integration, and microgrids. Created analysis tools for monitoring experimental and model based battery data sets. Simulated lithium-ion battery system life-cycle costs and value, delivering concise assessments. Received US Patent (#20140136169) for work in developing battery management systems to improve electric vehicle performance.

RESEARCH HIGHLIGHTS

- Developed system level models for environments utilizing large-scale lithium-ion battery storage and conducted life-cycle studies for batteries under application based cycling.
- Built a graphical user interface for our group battery optimization models allowing easy access and demonstration of codes.
- Experimental analysis of battery cycling large data sets including programming of analysis tools.
- Implemented optimal model-based charging protocols focused on reducing capacity fade.
- Refined numerical methods for solving differential algebraic equations by applying a perturbation approach with discrete switch for reducing consistency requirements.
- Funded in part by DOE ARPA-E award #DE-AR0000275 to develop better battery management systems for electric vehicles utilizing model-based control.

EDUCATION

Ph.D. Candidate Energy, Environmental, and Chemical Engineering *Aug. 2011-Dec. 2015*
Washington University, Saint Louis, MO GPA:3.83

B.S. Physics (with Honors) *Aug. 2007-May 2011*
Butler University, Indianapolis, IN *Minors: Astronomy and Math* GPA:3.81

High School, Saint Louis University High School *Aug. 2003-May 2007*

RESEARCH AND WORK EXPERIENCE

Washington University-Graduate Research Assistant (Ph.D.) *Jan. 2012-Present*

Thesis: “Modeling, Simulation, & Analysis of Lithium-Ion Batteries for Grid-Scale Applications”

Advisors: Venkat Subramanian and Pratim Biswas

- Built models for simulation of batteries in electric vehicle and electric grid environments focused on increasing battery life and utilization.
- Analyzed large battery cycling data sets to produce easy to use life metrics.
- Conducted techno-economic feasibility studies for grid scale battery implementation
- Collaborated with the National Renewable Energy Laboratory and Pacific Northwest National Laboratory.

Washington University Office of Sustainability-Intern *May 2014-Present*

- Analyzed potential for renewable energy projects (solar, wind, storage) on and off-campus
- Led team for producing educational outreach component for existing campus solar arrays

Washington University-Research Rotation Assistant in The Jay Turner Lab *Aug.-Dec. 2011*

- Implemented regional air dispersion models for emissions from St. Louis area

University of Idaho-Student Researcher *June-Aug. 2010*

As part of the National Science Foundation's Research Experience for Undergrads

Thesis: "Measuring Regional Regolith Depth across the Lunar Surface"

Advisor: Gwen Barnes

- Analyzed moon crater features with surface images from Lunar Reconnaissance Orbiter
- Calculated topsoil (regolith) depth in regions across the lunar surface

Butler University-Student Researcher *May-July 2009*

Advisor: Xianming Han

- Conducted experiments to analyze Fresnel diffraction patterns through pinholes
- Built a graphical user interface (in visual basic) to analyze diffraction patterns in digital images

PATENTS

V. R. Subramanian, V. Ramadesigan, P. W. C. Northrop, S. De, B. Suthar, **M. T. Lawder**, "Systems and methods for improving battery performance," US Patent: US20140136169 (May, 2014)

D. Sonawane, **M. T. Lawder**, M. Pathak, V. Ramadesigan, V. R. Subramanian, "Robust fail-safe iteration free approach for solving Index-1 DAEs arising from battery models," Provisional Patent Application Number: 62194678 (Submitted July, 2015)

ACADEMIC HONORS

- Electrochemical Society – IEEE Division student travel grant winner. *Spring 2014*
- MAGEEP 4th Energy and Environment Symposia Student video competition 2nd place. *2012*
- *Henry G. Swartz Jr. Fellowship* at Washington University in St. Louis *2011-2012*
- Member of Electrochemical Society *2012-Present*
- Member of Sigma Pi Sigma - Physics honor society *2010-Present*
- *Robert O. Whitesell Award* - given annually to a student in Butler's physics department *2010*
for academic excellence in Physics.
- *Howard Baker Award* - given annually to a student in Butler's physics department of *2009*
physics for excellence in the pursuit of a career in Physics and Astronomy

PUBLICATIONS

1. **M. T. Lawder**, V. Ramadesigan, B. Suthar, V. R. Subramanian. "Extending Explicit and Linearly Implicit ODE Solvers for Index-1 DAEs." *Computers and Chemical Engineering* (2015)
2. **M. T. Lawder**, V. Viswanathan, V. R. Subramanian. "Balancing Autonomy and Utilization of Solar Power and Battery Storage for demand based Microgrids." *Journal of Power Sources* **279** (2015)
3. **M. T. Lawder**, P. W.C. Northrop, V. R. Subramanian. "Model-based SEI Layer Growth and Capacity Fade Analysis for EV and PHEV Batteries and Drive Cycles." *Journal of the Electrochemical Society* **161**:14 (2014)
4. **M. T. Lawder**, B. Suthar, P. W.C. Northrop, S. De, C. M. Hoff, O. Leitermann, M. L. Crow, S. Santhanagopalan, V. R. Subramanian. "Battery Energy Storage System (BESS) and Battery Management System (BMS) for Grid-Scale Applications." *Proceedings of the IEEE* **102**:6 (2014)

5. G. D. Bart, R. D. Nickerson, **M. T. Lawder**, H. J. Melosh. "Global survey of lunar regolith depths from LROC images." *Icarus* **215**:2 (2011)
6. B. W. Murphy, A. N. Darragh, T. W. Harp, Z. J. Liu, B. B. Geiss, **M. T. Lawder**, M. J. McFall, K. A. Phifer. "Light Curve Analysis of Asteroids 619 Kolya, 9549 Akplatonov, 12466 1997 AS12, 15154 2000 FW 30, and 32505 2001 KF17." *Minor Planet Bulletin* **38** (2011)

PRESENTATIONS (FIRST AUTHOR)

1. Model-based Techno-Economic Analysis and Optimization of Battery Storage for Solar Energy (talk). *American Institute of Chemical Engineers Annual Meeting*. Salt Lake City, UT. November, 2015.
2. Model-based Techno-Economic Analysis of Battery Function for Energy Storage of Solar Energy (talk). *Electrochemical Society Fall Meeting*. Phoenix, AZ. October, 2015.
3. Techno-Economic Assessment of Battery Integration with Solar Power (talk). *MAGEEP-Solar Energy and Energy Storage Workshop*. Ankara, Turkey. June, 2015.
4. Model-Based Regional Comparison of Autonomy and Battery Utilization of Energy Storage Integration with Solar Power (talk). *Electrochemical Society Spring Meeting*. Chicago, IL. May, 2015.
5. Model-Based SEI Layer Growth in EV and PHEV Batteries for Standard Drive Cycles (talk). *Electrochemical Society Spring Meeting*. Chicago, IL. May, 2015.
6. Solar Powered Microgrid Autonomy and Battery Utilization (poster). *McDonnell Academy International Symposium*. St. Louis, MO. October, 2014.
7. Autonomy and Battery Utilization within Microgrids and Solar-Battery Applications (talk). *Electrochemical Society Fall Meeting*, Cancun, Mexico. October, 2014.
8. Modeling and Lifetime Assessment of Lithium-Ion Batteries Used for Solar Firming Applications and Grid Storage (talk). *Electrochemical Society Spring Meeting*, Orlando, FL. May, 2014.
9. Modeling and control of electrochemical energy storage systems for the renewable electric grid (poster). *Institute for Pure & Applied Mathematics Workshop III: Batteries and Fuel Cells*, Los Angeles, CA. November, 2013.
10. Modeling and Optimal Control of Energy Storage Devices for a Lithium-Ion Battery-Photovoltaic Hybrid System (talk). *Electrochemical Society Fall Meeting*, San Francisco, CA. October, 2013.
11. Modeling of a Lithium-ion Battery-Photovoltaic Solar Cell hybrid System (talk). *Electrochemical Society Spring Meeting*, Toronto, Canada. May, 2013.
12. Modeling and Simulation of Solar Cell Coupled with Recycled/reusable Lithium-ion Batteries (poster). *McDonnell Academy Global Energy and Environment Partnership 4th Energy and Environment Symposia*, Mumbai, India. December 2012.
13. Measuring Regolith Depth across the Lunar Surface (talk). *Butler Undergraduate Research Conference*, Indianapolis, IN. April, 2011.
14. Measuring Regolith Depth across the Lunar Surface (poster). *American Geophysical Union Fall Meeting*, San Francisco, CA. December, 2010.
15. Study of intensity pattern of Fresnel diffraction through a circular aperture (talk). *Butler Undergraduate Research Conference*, Indianapolis, IN. April, 2010.

CODING LANGUAGES

Worked on projects with Maple, MapleSim, Matlab, R, C++, Fortran, Visual Basic, HTML and SQL.

TEACHING ASSISTANT EXPERIENCE

Washington University in St. Louis

- Environmental Studies 405 Sustainability Exchange *Spring 2015*
- Mechanical Engineering & Materials Sci. 5610 Quant. Materials Science & Engineering *Fall 2014*
- Chemical Engineering 473 Chemical Engineering Lab *Fall 2013*
- Chemical Engineering 478 Process & Product Design *Spring 2013*
- Chemical Engineering 367 Transport Phenomena I *Fall 2012*

Butler University

- Physics 108 Elementary Physics (Lab) *Spring 2011*
- Physics 201/202 Introduction to Analytical Physics I and II (4 semesters) *2009-2011*

UNDERGRADUATE STUDENT RESEARCHERS

- Akanka Jagwani (IIT Gandhinagar, India), MAGEEP summer student, 2012
- Rachel Fenton, Washington University in St. Louis, 2014

COMMUNITY OUTREACH

- Big Brothers Big Sisters mentor, 2008-2011.
- LEGO Engineering in the Elementary Classroom, Spring 2012.
- ECS IEEE Division conference outreach, bi-annually at ECS meetings.
- Washington University Young Scientist Program, 2014-Present.

PERSONAL

- Enjoys running and racing marathons with a best time of 2 hours and 26 minutes (Boston, 2015-46th place). I also help organize a local Elite racing team (Big River Running) and have coached (assistant) cross country at a local high school (St. Louis University High).
- Energy and Environmental Blogger for Washington University in St. Louis' *The Common Reader* magazine and website (<https://commonreader.wustl.edu/blogs/>).

REFERENCES AVAILABLE UPON REQUEST